Technische Universität München
TUM School of Natural Sciences

Expanding the architecture of Single Ion-Conducting Polymer Electrolytes

Marina Wittig

Vollständiger Abdruck der von der TUM School of Natural Sciences der Technischen Universität München zur Erlangung einer

Doktorin der Naturwissenschaften (Dr. rer. nat.)

genehmigten Dissertation.

Vorsitz: Prof. Dr. Torben Gädt

Prüfende der Dissertation:

1. Prof. Dr. Dr. h.c. Bernhard Rieger
2. Prof. Dr. Tom Nilges

Die Dissertation wurde am 09.12.2024 bei der Technischen Universität München eingereicht und durch die TUM School of Natural Sciences am 15.01.2025 angenommen.

„Non, je ne regrette rien.“

-Édit Piaf

Die vorliegende Arbeit wurde in der Zeit von Februar 2021 bis Dezember 2024 am WACKER-Lehrstuhl für Makromolekulare Chemie, Technische Universität München, unter Betreuung von Herrn *Prof. Dr. Dr. h.c. Bernhard Rieger* angefertigt.

Acknowledgment

Vielen lieben Dank **Herr Prof. Dr. Dr. h.c. Bernhard Rieger** für die Möglichkeit, sowohl meine Bachelor- als auch Masterarbeit an Ihrem Lehrstuhl absolvieren und mit meinem Promotionsthema nochmal ein ganz neues Feld der Polymerchemie entdecken zu dürfen. Ihre Unterstützung während unserer wöchentlichen Lehrstuhlseminare, als auch der Austausch in persönlichen Gesprächen haben das Projekt zu dem gemacht, was es heute ist. Vielen Dank, dass Sie Ihre Expertise und Ihre Herangehensweise an große Projekte mit mir geteilt haben!

Ein großes Dankeschön geht auch an **Dr. Carsten Troll**! Egal bei welcher Gerätereparatur, bei fachlichen Fragen, Anmerkungen oder wenn man ein offenes Ohr bei chemischen Problemen gebraucht hat, du warst immer da. Das gemeinsame Tüfteln bei der TGA oder DSC, aber auch die Grillabende werde ich so schnell nicht vergessen. In diesem Kontext sollte auch **Dr. Sergei Vagin** erwähnt werden, der als wandelndes Lexikon in Sekundenschnelle lösungsorientierte Vorschläge parat hatte. Vielen Dank, dass du dein Wissen mit uns geteilt und für den ein oder anderen Denkanstoß gesorgt hast. Ein herzliches Dankeschön geht an **Annette Bauer**, die gute Seele des Lehrstuhls. Ein Gespräch mit Ihnen, sei es auch noch so kurz, hat es immer wieder geschafft, ein Lächeln aufs Gesicht zu zaubern. Sie sind eine wahrhaftige Meisterin der Organisation, was wir alle sehr zu schätzen wissen.

Ein Dank, den man nicht in Worte fassen kann, geht an den gesamten **Makrolehrstuhl**! Auch wenn sich der Lehrstuhl in einem steten Wandel befindet, es ist immer wieder schön, ein Teil davon sein zu dürfen. Während meiner Bachelorarbeit hat **Dr. Markus Pschenitza** das Interesse für makromolekulare Chemie geweckt, wofür ich dir sehr dankbar bin. Die Anfangszeit meiner Promotion kann man am besten mit vielen lustigen Stunden mit **Elli, Amelie, Paula, Moritz und Moritz, Jonas und Jonas, Sandra, Baohui, Lukas und Lukas, Kerstin, Brigita, Phil und Philipp und Philip, Anton, Alina, Steffi, Jin, Lena und Tim** beschreiben. Die Arbeitsatmosphäre mit euch war immer entspannt und angenehm, irgendwie ist man dann doch zu einer kleinen Familie geworden. Vielen Dank, dass ich all unsere tollen Masteranden wie **Emilia, Marvin, Schmiddi, Matthias, Hendrik, Stefan, Jana, Juli und Hannah** ein Stück auf ihrem Weg begleiten durfte und sehr viele herzliche Momente mit euch teilen konnte. Danke dir, **Jakob**, dass jedes Gespräch mit dir ein wahnsinnig lustiger Schlagabtausch ist! Und vielen Dank dir, **Zoe**, dass wir gemeinsam deine Ausbildungszeit am Lehrstuhl bestreiten durften und so viel gegenseitig voneinander gelernt haben.

Ein ganz besonderer Dank gebührt dir, **Amelie**! Deine gewissenhafte Art hat den Laboralltag an sehr vielen Stellen vereinfacht und erleichtert. Du hast immer ein offenes Ohr und eine freie Hand zum SET spielen, was mich in sehr vielen Momenten aufgebaut und dazu bewegt hat, einfach weiter zu machen.

Vielen Dank an euch, **Brigita** und **Kerstin**! Ihr wart der Hammer, seid der Hammer, und werdet auch immer der Hammer bleiben. Jede Sekunde mit euch war einfach lustig, hat viel Freude bereitet und wird nicht vergessen werden. Vielen Dank, dass ich eurer Unterstützung immer gewiss sein durfte und ihr mich durch die Zeit während der Promotion getragen habt.

Liebe **Steffi**, lieber **Johnny** und lieber **Anton**, vielen Dank für die schöne Zeit in Amerika. Es war wundervoll, euch auch außerhalb des Labors näher kennenlernen zu dürfen! Danke dir **Anton**, dass wir schon unsere ganze Studienzeit zusammen teilen und du mich immer wieder zum Lachen bringst. Vielen Dank dir, **Steffi**, für deine stetig währende Unterstützung und die schönen Momente bei unseren gemeinsamen Ausflügen.

Ein Dank von Herzen geht an meinen Polymerpowerpartner, den **Phili**! Unsere Kochabende sind so schön gewesen, weil man mit dir einfach über alles sprechen kann und bei dir einfach man selbst sein kann. Sei es über Chemie, das aufkommende Statusupdate der TUMint oder das Leben im Allgemeinen. Ich hätte mir keinen besseren Kooperationspartner als dich vorstellen können! Vielen Dank für Alles.

Vielen Dank an das Team der **TUMint Energy Research GmbH**. Das Arbeiten in einem interdisziplinären Team bietet so viele neue Perspektiven, die mich ein Leben lang begleiten werden. Der rege Austausch in den Seminaren hat mir gezeigt, wie Forschung funktionieren und kommuniziert werden kann. Vielen Dank an das tolle Team und die wunderschönen gemeinsamen Ausflüge!

Nicht zu vergessen sind meine Studenten **Vanessa, Lisa, Carolin, Farah, Aygün, Luis, Christian, Christopher, und Thanh**. Ihr habt mit eurer unermüdlichen und fleißigen Arbeit das Projekt vorangebracht und immer gerne mit mir zusammen getüftelt. Danke dir, **Christopher**, für all die täglichen Wohlfühlgespräche. Vielen Dank **Felipe**, für deine liebe Art und eine gemütliche Laborzeit!

Eva, dir möchte ich für so vieles danken. Wir haben so viel mehr als die Studienzeit miteinander geteilt und ich bin so dankbar für jeden Moment! Aus meinem Studienkreis möchte ich gerne euch, **Kathrin, Moni, Toni, Streifi, Sebo, Nicole, Tobi und Stefan** meinen Dank aussprechen. Egal ob ein Musicalabend, ein Nähprojekt, ein Stustaculumbesuch oder ein Mittagessen, es war immer wundervoll.

Zwei Menschen, ohne die meine Freizeit definitiv nicht so bunt wäre, seid ihr, **Fiona** und **Luise**. Vielen Dank, dass ihr mich immer wieder aufgebaut habt und es immer etwas leckeres zu essen gibt, wenn wir uns sehen.

Danke dir, **Ibrahim**, für unsere wundervolle Begegnung in Schweden, unsere Freundschaft ist jeden Tag immer wieder ein Geschenk.

Zu guter Letzt möchte ich gerne meiner **Familie** danken! **Mama** und **Papa**, wo soll ich anfangen. Auch wenn niemand von uns weiß, was mich dazu bewegt hat, das Chemiestudium zu beginnen, habt ihr

mich doch in jeder Sekunde unterstützt. Sei es mit einer warmen Mahlzeit, Umarmungen, unendlich vielen Stunden des Zuhörens und einem Zuhause. Ich weiß, dass ich ohne euch nicht da wäre, wo ich heute bin. Vielen Dank, dass ihr immer hinter mir steht und stolz auf mich seid, auch wenn meine Witze manchmal nicht so gut sind, wie ich es gerne annehmen würde. Vielen vielen vielen lieben dank dir, **Verena**! Du bist einer der warmherzigsten Personen, die ich kenne. Dich meine Schwester nennen zu dürfen, ist mehr, als man sich überhaupt wünschen kann. Vielen Dank, dass du mich kennst und trotzdem magst, dass du mich verstehst, ohne dass ich etwas sagen muss. Ich hätte diese Arbeit ohne all diese ganzen Kekse von dir niemals überlebt. Vielen Dank auch deiner besseren Hälfte, **Sylvester**! Manchmal sind deine Witze nicht so schlecht und bringen mich tatsächlich zum Lachen. Vielen Dank, dass du unsere Familie mit deiner Anwesenheit bereicherst.

Liebe **Sweeties**, ihr seid die Besten!

Abstract

The demographic progress and the related increase in energy consumption force the development of efficient and long-lasting energy storage technologies. In this context, solid-state batteries establish the possibility of improved energy and power densities in combination with thinner components using novel separator and electrode technologies. Looking into standard electrolyte classes, single ion-conducting polymer electrolytes (SICPEs) combine classical polymer advantages with enhanced cell performance. The immobilization of the anions on the respective polymer backbone permits a facilitated lithium migration behavior and prevents polarization effects during cycling. In the scope of this work, the architecture of standard SICPE matrices is enlarged by establishing a new monomer concept. The herein-designed monomer structure **1** offers a terminal epoxide and a protection group strategy that allows the anionic ring-opening-polymerization of the epoxide functionality towards the respective polyether. After post-polymerization functionalization, the target SICPE presents the first example of an immobilized anionic charge directly linked to a flexible PEO backbone. Every repetition unit presents one charge carrier that can be transported through the solid electrolyte. New polymer geometries are unlocked via copolymerization with styrene oxide and poly (ethylene glycol) diglycidyl ether. The thermal properties of the homo- as well as the copolymers are analyzed via thermogravimetric analysis and differential scanning calorimetry and discussed regarding their electrochemical performance.

The design of alternative monomer structures and the post-polymerization functionalization of poly (styrene oxide) open the discussion platform for additional reaction pathways to achieve the target SICPE. Their advantages and challenges are exemplified based on the feasibility of their synthesis protocols.

Zusammenfassung

Der demografische Fortschritt und der damit einhergehende Anstieg des Energieverbrauchs fördern die Entwicklung effizienter und langlebiger Energiespeichertechnologien. In diesem Zusammenhang eröffnen Festkörperbatterien die Möglichkeit besserer Energie- und Leistungsdichten durch neuartige Separator- und Elektrodentechnologien und dünnere Verarbeitungsschritte. Einzelionenleiter kombinieren klassische Polymervorteile mit einer insgesamt verbesserten Zellleistung. Die Immobilisierung der Anionen auf dem entsprechenden Polymerrückgrat ermöglicht ein erleichtertes Wanderungsverhalten der Lithiumkationen und verhindert Polarisationseffekte während dem Zellbetrieb. Im Rahmen dieser Arbeit wird der Aufbau und die Architektur gängiger Einzelionenleiter durch die Etablierung eines neuen Monomerkonzeptes erweitert. Das hierbei entworfene Monomer **1** bietet eine endständige Epoxidgruppe und eine Schutzgruppenstrategie, die die anionische Ringöffnungspolymerisation der Epoxidfunktionalität zu dem jeweiligen Polyether ermöglicht. Nach der Durchführung einer polymeranalogen Funktionalisierung stellt der in dieser Arbeit synthetisierte Einzelionenleiter das erste Beispiel für eine immobilisierte anionische Ladung dar, die direkt an ein flexibles PEO-Rückgrat gebunden ist. Jede Wiederholungseinheit beherbergt einen Ladungsträger, der durch den Festelektrolyten transportiert werden kann. Durch die Copolymerisation mit Styroloxid und Poly(ethylenglykol)-diglycidylether werden neue Polymergeometrien erschlossen. Die thermischen Eigenschaften der Homo- sowie der Copolymere werden mittels thermogravimetrischer Analyse und dynamischer Differenzkalorimetrie analysiert und hinsichtlich ihrer elektrochemischen Leistungsfähigkeit diskutiert.

Das Design alternativer Monomerstrukturen und die Postpolymerisationsfunktionalisierung von Poly (styroloxid) eröffnen die Diskussionsplattform für zusätzliche Reaktionswege, den gewünschten Einzelionenleiter zu realisieren. Ihre Vorteile und Herausforderungen werden anhand der Durchführbarkeit ihrer Syntheseprotokolle veranschaulicht.

Table of contents

Für meine Familie, Suki, Nala und den Gardasee

1. Lithium-ion batteries: a historic way to next-generation energy storage systems

Ever since human life has developed on this planet, energy has played a pivotal role in the evolution of civilizations. Daily tasks such as generating heat, cooling, transportation, or communication require a profitable energy supply. The population is steadily growing, and the demand for energy storage in portable electronics, smart grids, and electronic vehicles (EVs) is rapidly increasing. Monitoring the global car sales market, EVs show more than a tenfold increase in their market share from 9% (sales in 2021) to 14% (sales in 2022) with rising potential. Besides Europe and the United States, China, as a global player, holds the most EV market shares (see Figure 1, data from 2023).[1]

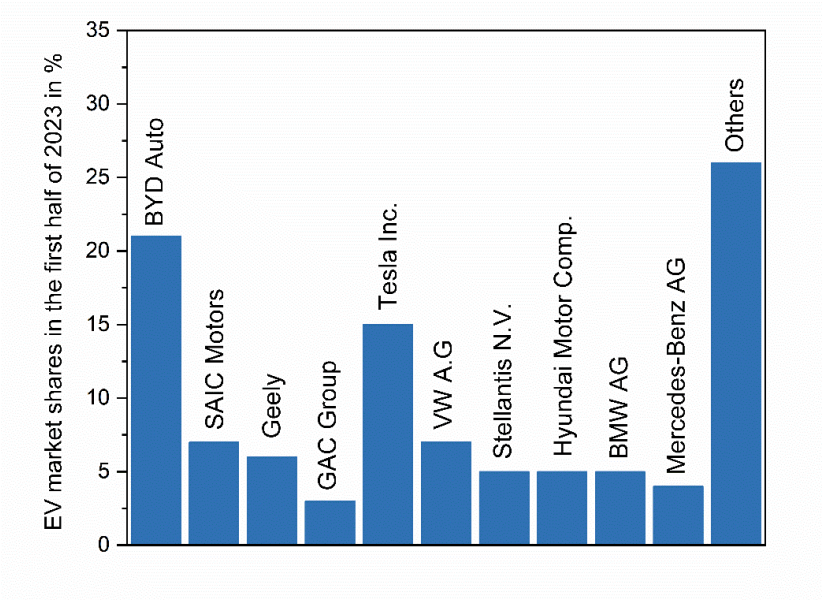

Figure 1: Overview of global market shares based on the top 10 battery-only and plug-in hybrid (battery can be additionally charged via combustion engines) EV producers in the first half of 2023; Chinese vendors: BYD Auto, SAIC Motors, Geely, GAC Group.

To cope with the ambitious demands of progress in our worldwide technological visions and people's current living standards, the principle behind energy storage has to be elevated to next-generation applications. Two main factors are mostly known to decide the success and consistency of a technology: secular safety and a sustainable, high-energy output.[2] Safety is guaranteed by preventing side reactions between all incorporated components, ensuring a secured technology implementation and operation over an elongated period.[3] To achieve storage systems with an outstanding energy density, each module's enhanced quality and power must be ensured to create a fruitful working environment.

With all these goals in mind, *Whittingham* started to revolutionize in the 1970s the nature of rechargeable batteries. By investigating the advantaged crystal structure-ion intercalation relationship of layered titanium disulfide, it was possible to bypass classical lead-acid batteries and molten salt systems based on molten lithium or sulfur.[4-5] He established a light and easily accessible cathodic intercalation system with low lattice expansion. Due to its nature as a metallic conductor, further addition of electrically conductive additives was not necessary.[6-7] Coupled with a metallic lithium anode, the Li/TiS_2 system could retain capacity over many working cycles. Even today, batteries of this type stored in the Nobel-Prize Museum in Stockholm show more than 50% of their original capacity.[8] *Exxon*, responsible for commercializing this battery type, switched to Li-Al alloys as a lower voltage alternative to pure Li anodes.[9] The reason was the deposition of thin dendrites on the lithium surface. Combined with liquid, non-aqueous electrolytes that could not prevent this growth, the batteries started shortening and catching fire.[10]

Aiming for higher energy densities and decreasing production costs, *Goodenough* left the field of sulfides by starting to take a deeper look into related, oxide-layered structures.[11] In this context, he postulated for the first time ternary transition-metal oxides with the chemical formula $LiMO_2$ (with M = V, Cr, Co, Fe, and Ni) after lithium cobalt oxide ($LiCoO_2$) showed up to be a promising, cathodic insertion candidate. [12-13] It outperformed TiS_2 about the measured open-circuit voltages and exhibited a theoretical energy density of 1.1 kWh kg^{-1}.[12] The oxidic cathode enabled the building of a rechargeable Li/$LiCoO_2$ battery with a power of already 4 V.[14] The ability to deintercalate lithium at high potentials reversibly allowed the battery design to be loosened from using unsafe lithium metal as an anode.[15-16] Cobalt provides stabilization effects on the cathode that support the consistency of $LiCoO_2$ cathodes till today.[17] However, mining and refining metal and related social and environmental concerns have raised attention to diminishing the amount of metal in the electrode.[18-19] The trend nowadays is going towards nickel, aluminum, and manganese oxides like $LiNi_{0.8}Co_{0.15}Al_{0.05}O_2$ (NCA) or $LiNi_{0.76}Mn_{0.14}Co_{0.10}O_2$ (NMC)[20-21].

Nevertheless, while the progress on cathode materials and technologies seemed to be evolving in a fast and effective manner, finding suitable anodes turned out to be more complicated. Side reactions between the liquid electrolyte and metallic lithium continued to support dendrite growth, and the battery security started to be questioned. In the 1980s, the focus of research was shifted towards novel anode designs.[22] In early work about carbonaceous materials, graphite was highlighted as negative intercalation side.[23] *Yazami* and his group at Grenoble were the first to prove that lithium-graphite intercalation was reversible while using polyethylene oxide in combination with lithium perchlorate as a solid organic electrolyte.[24-25] Its wide availability, the manifold possibilities of shape transformation

(particle size/shape), and its high capacity of 372 mAh g^{-1} made graphite an attractive material for lithium-ion batteries aiming for high energy densities.[26] However, the usage of graphite could not entirely prevent electrode fading or disruption of the carbon structure. These effects were caused by the small lithium cations intercalating into the regular stacking of carbon flat layers and the larger counter anions, leading to a widening of the structure.[27] Therefore, investigating the interfacial situation between anode and electrolyte was intensified.

Interphases are generated when the electrolyte cannot remain thermodynamically stable in the presence of the extreme potentials predominant in lithium-ion batteries (LIBs).[28] It is possible to protect graphite from exfoliation by forming a stable solid-electrolyte interface (SEI) via aggregating the decomposed electrolyte parts on the anode surface.[29-31] But not every electrolyte has the potential to create a stable SEI. Propylene carbonate (PC), which is still used as a common electrolyte in lithium-ion batteries, is one of the negative examples of destabilizing decomposition products.[32] *In collaboration with the Japanese battery supplier Asahi Kasei, Yoshino* focused on carbonates as electrolytes but shortened the carbon framework to end up with ethylene carbonate (EC).[33] Even though propylene and ethylene carbonate differ with only one carbon atom, there is a huge difference in stability.[28] The thin insulating layer formed on the graphite surface, consisting of the ethylene carbonate decomposition products, enabled a reversible and efficient lithium intercalation/deintercalation.[34] Although research is always searching for alternative anode materials, graphite remains dominant.

In 1991, *Sony* commercialized the concept of LIBs and boomed the progress in battery technologies and materials by applying all these carefully adjusted and well-designed components in one battery.[35] Their set-up consisted of graphite as anode, $LiCoO_2$ as cathode, and a diethylene carbonate/propylene carbonate (DEC/PC) mixture with lithium hexafluorophosphate ($LiPF_6$) as electrolyte.[36] A volumetric energy density of 200 Wh dm^{-3} and a gravimetric energy density of 80 Wh kg^{-1} was reached.[37] In 2019, for pathing the way to functional batteries, the founding fathers of this technology – *Whittingham, Goodenough, and Yoshino* - received the Nobel Prize "for the development of lithium-ion batteries".[14, 22] Their research was mainly motivated to create a future independent of fossil fuels. Figure 2 depicts a schematic representation of the first commercialized "*Sony* battery" and the essential material classes that made this development possible.

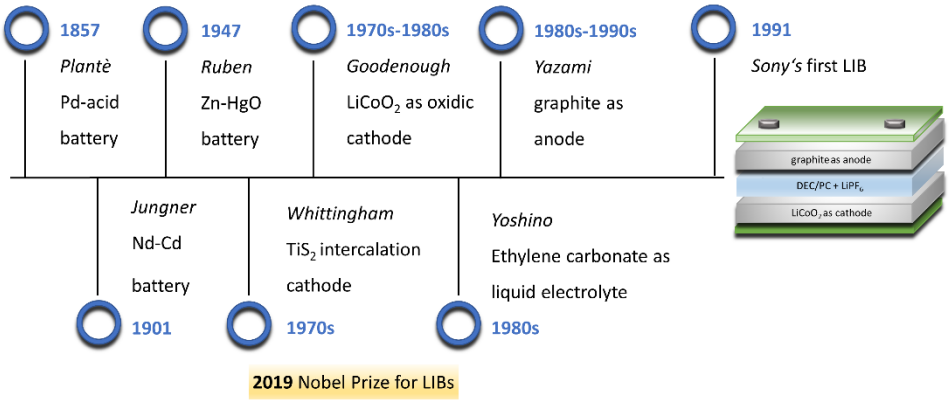

Figure 2: Milestones in the development of the first commercialized LIB by *Sony*.[38]

After establishing this first rudimentary and well-working concept of a LIB, the journey's end has not yet been reached. Continuous development is ongoing, addressing the questions of price, sustainability, power supply, and innovation.[39] As the production costs are effectively managed, LIBs can be considered the leading technology in rechargeable batteries.[40] Unfortunately, the growing market, especially in the e-mobility sector, demands more and more innovation power from the manufacturer. The biggest bottleneck with liquid LIBs is their low energy density, which is limited by the choice of suitable anodes that do not decompose with the electrolyte.[41] Pure lithium metal as a hostless material is the perfect candidate to unlock the potential of increased specific capacity on the anode side. It has a theoretical capacity of 3860 mAh g^{-1} and the lowest electrochemical potential of –3.04 V (versus standard hydrogen electrode) in the galvanic series.[42] This extremely high negative electrochemical potential enables, on the one side, the rise of energy and power density.[43] On the other hand, it is also the reason why nearly every applied electrolyte can be reduced on its surface, causing inhomogeneous lithium deposition, dendrite growth, and safety risks.[44-45]

To overcome this issue, a long-lasting and resilient alternative to liquid electrolytes must be invented. The SEI between electrolyte and electrode experiences stabilization effects by replacing common organic solvents with solid compounds.[46] In a liquid electrolyte-lithium interphase, the solvents and salts of the electrolyte decompose directly upon contact with the metal surface to form Li_2CO_3, ROLi, $ROCO_2Li$, and LiF (in the presence of $LiPF_6$).[47] The resulting SEI is mostly uneven and not robust enough to compensate volume changes during cycling.[48] In contrast, the solid electrolyte-anode interphase is not formed by decomposition but by structural transformation of the electrolyte. The resulting SEI benefits in dendrite suppression and problems concerning electrolyte consumption disappear.[49]

In the last few years, incorporating only solid components into a battery has gained much attention. These so-called “all-solid-state batteries” (ASSBs) use different classes of electrolytes, mainly oxide,

sulfide, polymer, and halide electrolytes.[50-53] Leaving critical anode-liquid electrolyte interactions behind, ASSBs offer increased intrinsic safety and feasible higher energy densities.[54] By incorporating lithium instead of a graphite anode, the specific energy is theoretically increased by 35%, opening up new horizons regarding our current energy use and storage.[55] Besides all the material classes that can be considered for ASSBs, solid polymer electrolytes (SPEs) show an innovative package of promising properties such as low density, low cost, and excellent processability.[56] In the following chapters, their function as both separators and solid electrolytes will be discussed in relation to different battery chemistries and compared with leading set-ups.

2. The implementation of polymers in batteries

Batteries are an efficient and intelligent answer to how we manage to store energy efficiently and long-lasting, ready to be used on the spot. Our daily lives would be significantly different if we were forced to bypass battery-driven technologies like smartphones, tablets, smartwatches, or laptops.[57] By supporting e-mobility in terms of the consistent development of EVs or e-bikes, the first milestones towards a more sustainable future, accompanied by a neutral CO_2 footprint, are set.[57-58]

Every battery cell component has a valuable input on the battery composition and, in reverse conclusion, the power and energy density. While the role of the anodic and cathodic materials is already strictly determined, polymers present a huge innovation portfolio concerning their electrochemical application.[59] They bear several advantages (see Figure 3), namely excellent thermal, mechanical, and electrical properties, low density, easy processability, high safety, and low production costs, that match various requirements demanded from the respective devices.[60] Polymers are present in nearly every commercial lithium-ion battery on the market, where their functions range from acting as electrode binders and porous separators to solid electrolytes and composite material supplements.[57, 59, 61-63] To get an inside into their diversity, the following chapters will highlight key polymer technologies and their battery applications.

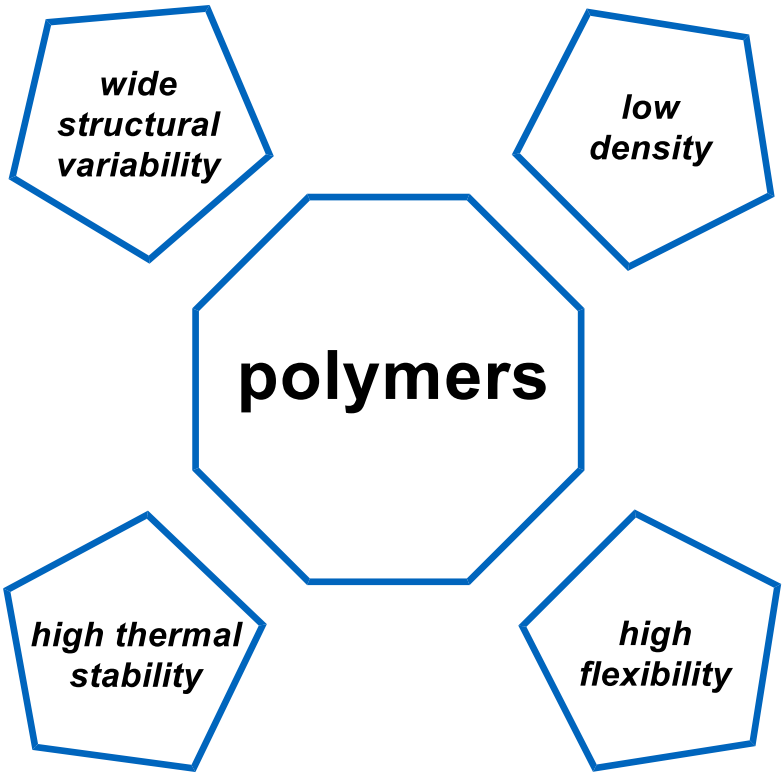

Figure 3: General merits of polymers that make them attractive candidates for battery application.

2.1. Polymers: a multitool in all types of batteries

2.1.1 Rechargeable, liquid LIBs

The most common and well-established polymer applications related to energy storage are found in secondary, rechargeable LIBs. Since the commercialization of the *Sony battery* in 1991[35], the general working principle of this battery type has not changed significantly. It is an electrochemical cell that converts stored chemical energy into electrical energy. This requires only four main components: an anode, a cathode, a liquid electrolyte with a dissolved lithium salt, and a separator (see Figure 4).[64] As mentioned above, a typical anode is made of graphite, as the layered structure allows the reversible intercalation and deintercalation of lithium cations without disrupting the material.[65] Common cathodes are often based on LCO due to its stabilizing effects during cycling, ease of synthesis, high initial Coulombic efficiency, and compact density.[66-67] Cobalt-free and, thus also, cheaper and more sustainable cathode alternatives are spinel-type structures such as lithium manganese oxide ($LiMn_2O_4$, LMO) or phosphates such as lithium iron phosphate ($LiFePO_4$, LFP).[68] This olivine structure type has a lower open circuit potential but a higher capacity than LCO.[5] Based on their different redox potentials, the anode and cathode generate an electric field and internal electrochemical reactions, forcing the present charge carriers to move from one electrode to the other.[69-71] During charging, the lithium cations, stored in the cathode, de-intercalate from the cathode material and diffuse into the liquid electrolyte. The electrolyte transports the lithium cations to the separator, where they can migrate through the pores to reach the anode side. There, the lithium cations are intercalated again. The electrons are cycled through the external electrical circuit. The process is reversed during discharging, meaning the lithium cations migrate from the anode to the cathode.[72] The following equations show the reactions during the charging of the battery (cathode: LCO, anode: graphite):

$$\text{Cathode: } LiCoO_2 \rightarrow Li_{(1-x)}CoO_2 + xLi^+ + xe^- \quad (1)$$

$$\text{Anode: } 6C + xLi^+ + xe^- \rightarrow Li_xC_6 \quad (2)$$

$$\text{Overall Reaction: } LiCoO_2 + 6C \rightarrow Li_{(1-x)}CoO_2 + Li_xC_6 \quad (3)$$

A liquid electrolyte that acts as a lithium-ion carrier is needed to enable ion transfer within the LIBs. The electrolyte is an essential part of the secondary battery, as it influences parameters like the overall thermal stability and the ongoing processes at the interphases (e.g., SEI formation).[73] While the chemical nature of the electrodes defines the energy output, the electrolyte controls the mass flow and its velocity within the battery.[74] The choice of a liquid electrolyte is affected by several requirements, focusing on electrochemical stability and intrinsic electrolyte properties. The dielectric constant must

have a specific value to dissolve the added lithium salt. The viscosity of the electrolyte-salt solution should be kept at a minimum level to facilitate the migration of the lithium cations. To avoid interfacial instabilities between the electrolyte and the anode or cathode, the solvent must have sufficient compatibility with the electrodes within the operating range of the battery. This stability is often challenged by the cathode and anode's strong oxidizing and reducing properties. That's why liquid electrolytes are forced to have a wide electrochemical stability window. The intrinsic properties of the solvent should include a low melting, high boiling, and flash point. Additionally, safety should be guaranteed by using only non-toxic and harmless reagents.[44]

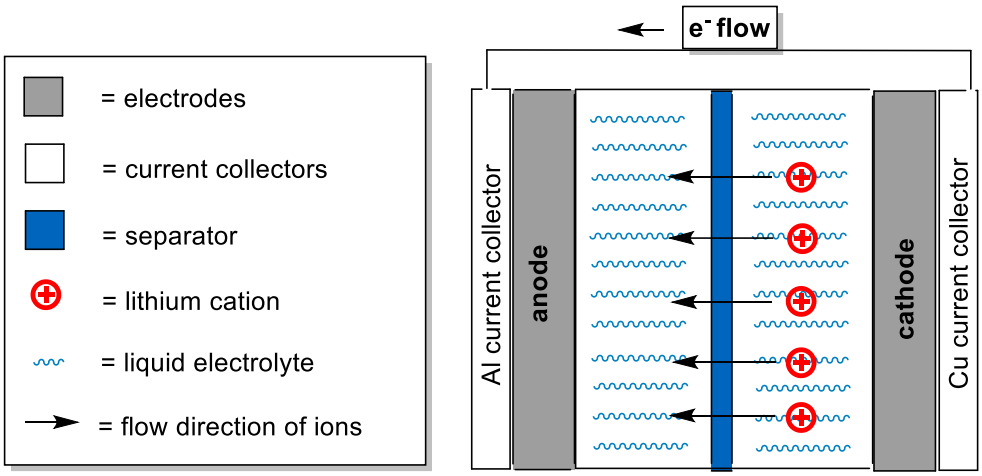

Figure 4: General set-up of a liquid LIB[64] during the discharge process, consisting of a negative anode (here: graphite), a positive cathode (here: $LiCoO_2$), a liquid electrolyte (here: cyclic carbonate) with a dissolved salt (here $LiPF_6$), and a porous, polymeric separator.

The chemistry behind the used electrolytes has also changed as technology constantly evolves. When *Volta* established his first concept of an "artificial electrical organ", or his so-called "pile" in 1799, water was the solvent of choice as an electrolyte, because it easily dissolves most kind of salts.[75-76] Following the battery history, subsequent technologies picked up this trend. In 1860, *Planté* demonstrated the first practical rechargeable lead-acid battery.[77] Besides using large lead sheets as electrodes, the electrolyte was found to be based on sulfuric acid diluted in water.[78] Aqueous potassium hydroxide or acids were standard electrolytes in alkaline batteries, including nickel-cadmium, nickel-metal hydrides, or zinc-manganese dioxides.[79-80] Aqueous electrolytes already formed the basis for many important battery working principles that are still used and researched today. Nevertheless, a switch from aqueous to non-aqueous electrolytes prevailed in the 1960s to 1980s. Water encountered restrictive cell potential barriers, manifesting in an intrinsic limit about the battery's respective volumetric and gravimetric energy density.[75, 81] With the increasing demand for energetically more prosperous energy storage systems, the incorporation of lithium as an anode made water as an electrolyte nearly impossible.

Non-aqueous electrolytes gained interest when *Yoshino* highlighted carbonates in their role as working electrolytes.[33] They also facilitated the way to lithium-enriched anode concepts because they could form a stable and passivation layer on the anode side.[82] *Dahn et al.* were among the first groups to investigate that PC and EC exhibit irreversible reactions only at the first discharge, producing the anode-protecting SEI (see Figure 5).[83] As far as the composition of the SEI is understood, in the case of PC, it is formed out of lithium alkyl carbonates, alkenes, and a complicated mixture containing lithium oxalate, oxide, alkoxides, and reduction products based on the added salts.[84-86]

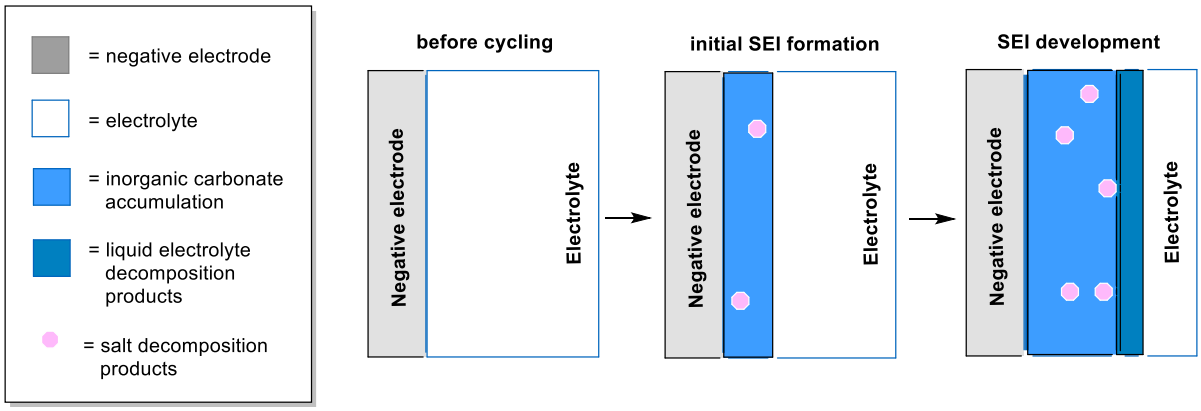

Figure 5: SEI formation between the negative electrode and the non-aqueous electrolyte in a LIB during the first cycling; the electrolyte decomposes to yield liquid electrolyte decomposition products; the added salt decomposes as well and produces, for example, LiF (in the case of $LiPF_6$ as conductive salt).[82, 84]

Lithium electrolytes are a mixture of one or two non-aqueous electrolytes with one lithium-conducting salt. To create a good solubility of the salt, the electrolyte needs to offer polar groups such as carbonyl (C=O), nitrile (C≡N), sulfonyl (S=O), or an ether linkage (-O-).[44] Besides cyclic carbonates like PC and EC or cyclic ethers like tetrahydrofuran (THF), linear carbonates can also be applied as co-solvents.[87] Prominent examples are dimethylcarbonate (DMC) or DEC.[88-89] The stability of carbonate electrolytes has a major bottleneck, which lies in their instability against the anodes.[90] Other classes of liquid electrolytes have been invented to counteract the capacity fading that is regularly observed as a consequence. Figure 6 gives an overview of standard carbonates and the respective alternatives, such as sulfones, fluorinated carbonates, isocyanates, and dinitriles.[91-94]

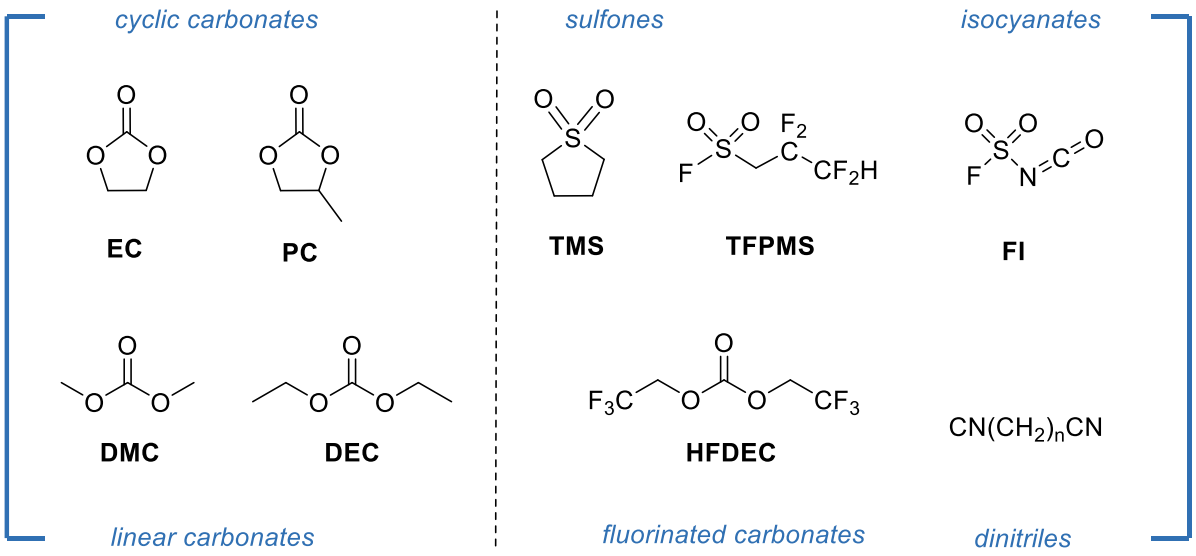

Figure 6: Conventional liquid electrolytes for LIBs; left: cyclic (EC and PC) and linear carbonates (DMC and DEC); right: sulfones (tetramethylene sulfone (TMS) and *β*-fluorinated sulfone (TFPMS)), isocyanates (fluorosulfonyl isocyanate (FI)), fluorinated carbonates (bis(2,2,2-trifluoroethyl) carbonate (HFDEC)), and dinitriles ($CN(CH_2)_nCN$)).[91-94]

The charge carriers in a LIB are the lithium cations, which move contrary to their counter anions. Their movement balances the external electron flow observed between the cathode and the anode. To be applicable as an efficient conducting salt, lithium salt must have a high solubility in organic solvents and a high conductivity within the medium.[73] The degree of solubility is often dictated by the dissociation properties of the salt, meaning that the lithium cations should be able to move freely within the media with high mobility. The anions and the cations should exhibit high thermal and chemical stability towards all cell components, including the electrodes and the separator. At this juncture, the anion should offer increased stability against oxidative decomposition at the cathode side and an inert behavior against the electrolyte solvent. As mentioned above, the formation of the SEI between the electrolyte and the electrodes plays a critical role in the battery's lifetime and safety. Therefore, the lithium salts should also be able to contribute to the formation of a stable and less-resistive SEI.[95]

Over the years, several lithium salts were established as familiar applicants in LIBs, which use different settings of the anionic structure motif. A well-known example is lithium perchlorate ($LiClO_4$), the salt of a strong acid with high solubility and good ionic conductivity in non-aqueous solvents (approximately 9 mS cm^{-1} in EC or DMC at room temperature).[96] Due to its strong resistance against hydrolysis and its strengthened ability to form films on carbonaceous and lithium metal anode surfaces, it is a famous model salt for testing electrolytes under various laboratory conditions. Nevertheless, as a daily candidate in LIBs, $LiClO_4$ is hardly applicable. Due to the nature of the chlorine and its high oxidation state of +VII, the perchlorate likely reacts with organic species at higher temperatures. During cycling, the side

product $LiClO_3$ can form, and its hygroscopic character leads to moisture absorption, which can result in the cell's explosion.[95, 97-98]

Leading over to fluoro-type anions, three commonly used salts are known to be used in a majority of LIBs: lithium tetrafluoroborate ($LiBF_4$), lithium hexafluoroarsenate ($LiAsF_6$), and lithium hexafluorophosphate ($LiPF_6$). Compared to perchlorate-based salts like $LiClO_4$, these salts have a lower risk of explosion, although they are still susceptible to hydrolysis. The side product that is formed when fluoro-type anions are hydrolyzed is hydrofluoric acid (HF). It is critical for trapping the lithium cations and decomposing the transition-metal elements in the cathode.[95] The fluoroborate anion BF_4^- is a relatively small anion that shows a high association with the lithium cation based on its localization of the negative charge and its size. This fact can be seen as the reason for low conductivity, as the cations are firmly bound to the anionic counterpart.[99] Comparing the ionic conductivity of 10 mS cm^{-1} of the related $LiPF_6$, $LiBF_4$ only exhibits a moderate ionic conductivity of 5 mS cm^{-1} in an EC/DMC mixture.[100-101] Additionally, fluoroborate does not form stabilizing products on the anode surface, as its symmetric structure provides intrinsic stabilization. This fact impedes the battery's cycling, leading to self-discharging and capacity fading.[102] Nevertheless, the good thermal stability still keeps $LiBF_4$ in the pool of regularly applied lithium salts.

An extensively studied and also nowadays one of the most dominant fluoro-type anions in lithium salts is $LiPF_6$.[103] The advantages of fluorophosphate lie in its high ionic conductivities at room temperature, its ability to form a stable SEI on the anodic side, and its flame-retardant properties due to the presence of phosphate groups.[104-106] The chemical structure of $LiFP_6$ is formally composed of a fluoride anion complexed by the Lewis acid PF_5, enabling effective delocalization of the anionic charge. This structure enhances the dissociation of lithium cations from anions, thereby promoting efficient ion mobility.[95] As is seen for almost every technology, $LiPF_{6\,also}$ has some drawbacks. The P-F bond is highly susceptible to moisture, leading to salt decomposition, forming POF_3, LiF, and HF.[84] These side products dissolve cathode active materials, like, for example, in the spinel oxide LMO.[107] Not only do water traces destroy the salt, but temperature can have the same effect. Due to its elevated thermal instability, $LiPF_6$ can produce PF_5, which is capable of further reacting with the electrolyte. Gaseous products are the consequence, that accelerate the ongoing thermal decomposition. Even though the salt can form stable SEIs on the anode, the proposed operating conditions of a LIB in combination with $LiPF_6$ is in a low moisture electrolyte and at low to moderate temperature (< 60 °C).[102, 108] $LiAsF_6$ exhibits slightly higher ionic conductivity than $LiPF_6$ (11 mS cm^{-1} in comparison to 10 mS cm^{-1} in a EC/DMC mixture at room temperature), a very high anodic stability up to 6.3 V (vs. Li/Li^+), and consists an average cycling efficiency of > 95%.[101, 109-110] The stable SEI formed during cycling is mainly based on lithium alkyl

carbonates and not LiF, as seen for its related fluoro-type anions.[111-112] As the As-F bond is less prone to undergo hydrolysis, the formation of HF inside the battery is prevented. However, $LiAsF_6$ has a tendency to react with ether-based solvents, producing gaseous side products that can lead to cell rupture.[113] This safety risk is accompanied by the high toxicity of arsenic side products in the oxidation states +III and 0, making $LiAsF_6$ less favorable for commercial application.[110] Comparing these four standard lithium salts to their ionic conductivities, the following row can be established (with decreasing ionic conductivities):[73]

$$LiAsF_6 > LiPF_6 > LiClO_4 > LiBF_4$$

Lithium salts, that are conventionally used in LIBs, graded with decreasing ionic conductivities.

To continuously improve the battery performance, researcher put a lot of effort into the development of new lithium salts and the performance of combined lithium salt mixtures. Thereby, two main bottlenecks of the salts are addressed: poor solubility in organic solvents and the association interferences of the cations with the anions. By introducing perfluorinated alkyls to the salt, their solubility in common organic solvents can be increased.[114] Starting with lithium trifluoromethanesulfonate ($[Li(CF_3SO_3]$), the $[CF_3SO_3]^-$ group demonstrates on one side a hydrophobic character that can resist hydrolysis, such as it is seen in the perchlorate and fluoro-type based anions. On the other side, the fluorination facilitates the solubility tremendously, due to its electron-withdrawing effect.[114] Even though the sulfonate moiety generates high thermal stability and insensitivity towards moisture, the elaborated corrosion of the aluminum current collector by producing aluminum triflate ($Al(CF_3SO_3)$) hinders practical usage in LIBs. In 1984, *Foropoulos* and *DesMarteau* stayed with the concept of perfluorinated anionic structure motifs but incorporated an enhanced delocalization of the negative charge over the whole molecule.[115] They modified $Li(CF_3SO_3)$ by combining two trifluoromethane sulfonyl groups over an imide functionality. This salt is called lithium bis(trifluoromethanesulfonyl)imide ($[Li(CF_3SO_2)_2]$ or with the short name LiTFSI) and was commercialized for research and industrial purposes.[44] The oxidation potential of 4.3 V (vs. Li/Li^+ in EC/DEC solution) is far higher than for $LiClO_4$, $LiBF_4$, or $LiPF_6$, meaning the LIB can be operated in a large electrochemical stability window. Even though a slightly lower conductivity compared to $LiPF_6$ or $LiAsF_6$ is observed, its thermal stability up to 360 °C, the facilitated dissociation in solvents with a low dielectric constant, and the active participation in the formation of stable SEIs via the NSO_2^- group strongly highlight LiTFSI in its role as a powerful lithium salt in LIBs.[95] The progression in salt design does not have a limit. The imide structure type can

also be fused with phosphates, borates, or for example longer alkyl chains as functional groups.[95] Figure 7 gives an overview of the commonly used salts.

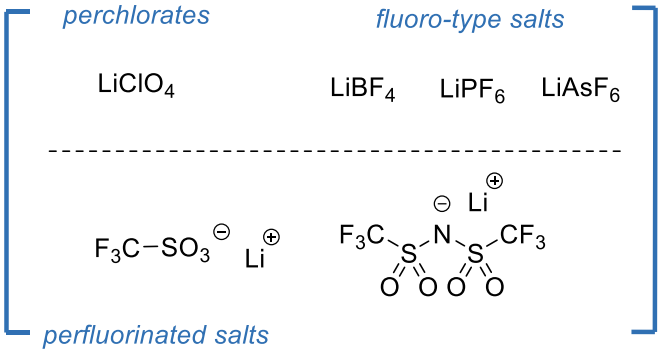

Figure 7: Lithium-salt examples for the usage in LIBs; classified in perchlorate, fluoro-type salts, and perfluorinated salts.

The separator is the last component necessary to make a LIB run. This is the part, where the main focus of polymer applications lies in a liquid battery. The function of the separator is to ensure free flow of the Li ions between the electrodes while inhibiting electron movement from one electrode to the other.[116] It operates as a spacer between the anode and the cathode and prevents their physical contact. The structure and the internal properties of the separator can have a strong influence on the battery capacity, its safety, polarization, and cycle life, although it does not chemically participate at the cell processes. Decreasing for instance the thickness of a separator, the overall energy and power density of the battery can be increased, but often the mechanical strength suffer as a consequence.[117] To fabricate a high performance separator, some requirements have to be fulfilled: The separator should be porous enough to be able to exhibit a high wettability in liquid electrolytes, while maintaining a robust mechanical strength. Showing infinite electronic resistance, the internal ionic resistance should come closer to the lowest point as possible. As it should be given for all cell components, a uniform thickness of the separator and a sufficient thermal stability is mandatory.[118] Separators for liquid LIBs can be divided in three groups, namely polyolefin microporous separators, heterochain polymer microporous separators, and non-woven separators (see figure 8).[117]

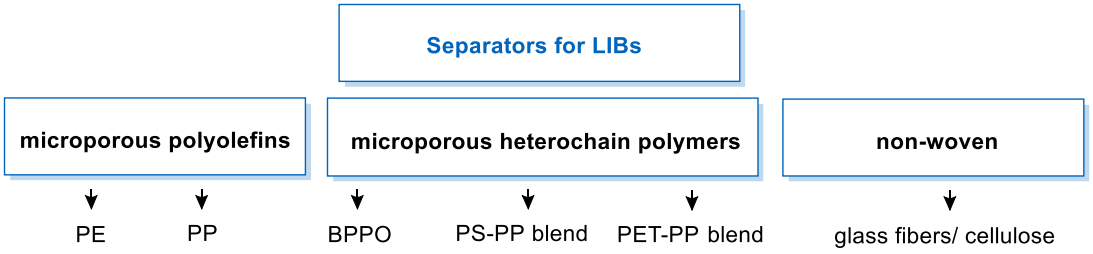

Figure 8: Separator classes that are used in LIBs; classification into microporous polyolefins (PE, PP), microporous heterochain polymers (BPPO, PS-PP blend, PET-PP blend), non-woven (glass fibers, cellulose) separators.

The most represented class is separators made of polyolefins like polyethylene (PE) or polypropylene (PP). The pore size and shape can be finetuned depending on the manufacturing process.[119] If the porous separator is dry processed, the melt-extruded polymer films are annealed at temperatures where the crystallization starts. After stretching at low and high temperatures, the pores are fixed, ending up with straight-through and slit-like shapes. In the wet process, plasticizers with low molecular weight are inserted into the polymer before the extrusion takes places. Calendaring is necessary to densify the polyolefin, then the plasticizer is removed with the help of solvent. After the solvent is completely removed as well, round-shaped pores are the result of this manufacturing route.[116-117] Generally, the inserted separator is usually a composite of different multilayers, to address mechanical stability and related to this, also safety assurance.[117] A prominent example is the sandwiched separator made out of PE and PP, where PE with a lower melting point (135 °C) controls the thermal shutdown of the battery and PP with its higher melting point (165 °C) retains the mechanical integrity and rigidity of the separator.[117, 120] Besides that, the surface of the polyolefin films can be modified via surface coating with polar components, gel polymer electrolytes, or nanoparticles. The aim is to improve the wettability and the thermal stability of the separator itself. Addressing the hydrophobicity of the polyolefin separators, surface grafting with hydrophilic agents like methyl methacrylate (MMA) or poly (methyl methacrylate) (PMMA) can mainly increase the uptake of liquid electrolytes up to 380%.[117, 121-122] Grafting changes the polarity of the separator by attaching functional groups directly on the surface through the formation of covalent bonds.[123] Heterochain polymer microporous separators exhibit a multitude of different polymer compositions and geometries. Well-known examples in this context are brominated poly(phenylene oxide) (BPPO), isotactic poly (4-methyl-1-pentene), polyoxymethylene, poly styrene (PS)–PP blend, and poly (ethylene terephthalate) (PET)– PP blend polymers.[117] The advantages of non-woven separators over alternative traditional polyolefin separators include lower processing costs, high porosities, and lower masses. The related manufacturing routes are generally based on wet processing, such as paper-making, solution extrusion, or wet-laid methods.[117] However, their performance is not compatible with standard polyolefin separators, as their pore shapes and sizes differ drastically. Non-woven separators like glass fibers or, for instance, cellulose have such large pores that internal shirt circuits, lithium dendrite growth, self-discharge, and performance fading occur.[124-125] In summary, polyolefins remain the dominant choice for separators in commercial LIBs due to their combination of electrochemical stability, balanced pore structure, and good mechanical strength. Via surface modification, disadvantages as thermal shrinkage or a hydrophobic nature can be easily compensated.

In a LIB, polymers can show their importance for battery performance not only in their function as separators. They can also be supporting components such as redox polymers, conductive polymers, or polymeric binders within the cathode (see Figure 9).

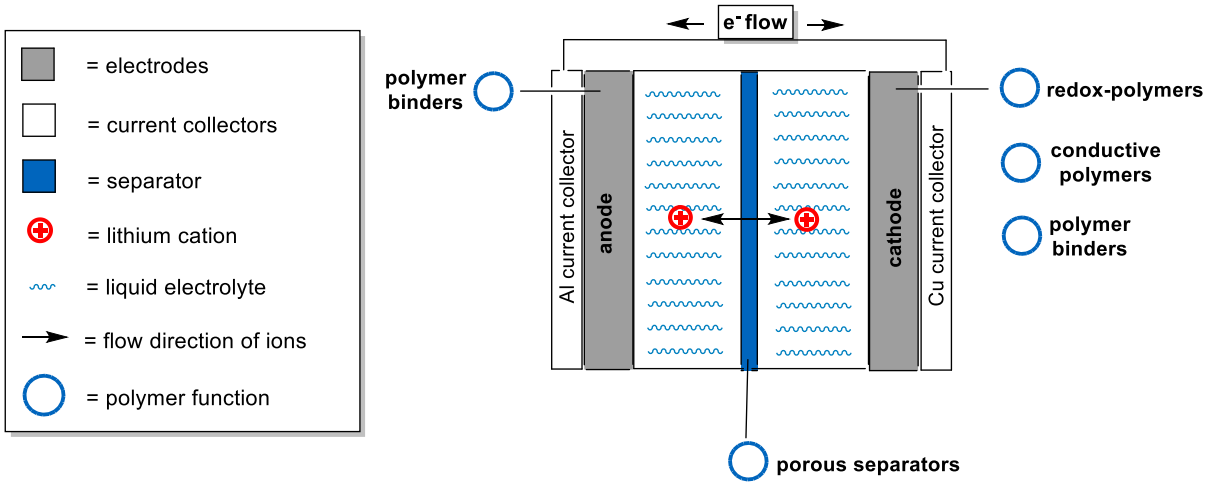

Figure 9: Overview of polymer application fields in LIBs: polymers as porous separators between the electrodes, redox active material/conductive-polymer/polymeric binder as cathode additives.

During intercalation of the lithium cations into the layered cathode structure, the size of the ion can lead to volume expansion or phase transition of the cathode materials.[126] Redox-active polymers can provide a platform for a smoother and milder intercalation reaction while keeping a high battery capacity. Conjugated polymers stand out in this category, as they depict optimized ionic diffusion and accommodation of the inserted ions. Since their discovery in 1977, a multitude of different geometries were invented.[127] The base is preferably a π-delocalized core structure that can undergo redox reactions in rechargeable batteries. The delocalized polymers can form +1/-1 charged states by accepting and realizing electrons. A lithium cation or optional anion can be bonded to the charged anchor points, making conjugated polymers an accessible material for LIB cathodes. This so called “doping” of these polymers describes the transfer of a neutral polymer into its oxidative (p-doped) or reductive (n-doped) state by offering counterions or anions as binding partners. Depending on the underlying constitution of the polymer (nitroxide radical polymer, organosulfur polymer, carbonyl polymer, polymers based on unsaturated C-N or C-C bonds, arylamines), varying chemical species can be formed. The doping has a main influence on the final capacity of the LIB, although side reactions or instabilities at certain doping levels limit the total consumption of the theoretical capacity.[126, 128] For LIB application, four conjugated polymers in particular are known for LIB application: polyaniline (PANI), polypyrrole (PPy), polythiophene (PTh), and poly(3,4-ethylenedioxythiophene) (PEDOT) (see Figure 10).[129-132]

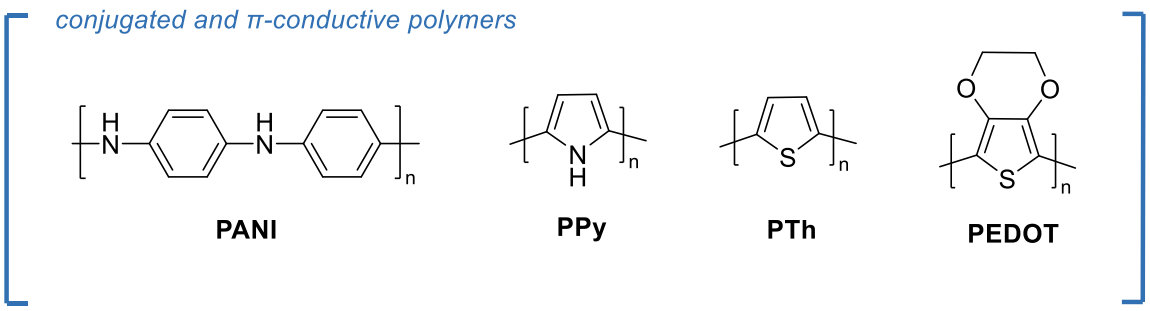

Figure 10: Chemical structures of established conjugated polymers used in LIBs as cathode additives; from left to right: PANI, PPy, PTh, PEDOT.

Examining PANI as a model system, the advantages of applying conjugated polymers in cathodes can be directly seen in the resulting cell capacity. Using a polyacid route to manipulate the three redox states that PANI can adopt, the PANI/polyacid electrode delivers a capacity of 230 mAh g^{-1} over 800 cycles. Additionally, the n-doped PANI reaches an energy density of up to 460 Wh kg^{-1} and a coulombic efficiency greater than 99%.[133] Also, PEDOT has the potential to act in place of conventional, non-redox polymer-based cathodes. When PEDOT as cathode material is combined with $LiN(CF_3SO_2)_2$ as salt and 1,2-dimethoxyethane/1,3-dioxopentane as an electrolyte mixture, it can afford an even higher specific capacity than PANI of 330 mAh g^{-1}. The redox mechanism is proposed to be stated on a 4-electron redox process, where the sulfur atom changes its oxidation state proportional to the electron uptake.[132]

Looking back to Figure 9, the one point that has not yet been discussed is polymers' function as polymer binders in LIBs. Via its adhesive properties, the binder acts as the glue between the active materials of the electrode, yielding an interconnected electrode structure and mechanical integrity during cycling. Therefore, it has a significant impact on the battery performance and serviceability. A polymer that offers good chemical resistance in common carbonate-based solvents like EC, DEC, or DMC is polyvinylidene fluoride (PVDF). It dissolves in *N*-methylpyrrolidine (NMP) and allows the preparation of cathode slurries with tunable viscosities.[134] Nevertheless, it has to face several limitations. The non-polar structure of PVDF prevents intermolecular solid interactions between the active material and the current collector. During the charging/discharging cycles, contact loss can occur due to the disruption of the cathode composite from the current collector.[135] In addition, its electronically insulating nature makes the addition of carbon additives unpreventable. Even though it is expected to add active carbon into the cathode, its tendency to form agglomerates is one reason researchers try to prevent its usage.[136-137]

For this reason, several alternative polymer binders were investigated. The main focus was their ability to build strong adhesion with the active material and the current collectors to prevent internal contact

losses and exfoliation during cycling. The volume changes during the intercalation/deintercalation must be balanced, while the overall polymer binder should electrochemically and chemically withstand the reaction conditions that are predominant in a battery.[136] To fulfill all these requirements simultaneously, conductive polymers are again the material of choice. As described above, doping the π-conjugated polymers changes the nature of these polymers from semiconductors to metal-like behavior, enabling the movement of charge carriers along the polymer backbone.[138] Although the low thermal stability of conductive polymers makes their processing difficult, several groups have already presented applicable synthesis and processing concepts. An example of an elegant combination of a conductive polymer structure and feasible processability is PEDOT: poly (styrene sulfonate) (PEDOT: PSS). PEDOT represents the conductive moiety, while PSS increases wettability and processability due to its hydrophilic character. Besides PSS, more hydrophilic additives such as formic or sulfuric acid can also drastically enhance the electrical conductivity of the composite in a secondary doping step.[139-140] The electrochemical stability over a sufficiently wide operating potential window allows PEDOT: PSS to be used as a binder in a variety of cathode materials like LFP or NCM and, to some extent, also as additives and coatings in the anode itself.[141] PEDOT: PSS composites' competitiveness over conventional PVDF binders can be shown by setting a conductive and robust framework.[136]

Other binder concepts focusing on lower production costs start with conjugated polymers like PANI, PPy, or PTh as a conductive matrix. Carboxylate-containing polymers such as carboxymethyl cellulose or sodium alginate serve as dopants and dispersing agents and can be mechanically mixed or *in situ* polymerized inside the conductive matrix. The resulting binders are known to form strong hydrogen bonds with their surroundings. This concept is preferably used in silicon-nanoparticle anodes, where the carboxylate groups click with the hydroxy group on the nanoparticle surface.[142] Instead of mixing the conjugated polymers with hydrophilic components, they can be intrinsically modified without establishing a polymer blend. By grafting, hydrophilic monomers can directly be linked to the side chains of the conductive polymers. With this setup, an LFP cathode with sodium alginate-modified PEDOT achieved a capacity of 170 mAh g^{-1} without significant capacity reduction over 400 cycles.[143]

2.1.2 Lithium-sulfur batteries

As it is impressively demonstrated in their application in LIBs, conjugated polymers can be an interdisciplinary allrounder for all sorts of applications inside a battery setup. In the case of lithium-sulfur batteries, conjugated organosulfur polymers could support or replace the pure sulfur electrode to a certain extent. In a classical lithium-sulfur battery, the electrodes consist of a pure lithium anode on one side and a pure sulfur cathode on the other. This constitution would promise a battery with the highest possible theoretical energy density outcome, as the sulfur itself has a very high theoretical specific capacity of 1673 mAh g^{-1} and pure lithium is the favorable anode material.[144] Between the electrodes, similar to the setup in liquid LIB, an organic solvent and a separator divide the battery into two half-cells (see Figure 11). As organic solvents, mostly 1,2-dioxolane, 1,3-dimethoxyethane, or fluorinated ethers are used.[145] Despite their promising theoretical capacity values, lithium-sulfur batteries still struggle to enter the commercial market. This can be reasoned with inherent issues of low conductivity of sulfur, the so-called "shuttle effect" of polysulfides, and material deformation based on significant sulfur expansions.[146]

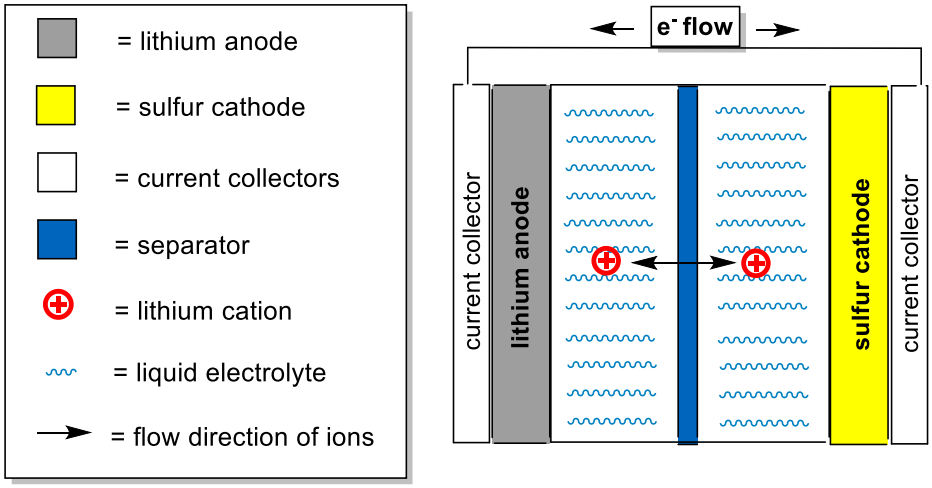

Figure 11: Schematic representation of a lithium-sulfur battery and its components.

The lithium anode is oxidized during charging to form Li^+ cations that move through the electrolyte from the negative to the positive electrode. The cations combine with sulfur at the sulfidic cathode side to form polysulfides (Li_2S_x, with x = 1-8) in various reactions. When the discharging starts, the ring-structural octasulfur S_8 is stepwise reduced to form in the first place high-order polysulfides like S_8^{2-}, S_6^{2-}, and S_4^{2-}, that are soluble in the electrolyte. In the second process, insoluble low-order polysulfides like Li_2S_2 and Li_2S are generated. The formation of soluble and insoluble sulfur species can be easily monitored by two distinct voltage plateaus at 2.4 V and 2.15 V, respectively. [147] As the high-order

polysulfides dissolve in the electrolyte, they move toward the lithium anode, triggered by an internal concentration gradient. They are converted to insoluble, low-order polysulfides at the negative electrode and migrate back to the cathode, forming longer-chain polysulfides.[148] This shuttling of the polysulfides between the electrodes has several severe consequences: The cathode constantly loses active material, reducing overall capacity. In addition, the shuttled polysulfides tend to react with pure lithium, provoking lithium corrosion and enhancing dendrite growth from the lithium and the sulfur side. As the low-order polysulfides accumulate at the interfaces between electrolyte and electrodes, the formation of densified polysulfide films tremendously increases the battery's impedance. In the worst case, the surfaces are covered to such an extent that the battery stops working.[149]

Conjugative binders like PEDOT: PSS can address the problem of sulfur delamination and shuttling of the polysulfides, but an overall replacement alternative to pure sulfur cathodes is wished. This is where the organosulfur compounds come into account. In 1988, *Visco* and *DeJonghe* started to use organosulfide compounds as cathode materials.[150] They have the same storage mechanism as lithium-sulfur batteries, meaning they can reach nearly the same specific capacities.[126] The essential advantages lie in their higher stability, mainly if the polymer is constructed so that the S-S bonds are not directly incorporated in the main core of the polymer backbone. Figure 12 depicts several examples of possible organosulfur geometries divided into main-chain-type, side-chain-type, p-type organosulfur polymers, and organosulfur polymers containing polysulfide bonds.[126]

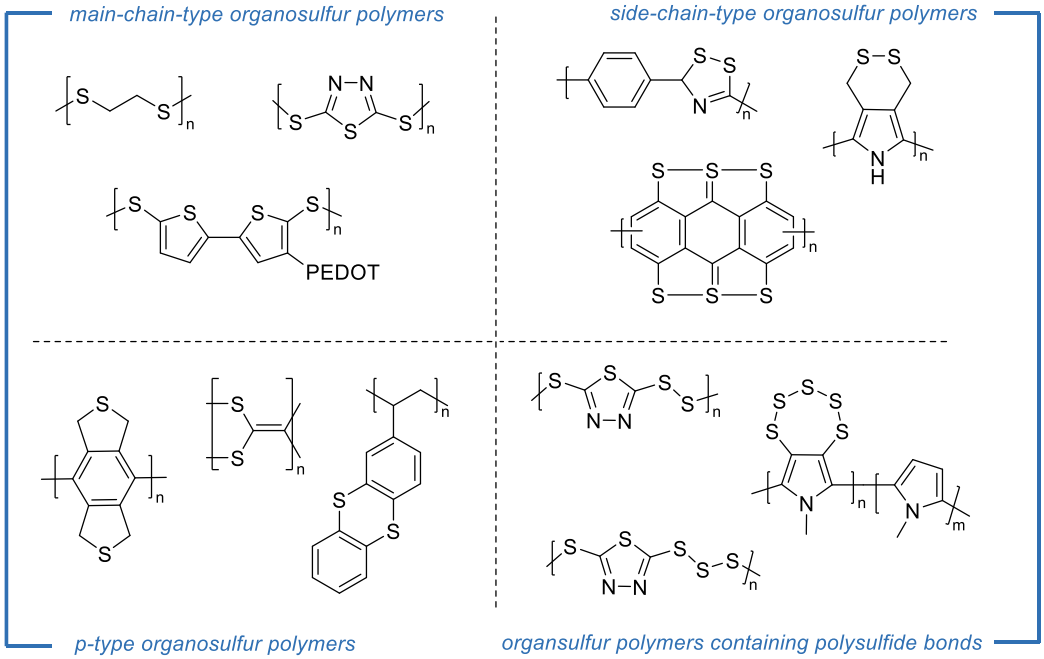

Figure 12: Overview of applied organosulfur polymers in lithium-sulfur batteries, categorized into four main groups.

2.1.3 Lithium-air batteries

Switching from sulfur to oxygen, we end up with lithium-air batteries. In recent years, they gained interest, as it is possible to reach a high theoretical specific energy of 3505 Wh kg^{-1} and a theoretical energy density of 3436 Wh L^{-1}.[151] In general, four different geometries of this battery type exist. Three use liquid electrolytes (aprotic, aqueous, or a mixed system), while the last approach is based on a solid electrolyte. Since Abraham and Jiang discovered the aprotic lithium-air battery, this setup can still be considered the most typical one.[152] It contains a lithium metal anode in direct contact with an electrolyte, forming a stable SEI. The electrolyte consists of an aprotic solvent, like EC or PC, that dissolves lithium salts such as $LiPF_6$, $LiAsF_6$, or $LiN(SO_2CF_3)_2$. As a counterpart to the anode, a highly porous O_2-breathing cathode is necessary (see Figure 13).

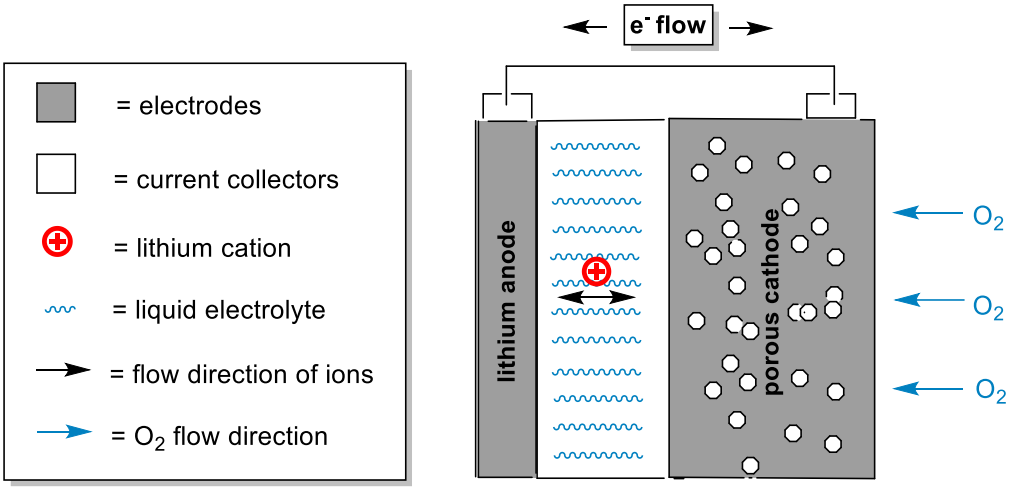

Figure 13: Schematic representation of a lithium-air battery and its components.

Usually, a mesh is applied, to which large surface area conductive carbon and catalyst particles are bonded and supported by a polymeric binder. During discharge, the lithium is oxidized at the anode, producing lithium cations and an external circuit electron flow. The ions reduced the oxygen on the cathode side to superoxide radical anions, leaving Li_2O and Li_2O_2 as cathode products. This process generates an average voltage of 2.96 V. When the battery is charged again, the processes are reversed (see following equations). Lithium metal is plated out on the anode, and oxygen is released.[153]

$$\text{Discharge: } 2Li + O_2 \rightarrow Li_2O_2 \qquad (4)$$

$$\text{Charge: } Li_2O_2 \rightarrow 2Li + O_2 \qquad (5)$$

Also, polymers play a decisive role in the function of cathode binders in this type of battery. As the catalyst particles are held on a mesh that is flowed through by oxygen, it is even more critical that all

components are tightly glued together. The difficulty in lithium-air batteries is the high reactivity of the superoxide radicals formed during the battery operation.[154] Not only are carbonate-based electrolytes attacked and decomposed by radicals, but polymers also show instabilities and battery failures. In this context, PVDF is a good example, as its backbone is dehydrofluorinated in the presence of LiO_2, generating lithium fluoride at the interfaces of the lithium-air battery.[155] Other representatives such as poly (acrylonitrile) (PAN), poly (vinyl chloride) (PVC), copolymers of PVDF, and hexafluoropropylene (PVDF-*co*-HFP), or poly (vinylpyrrolidone) (PVP) are not stable against the attack of the oxygen-based radicals. The halogenated polymers in this row present a labile hydrogen atom near the halogen substituent that can easily be abstracted in a dehydrohalogenation reaction. To reduce the potential for side reactions and hydrogen abstraction, the geometry of the polymers must be adjusted. Incorporating worse leaving groups like fluorides in poly (tetrafluoroethylene) (PTFE) and Nafion® or introducing methyl or methoxy functionalities, as seen in PMMA, increases the polymeric stability behavior. Poly (ethylene oxide) (PEO) can be seen as a semi-stable polymer in lithium-air batteries, which can undergo cross-linking reactions.[153] Figure 14 depicts an overview of polymer types commonly used in lithium-air batteries, divided into stable and unstable categories.

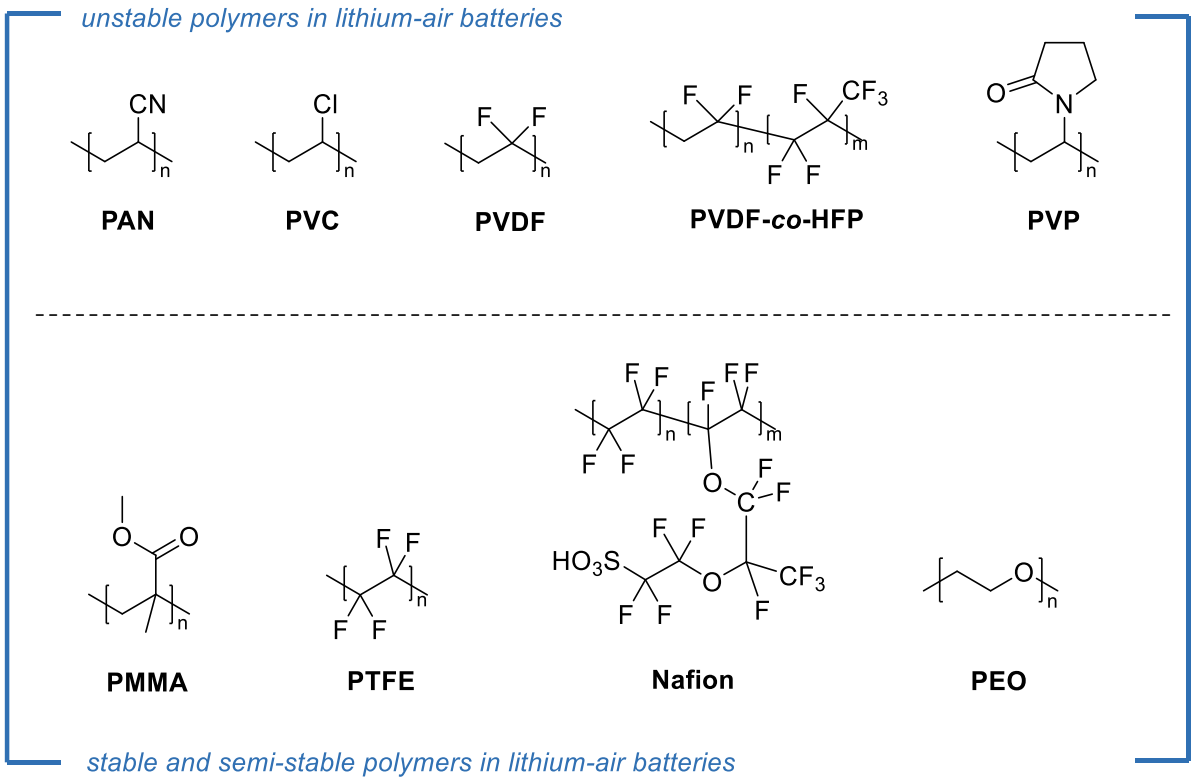

Figure 14: Unstable (PAN, PVC, PVDF, PVDF-*co*-HFP, PVP), stable (PMMA, PTFE, Nafion), and semi-stable (PEO) polymer types in lithium-air batteries; instabilities are evoked due to the superoxide radical formation during cycling.

Although polymeric binders can effectively support the maintenance and performance of lithium-air batteries, their commercialization still needs to be slowed down. Researchers today shed light on the poorly understood internal electrochemical reactions that influence battery cycling and efficiency. On the material side, the development points towards oxidation-resistant electrolytes and cathode compounds, the optimization of transport properties of all reactants, and the establishment of robust SEIs. As the high reactivity of the superoxide radicals will always stay a bottleneck in this type of battery, stable battery compounds will be the key to success.[156]

2.1.4 Organic radical batteries

The organic radical battery is another battery type in which polymers are prominently represented. When polymer-based batteries were developed, the aim was to get away from dependencies, availabilities, and accessibilities. Regarding LIBs or any battery type that uses lithium, cobalt, or rare earth metals in any treatment, the question of mining and the life span of natural resources remains.[157] Substituting conventional metals for organic and polymeric materials facilitates access to energy storage. A milestone was set in the 1970s when poly (acetylene) transformed from an insulator to a semiconducting or conducting material. After doping the polymeric film with chlorine, bromine, and iodine vapor, the ionic conductivity at room temperature remarkably increased.[127] Research was then mainly focused on conjugated polymers like PPy or PTh in their function as electrode materials, as the π-delocalized systems can successfully store electric energy via the delocalization of charge carriers. However, one major problem of these systems is that their resulting redox potential is always dependent on the state of doping. Due to the degree of doping changes during charging and discharging, it is impossible to create distinct redox sites with defined cell voltages.[158]

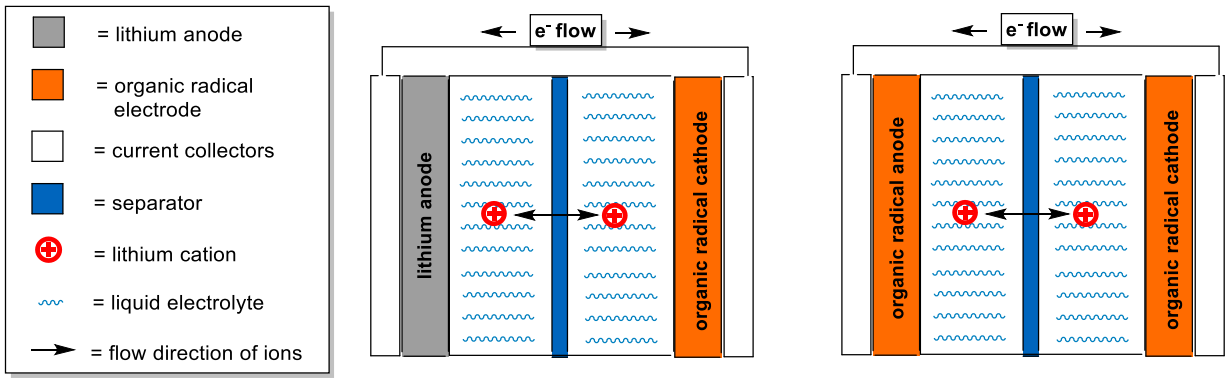

Figure 15: Schematic representation of an organic radical battery and its component; left: mixed electrodes (radical polymer/Li metal), right: uniform electrodes (only radical polymers as anode and cathode).

Radical polymers with defined electrochemically active moieties were designed to overcome this issue. The polymeric electrode structure comprises two parts: a non-conjugated or conjugated polymer backbone and a radical unit that is grafted onto the backbone.[126] The most famous and well-known nitroxide radical in this setting is 2,2,6,6-tetramethyl-1-piperidinyloxy (TEMPO). In 2001, TEMPO was linked to a PMMA backbone and applied as cathode active material in a rechargeable battery. By stacking the organic radical polymer cathode with an EC/DEC liquid electrolyte and a lithium anode, an average discharge voltage of 3.5 V and a discharge capacity of 77 Ah kg^{-1} was achieved, even after cycling the battery for over 500 cycles with a high current density of 1.0 mA cm^{-2}.[159] If the battery is to contain

electrodes that are metal-free, that means being fully polymer-based, then both electrodes must be built up on organic radicals (see Figure 15).[160]

This is possible due to the nitroxide radical exhibiting a perfect redox couple. P-doping implies the oxidation of TEMPO to reversibly form an oxoammonium cation, while n-doping means the reversible reduction to an aminoxyl anion (see Figure 16). In an organic battery based exclusively on polymers, the bifunctionality of TEMPO can, therefore, be used both on the cathodic and the anodic side.[157]

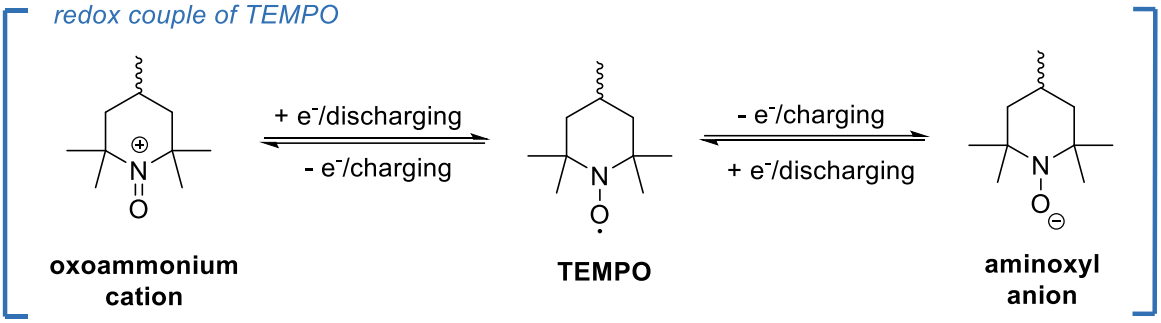

Figure 16: Representation of the TEMPO redox behavior; oxidation leads to the oxoammonium cation (left) and reduction to the aminoxyl anion (right); both reactions are reversible upon electron uptake.

In relation to metal-based cathodes, organic radical cathodes containing TEMPO do not rank behind in cell voltages, as they achieve values between 1.2 to 3.6 V. [161] Coulombic efficiencies are in the range of 95 to 97%.[162] Due to the possibility of linking the TEMPO radical to various polymeric backbones, organic radical batteries leave an impressive space for molecular design tailoring.

This chapter took the opportunity to first introduce multiple applications that polymers can exploit in different setups of batteries. Their fields of operation can incorporate polymers as binders, cathode additives, cathode and anode materials, and a lot more. The following chapters should open the horizon to another working principle. The polymer experiences an entirely new function: a polymer as a solid electrolyte.

2.2 Road to a solid future: solid electrolyte representatives

Batteries are in a constant mode of development. The historic pathway started with the idea to convert chemical into electric energy. Multitude battery concepts passed, always aiming to construct a safe, robust setup with higher energy and power densities than the previous ones. As described above, many technologies already exist that present approaches that can be widened to future applications. Nevertheless, improvements are often accompanied by new bottlenecks. Current battery research tries to address three main challenges:

1) increased battery performance, meaning maximal efficiency regarding energy and power densities, to fulfill our demanding electrical future visions;
2) a high intrinsic safety without the need for particular safety regulators;
3) sustainability, which should be reached with easily processable and long-living components.

Research is questioning which new technology could combine all these requirements. The battery types discussed in the previous chapter all use polymers in different parts of their setting. May it be as porous separators in LIBs, conductive redox-polymers in cathode additives, binders for cathode active materials, cathode replacement in organosulfur batteries, or anodic or cathodic electrode material for organic-based batteries. One function still missing from this list will be discussed in this chapter: polymers acting as solid electrolytes between the electrodes.

Visualizing a LIB again, the main components are an anode, a cathode, a liquid electrolyte, and a separator. Since the processing and working principle of LIBs are well-established nowadays, a significant part of portable electronics bear LIBs due to their inherent advantages over other battery systems.[163] However, their implication in EV applications could be improved. One reason for this is the safety problem, that comes along with the liquid electrolyte. Flammable organic electrolytes can leak if the cell is damaged, causing the battery pack to catch fire. These thermal runaways and fire ignitions make conventional LIBs unfavorable in applications with high currents.[164] Additionally, looking at a LIB's power, there is always a limitation present. Incorporating lithium metal as the anode is nearly unavoidable to reach increased energy and power densities. Safe cycling against lithium metal is challenging with a liquid electrolyte. Due to unpredictable side reactions, the lithium deposits unevenly on the negative electrode, forming dendritic structures (see Figure 17).[165] Theoretically, the porous polymeric separator, which splits the battery into cathodic and anodic half cells, should block the growth of dendrites.[166] Nevertheless, it is often the case that the polymer shear modulus is insufficient to suppress the penetration of the dendrites. Internal short circuits occur, where the mechanical integrity of the cell is maintained, but the stored electrochemical energy continues to be converted into internal heat.[167]

Preventing this safety risk is one primary reason to consider a battery without an organic solvent as a liquid electrolyte.

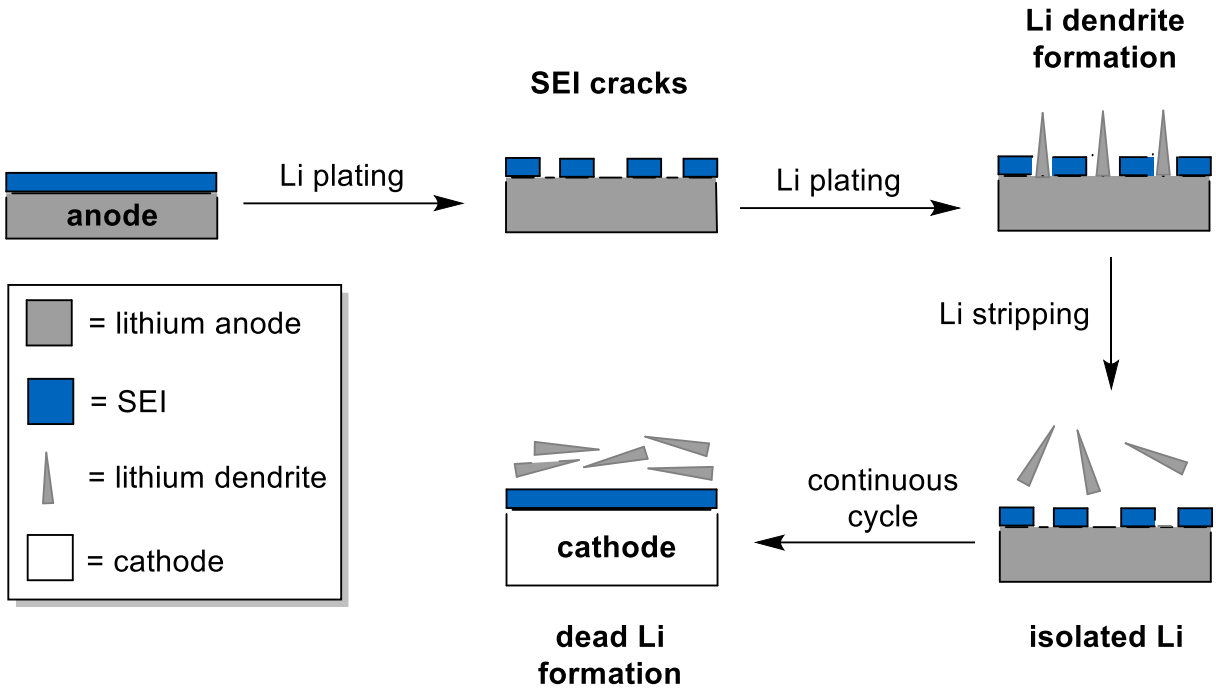

Figure 17: Schematic representation of the uneven deposition of lithium on the lithium anode side; continuous formation of lithium dendrites and "dead lithium".[168]

Besides the thermal safety issues, the inability to incorporate a lithium anode in the presence of a liquid electrolyte is also another significant disadvantage. Lithium has the lowest electrochemical potential of –3.04 V (versus standard hydrogen electrode) in the galvanic series and one of the highest theoretical capacities of 3860 mAh g^{-1}.[42] These properties enable the building of an extremely powerful battery when the anode is combined with a high-voltage cathode. As our requirements for EV power with longer distances and faster charging continuously increase, conventional LIB with graphite intercalation anodes can no longer compete with these obligations.

The answer to this problem is simple. As the significant bottleneck of LIBs is the liquid electrolyte, this part of the battery needs to be replaced by a safer alternative. This is how the concept of all-solid-state batteries (ASSBs) was born. The idea of a battery, where all components are solid, was already discovered in the 1830s by *Faraday*. He found the first motion of mobile ions in the solid compounds Ag_2S and PbF_2 by observing the transition from poorly conduction to conduction materials under the influence of heat.[169-170] In 1914, the archetype of the solid electrolyte was born. *Tubandt* and *Lorenz* first looked into silver halides, namely AgCl, AgBr, and AgI. Especially the α-AgI showed an extraordinarily high ionic conductivity comparable to the best conducting liquid electrolytes.[171] The silver cations'

transport mechanism inside the crystallographic network kept the research community discussing for a long time. It was found that the ionic transport was mainly based on the degree of disorder inside the body-centered cubic structure of the iodine ions.[172] In this context, the concept of point defects was mainly established and explored by *Frenkel, Schottky,* and *Wagner*.[169] Their work facilitated the visualization of ionic and electronic transport in ionic crystals. In the meantime, other compounds such as *α*-CuI, *α*-/*β*-CuBr, as well as the high-temperature phases of Ag_2S, Ag_2Se, and Ag_2Te, which also belong to the same structural family, followed the example of *α*-AgI. As this battery type needed silver as anode material, only low cell voltages of around 0.5 to 1.0 V and low energy densities were achieved.[172]

Over the years, the crystalline materials with their defects were replaced by ion-conducting glasses. The advantages seen here were their physical isotropy, a variable tunable composition, and the absence of grain boundaries, which can produce high impedances.[173] A usually applied composition was made out of a network former, like SiO_2 or B_2O_3, supported by a network modifier, such as Na_2O or Ag_2O. The doping of the glass with halide-based salts, for example, NaCl or AgI, enabled the rise of ionic conductivities. Glass compositions like Na_2O x 3 SiO_2 mainly dictated the field of ion-conducting glasses in the direction of sodium as mobile ion and charge carrier.[169]

The search for energetically richer solid-state batteries favored the switch to lithium-ion conducting materials. Also, in this case, LiI or Li_2S glasses based on ternary compositions were representatives for high ionic conductivity compounds. The breakthrough for ASSBs was reached when *Fenton* and *Wright* proposed the first ion-conducting polymers.[174] PEO was mixed with sodium iodide and sodium, potassium, and ammonium thiocyanates. At different temperatures, *Wright* investigated the behavior of activation energies of the polymer-salt complexes. He was already able to figure out that the cations are coordinated with the oxygen atoms in the polyether backbone and that the amorphous phase of the polymer must significantly influence the polymer transitions and the cation movement.[175] So far, the history of solid-state batteries has evolved, and many different battery concepts have been presented. The following listing should give an overview of the most popular ones (also including chemistries that were not discussed in detail) (see Figure 18):[172]

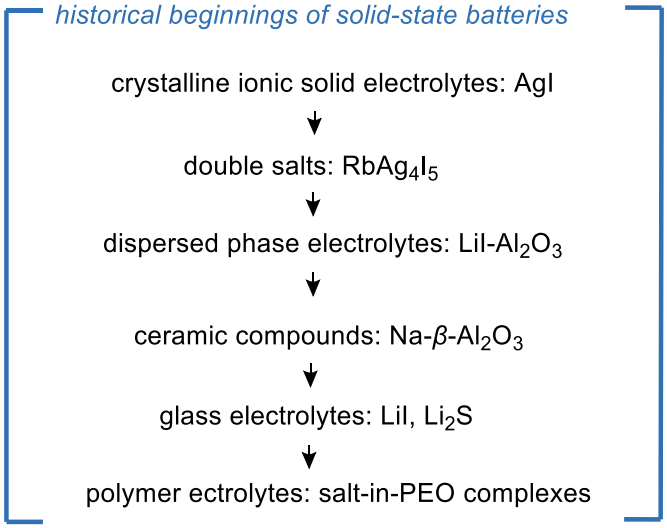

Figure 18: Overview of the historical development of solid-state electrolytes.

Immediately after the salt-in-polymer electrolyte discovery, *Armand* recognized the potential of this finding and proposed its application in electrochemical cells. In the beginning, the ionic conductivities that *Armand* reported with its PEO-salt electrolytes were not very high, only about 10^{-5} S cm^{-1} at 40 to 60 °C.[176] Even though the ionic conductivities were lower than for previously reported glassy alternatives, researchers worldwide saw the benefits that polymers offer with their properties. In contrast to brittle glass-based electrolytes, mechanically soft and flexible polymers were the ideal candidates to provide excellent interfacial contact between all the solid components.[169]

Since the prototypes for polymer-based ASSBs started to be realized, time has passed. New technologies and cell chemistries were developed. The upcoming chapters will discuss the most popular ones (sulfidic, oxidic, polymer, halide, and other electrolyte classes). What all ASSBs have in common are their advantages over conventional LIBs (see Figure 19). Regarding safety, ASSBs offer an intrinsically safe concept, as no volatile components are incorporated. Based on the possible integration of a pure and light lithium anode and the thinner processing of the solid electrolytes compared to the liquid part, the volumetric and gravimetric energy densities are increased by 70% and 40%, respectively.[177] As the polymeric separator is not needed anymore in the ASSB setup, the material and processing costs can be reduced. The packing process can also be simplified by stacking bipolar electrodes and solid electrolytes.[164]

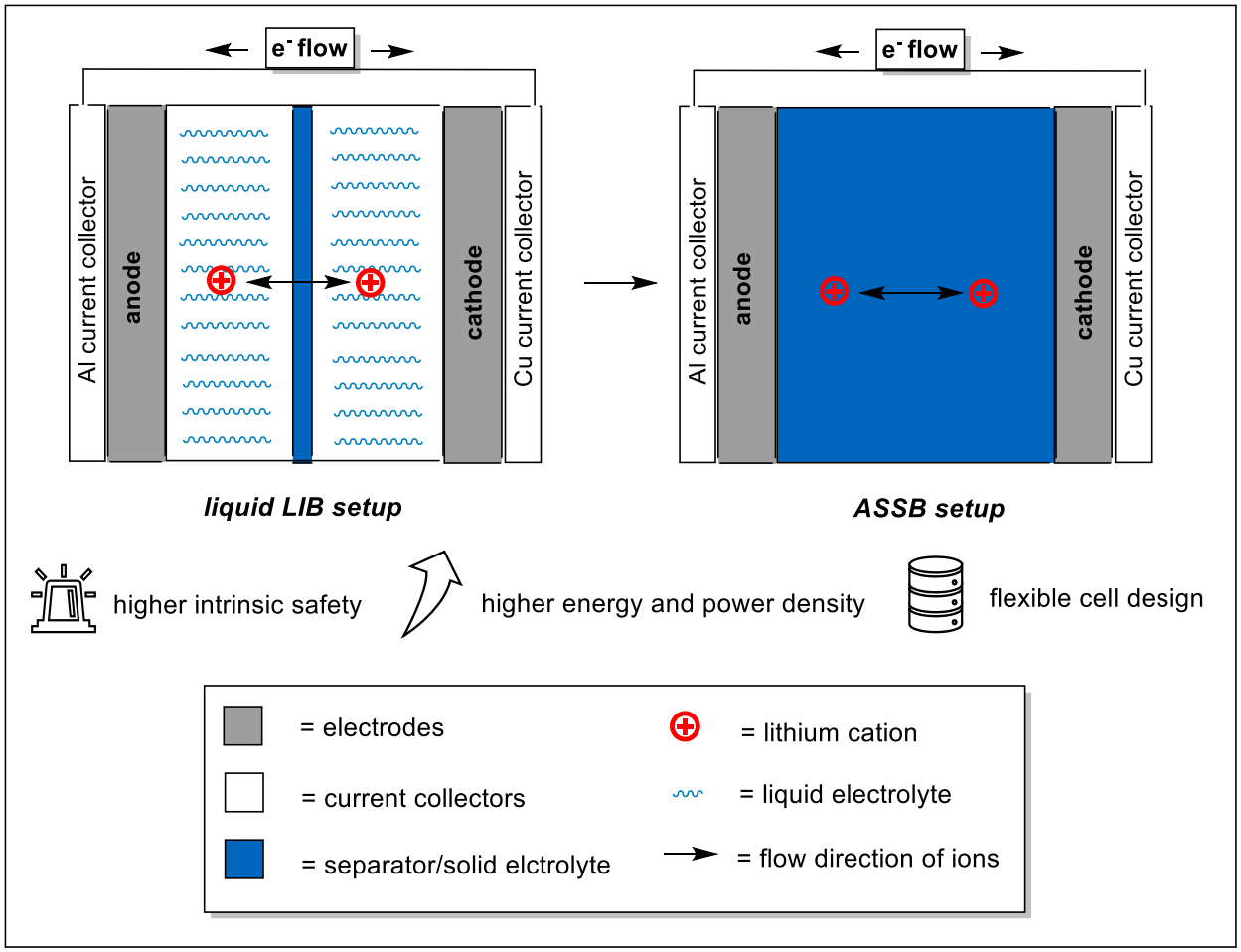

Figure 19: Replacement of rechargeable, liquid LIBs against ASSBs; transition from LIB limitations to higher energy and power densities by incorporating only solid components and lithium as anode material.

2.2.1 Sulfidic electrolytes

The so-called sulfidic electrolytes are the first solid-electrolyte class conventionally used today in larger-scale applications. They belong to the group of inorganic electrolytes and can be separated into crystalline and amorphous sulfides. The examples of the most common crystalline compounds, namely thio-lithium ion superconductors (LiSICONs) such as $Li_{10}GeP_2S_{12}$ (LGPS) or the argyrodite-type Li_6PS_5X (X = Cl, Br, I) (LPS), and the amorphous sulfidic compounds such as Li_2S-SiS_2 (see Figure 20), are discussed in detail below.[178]

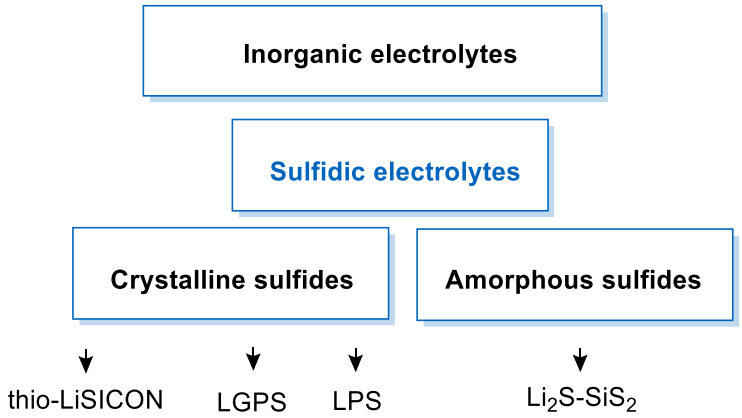

Figure 20: Classification of the sulfidic electrolytes into the solid-state electrolyte overview; sulfidic electrolytes are composed of crystalline and amorphous sulfides, whereas the most important examples (thio-LiSICON, LGPS, LPS, Li_2S-SiS_2) are listed.

The element sulfur forms relatively large ions in size, evoking a polarizable character. This fact favors the lithium ion mobility, pushing the ionic conductivities to values around 10^{-2} S cm^{-1}.[179] Crystalline sulfides of the thio-LiSICON family consist of the general formula $Li_xM^1_{1-\delta}M^2_\delta S_4$, with M^1 that can be occupied by Si, Ge, Sn and M^2 by P, Ga, Al or Zn.[180] Within this family, the most famous representatives are LGPS and LPS. LGPS, with its formula $Li_{10}GeP_2S_{12}$, exhibits a room temperature ionic conductivity of 1.2 x 10^{-2} S cm^{-1}.[181] Its structure is a 3D framework whose core comprises three different types of tetrahedra ($Ge_{0.5}P_{0.5}$)S_4, PS_4, and LiS_4) fused with LiS_6 octahedra. The high ionic conductivity in this system can be traced back to the formation of 3D diffusion pathways constructed along the c-axis and in the a-b plane.[182-183] Due to its high electrochemical stability and neglectable electronic conductivity, it can be applied with various common cathode materials like LCO or NMC.[182] A battery with LCO as a cathode, LGPS as an electrolyte, and lithium as a metal anode can exhibit a discharge capacity of 120 mAh g^{-1}.[184]The challenge in using LGPS is more on the anodic side, as it is labile to elemental lithium at specific potentials. Some of the decomposition products formed at this contact, like Li_3P or Li_2S, are considered to support ionic conductivity. Others, like Li_xGe alloys, evoke drastic volume changes at the anode side.[185]The battery performance losses that are a consequence of this decomposition can be lessened

when protective layers between the anode and LGPS are used. One example is LiH_2PO_4, with which LGPS/Li-cells can reliably cycle up to 500 cycles with a discharge capacity of 113 mAh g^{-1}.[186]

Argyrodites also take part in the crystalline classification of sulfidic electrolytes. Via milling and annealing of the starting materials Li_2S, P_2S_5, and LiX (with X = Cl, Br, I), the cubic lithium argyrodites with the general formula Li_6PS_5X (LPS) are obtained with different ionic conductivities at room temperature depending on the choice of halide.[187] Li_6PS_5Cl (LPSCl) and Li_6PS_5Br (LPSBr) have the highest values of 10^{-3} S cm^{-1}, whereas Li_6PS_5I (LPSI) only reaches an ionic conductivity of 10^{-7} S cm^{-1}.[187] The reason is found again in the crystal structure of the materials. All LPS consist of low-energy local pathway cages essential for the lithium movement but slightly differ from each other. In LPSCl and LPSBr, a direct in-between connection across the cages builds up a 3D extended-range pathway network that can support an efficient movement of the lithium cations. However, in LPSI, the setting of the disordered lithium cation distribution changes, and with this, the activation energies for the long-range transport are also unfavorable.[187] As the high ionic conductivities nevertheless classify LPS as preferred solid electrolytes at room temperature, *Samsung* used the chance to integrate them in an intelligent cell setup. A silver-carbon interlayer substitutes lithium to suppress contact losses and dendrite formation at the LPS/lithium anode interface. Therefore, the only lithium source is the cathode itself, and the lithium deposits directly on the current collector. Energy densities greater than 900 Wh l^{-1} over 1000 cycles were achieved.[188]

Switching from crystalline to amorphous sulfidic electrolytes, the material properties change entirely. Amorphous or so-called glassy electrolytes have the advantage of showing isotropic ionic conduction, not having to handle grain-boundary resistances, and their conductivities usually are slightly higher based on their structural alignment. [189-190] In Li_2S-SiS_2, ionic conductivities up to 10^{-3} are reached. [191] Their conductivities can be tuned by mixing lithium halides, ortho-oxo salts, and network modifiers like SeO_2 into the glass.[181] Therefore, it has to be noted that the modifier amount does not exceed a specific value, as it increases the crystallization of the glass. Consequently, higher temperatures during cell assembly are required to preserve their glassy state.[192]

In summary, sulfidic electrolytes present robust ionic conductivities at room temperature, reaching 10^{-2} S cm^{-1} with their best-performing crystalline compounds. Their ductile character facilitates energy-saving cold-pressing techniques, where the separator and the electrode ingredients can be perfectly densified. [164] Nevertheless, the remaining challenges lie on the one hand in the interfacial instabilities against metallic lithium. On the other hand, sulfides present the problem of heavily reacting with humidity to form H_2S.[193-194] The necessity of handling all the components for each step under an inert

atmosphere tremendously increases manufacturing costs. The main advantages and disadvantages of sulfides are shown in Figure 21.

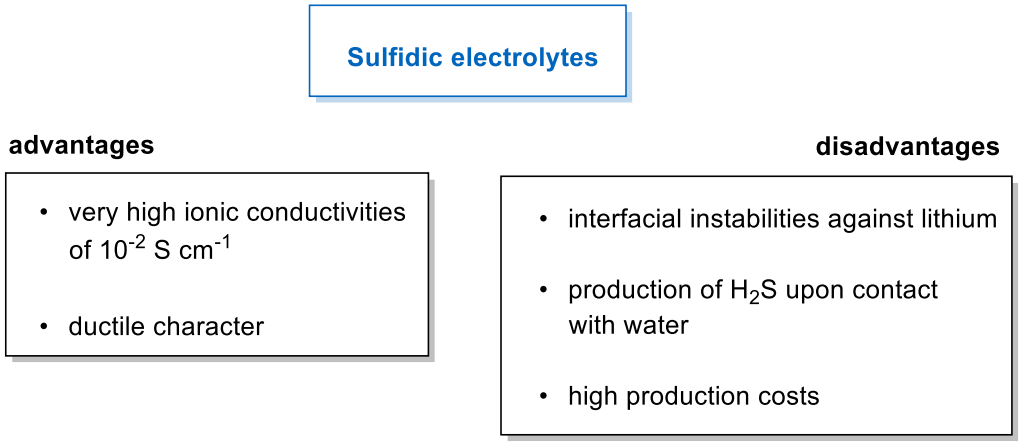

Figure 21: Summary of advantages and disadvantages of sulfidic electrolytes for ASSB application.

2.2.2 Ceramic electrolytes

The second well-known class of solid electrolyte representatives are the ceramic electrolytes. Figure 22 depicts a schematic overview of the existing classification inside of this material class. In general, they can be divided into garnet-($Li_7La_3Zr_2O_{12}$ (LLZO)), perovskite-($Li_{3x}La_{(2/3)-x}V'_{(1/3)-2x}TiO_3$ (with V' = vacancy and $0 < x < 0.16$) (LLTO)) type, glass-type ($LiA_2^{IV}(PO_4)_3$ (with A^{IV} = Ti, Zr, Ge, Hf) (NASICON)) and amorphous ceramic electrolytes ($Li_xPO_yN_z$ (with $x = 2y + 3z - 5$) (LiPON)).[181] "Ceramic" means that the main core of the compounds is based on oxidic structure motifs. Their characteristic properties are manifested in relatively high ionic conductivities and, in most cases, a distinctive stability against lithium metal.[181]

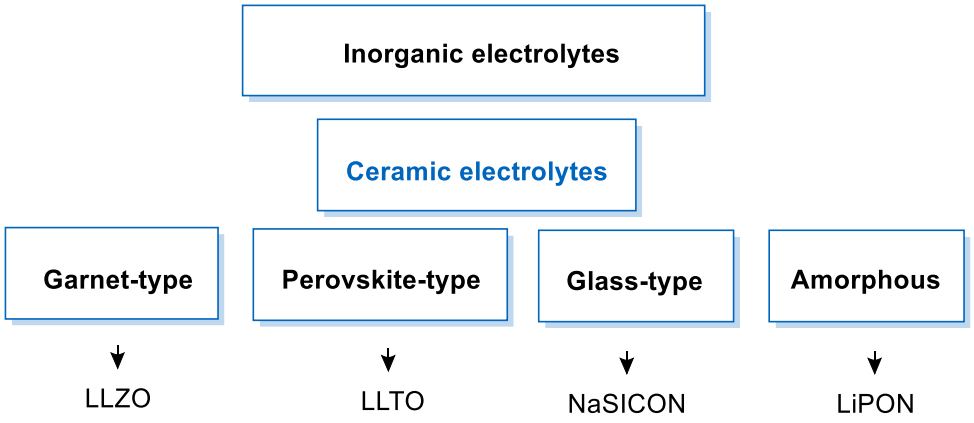

Figure 22: Classification of the ceramic electrolytes into the solid-state electrolyte overview; ceramic electrolytes are composed of garnet-, perovskite-, NaSICON-, and glassy-type oxidic compounds.

Starting with the most prominent ceramic class, the garnet electrolyte LLZO gained much attention since its discovery in 2007.[195] The cubic LLZO structure consists of dodecahedrons of eight oxygen atoms coordinated to one La center. The Zr coordinates six oxygen atoms and builds up an octahedron. The polyhedrons construct a 3D lattice framework through which the lithium ions can migrate.[196] The challenge concerning using LLZO is the material's phase transition, which occurs at higher sintering temperatures. Besides the cubic phase, LLZO can also be present in a tetragonal phase that shows two orders of magnitude lower ionic conductivity than its cubic relative.[197] To use the ionic conductivity of 10-4 S cm-1 of cubic LLZO, stabilization techniques like doping the structure with Al^{3+} ions can be applied.[198] Owing to the combination of moderate to high ionic conductivities, a wide electrochemical stability window, and an established resistance against lithium metal, LLZO is likely to be implied in ASSBs.[199]

Perovskite-type electrolytes like the lithium-lanthanum-titanate LLTO exceed the bulk conductivity of LLZO with 10^{-3} S cm^{-1} at room temperature (for x = 0.11).[200] Perovskites have the general formula ABO_3, whereas B-cations (substitutional for titanium in the case of LLTO) coordinate six oxygen atoms, forming corner-shared octahedra. The A-cations (in the case of LLTO lithium or lanthanum) are regularly filled into the voids generated by this 3D network. LLTO offers a mixture of cubic α- and tetragonal β-phases, whereas the tetragonal one can explain the high conductivity by a large concentration of A-cation vacancy sites. These allow an effective movement of the lithium cations based on a vacancy mechanism.[201] Even though LLTO exhibits stability over a wide temperature range, against humidity, and high potentials (up to 8 V), two bottlenecks make its practical application in ASSBs difficult. It has a low grain boundary ionic conductivity of 10^{-5} S cm^{-1}, evoking higher impedances during cycling.[202] Additionally, it is unstable against lithium. This instability can cause the reduction of the titanium cations and, therefore, increase the electronic conductivity.[203]

Similar to the sulfidic electrolytes, oxides also consist of glass-type electrolytes. The most popular and studied systems for oxides are the NASICON electrolytes with the basic formula of $A_xMM'(XO_4)_3$. They are known for their fast ion conduction and their structural flexibility, as the positions of A, M, and M' can variably be occupied (e.g., A = Li, Na, K, Mg, Ca; M or M' = Fe, V, Ti, Zr, Sc, Mn, Nb, In; X = S, P, Si, As). Depending on the choice of metals, the crystal structures of the compounds can vary between rhombohedral and monoclinic structure types. Nevertheless, the main core of NASICON is based on MO_6 and $M'O_6$ octahedra, which share corners with XO_4 tetrahedra. The number of alkali ions in the interstitial spaces depends on the respective oxidation states.[204] Glass ceramics can be easily manufactured out of their mother glasses. Their size and shape can be finetuned via sintering, and the microstructure is readily densified.[205]

$Li_{1+x}Al_xTi_{2-x}(PO_4)_3$ (LATP) is a well-known member of the NASICON family. It is made out of Li_2O-Al_2O_3-TiO_2-P_2O_5 glasses that are heat-treated at 700-1000 °C for 12 h.[205] Its bulk ionic conductivity is around 10^{-3} S cm^{-1} at room temperature.[206] The presence of titanium ions favors the increase in conductivity, as the size of the lithium cation matches well with the framework established by the TiO_6 octahedra.[207] To reduce the increase in impedance and influence grain-boundary ionic conductivity (approximately 10^{-5} S cm^{-1}), LATP can be mixed with $Li_{1.5}Al_{0.5}Ge_{1.5}(PO_4)_3$ (LAGP). LAGP is also a NASICON-type electrolyte, so the high bulk ionic conductivities can be preserved. Only the grain boundary conductivity can be finetuned by the ratio between LATP and LAGP.[206]

Although amorphous ceramic electrolytes like LiPON show high stability in contact with lithium metal, their ionic conductivities of 10^{-6} S cm^{-1} are still too low to be competitive with other material classes.[208]

Compared to sulfidic compounds, oxides have higher stability in air and water. No toxic gases will be released upon the contact with air. Hence, their cell assembly is less dependent on inert atmosphere conditions than when using sulfidic solid electrolytes.[209] Nevertheless, the processing of oxidic electrolytes can be challenging. Depending on their low fracture toughness, garnet, perovskite, and glass-type ceramic electrolytes exhibit fragile and brittle behavior.[210] Considering only solid-solid interfaces in ASSBs, volume changes during cycling cannot be smoothly balanced. This could lead to contact losses, increased impedance, and a worse overall battery performance. To compensate for the disadvantages of sulfides and oxides, the next chapter will lead to soft polymer electrolytes and their effectiveness in solid batteries. The main advantages and disadvantages of oxidic electrolytes are shown in Figure 23.

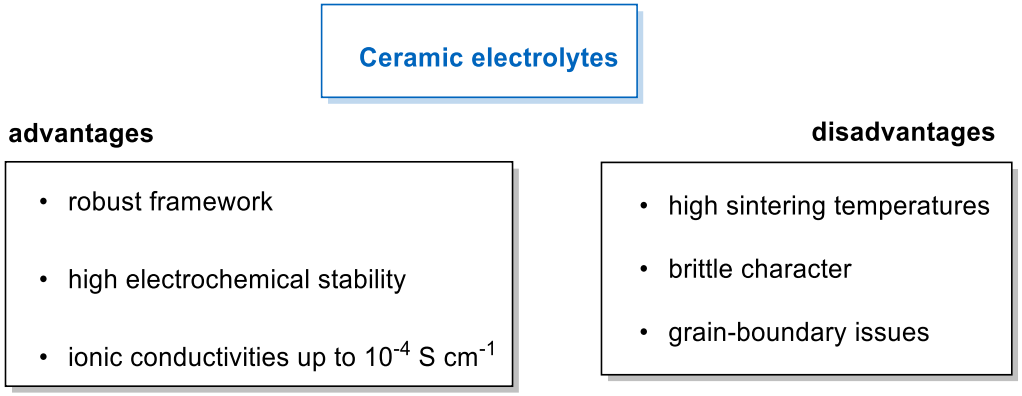

Figure 23: Summary of advantages and disadvantages of oxidic electrolytes for ASSB application.

2.2.3 Polymer electrolytes

In addition to inorganic electrolytes, in which sulfidic and ceramic electrolytes are widely represented, solid electrolytes are divided into a second class of materials: polymer electrolytes. As described in the previous chapters, polymers can be commonly applied in all battery setups. These include liquid LIBs, lithium-sulfur or lithium-air batteries, organic radical batteries, and others not covered in this work. Their widespread application is mainly based on their intrinsic flexibility, which sets them apart from crystalline materials. Especially in their use as solid electrolytes in ASSBS, their adaptability creates a perfect glue between solid components, preventing contact losses, lithium dendrite growth, and the increase of interfacial resistances during lithiation.[40, 211] In addition, polymers are lightweight. Hence, the weight of the finally assembled ASSBs will not depend tremendously on the selected polymer electrolyte. Their soft nature often allows reasonable thickness control using simple preparation techniques such as extrusion or pressing.[40] Solid polymer electrolytes can be divided into three main categories: polymer-salt-complexes, gel polymer electrolytes, and composite polymer electrolytes (see Figure 24).

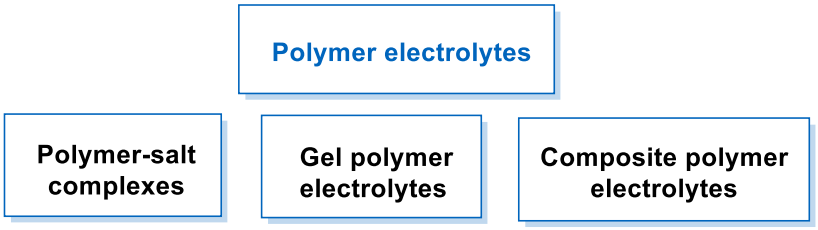

Figure 24: Classification of the polymer electrolytes into the solid-state electrolyte overview; polymer electrolytes comprise polymer-salt complexes, gel polymer electrolytes, and composite polymer electrolytes.

Independent of the polymer category, the story of almost every solid polymer electrolyte starts with PEO. The exploration of the polyether in its function as an ion-conducting polymer happened stepwise. After the discovery that PEO can dissolve lithium salts, Armand considered, via nuclear-magnetic-resonance (NMR) and differential-scanning-calorimetry (DSC) measurements, that the movement of the lithium cations must be related to the segmental motion of the polymer.[212] Since then, the transfer of the lithium cation through the solid polymer electrolyte can be visualized in three steps. First, the lithium cation is coordinated by five neighboring oxygen atoms located on one strand of the polyether backbone. Secondly, the polymer backbone switches into a five-membered, empty oxygen pocket when a chain is near the coordinated lithium-ion. The coordination of the cached lithium cation is loosened so that it can jump from one strand to the other into a new oxygen pocket. The last step is the coordination of the cation in the new pocket via the development of oxygen-lithium coordination bonds (see Figure 25).[213]

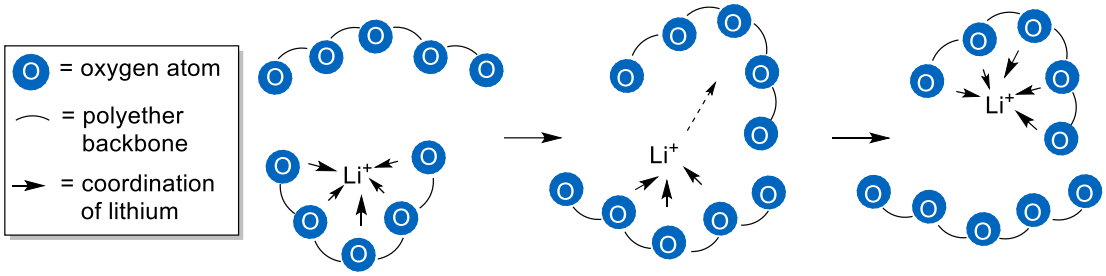

Figure 25: An assumed mechanism for the lithium-ion hopping through the PEO solid electrolyte; five oxygen atoms coordinate the cation by forming a pocket-shape, then the lithium cation jumps from one pocket to the next along the polymer backbone.

PEO is the ideal host material for lithium salts, as it exhibits high polarity that enables to easily dissolve a variety of different salts like $LiClO_4$, $LiBF_4$, $LiPF_6$, $LiAsF_6$, $LiCF_3SO_3$, or LiTFSI. The most-studied polymer-salt combination is PEO-LiTFSI due to the unique delocalized character of the TSFI anion.[214-215] Although PEO can be classified as a rather soft and flexible material, the ionic conductivities of these polymer-salt complexes at room temperature are relatively low, ranging around 10^{-7} S cm^{-1}. For the researchers in the early days, this was the first hint that some process must hinder lithium mobility. The answer can be found in the semi-crystalline character of PEO. Under 60 to 70 °C, the polymer composition is dominated by crystalline spherulites embedded inside amorphous regions.[216] NMR studies found that the ion motion takes place preferably in the amorphous regions of the polymer.[217] This implies that the lack of segmental motion of the polymer chains slows down or rather prevents cation movement. Suppose the temperature is below the glass transition (T_g) or melting temperature (T_m) of the polymer-salt complex. In that case, the amorphous polymer chain segments are too rigid to guide the cation from the anode to the cathode and vice versa (see Figure 26).

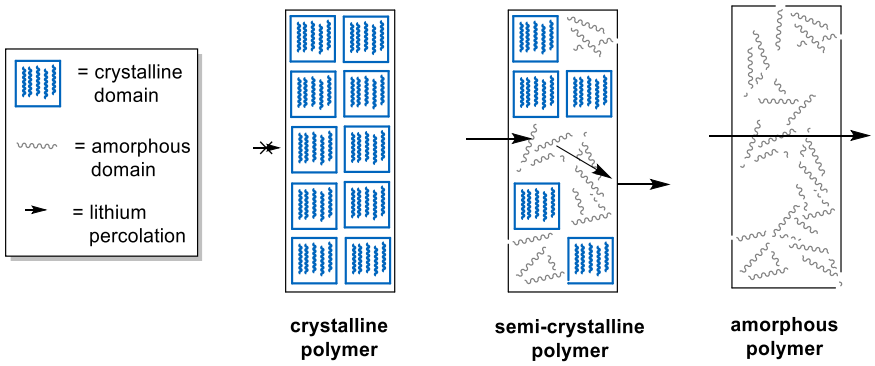

Figure 26: Schematic representation of the possible lithium migration pathways through PEO as a semi-crystalline polymer; crystalline domains hinder the cation passing, and amorphous domains support the movement.

That's why the overall aim, when working with PEO solid electrolytes, is always to reduce or suppress the crystallization of the polyether. Raising the temperatures over the T_g increases the amorphous

regions of the polymer but provokes a loss of mechanical strength of the whole solid electrolyte.[211] Furthermore, operating a battery pack at temperatures over 80 °C reduces battery safety, as dendrites can occur.[218] Adding bulky lithium conducting salts can also decrease the T_g, as the anions disturb the regular alignment of the polymer chains.[219] Thereby, the salt concentration significantly influences the resulting thermal properties and ionic conductivities (salt-in-polymer versus polymer-in-salt complexes).[220] Other efforts that have been devoted to creating amorphous enriched PEO-states include

1) blending of polymers
2) copolymerization to simultaneously finetune the ionic conductivity and the mechanical properties of the solid electrolyte
3) introduction of side chains on the PEO backbone or the formation of comb-shaped polyether matrices
4) addition of plasticizers, e.g. a small amount of organic liquids to form gel polymer electrolytes.

Blending is the most straightforward approach, as two respective polymers are separately dissolved and mixed. A second kind of molecular chain destroys the regularity of the PEO arrangement, inhibiting crystallization. Blending PEO in an 8:2 ratio with poly ethylenimine (PEI) and mixing the blend with $LiClO_4$ results in an ionic conductivity increase of up to 10^{-3} S cm^{-1} (at 30 °C).[221]

Via copolymerization, an optional number of polymers are covalently linked to each other. In a system with two polymer species, one component is often responsible for the mechanical stabilization of the copolymer, while the other exhibits more soft and ion-conducting properties.[222] The distribution of the monomers inside the copolymer decides, in the end, the thermal, mechanical, and electrochemical performance of the copolymer. The A-B copolymer of poly (acrylonitrile) (PAN) and PEO comprises PAN as hard component A and PEO as rubbery and soft segment B. PAN strengthens the dimensional stability of the copolymer by acting as reinforcing fillers, PEO dissolves the lithium salts and supports the ion movement through the electrolyte. This mélange pushes the ionic conductivity to a value of 10^{-4} S cm^{-1} (at room temperature) and assures electrochemical stability up to 4.8 V vs. Li/Li^+.[223] Alongside A-B block copolymers, also B-A-B triblock copolymers are commonly used polymer architectures. The hard segments like poly (styrene) (PS) surround the soft and ion-conducting polymer part to build up a strong and stable core. This strategy can achieve excellent mechanical and electrochemical stability without sacrificing the polymer chain mobility and ionic diffusion pathways.[224] Figure 27 shows a classical A-B-type block-copolymer compared to B-A-B-type copolymers.

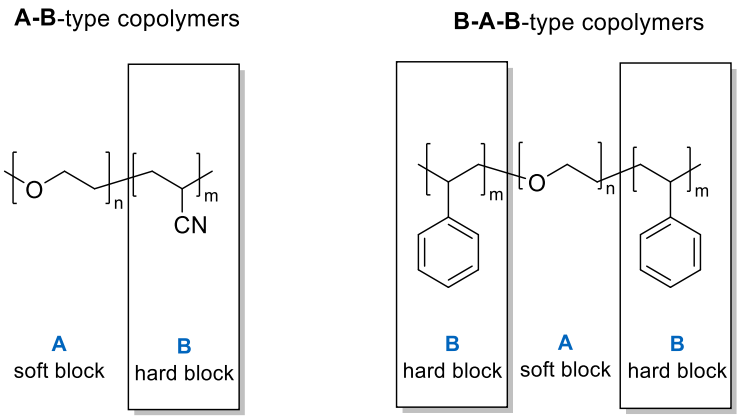

Figure 27: PEO-copolymer types with A = soft, ion-conducting fragment and B = hard, mechanically stable fragment; left: **A-B**-type copolymer with A = PEO and B = PAN; right: **B-A-B**- type copolymer with A = PEO and B = PS.

Another useful method to suppress the crystallization of PEO is to introduce side chains that disturb the alignment of the PEO main chains by intercalating in their regular setting. If the side chains exhibit polar functionalities, as is the case for ether moieties, they can contribute to the ion solvation and, subsequently, the ion transport.[211] Therefore, oxyethylene units are preferable for this modification. The macromolecules can get comb or bottlebrush shapes depending on the magnitude of side chain functionalization. Either the PEO moieties form the main polymer backbone, or they are grafted on a bigger alliance. An example of the first case is poly (ethylene oxide-*co*-2-(2-methoxyethoxy)ethyl glycidyl ether) (PEO/MEEGE) (see Figure 28). The ether chains in MEEGE are highly mobile and enable a more efficient and faster ion transport. That's why the ionic conductivity with 10^{-4} S cm^{-1} is already much higher than pure PEO.[225]

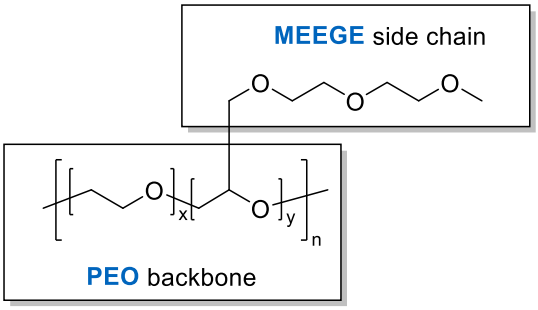

Figure 28: Structure of PEO/MEEGE macromolecule; PEO acts as the main backbone, and MEEGE is covalently bonded as a side chain to support the ion transport.[225]

An example of a bottlebrush-type macromolecule, where PEO is not part of the main backbone but of the side chains, is poly 2-((propionyloxy)-methyl) lithium acrylate graft PEG_{950} (PPMALi-*g*-PEG_{950}) cast on a PVDF-HDF mold. Through a combination of atom transfer radical polymerization (ATRP) and reversible addition−fragmentation chain transfer (RAFT) polymerization techniques, precise and well-

controlled structures of various molecular brushes can be synthesized. The densely grafted PEO chains are located at the end of the brushes, and their superior position enables high chain mobility. The rigidity in the aliphatic backbone provides stable thermal and mechanical performance for a battery with high capacity and robust cycle performance.[226]

Plasticizers can be all sorts of molecules or compounds that have the ability to intercalate into the polymer chain network to soften the whole matrix. Low molecular weight poly (ethylene glycol) (PEG) can, for example, effectively plasticize blends made out of starch, poly (lactic acid) (PLA), and PEG.[227] In the context of solid electrolytes, it was reported that the ionic conductivities of a PEO-$LiCF_3SO_3$ complex increase with decreasing molecular weight of PEO.[228] Another simple approach to produce a plasticizing effect is the addition of salts like $LiCF_3SO_3$ or LiTFSI. The intrinsic change in thermal properties of the polymer-salt complexes influences the ionic conductivities, forcing them to increase.[229] This effect can be reinforced, when additionally the salt dissociation is optimized. This is where the gel polymer electrolytes come into play. By adding a certain amount of liquid, such as EC, PC, dimethyl sulfoxide (DMSO), DMC, or DEC, a macromolecule that is trapped between liquid and solid state is invented.[230-231] The concept of gel polymer electrolytes was first introduced to the market in 1975 by *Feuillade* by mixing a solution of aprotic solvent and an alkali metal salt into a polymer matrix.[232] The transport of the ions in such a gel polymer electrolyte is no longer dominated by the polymer segmental motion. It takes place in the swollen gelled or liquid phase (see Figure 29).[232]

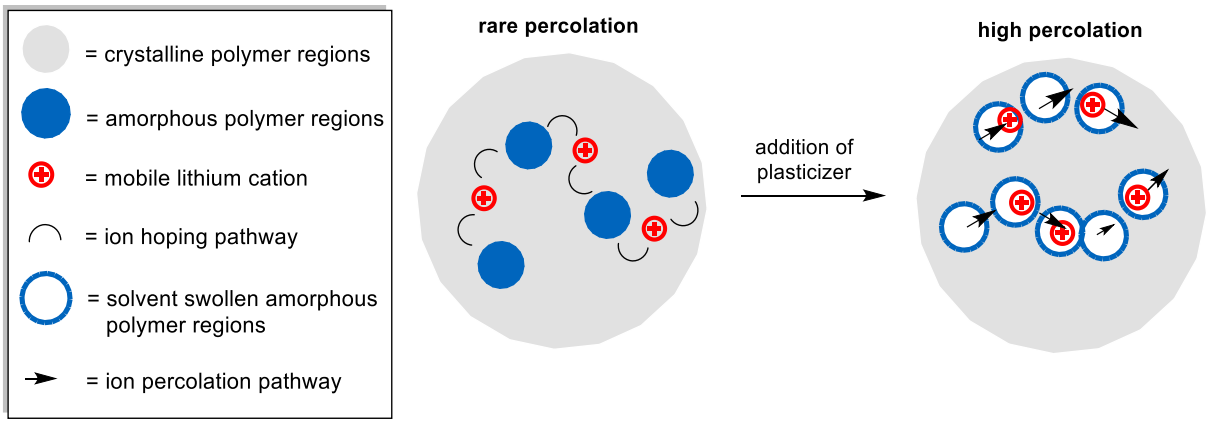

Figure 29: Changing ion transport from a dry solid polymer electrolyte to a swollen gelled one; the swelling with liquids leads to a growing amount of amorphous polymer regions, building up augmented percolation pathways for the lithium cation.[233]

The requirement for gel polymer electrolytes is to keep mechanical strength, even though a certain amount of liquid is added. Furthermore, they should be able to hold the liquid electrolyte and not release it during cycling to prevent electrochemical instability against the electrodes. High ionic conductivities are supported by the more free movement of the lithium cations flowing through the gel

polymer electrolyte.[232] Not only PEO can be used as host matrix, also other polymeric frameworks are reported as common gel polymer electrolytes. PVC, PAN, PMMA, PVDF, the copolymer PVDF-HFP, and polysiloxanes have been widely studied and applied as skeleton materials.[206, 232] As an alternative to organic liquids, ionic liquids can be applied. They are room-temperature molten salts that are assembled of a bulky organic cation and a large delocalized inorganic anion. Common cations can be based on pyridinium, imidazolium, piperidinium, or quaternary ammonium. The anion choice matches the anion of the applied lithium salt in most cases due to better solubility issues. Therefore, $[BF_4]^-$, $[PF_6]^-$, $[N(CF_3SO_2)_2]^-$, $[CF_3SO_3]^-$, $[C_4F_9SO_3]^-$, $[N(CN)_2]^-$, or $[CF_3CO_2]^-$ are often suitable choices.[232] Compared to liquid electrolytes, ionic liquids have much higher electrochemical stability against the lithium metal anode, thus facilitating the application in ASSBS.[234] Ionic conductivities of polymer electrolytes that are swollen with ionic liquids can be found in the range between 10^{-4} to 10^{-3} S cm^{-1}.[232]

Coming back to the classification of solid polymer electrolytes into three main categories (see Figure 24), composite polymer electrolytes have not yet been discussed. A composite is a mixture of a polymer framework with some filler. Usually, ceramics are applied as they exhibit robust mechanical properties and can, therefore, be the counterpart to the softness of the polymeric framework.[235] Especially at elevated temperatures, when the polymer matrix gets softened, a secondary mechanical stability provider can be the key to healthy and long-lasting battery cycling. By adding the fillers to the polymer, the question remains: how does this additional component affect the cation transport mechanism? To clarify this open question, fillers must be classified into active and passive fillers (see Figure 30).

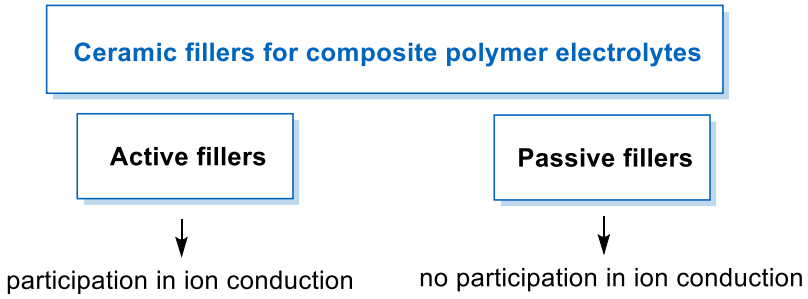

Figure 30: Schematic overview of the two types of ceramic fillers in composite polymer electrolytes; the active fillers participate in ion conduction; the passive fillers do not participate.

Examples of inert fillers are Al_2O_3, SiO_2, TiO_2, or MgO, while passive fillers consist of materials like Li_2N, $LiAl_2O_3$, LLTO, or LATP.[236-237] Independent of the filler choice, composite polymer electrolytes, in general, provide increased ionic conductivities, valuable electronic insulation, and stability in mechanical, chemical, and thermal belongings.[238] The increase in conductivity can be traced back to the inhibition

of polymer crystallization, favoring the amorphous phases in the polymer state. Passive fillers do not actively contribute to the amelioration. That means they do not build migration pathways for the ions or act as a source of charge carriers. In contrast, active fillers offer their particle surface or interfacial regions for ionic transport. Thus, an additional hopping mechanism for the lithium cations is invented. They can now move via the segmental motion of the polymer chains and hop along the surface of the active fillers.[239] The amount of added fillers has to be gently balanced, as fillers tend to aggregate to form huge particle aggregations.[240] These can hinder the ion percolation pathways (see Figure 31).[241]

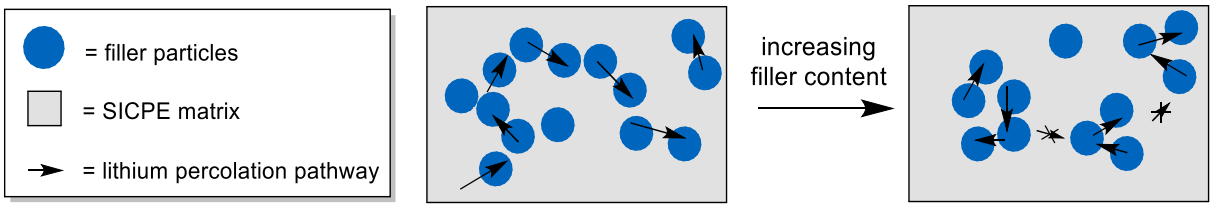

Figure 31: Schematic representation of the filler influence on the ion transport inside of a composite electrolyte; left: ion percolation pathway formation at small filler contents; right: destroyed ion percolation pathways after the agglomeration of filler particles at high filler contents.

Adding, for example, 1% of LGPS-nanoparticles to a PEO-based solid electrolyte, the ionic conductivity increases from 10^{-6} to 10^{-5} S cm^{-1}. Increasing the amount of LGPS to 5 or 10% leads to decreased conductivity. To counter this trend, the surface of the nanoparticles can be modified with molecular brushes to enhance the present surface and increase the ionic conductivity to a value up to 10^{-4} S cm^{-1}.[242]

2.2.4 Summary and future perspective of solid electrolytes

Having an overview of the three main classes of solid electrolytes – the sulfidic-, the oxidic-, and the polymer electrolytes, it can be summarized that every material has advantages and disadvantages. Oxidic electrolytes can be categorized as robust materials with high mechanical stability and stable electrochemical stability performance. Unfortunately, due to their brittleness, they can hardly be used as a pure solid electrolyte. Their usage is more often dedicated to protective coatings. Rating ionic conductivities, sulfidic electrolytes are the candidates of choice, as they possess the highest conductivities of all three representatives. Importantly, the conductivity can compete with liquid LIBs, which should drive commercialization in the current market. Their downsides are the high instability against humidity and lithium metal and the consequently high costs when considering scalable manufacturing technologies. As the H_2S production needs to be strictly controlled, every processing step must be under an inert atmosphere. This requires a complete restructuring of the already established LIB manufacturing lines. The challenge of polymer electrolytes is their low ionic conductivities, which can almost exclusively be increased by raising the operating temperature of the cells. The consequent loss of mechanical stability can be critical but can also be avoided with a good concept of adding stabilizing fillers. In addition, the polymer softness can easily balance volume changes during cycling, and their lightweight and low production costs define them as promising candidates. In the long run, ASSBs will need flexible components that are able to tackle the challenge of high solid-solid interface resistances. The following chapter will highlight a strategy and how researchers are currently trying to improve the polymer electrolyte properties to make them even more suitable for application in ASSBs.

2.3 Single ion-conducting polymer electrolytes

The polymer electrolytes discussed in Chapter 2.2.3 generally all have one major characteristic: they are all dual ion-conducting systems. That means a lithium salt, consisting of lithium cations and counter anions, is dissolved in a polymer matrix. The polar groups of the polymer support the salt dissociation and manage to coordinate the cations. Consequently, the anions can freely move inside the electrolyte and preferably migrate to the anode. The accumulation of an anionic layer on the negative electrode initializes concentration gradients. The resulting polarization leads to worsened ionic conductivity and increased cell performance.[243] In addition, the anionic movement is 5-10 times faster than the cationic one due to the strong coupling of the lithium cations to the Lewis basic sites on the polymer chain.[208, 244] Thus, it can be assumed that the anions contribute more to the overall conductivity than the cations. This fact is reflected in the lithium transference number (t_{Li^+}), a prominent tool for measuring how many lithium cations are actively participating in the ion conduction. Dual ion conductors usually exhibit t_{Li^+} lower than 0.5. Single ion-conducting polymer electrolytes (SICPEs) are invented to prevent polarization effects. They theoretically exhibit a t_{Li^+} of 1 and improve the battery cycling performance by preventing polarization gradients. The general aims of this new technology can be seen in Figure 32.[244]

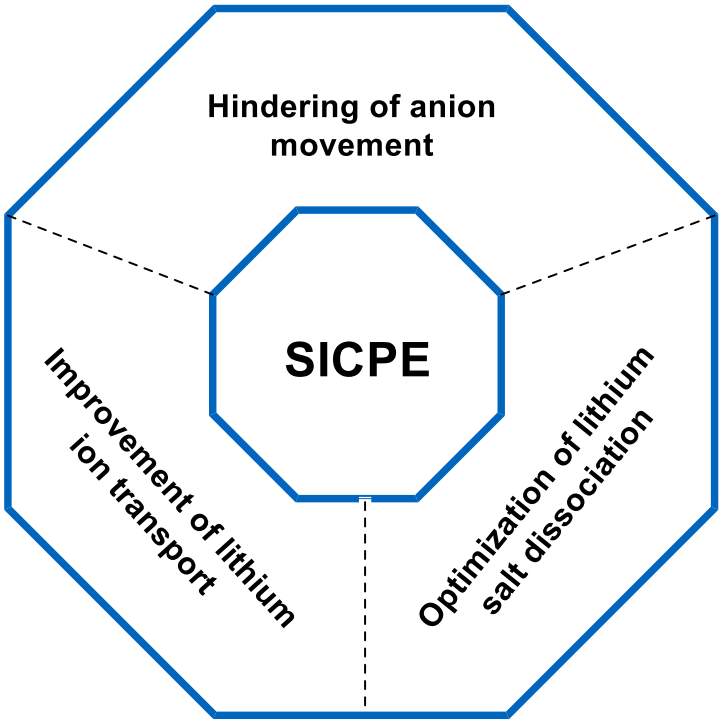

Figure 32: Schematic representation of the main goals, that SICPEs are aiming for: hindering of anion movement through the polymer electrolyte, improvement of lithium ion transport, and optimization of lithium salt dissociation.

The anions must be immobilized to hinder and restrict the anionic movement. Three methods can be applied to create a SICPE:[244]

1) Immobilization of the anionic structure motif on the respective polymer backbone via covalent bonding
2) Introducing an anion receptor concept
3) Increasing the ion pair dissociation in the respective lithium salts by a higher degree of anionic charge delocalization

For the immobilization of the anion on the respective polymer backbone, mostly carboxylates (-CO_2-), sulfonates (-SO_3-), sulfonyl imides (-SO_2NSO_2-), and borates (-B-) are studied in their function as poly-anionic matrices.[245-247] Figure 33 depicts some common SICPE architectures in their homopolymer form. They all contain aliphatic backbones, meaning only C-C bonds without incorporating other heteroatoms.

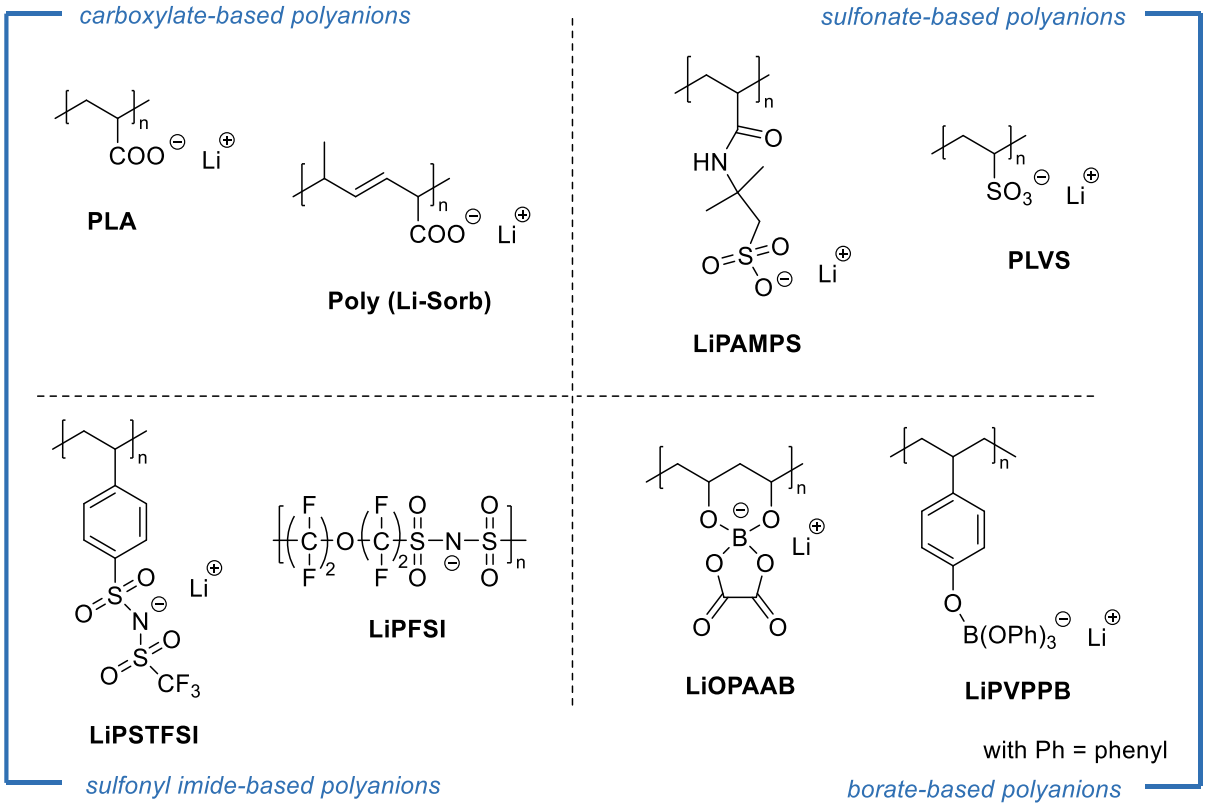

Figure 33: Overview of commonly used polyanions for ASSBs categorized into four groups: carboxylate (PLA, Poly (Li-Sorb))-, sulfonate (LiPAMPS, PLVS)-, sulfonyl imide (LiPSTFSI, LiPFSI)-, and borate (LiOPAAB, LiPVPPB)-based.

Starting with the carboxylate- and sulfonate-based polyanions, *Ito et al.* synthesized poly (lithium acrylate) (PLA) and poly (lithium vinylsulfonate) (PLVS) as SICPE proposals. Under 50 °C, the SICPEs show

nearly no conversion due to an extended crystallization behavior. In a range between 60 to 130 °C, the highest ionic conductivities reached values of 10^{-6} S cm^{-1}. The addition of $BF_3{\cdot}OEt_2$ (with Et = ethyl) was able to support lithium migration, but elevated temperatures were still necessary to achieve high ionic conductivities and $t_{Li}{}^+$.[248] The electrochemical performance of poly (lithium sorbate) (poly(Li-Sorb)) likewise shows that carboxylate-based SICPEs can barely reach lithium ion conductivities that are competitive with dual-ion conducting polymer electrolytes without the help of an additive.[249] The reason can be traced back to the strong coordination of the lithium cation to the anion.[244] If the dissociation of the lithium salt is not strong enough, the lithium cations are hindered in their mobility. Hence, lower ionic conductivities and $t_{Li}{}^+$ are observed as a consequence. Similar behavior is seen for sulfonate-based polyanions like poly (2-acrylamido-2-methylpropanesulfonic acid) (LiPAMPS). Even though the SICPE shows high thermal stability up to approximately 300 °C and a robust dimensional and electrochemical stability up to 4.4 V (vs Li/Li^+), ionic conductivities of 10^{-5} S cm^{-1} can primally be reached if organic liquids like EC or DMC are added.[250]

Therefore, research focused on a better dissociation behavior between anion and cation by strengthening the delocalization of the anionic charge over a broader structure range. *Meziane et al.* interconnected a sulfonyl imide anionic group to a PS-main chain, resulting in the synthesis of lithium poly (4-styrenesulfonyl(trifluoromethylsulfonyl)imide) (LiPSTFSI). This approach reported a rise in $t_{Li}{}^+$ close to unity and ionic conductivity of about 10^{-5} S cm^{-1} (above the melting temperature of pure PEO).[251] The polymerized version of an anion similar to the TFSI-motif is observed in the SICPE lithium poly (perfluoroalkyl sulfonyl)imide (LiPFSI). Blended with different ratios of PEO, the polyimide anion exhibits ionic conductivities of 10^{-4} S cm^{-1} (at 80 °C), high $t_{Li}{}^+$, and excellent electrochemical stability.[252]

The last material class of SICPEs based on an aliphatic backbone are polyanions, that depict borates as immobilized anions. Figure 33 shows two examples, lithium oxalate polyacrylic acid borate (LiOPAAB) and lithium poly (4-vinylphenol) phenolate borate (LiPVPPB). While LiOPAAB only exhibits an ionic conductivity of 10^{-6} S cm^{-1} (at room temperature after absorbing liquid PC)[253], LiPVPBB demonstrates a nice concept of how charge delocalization can positively influence the electrolyte performance. Due to the phenol rings promoting charge delocalization via π-conjugation, the ionic conductivity can be pushed up to the region of 10^{-4} S cm^{-1} at room temperature.[247]

The comparison of the different polyanion frameworks shows that one bottleneck of SICPEs is their low ionic conductivity. Via copolymerization, this issue was tried to be neglected, as the mixing of two different polymers can be an efficient tool to combine multiple polymer properties. As was already

reported in the previous chapter, the sequence of structure motifs can be varied in the copolymer. Figure 34 depicts an A-B- and a B-A-B-type copolymer that are well-established SICPEs.

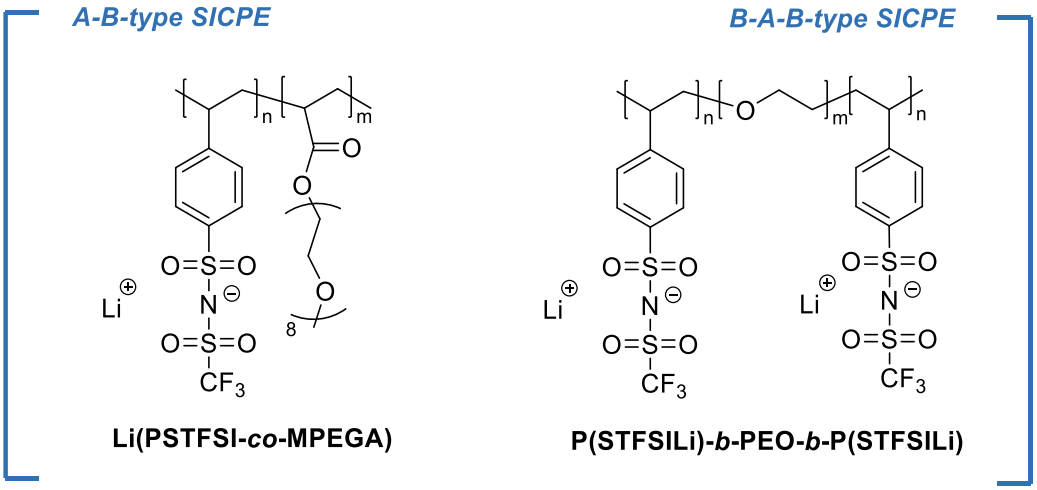

Figure 34: SICPE copolymers based on different copolymer frameworks; left: A-B-type Li(PSTFSI-*co*-MPEGA); right: B-A-B-type P(STFSILi)-*b*-PEO-*b*-P(STFSILi).

Zhou et al. were able to synthesize the A-B-type SICPE Li(PSTFSI-*co*-MPEGA) by combining the well-established LiPSTFSI SICPE with a methoxypolyethylene glycol acrylate (MPEGA). The idea was to introduce PEG-side chains into the second monomer to expand the lithium anchoring point density and the softness of the material. Despite the nice concept, the ionic conductivities at room temperature were kept at 10^{-6} S cm^{-1} and could not be further increased.[254] *Bouchet et al.* used the sandwich principle for constructing a B-A-B-type P(STFSILi)-*b*-PEO-*b*-P(STFSILi) SICPE. The LiPSTFSI units are the hard B-units, while the PEO A-segments act as polymer plasticizers. The resulting properties were observed as t_{Li^+} close to unity, an ionic conductivity of 10^{-5} S cm^{-1} (at 60 °C), excellent mechanical properties, and high electrochemical stability up to 5 V.[218] These results promise a huge innovation potential concerning new SICPE copolymer designs.

The immobilization of anions on the polymer backbone is the major concept behind SICPEs due to their advantages in improving the overall battery performance. Nevertheless, the lack of high ionic conductivities at room temperature still remains a challenge in the current situation. Instead of classical SICPE frameworks, there is also the possibility of introducing anion receptors into the polymer electrolyte. They trap the anions, promote ion dissociation, and thus increase the independence of the lithium-ion mobility. The results can be a rise in conductivity and t_{Li^+}.[232] Since in these systems, only the lithium cation can be seen as the actively moving species, they can be classified as SICPE. Without going into further details, Figure 35 reveals how such a potential anion receptor might look like.[255]

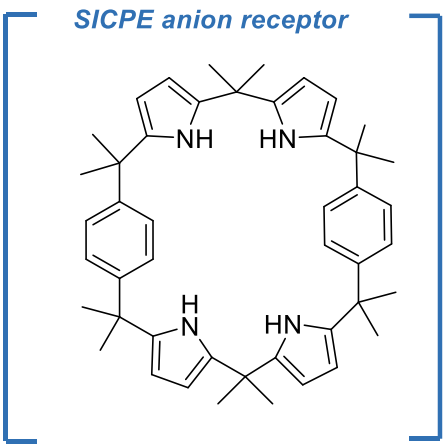

Figure 35: Structure of a potential anion receptor as an alternative to polyanion-based SICPEs.

3. Aim of this thesis

The wide and expressive presence and representation of polymers in a huge variety of battery setups clearly show that they are inevitable components for safe and smooth cycling. Especially when ASSBs come into play. With our current demographic evolution and our demanding technological visions, we are forced to work on the development of efficient and long-lasting energy storage solution systems. In this context, ASSBs can fulfill most of the general expectations. On the one side, they exhibit a very high intrinsic safety. If the battery gets damaged, no liquid and flammable electrolytes will leak out, as only solid components take place in the internal current provision. The risk that a battery cell package in an EV can spontaneously catch fire is, therefore, drastically reduced. Conversely, the simple setup of three main components - an anode, a cathode, and a solid electrolyte - reunites several advantages that tackle the question of energy density and production cost. Incorporating a pure lithium metal anode pushes the battery performance and directs its application to prospective high energy and power densities. High-capacity cathode designs enable the creation of the perfect opponent for the negative electrode. Changing the liquid against a solid electrolyte, much space can be saved concerning cell design. A thin processing of the solid electrolyte supports the fact that there is more energy available in less space. In addition, one component less than for LIBs is needed, conversely implying a decrease in production cost.[40]

Nevertheless, by switching from a solid-liquid to a solid-solid interface, new challenges are unlocked. At the anode side, bad contact with the solid electrolyte provokes the uneven deposition of lithium on its surface. With continuous cycling, more and more lithium will be deposited till the formed dendrites are big enough to spark an internal short circuit. At the cathode side, serious physical contact problems can arise due to the hard texture of the active material and the solid electrolyte (when sulfidic or oxidic solid electrolytes are applied). Contact loss always produces electrochemical instability at the interfaces. In many cases, this results in the increase of impedance and the worsening of battery performance.[256]

That’s why ASSBs depend on soft and flexible materials such as polymers, which can act like glue between the solid components. Not only in cathode composite, they are ubiquitous as well-established binder components. Also, in their function as solid electrolytes, they can unfold their potential. The interplay of two solid electrodes that are separated by a soft solid polymer electrolyte intensifies the interfacial connection. The volume changes of the electrodes, occurring during lithium plating and stripping, can easily be compensated.[211]

Nowadays, a huge variety of polymer matrices exist that show good flexibility, robust electrochemical stability, and tolerant compatibility with common ASSB components. At this juncture, especially PEO can be seen as the most-studied and -examined polymer electrolyte. Its low T_g and excellent ability to dissolve all kinds of lithium salts make it suitable for ASSB battery application. Unfortunately, it has to deal with the same challenge that a lot of solid polymer electrolytes have to face: low ionic conductivities at room temperature. Due to its semi-crystalline nature, the dissociated lithium ions mostly increase their mobility when the temperature exceeds the T_m of PEO.[214] As raised temperatures bear disadvantages for the mechanical stability of the electrolyte, researchers invented the concept of SICPEs. In contrast to dual ion-conducting polymer electrolytes, immobilizing the anionic charge on the polymer backbone neglects the anion movement through the electrolyte (see Figure 36).

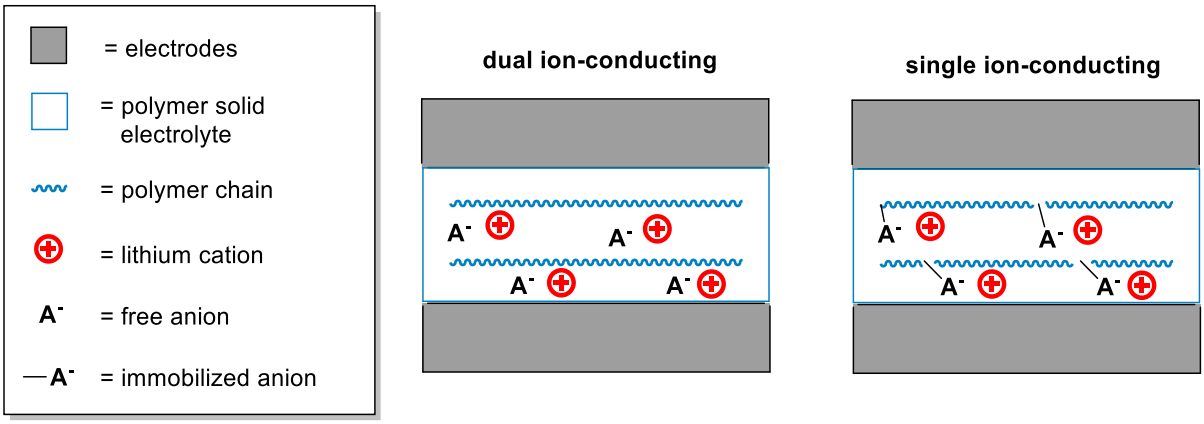

Figure 36: Schematic comparison of dual ion-conducting and single ion-conducting polymer electrolytes (SICPEs); left: anions and cations can move through the polymer electrolyte; right: anions are immobilized on a polymer matrix, only the lithium cations migrate through the electrolyte.

Less polarization effects and dendrite growth occur, and the t_{Li^+}s increase, showing that the concept is able to lead to a more effective battery status. Nevertheless, the ionic conductivities of SICPE nowadays can hardly compete with the conductivities of liquid batteries of about 10^{-2} S cm^{-1}.[40] A reason for this can be found in the lithium-ion transport mechanism inside solid polymer electrolytes. Lithium cations move along the amorphous polymer domains. The presence of crystalline domains hinders their movement. Therefore, sufficient lithium ion mobility is usually primally to be observed, when the temperature of operation is above the T_g of the polymer. Then, the segmental motion of the polymer chains is enhanced, and the cations have to face fewer barriers.[214]

Considering literature-known SICPEs, the thermal transitions of homopolymerized polyanions are, in some cases, strikingly high. Taking the sulfonyl imide SICPE published by *Meziane et al.* as an example, its melting temperature is close to that of pure PEO (around 60 °C).[251] By knowing that a more amorphous character can have a huge impact on ion mobility, literature approaches generally try to lower

the crystalline fractions in the polymer and the Tgs by adding plasticizers, creating composites, or co-polymerizing polyanions with soft PEG segments.

In this work, a solid polymer electrolyte is designed that is able to combine two leading polymer trends in one repetition unit:

1) A SICPE structure motif that shows one charge carrier per repetition unit;
2) A soft and flexible polymer backbone that can outperform regularly used aliphatic backbones.

The flexible backbone should soften the SICPE and lower its T_g, so that the battery cell could be cycled at moderate temperatures. Figure 37 demonstrates what the target SICPE and the respective monomer structure should look like.

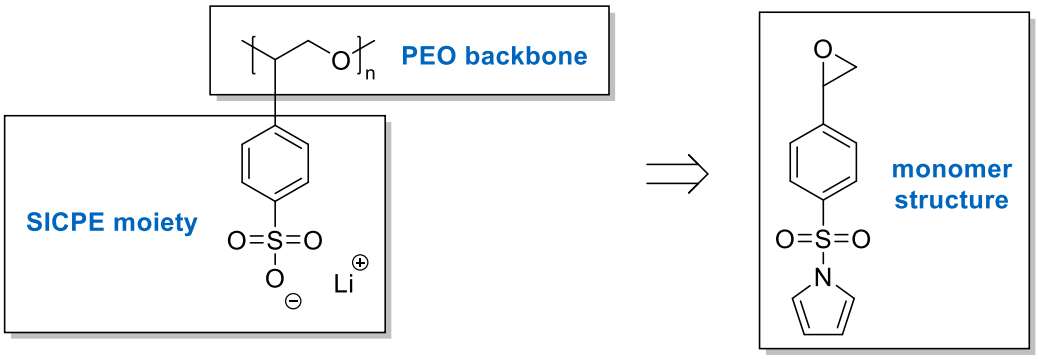

Figure 37: Structure of the target SICPE, combining a sulfonate-based SICPE and a flexible PEO-backbone, and its respective monomer structure, proposed via retrosynthesis.

To realize the SICPE setting, the research has to begin with the smallest unit of the polymer, namely the monomer moiety. In the first part of this thesis, a kind of retrosynthetic approach towards the herein-designed monomer 1-((4-(oxiran-2-yl)phenyl)sulfonyl)-1*H*-pyrrole (**1**) is depicted. The synthesis includes three steps, where every step is questioned after the right parameter choice (e.g., temperature, reaction time, reagent choice, and equivalents) and the based reaction mechanism. Both the challenges that occurred during the process, as well as the applied solutions, will be discussed in detail. Furthermore, thoughts are discussed, that relate to the ability to polymerize this monomeric structure or alternative structural frameworks.

The second part of this thesis will focus on the ring-opening-polymerization (ROP) of the terminal epoxide group that is generated as part of the monomer structure. Different catalyst designs with varying metal centers and ligand surroundings will be examined. In a broad screening, the perfect fit between monomer and catalyst is explored. Via gel permeation chromatography (GPC), molecular weight development can be monitored along the process of adjusting polymerization conditions.

Due to the specific monomer design, a post-polymerization modification is necessary to yield the structure of the target SICPE. In this context, different working techniques and reagents to achieve post-polymerization functionalization are discussed. The focus is thereby set on a mild treatment of the polymer and polymer preservation. This thesis should highlight the difficulties of the polymer analogous reaction and clear the points that have to be considered when working with high polarity changes. In addition, it is investigated, if also alternative synthetical pathways could lead to the target SICPE. Therefore, different approaches concerning the post-polymerization functionalization of poly (styrene oxide) (PSO) are analyzed and evaluated, related to their practicability and conditions of polymer treatment. Figure 38 gives a schematically overview of the pathways, that are aiming to realize the target SICPE.

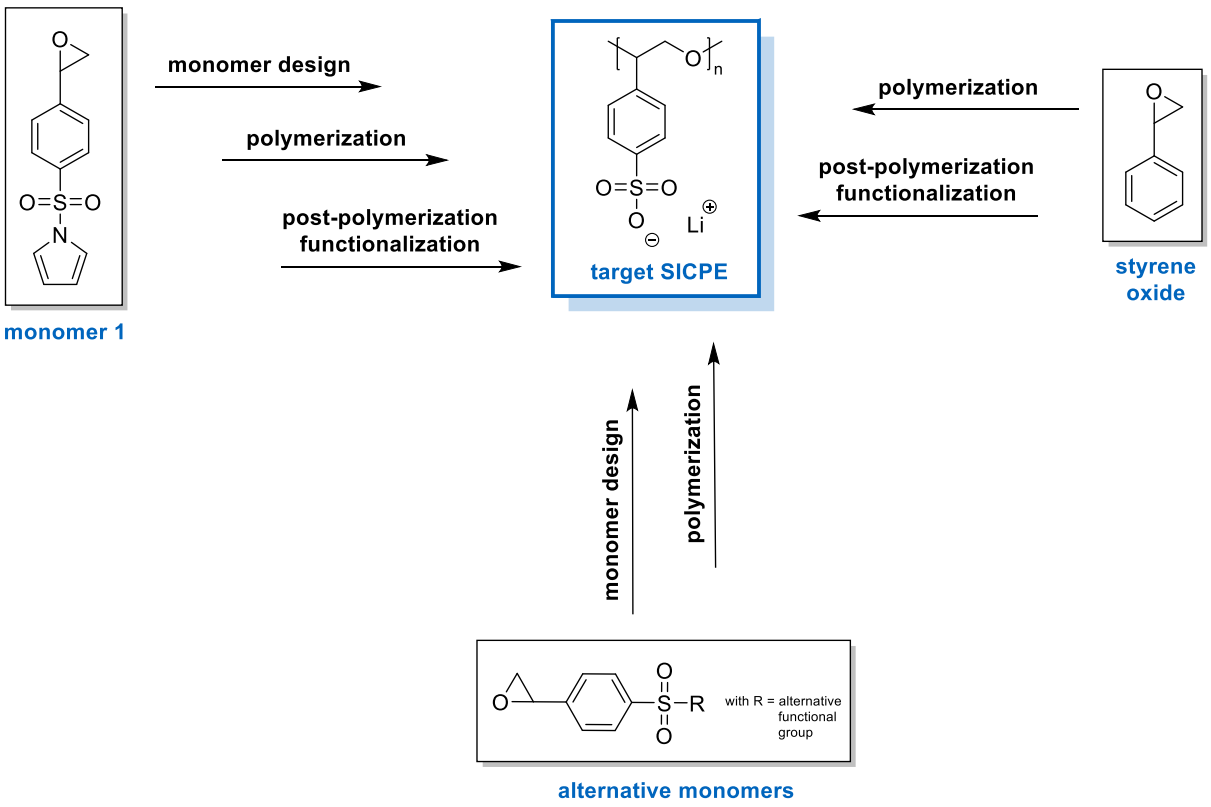

Figure 38: Overview of the working packages that are in the scope of this work to achieve the target SICPE; three different approaches are presented, starting from varying initial points (the herein-designed monomer **1**, alternative monomers, or styrene oxide (SO)).

Besides investigating the homopolymer of the target SICPE, copolymerization is also outlined in this thesis. After screening for suitable comonomers, two comonomers – SO and poly(ethylene glycol) diglycidyl ether (PEG 2000) – are selected, and the respective copolymers are tested regarding their structural and thermal properties. Similar to literature attempts, copolymerization, in this case, aims to fuse a multitude of properties in one solid copolymer electrolyte.

To conclude this thesis and to establish the connection back to solid-state batteries, the herein synthesized homo- and copolymers are prepared for electrochemical characterization. The process of polymer film-making and first electrochemical impedance spectroscopy (EIS) measurements are recorded.

5. Results and discussion

This results and discussion part is split into four main subchapters. The first part will talk about the development of the monomer synthesis pathway and its related parameter variations. The herein-designed monomer will be abbreviated in the following with **1.** In the second part, the focus is set on homopolymerizations. It includes the screening of suitable catalysts that support the anionic ROP of **1**. Furthermore, post-polymerization functionalizations are shown and related to two different types of homopolymers (the first homopolymer is based on polymerization of **1**, the second one on PSO). Additionally, modified monomer structures that could enable alternative polymerization routes are proposed and critically questioned. The chapter closes with comparing the thermal properties of all homopolymers that are synthesized as part of this thesis. The results, which are shown in the first two chapters, take part in already published work.[257] The third chapter demonstrates the copolymerization of **1** with SO and PEG 2000 (M_n = 2000 g mol^{-1}), respectively. Again, at the end of the chapter, the thermal characteristics of all copolymers are related to each other. The main part is closed by displaying the polymer film-making process and evaluating the primal electrochemical results.

5.1 Establishment of monomer 1

Looking at the structure of **1** (see Figure 38), it can be seen that the main core consists of an aromatic ring that is substituted in two positions. The first substituent is a terminal epoxide, located in *para* position to the second substituent, a sulfonyl group in the form of a sulfonamide. Thinking about the later application as a solid electrolyte, this setup combines three advantages:

1) The terminal epoxide can be polymerized to get a flexible polyether backbone. With this feature, low T_gs are pursued.
2) The sulfonamide can be modified to give a free sulfonate group that can act as an immobilized anchoring point for the lithium cations, giving the resulting homopolymer the right to be classified as SICPE.
3) The incorporation of an aromatic ring guarantees a certain amount of rigidity inside the structure, which can have a positive influence on the mechanical stability of the resulting solid electrolyte. Similar styrene structure motifs can already be found as established and stable polymer electrolytes in solid-state batteries.[251]

Concerning the second point of the listing, it could be questioned why the sulfonamide is introduced into the monomer structure instead of a free lithium sulfonate. It makes further post-polymerization

functionalization inevitable (detailed discussion see Chapter 5.2.3). The underlying protection group strategy is designed in relation to the following polymerization purposes and will be discussed in detail in the next chapter.

The synthesis of **1** consists of three steps (see scheme 1) that can be divided into a chlorosulfonation reaction, a protection and elimination step, and a classical epoxidation of a vinylic double bond.

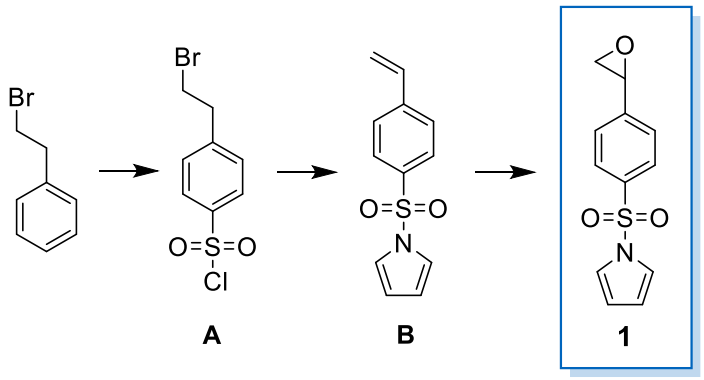

Scheme 1: Sketch of the three-step synthesis to achieve **1**; the three steps exhibit chlorosulfonation, protection and elimination, and epoxidation.

Starting with 2-bromoethylbenzene, adding a chlorosulfonyl in the *para* position is known as classical chlorosulfonation.[258] Chlorosulfonic acid is added in excess at cold temperatures, and the reaction is kept at room temperature for several hours before it is quenched. The mechanism involves an electrophilic aromatic substitution reaction, undergoing a *Wheland*-intermediate formation and the reconstitution of the ring aromaticity. After this step, a *para*-substituted sulfonyl-intermediate is generated. Due to the excess of chlorosulfonic acid, the sulfonyl can finally be converted into a chlorosulfonyl by splitting of sulfuric acid (see scheme 2). Besides the secondary substitution in *para*-position, the positive inductive (+I) effect of the alkyl substituent conducts the chlorosulfonyl also in *ortho*-position to the primary substituent. The localization of the chlorosulfonyl group in *ortho*-position would disturb during the advancing synthesis progress, as it could induce sterically repulsion in the subsequent epoxidation reaction. Therefore, it is removed via column chromatography to yield 4-(2-bromoethyl)-benzene sulfonylchloride (**A**) (^{1}H- and ^{13}C-NMR of **A** see appendix). As the steric conducts the secondary substituent with a major percentage into *para*-position, high yields of 76% are the outcome.

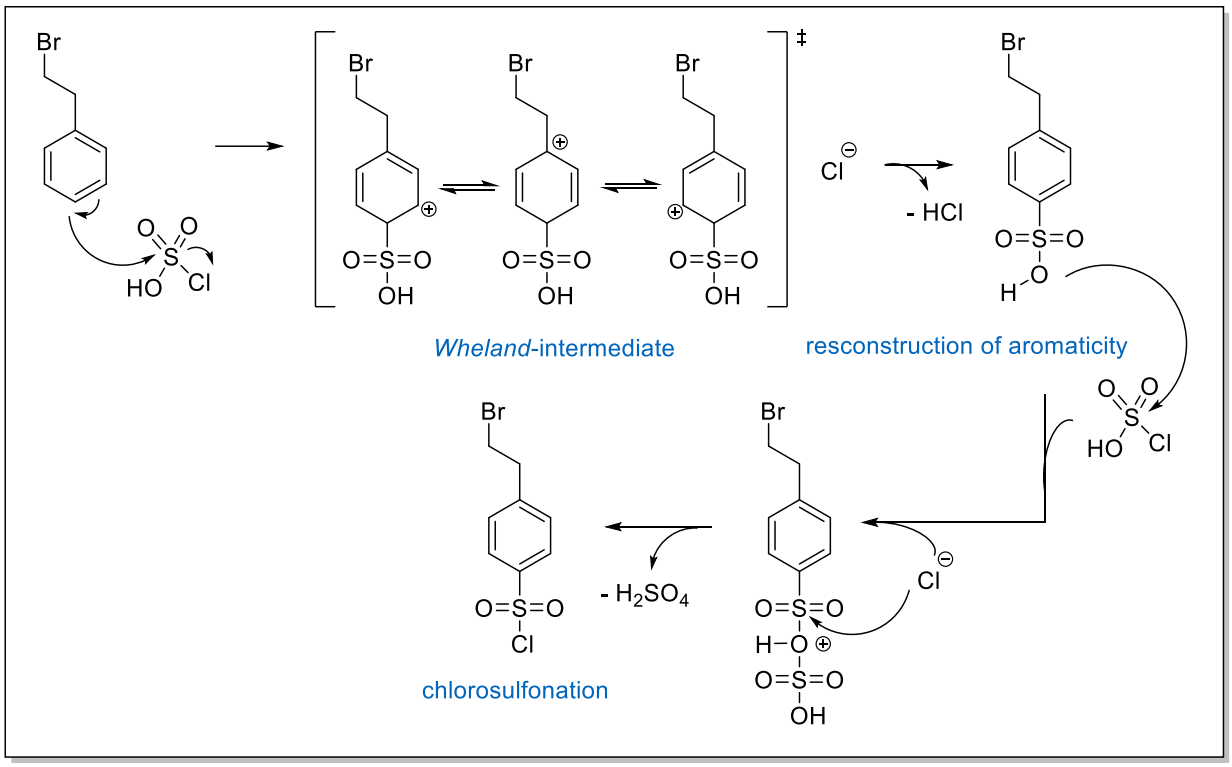

Scheme 2: Reaction mechanism for the chlorosulfonation of 2-bromoethylbenzene, yielding *para*-sulfonyl substituted **A**.

During the second step of the overall synthesis, the above-mentioned protection group strategy of the sulfonyl group is introduced. Via S_N2 reaction, deprotonated and, as a nucleophile-activated pyrrole, induces the cleavage of the halide from the chlorosulfonyl group. A sulfonamide is formed.[259] Due to the excess of deprotonated pyrrole in the solution, elimination leads to the release of hydrogen bromide and the generation of a vinylic double bond (see scheme 3). The excess of pyrrole is removed by column chromatography. To ensure perfect purity for the following epoxidation step, the raw material was sublimated twice (^{1}H-NMR of **B** see appendix).

The efficiency of the 1-[(4-vinylphenyl) sulfonyl]-pyrrole (**B**) synthesis is not only shown in its high yields of 78% but also in the fact that two reactions,

1) the introduction of an amide protecting group
2) and the generation of a vinylic double bond

take place in one reaction step.

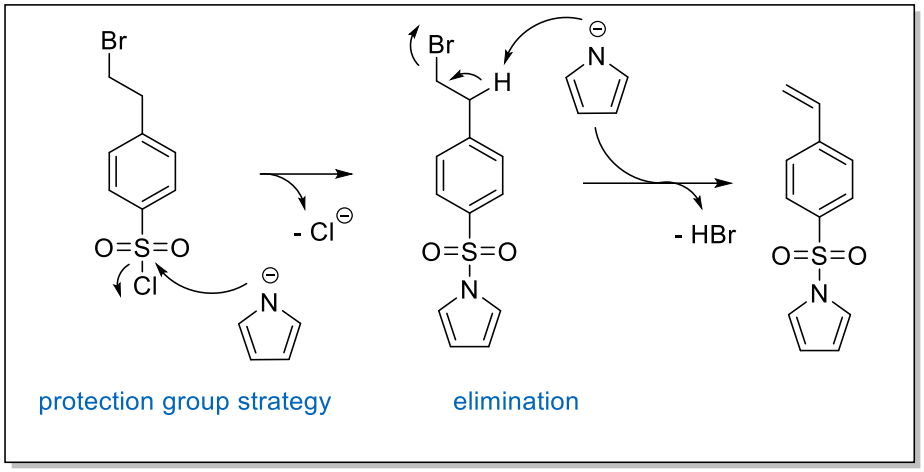

Scheme 3: Reaction mechanism for forming **B**, involving a protection group strategy and the generation of a vinylic double bond via elimination.

The structure after this synthesis resembles styrene, which is functionalized with a sulfonamide group. Literature attempts to replace the sulfonyl group against a TFSI-moiety and subsequently polymerize the terminal double bond via radical polymerization (see LiPFTFSI, Figure 33). The resultant SICPE is based on an aliphatic backbone that exhibits a rather rigid character. Thus, often unfavourable high thermal transition temperatures and impeded ionic conductivities at room temperature result from the lack of polymer chain flexibility.[251]

5.1.1 Epoxidation strategies and related side reactions

To decrease the temperature of thermal transitions, a flexibility input into the resulting polymer is necessary. That is why the vinylic double bond is converted in the last step of the monomer synthesis into a terminal epoxide group. The epoxide is able to be ring-opened to yield a polyether backbone that should exhibit a similar low T_g and enhanced segmental polymer chain mobility like PEO.

The definition of epoxidation indicates the transfer of an oxygen atom in a [2+1] cycloaddition in the presence of a peracid (see scheme 4).[251] Electron-rich double bonds facilitate the transfer. These can be adjusted, for instance, by an electron-donating nature of the alkene substituents.

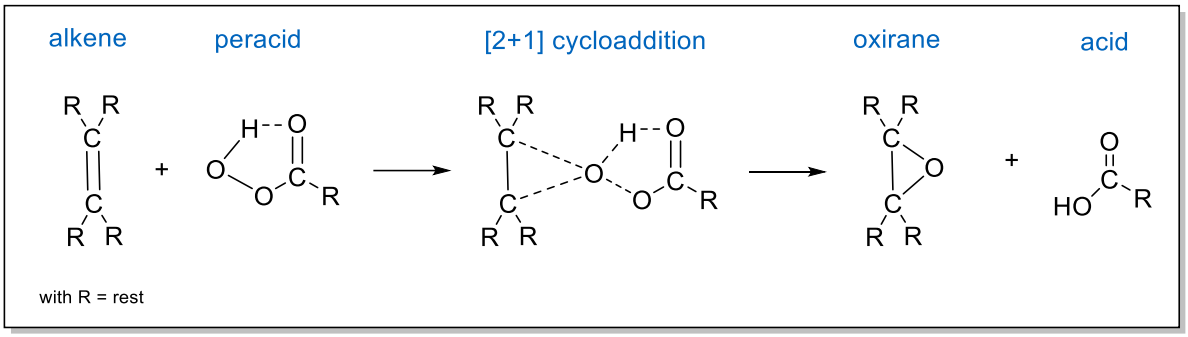

Scheme 4: Schematic reaction mechanism for a [2+1] cycloaddition.

In the case of **B**, both the aromatic ring and the sulfonamide exhibit electron withdrawing effects, as the sulfonyl can delocalize energy density on its oxygen atoms. Hence, a terminal, electron-deficient double bond is created. Initially, conventional and well-established epoxidation reagents are tested for their function as feasible reagents. Table 1 gives an overview of the respective outcomes per tested reagent.

Table 1: Overview of the applied epoxidation reagents and the relative yields of **1**.

reagent	***eq.***	***T [°C]***	***t [d]***	***yield [%]***
m-CPBA (purified)	2.0-5.0	–78 °C to RT	1	–
H_2O_2 (35%)	1.5-2.0	0 °C to RT	1-5	–
NaOCl	1.5-2.0	0 °C to 40 °C	1-5	–
performic acid	0.5-2.0	0 °C to 45 °C	1-3	–

Approaches that use *meta*-chloroperoxybenzoic acid (mCPBA), hydrogen peroxide (H_2O_2), sodium hypochlorite (NaOCl), or performic acid end with no conversion. In the ^{1}H-nuclear magnetic resonance (NMR) spectra, no distinct epoxide signals can be detected. In fact, the presence of plenty of unspecifiable signals (for example, for *m*-CPBA entry, see appendix) leads to the conclusion that the host structure is destroyed during the reaction.

To balance the difficult energetic situation, the search for a more powerful epoxidation reagent directs dimethyldioxirane (DMDO) into the focus of investigation. DMDO is the oxirane of acetone, hence, it can be prepared via oxidation of acetone with potassium peroxymonosulfate $KHSO_5$ in the presence of $NaHCO_3$. The non-metallic, organic oxidant is known for its high tolerability with various functional groups such as sulfides, sulfoxides, amines, or carbon double bonds (see scheme 5).[260]

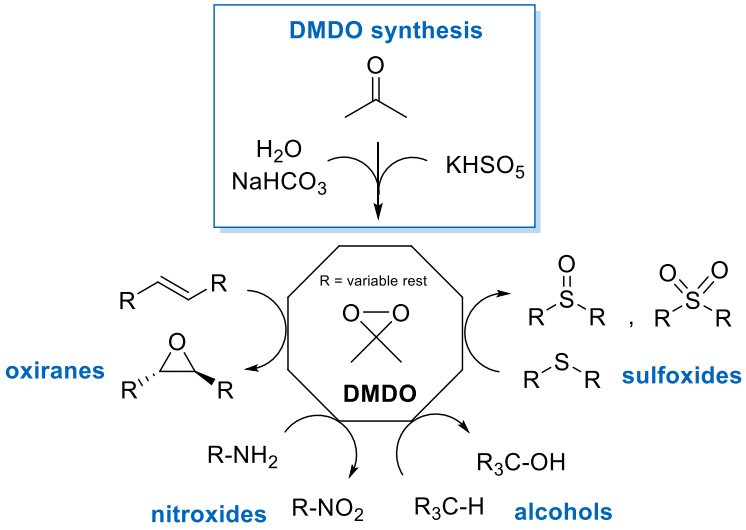

Scheme 5: Transfer of various functional groups in their oxidized form via epoxidation with DMDO.

The preparation and usage of DMDO have to be carefully adjusted. The ring tension inside of the peroxide is high, increasing the molecule's reactivity. Therefore, DMDO solutions are usually kept at cold temperatures, both during the preparation and when applied to a substrate.[261] The scale-up of the epoxidation reagent is difficult. Using standard laboratory equipment, a maximum of 350 mL of DMDO solution can be synthesized with a concentration ≤ 100 mM. As the stability of the solution is only valid for a maximum of one week, the consumption should immediately follow after the preparation.[260] Nevertheless, its usage bears many advantages. As DMDO decomposes to form acetone, the solvent can simply be evaporated and reused. Compared to other peroxides like *m*-CPBA, the respective acids (in this case, benzoic acid) have to be separated from the reaction mixture in an additional purification step. The yields of DMDO epoxidation are generally quantitative and accompanied by high purities.

Mild reaction conditions support a selective epoxidation of acid- as well as base-sensitive substrates without destroying core structures.[260]

To create a reference for the following screening conditions, a standard experiment is set. It contains the application of 1.3 eq. of freshly prepared DMDO solution (concentration was assumed to be 100 mM) in relation to **B** in an acetone/DCM (10/1) mixture. The epoxidation reagent is added at 0 °C and the reaction mixture is slowly warmed up to room temperature over the period of one day. After the evaporation of the solvent, a ^{1}H-NMR spectrum is taken from the crude product to monitor the conversion of the vinylic double bond signals translating into epoxide signals. The ratio of vinyl-sulfonate/epoxide content can be calculated based on the integrals of the respective ^{1}H-proton signals (see Figure 39).

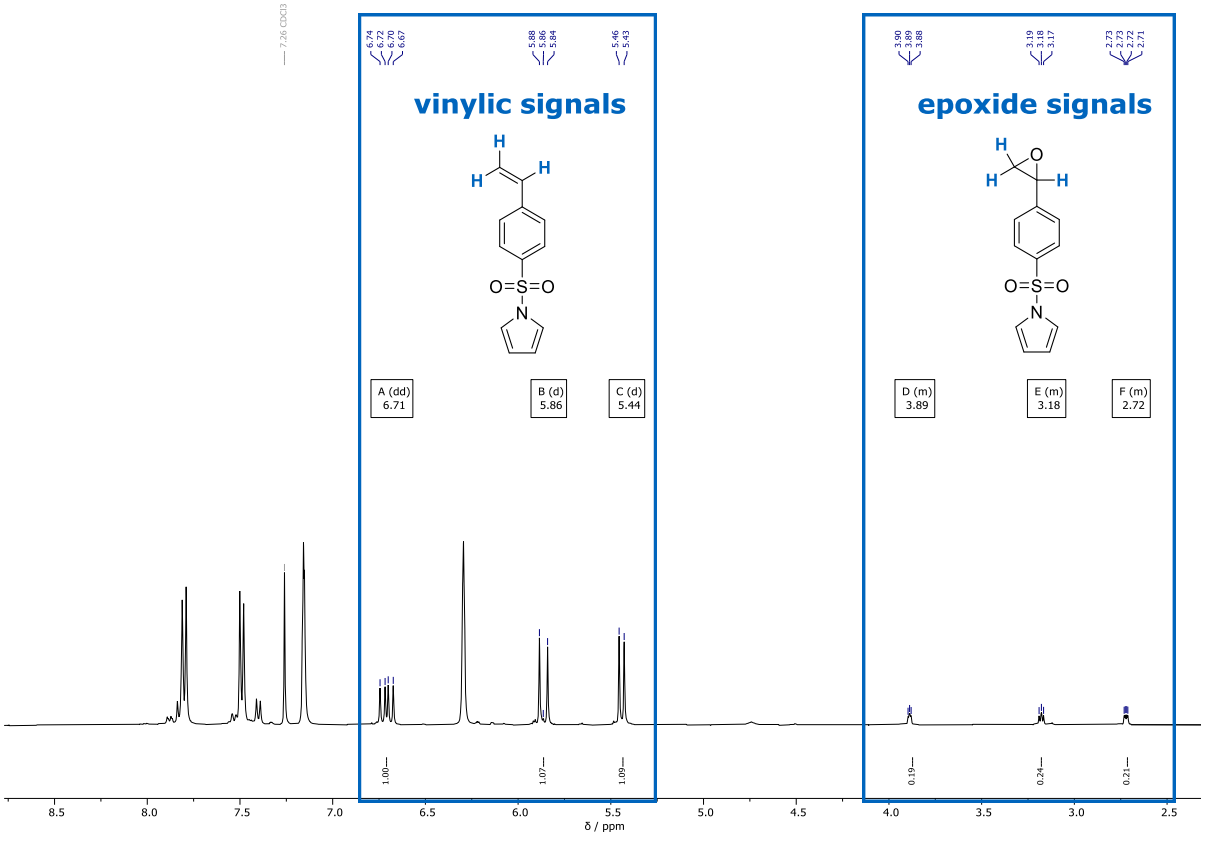

Figure 39: ^{1}H-NMR spectrum of standard DMDO experiment (taken from raw material, not purified); comparison of vinyl-sulfonate ^{1}H-NMR signal against epoxide signal gives ratio of **B** converted to **1**.

The ^{1}H-NMR clearly indicates that 20% of vinylic groups of B are successfully converted into epoxide functionalities by using DMDO as an epoxidation reagent. Aiming to increase this ratio, a set of parameters is screened. Table 2 depicts an overview of the performed variations, where the standard experiment is marked in blue as a reference.

Table 2: Executed parameter variations in the epoxidation of **B** with DMDO and their reaction outcomes; the ratio of **B**/**1** is calculated based on the ^{1}H-NMR signals of the respective non-purified reaction mixtures.

parameter variation	***eq. (DMDO)***	**T [°C]**	***t* [d]**	***solvent***	***ratio B/1***
standard experiment	1.3	0 °C to RT	1	acetone/DCM	80/20
eq.	**3.0 to 5.0**	0 °C to RT	1	acetone/DCM	80/20
reaction time	3.0 to 5.0	0 °C to RT	**5**	acetone/DCM	40/60
solvent	3.0 to 5.0	0 °C to RT	5	**acetone or acetone/MeCN**	80/20
temperature	3.0 to 5.0	**RT to 35 °C**	5	acetone/DCM	80/20
water content	3.0 to 5.0	0 °C to RT	5	**dry DMDO solution**	80/20

With the variation of parameters, several goals were pursued. The increase in DMDO content could offer more active reagents participating in the epoxidation of the vinylic double bond. Increasing the reaction time generally supports the diffusion of the molecules. Changing the solvent to pure acetone or an acetone/acetonitrile (MeCN) mixture should eliminate the probability that DCM can act as a disruptive factor related to the stability of DMDO. The temperature increase up to 35 °C is aiming to influence the reaction kinetics and lower the activation energies. As it is literature-known, that water can have an effect on the DMDO driven epoxidation depending on the substrate that is used,[261] the last attempt tries to exclude water by drying the DMDO solution over molecular sieve for 2 days. The equivalent increase of DMDO in the range of 3.0 to 5.0 eq. did not reach an increase of **1** in the raw reaction mixture. The same results were achieved for the solvent switch to pure acetone or a mixture of acetone and MeCN, the temperature increase to 35 °C, or the utilization of a dried DMDO solution. Only the elongation of reaction time shows a ratio shift to 40/60 (**B**/**1**). Based on these results, it can be assumed that the kinetics of the epoxidation of B are slow, which can probably be reasoned with the electron-deficient double bond. The standard protocol was aligned to longer reaction times for further experiments, keeping equivalents, temperature, reaction time, and solvents fixed.

After the purification of the raw solid mixture of **B**/**1** via column chromatography, only low yields (15 to 20%) of epoxide are obtained. The switch from acidic silica to neutral aluminum oxide as column material excludes the destruction of the epoxide moiety within the scope of ring-opening events. Looking deeper into the ^{1}H-NMR spectrum of the non-purified solid mixture, the reason for the low yields can be found in side reactions that occur during epoxidation (see Figure 40).

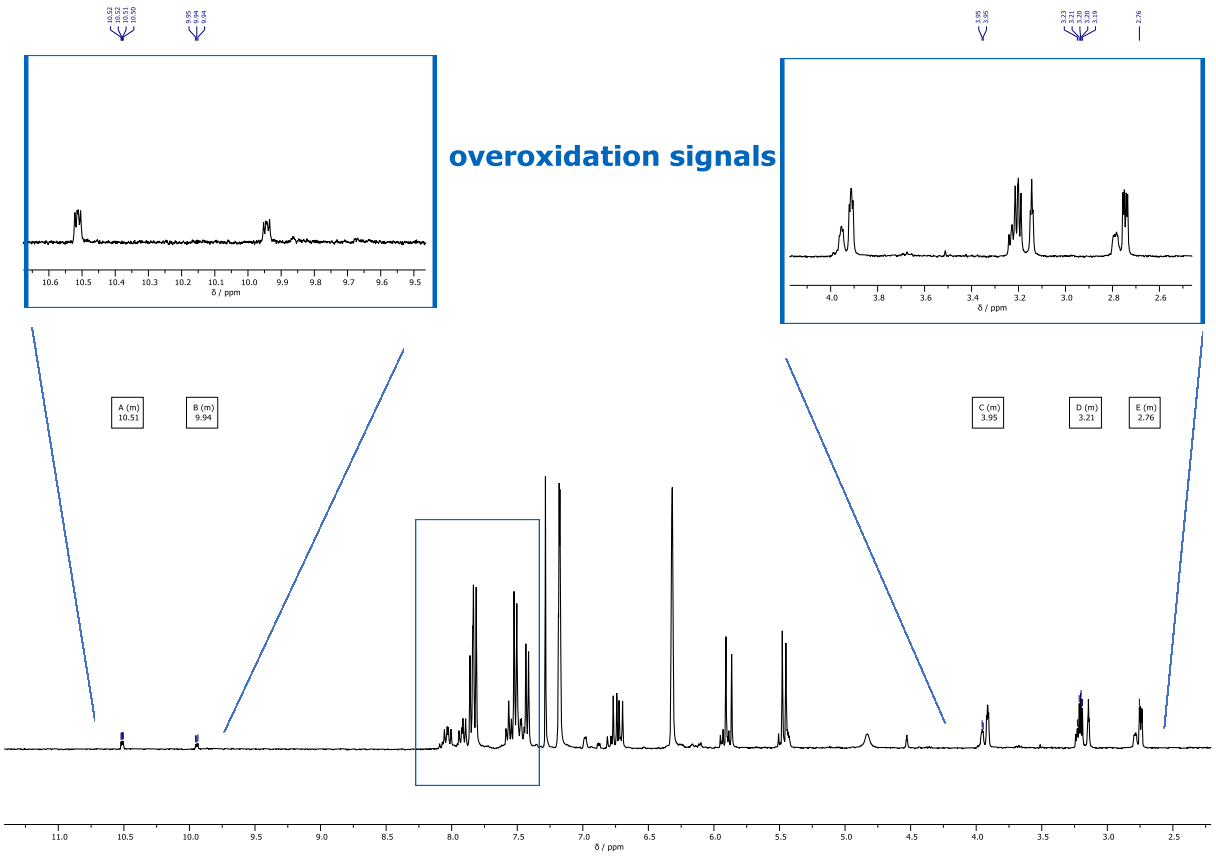

Figure 40: ^{1}H-NMR spectrum of standard DMDO experiment with new reaction conditions (taken from raw material, not purified); undetermined signal appearance in the region from 10.5 to 9.94 ppm and 3.95 to 2.76 ppm.

Three phenomena occur in the ^{1}H-NMR spectrum: downfield shifted multiplets at 10.5 and 9.94 ppm, the multiplication of the aromatic signals, and splitting of the epoxide signals into six instead of three proton responses. Owing to ^{13}C- and 2D-NMR experiments, the side products are identified as phenyl acetaldehyde and benzaldehyde, which occur due to isomerization of the epoxide and overoxidation. Similar behavior can be found when aqueous H_2O_2 is used in the epoxidation of styrene. In the presence of highly polar water, the acid-catalyzed isomerization to phenylacetaldehyde is facilitated.[262] It can be assumed that longer reaction times favor the conversion of B to 1 and the occurrence of side reactions. To prevent these, finding a more efficient pathway for the epoxidation of **B** is inevitable.

5.1.2 Parameter optimization and up-scaling

After figuring out, that the previously selected reaction conditions and the instability of the terminal epoxide can lead to side reactions and loss in yield, the idea of epoxidation has to be reconstructed. To support the reaction kinetics, catalysts are brought into play. For the epoxidation of styrene to SO, various catalytic frameworks already exist. Widely represented are transition metal complexes that consist of a distinct ligand surrounding. Examples are, for instance, cobalt phthalocyanines or manganese porphyrins, which are combined with classical epoxidation reagents like *m*-CPBA, H_2O_2, or *tert*-butyl hydroperoxide. These systems highlight mild reaction conditions, short reaction times, and high yields.[263-264] In the 1990s, *Jacobsen et al.* postulated a highly enantioselective and low-temperature epoxidation of styrene with a (*R,R*)-(-)-*N,N'*-bis(3,5-di-*tert*-butylsalicylidene)-1,2-cyclohexanediaminomanganese(III) chloride ((salen)Mn(III)) catalyst (see Figure 41). [265]

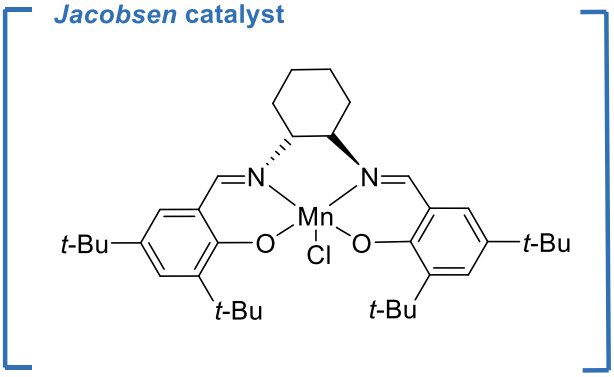

Figure 41: Structure of (salen)Mn(III) catalyst developed by *Jacobsen et al.*

The chiral environment of the catalyst, in combination with an excess of *N*-methylmorpholine-*N*-oxide (NMO) as co-catalyst and low temperature, enables the enantioselective oxo transfer with an enantiomeric excess (ee) up to 91% in relation to SO.[265] Transferring this (salen)-based catalyst to **B**, the same reaction conditions are adopted as described by *Jacobsen et al*. The epoxidation reagent *m*-CPBA and the co-catalyst NMO are added in excess (2.0 and 5.0 eq.) at −78 °C to a solution of **B** and 4 mol% of (salen)Mn(III) catalyst in DCM. After a short reaction time of 45 min, the excess remaining *m*-CPBA is quenched with NaOH, and the crude product is purified via extraction and subsequent column chromatography. The yield of 50 to 55% after purification drastically differs from the results obtained by the epoxidation with DMDO. It justifies that the catalytic input can support and fasten the cycloaddition. The structure of **1** is confirmed by ^{1}H- and ^{13}C-NMR spectra (see appendix). Aiming for increased yields, different parameter variations are screened (see Table 3). The parameters, that are adapted from the enantioselective epoxidation of *Jacobsen et al.*, are set as standard conditions and marked in blue. In this context, the temperature is not varied to prevent side reactions like isomerization or overoxidation.

Besides *m*-CPBA, other epoxidation reagents like H_2O_2 or NaOCl are tested. As they did not show any conversion, these approaches are not listed in Table 3.

Table 3: Parameter screening of the catalytically supported epoxidation of **B** by utilizing 4 mol% of (salen)Mn(III) *Jacobsen* catalyst.

parameter variation	*eq. (m-CPBA)*	*eq. (NMO)*	*T [°C]*	*t [min]*	*yield of 1 [%]*
standard experiment	2.0	5.0	–78 °C	45 min	50 to 55
m-CPBA content	**2.0 to 5.0**	5.0	–78 °C	45 min	50 to 55
NMO content	2.0	**0.5-2.0**	–78 °C	45 min	40 to 45
reaction time	2.0	5.0	–78 °C	**360 min**	50 to 55

Increasing the *m*-CPBA content or its purity does not positively influence it, probably because the solubility level is reached at cold temperatures in DCM. The same results are observed for the elongation of the reaction time or the doubling of the catalyst amount. To exclude an influence of enantioselectivity that could be induced by using the *R,R*-enantiomer of the (salen)Mn(III) catalyst, the epoxidation is one time performed with the *S,S*-enantiomeric and the other time with the achiral catalyst version. All approaches show a similar conversion of 50 to 55%. Thus, it can be assumed that the enantioselectivity of the catalyst is not decisive for the epoxidation. Lowering the NMO content leads to a worsening of yield of about 10%, which can be traced back to the function of NMO in the catalytic system. Adding NMO as a co-catalyst to the reaction mixture induces two processes:

1) the change of the (salen) ligand structure via the coordination of the co-catalyst
2) the suppression of the Lewis acidity of the manganese complex

As Lewis acidity can be a bottleneck concerning the decomposition of sensitive epoxides, adding NMO in a high content is indispensable and guarantees high yields. This thesis can be confirmed based on a control experiment. When no NMO is added or when another co-catalyst like bis(triphenylphosphine)iminium chloride (PPNCl) overtakes the role of NMO, the epoxidation of **B** does not take place. The success in achieving 64% of **1** is finally reached by decreasing the amount of NaOH during the quenching process. The less basic environment can be a hint that the epoxide is unstable not only in relation to acidity but also in basic conditions. Scheme 6 presents the whole monomer synthesis pathway with all relevant reaction conditions.

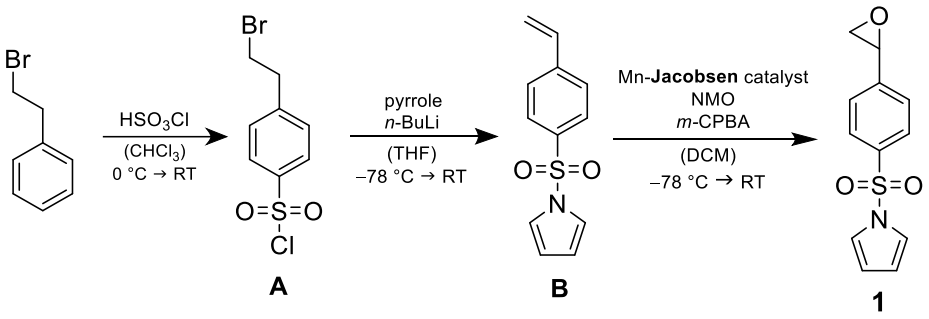

Scheme 6: Finalized reaction pathway for the three-step monomer synthesis of **1**.

In summary, it should be highlighted that the switch to a catalytically supported epoxidation makes the realization of a new, preliminary monomer for a promising SICPE possible. In addition, the elevation of isolated yields supports the upscaling process from mg to g scales. In Chapter 5.2, the ROP of **1** and the thermal properties of the resulting SICPE homopolymer will be discussed in detail.

5.2 Unlocking a polyether-based SICPE

The difference between the literature-known SICPEs and the one that is realized in this thesis lies in their polymer backbones. While already established SICPEs demonstrate aliphatic, siloxane, polyphosphazenes, or, for instance, carboxylate-based backbones,[242, 266] the target SICPE stands out due to its polyether main core. Owing to the design of **1**, a terminal epoxide creates the possibility for ROP (see scheme 7). As the structure of **1** is novel and literature-unknown, the access to polymerization is started with a broad catalyst screening.

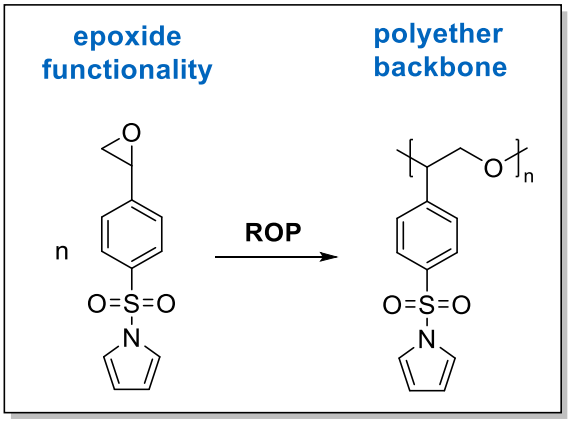

Scheme 7: Schematically representation of the ROP of **1** forming a polyether backbone.

5.2.1 Catalyst screening

The following catalyst screening is focused on different executions of ROP. For this purpose, the chapter is divided into the categories of non- and transition-metal-based catalysts. Most catalysts are tested under solution polymerization conditions, as the polymerizations must often be initialized at cold temperatures. For bulk polymerization purposes, the reaction temperature has to exceed the T_m of 108 °C of **1** (DSC measurement see appendix) to get the catalyst to be dissolved in the molten monomer. Depending on the catalyst stability, these conditions are impossible for every setup. As long as not explicitly stated, the following polymerizations are carried out in solution.

In 1863, already the first polymerization of ethylene oxide (EO), initiated by alkali metal hydroxides or zinc chloride, was reported by *Wurtz*.[267] The ensuing 70 years realized enhanced progress in this field until PEG was commercialized in the 1930s.[268] Nowadays, ROP is well-established and has been developed for a variety of industrial-relevant polymers, such as PEO, polysiloxanes, polyphosphazene, polyoxymethylene, and many more.[269] To get the possibility of finding accessible model systems for the

ROP of **1**, its structure is formally simplified to the one of a functionalized epoxide (see Figure 42). Thus, its transformation into the respective polyether can be described by three main mechanisms that have already been explored for the ROP of EO, propylene oxide (PO), or SO: anionic, cationic, and coordinative ROP.

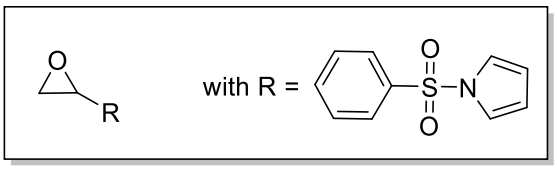

Figure 42: Simplifying the geometry of **1** to model its ROP behavior with already established epoxides like EO, PO, or SO.

The oxyanionic polymerization of EO can be seen as the most prominent pathway to receive PEG. Depending on the molecular weight that should be achieved, alkali metal compounds with high nucleophilicity (for low molecular weight PEG) or hydroxides, hydrides, or, for instance, alkoxides (for higher molecular weight PEG) are used. Their counterions should not be Lewis acidic or chain end coordinating to prevent side reactions like chain termination or cyclization and to support the living character of the chain elongation. Usually, the polymerization is carried out in polar and aprotic solvents like THF, dioxane, or DMSO.[270] Visualizing the anionic ROP mechanism on the basis of alkali metal compounds, the initiation step is started with the nucleophilic S_N2 attack of the alkoxide on the first EO unit. An active alkoxide species is formed that can ring open further EO moieties. The polyether chain is elongated in this propagation step and carries an active chain end. To terminate chain elongation with a hydroxy functionality, polar groups like alcohols, water, or amines are added (see scheme 8).[271]

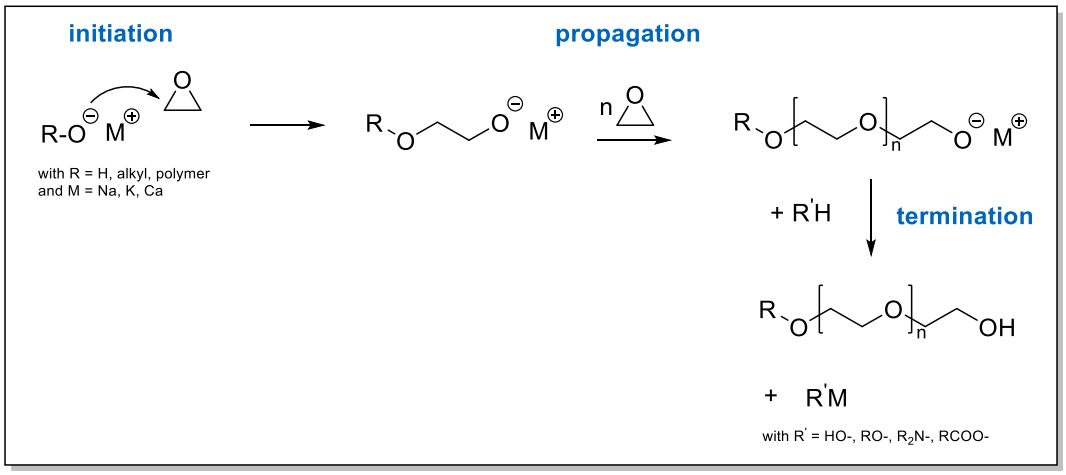

Scheme 8: Mechanism of anionic ROP for EO, using alkali metal compounds as initiators; the ROP is divided in three steps (initiation, propagation, termination step).

Cationic polymerization is rather uncommon for EO or PO polymerization and is generally applied for four-membered or higher cyclic ethers. The reason is that for smaller ring-size molecules, a certain amount of cyclic polyether is formed during propagation. The outcome is a mixture of low molecular weight linear polymers and cyclic oligomers.[268] The mechanism is split into two principles (see scheme 9). The activated chain-end (ACE) mechanism focuses on a tertiary oxonium ion as the chain end and active center. Via nucleophilic attack of the oxygen atom from the cyclic monomer on the carbon atom, which is sitting in α-position to the positively charged oxygen, the propagation of the polymer chain starts. The bottleneck hereby is the increased number of nucleophilic centers that are also present in the polymer chains. They induce inter- and intramolecular cyclic byproduct formation and decrease the molecular weights of the chains. Contrary to the ACE principle, the activated monomer (AM) mechanism allows better control over the internal polymerization processes, as the addition of an initiator can control, to a certain extent, the formation of cyclic byproducts. Suitable initiators can be based on alkynes, formyl-, hydroxyl-, or, for instance, amine groups.[272-275] The protonated cyclic monomer reacts with another monomer or hydroxyl group, starting the propagation of the polymer chain. As the monomer stays the active center, no charge is loaded onto the growing polymer chain. The resulting polymer backbone neutrality reduces side reactions like backbiting.[268-269]

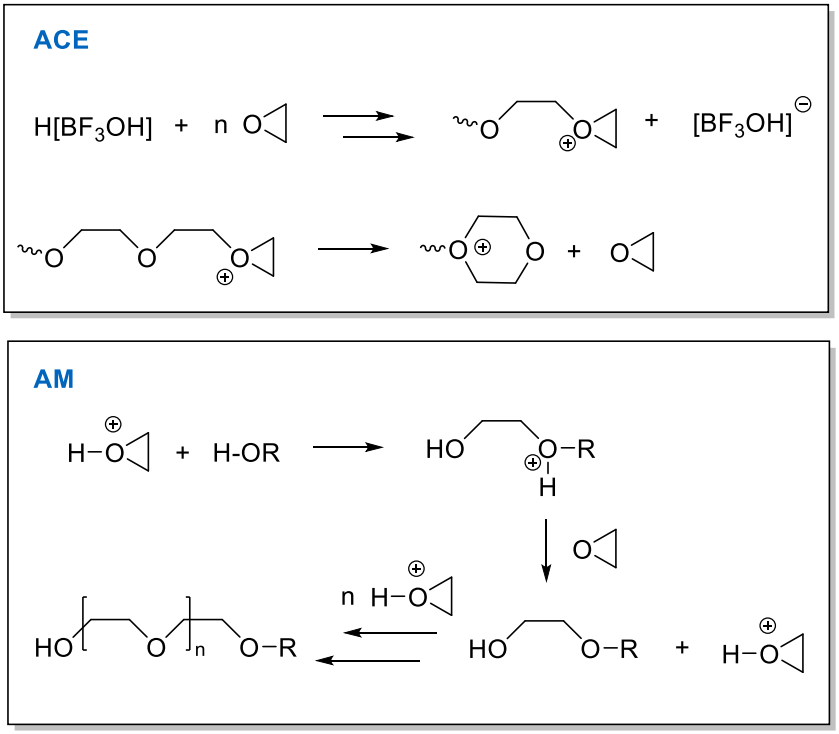

Scheme 9: Two different cationic ROP mechanisms: ACE- and AM mechanism.

Both anionic and cationic ROP are limited in their molecular weights, meaning that their mechanical properties and character can be described as rather soft. Coordination polymerization can open the field to molecular PEO weights exceeding several million. The catalyst exhibits an active metal-heteroatom, that is often coordinated to a nucleophile and surrounded by a ligand shell. The general formula can be depicted as $(LX_n)Met(Nu)_m$, where LX_n is mono-, di-, or trianionic (n = 1–3), Met is a main group transition metal like aluminum or zinc, and Nu can be represented by alkyl, amido, alkoxide, or halide functionalities.[276] The ROP mostly follows a coordination-insertion mechanism.[277] When the epoxide is added to the catalyst solution, the active metal center coordinates one epoxide moiety by releasing the bound nucleophile. Thereby, the C-O bond of the cyclic monomer is polarized, facilitating the attack of the nucleophile at the α-carbon next to the oxygen atom. The activated, cyclic monomer is able to start the propagation of the polymer chain till the active chain end is terminated. Scheme 10 shows the mechanism of the catalytically supported, anionic ROP and depicts an example of a catalyst structure that is commonly used.[278]

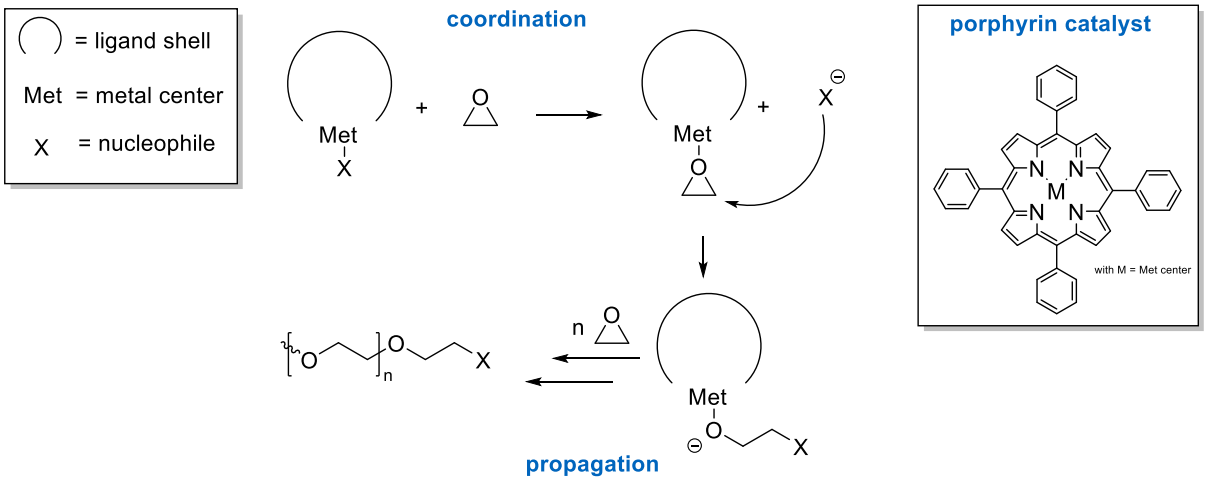

Scheme 10: Reaction mechanism for the coordinative, anionic ROP of a cyclic, three-membered ring and depiction of a commonly used catalyst for this type of polymerization; the process can be described as coordination-insertion mechanism.

Non-transition metal-based catalysts

Four catalysts are tested for the ROP of 1, which are based on the application of a non-transition-metal catalyst (see Figure 43). The choice of catalyst is able to examine different initiation processes, with *n*-buthyllithium (*n*-BuLi) being an alkyl initiator, the triethylaluminum complex ($AlEt_3$) presenting the concept of a Lewis acid in its function as initiator, sodium hydride (NaH) initiating the polymer chain growth based on a hydride as a nucleophile, and the phosphazene base (*t*-Bu-P_4) symbolizing an example for an organobase catalyst. The reaction progress and outcome are monitored via ^{1}H-NMR data. ^{1}H-NMR spectra for unsuccessful polymerization approaches are not specifically added to the appendix, as they are similar to the ^{1}H-NMR of pure monomer **1** (see appendix).

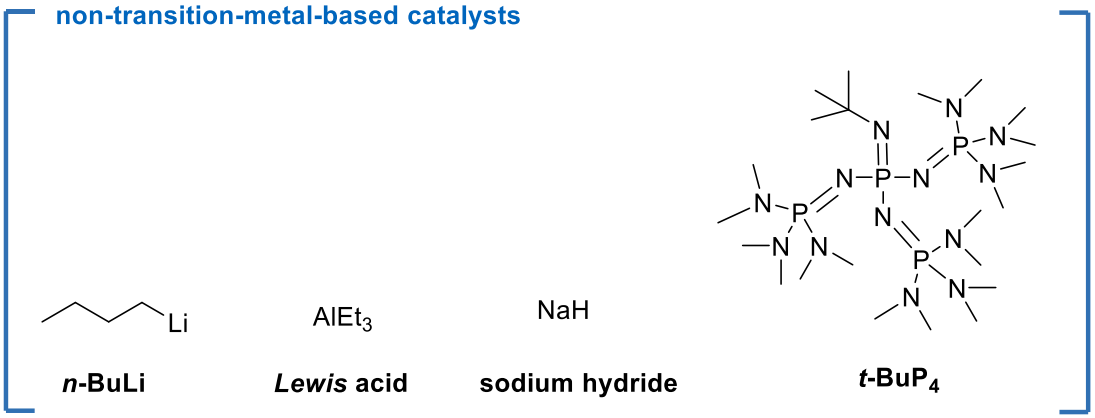

Figure 43: Structural overview of non-transition-metal-based catalyst, that are applied for the ROP of **1**; alkyl-initiator *n*-BuLi, Lewis acid ($AlEt_3$), hydride initiators (NaH), and organobase catalyst (*t*-BuP_4).

Starting with the alkyllithium compounds, they can be seen as classical initiators for anionic ROP. They are prepared out of the respective alkyl chloride compounds by the addition of elemental lithium. In addition, their solubility in various solvents makes them easily applicable for a broad monomer scope.[279] The covalent-ionic character of the C-Li bond enables, on one side, the unique property of elaborated solvation in hydrocarbon solvents, but it can also be a challenge. Alkyllithium compounds tend to form aggregates that reduce the reactivity of the initiator. The lower the degree of carbon-lithium association, the higher their reactivity.[280] To monitor the initiator behavior of *n*-BuLi, a 2.5 M solution (in hexane) is added to **1** in DCM at −78 °C (ratio of 1/20 or 1/100 *n*-BuLi/**1**). ^{1}H-NMR-aliquots, taken after 1 day of reaction time, reveal that the structure of **1** remained intact without being ring-opened. Hence, the hypothesis occurs that agglomeration of *n*-BuLi hinders its reactivity in relation to its ROP initiation efficiency. Nevertheless, using a more reactive alkyl lithium compound, namely *sec*-BuLi, exhibits similar results as *n*-BuLi. Solvent as well as temperature variations do not achieve the

ring-opening of **1**. That's why a complexing agent is added to suppress the agglomeration of *n*-BuLi. For instance, in the case of the anionic ROP of 1,3-cyclohexadiene, applying *n*-BuLi in the presence of *N,N,N',N'*-tetramethylethylenediamine (TMEDA) could narrow the dispersity and produce well-controlled polymer chain lengths.[281] Unfortunately, the *n*-BuLi/TMEDA addition at −78 °C in toluene cannot initialize polymerization of **1**.

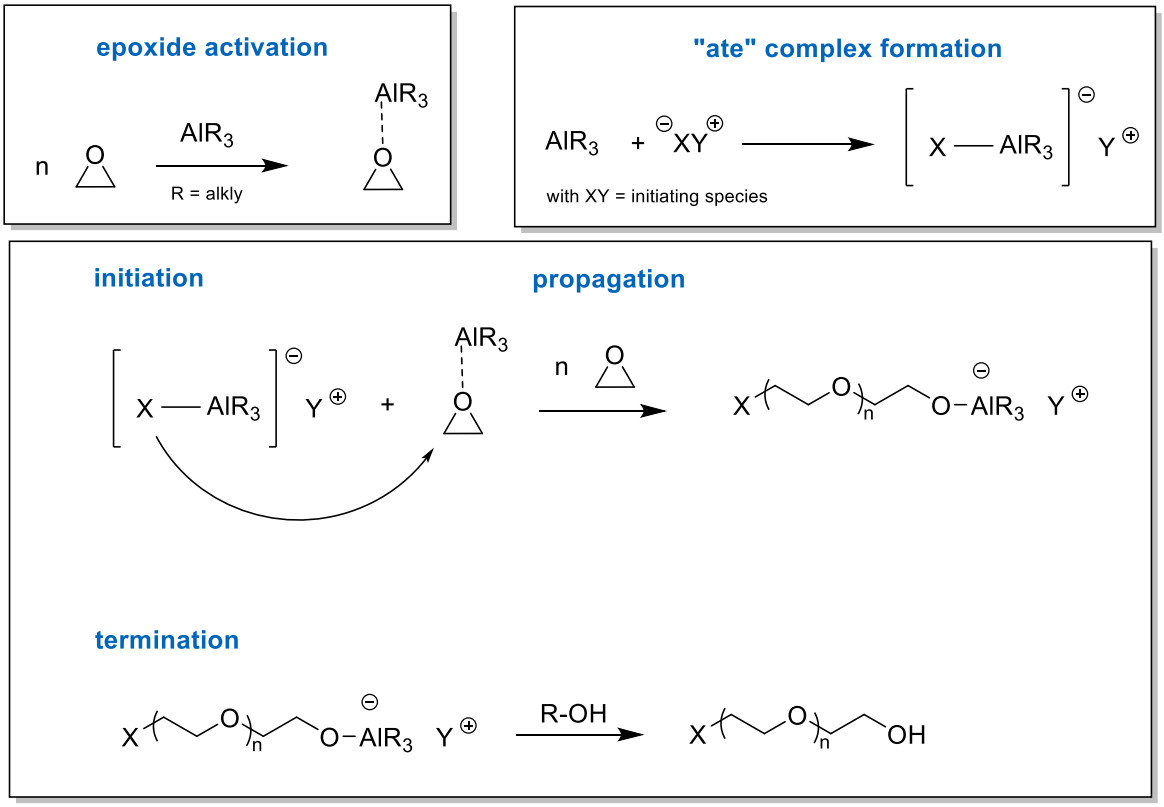

Scheme 11: Lewis acid supported ROP of EO; AlR_3 (with R = alkyl substituent) as Lewis acid precoordinates the epoxide, forms an "ate" complex, and enables an activated monomer pathway.

Substituted epoxides are often harder to polymerize because the substituents can force disturbing chain transfer reactions to the monomer. Lewis acids can establish a basis for the activated monomer strategy of anionic ROP developed by *Carlotti* and *Deffieux*.[282] The coordination of the Lewis acid to the oxygen atom of the cyclic monomer reduces the electron density inside of the ring. Thus, subsequent ring-opening is facilitated. Before starting initiation, the Lewis acid forms an "ate" complex with the initiating species (e.g., a weak nucleophile). This complex attacks the coordinated cyclic monomer, yielding a growing polymer chain (see scheme 11).[268] The strong coordination of the monomer enables mild polymerization conditions with low temperatures and weak nucleophiles as propagating species. Fewer transfer reactions to the monomer occur, suppressing high molecular weight formation and narrow distribution.[268, 283] After adding $AlEt_3$ and sodium 2-propanolate to a solution of **1** in *n*-hexane

(ratio of 1/20 or 1/100 of Lewis acid/**1**) at −78 °C, no polymerization is observed based on the ^{1}H-NMR signals taken after 1 to 2 days of reaction time. The same results are gained when sodium hydride acts as a nucleophilic initiator in the ring-opening event of **1**.

Taking SO as a model system to mimic the structural composition of **1**, organobases are prominently present in its ROP. The absence of metals makes these bases cost affordable and their usage depicts an easy purification strategy. Additionally, when comparing SO to less substituted and more reactive epoxides like EO or PO, these bases can nevertheless reach an effective ROP for sterically demanding systems. The most-established phosphazene bases are 1-*tert*-butyl-2,2,4,4,4-pentakis(dimethylamino)-2λ^5,4λ^5-catenadi-(phosphazene) (*t*-BuP$_2$) (see Figure 44) and 1-*tert*-butyl-4,4,4-tris(dimethylamino)-2,2-bis[tris(dimethyl-amino)-phosphoranylidenamino]-2λ^5,4λ^5-catenadi(phosphazene) (*t*-BuP$_4$).[268] *t*-BuP$_4$ is a strong base with a pK$_a$ of 30.2 (in DMSO) and consists of soft and bulky cation.[284] When *t*-BuP$_4$, in its function as organocatalyst and 3-phenyl-1-propanol as initiator, is added to a SO solution in toluene, living-type polymerization at room temperature occurs. After 24 h of reaction time, chains with high molecular weights up to 21.8 kg mol^{-1} and narrow dispersities of 1.14 were reached.[285] Due to the structural similarity of SO and **1**, it can be assumed that the organobase could also work with a high probability in the anionic ROP of **1**. Unfortunately, the polymerization results indicate the opposite trend. Equivalent variations (1/1/10, 1/1/50, 1/1/100 3-phenyl-1-propanol/*t*-BuP$_4$/**1**), as well as a stepwise increase in temperature up to 45 °C, do not lead to polymerization. The reason for the refusal of ROP can probably be explained by an attachment of the phosphazene base to the sulfonamide due to the intense oxophilic character of the organobase.

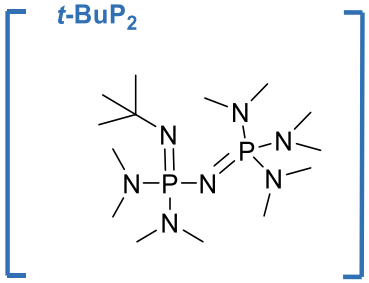

Figure 44: Chemical structure of the organobase *t*-BuP$_2$.

In summary, the above-tested non-transition-metal-based catalysts do not show promising ROP behavior of **1**. Even though there is the possibility to invest more effort in the finetuning of the different initiating methods, the screening is primarily focused on finding a well-matching and easily applicable, working catalyst. Therefore, the screening is extended by switching to transition-metal-based catalysts.

Transition-metal-based catalysts

Transition-metal-based catalysts often catalyze ROPs of epoxides like EO, PO, or SO.[286] In Figure 45, five catalytic systems are shown, that are tested for the ROP of **1**. Concerning the catalyst choice, not only do the transition metals differ from each other, but the ligand architectures are strikingly varied.

Zinc catalysts bearing *β*-diimine ligands (Zn-BDI) have been developed and aligned to the copolymerization of epoxides with CO_2. Most of the Zn-BDI catalysts show exclusively activity towards the ring-opening of cyclohexene oxide or PO.[287] This monomer scope cannot be enlarged when using the herein-designed monomer **1**. Applying Zn-BDI in a solution of **1** in toluene (1/10 or 1/100 ratio of Zn-BDI/**1**) at room temperature to 60 °C does not show conversion, as monitored by ^{1}H-NMR measurements. Same results are observed in bulk conditions at 115 °C.

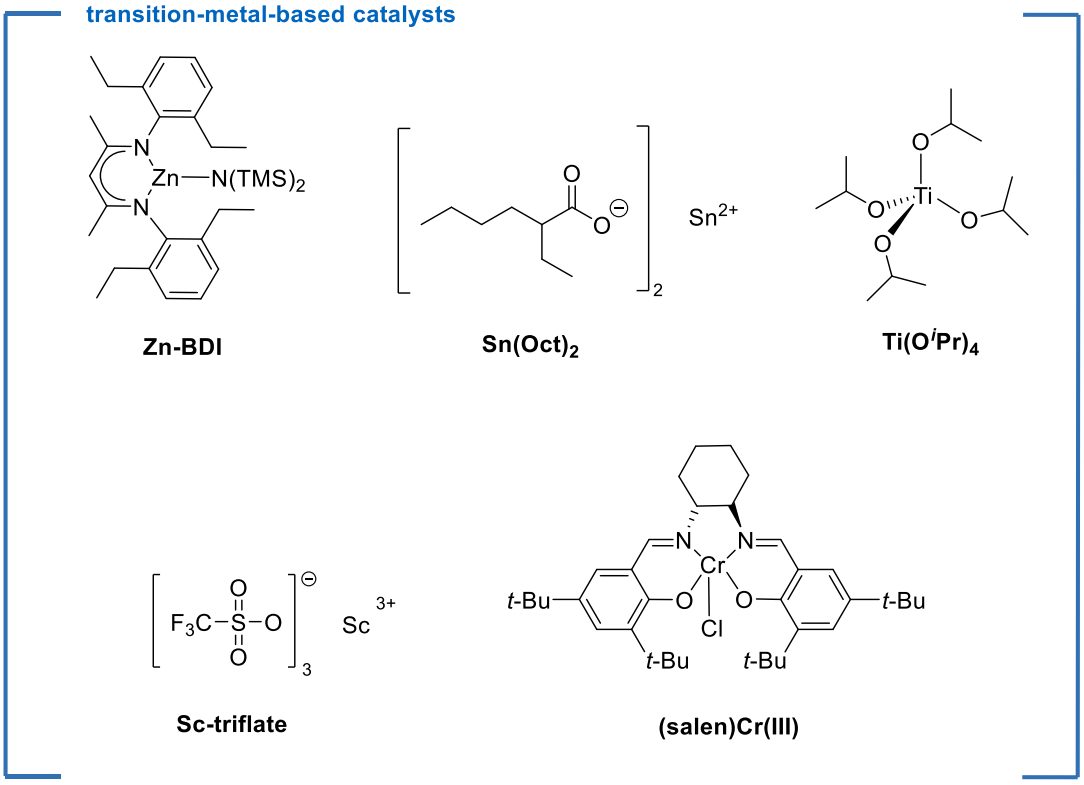

Figure 45: Structural overview of transition-metal-based catalysts that are applied for ROP of **1**.

In contrast to these findings, the other four transition-metal-based catalysts are the first ones showing ring-opening behavior upon addition to **1**. Their effectiveness in initializing the ROP of **1** differs depending on the choice of polymerization conditions (see Table 4). The conversion of **1** is determined by integrating the polyether and the remaining epoxide ^{1}H-NMR signals in the crude reaction mixture and setting them into correlation. All polymerizations are carried out with the ratio of 1/100 of catalyst to **1**. Solution polymerizations proceed at 110 °C, while bulk polymerizations are executed at 115 °C. During the polymerizations, aliquots are taken and analyzed via ^{1}H-NMR spectroscopy. The reaction is terminated when the conversion reaches a linear plateau.

Table 4: ROP of **1** with four transition-metal-based catalysts; parameter variation is mainly focused on the examination in solution or bulk; conversion of **1** is determined based on the ^{1}H-NMR signals of the polyether functionality in comparison to the distinct epoxide signals.

catalyst	*eq. (1)*	*solution or bulk*	*T [°C]*	*t [d]*	*conversion of 1 [%]*
Sn(Oct)$_2$	100	in toluene	110	7	90
Sn(Oct)$_2$	100	bulk	115	7	90
Ti(O^{i}Pr)$_4$	100	in toluene	110	10	–
Ti(O^{i}Pr)$_4$	100	bulk	115	10	65
Sc-triflate	100	in toluene	110	6	30
Sc-triflate	100	bulk	115	6	35
(salen)Cr(III)	100	in toluene	110	3	90
(salen)Cr(III)	100	bulk	115	3	95

Tin(II) 2-ethylhexanoate (Sn(Oct)$_2$) is commonly applied in the synthesis of poly(lactides). Even though the ring-opening mechanism is still not clearly examined, the catalyst usually exhibits high reaction and conversion rates and increased molecular weights.[288] The polymerization in toluene and bulk both reveal conversion up to 90%, implying that the catalyst activity is not influenced by the solvent. This is different for titanium isopropoxide (Ti(O^{i}Pr)$_4$) which only shows a conversion of 65% in bulk after a long reaction time of 10 days. Scandium(III) triflate (Sc-triflate) supports the ROP of **1** equally in solution and bulk, yielding a 30 to 35% conversion. The highest conversion with the lowest reaction time of 5 days can be attributed to the application of the (salen)Cr(III) catalyst. In solution and bulk, a conversion of

90 to 95% is reached. Figure 46 displays an overlaying NMR data set of the polymerization approaches with these four catalysts.

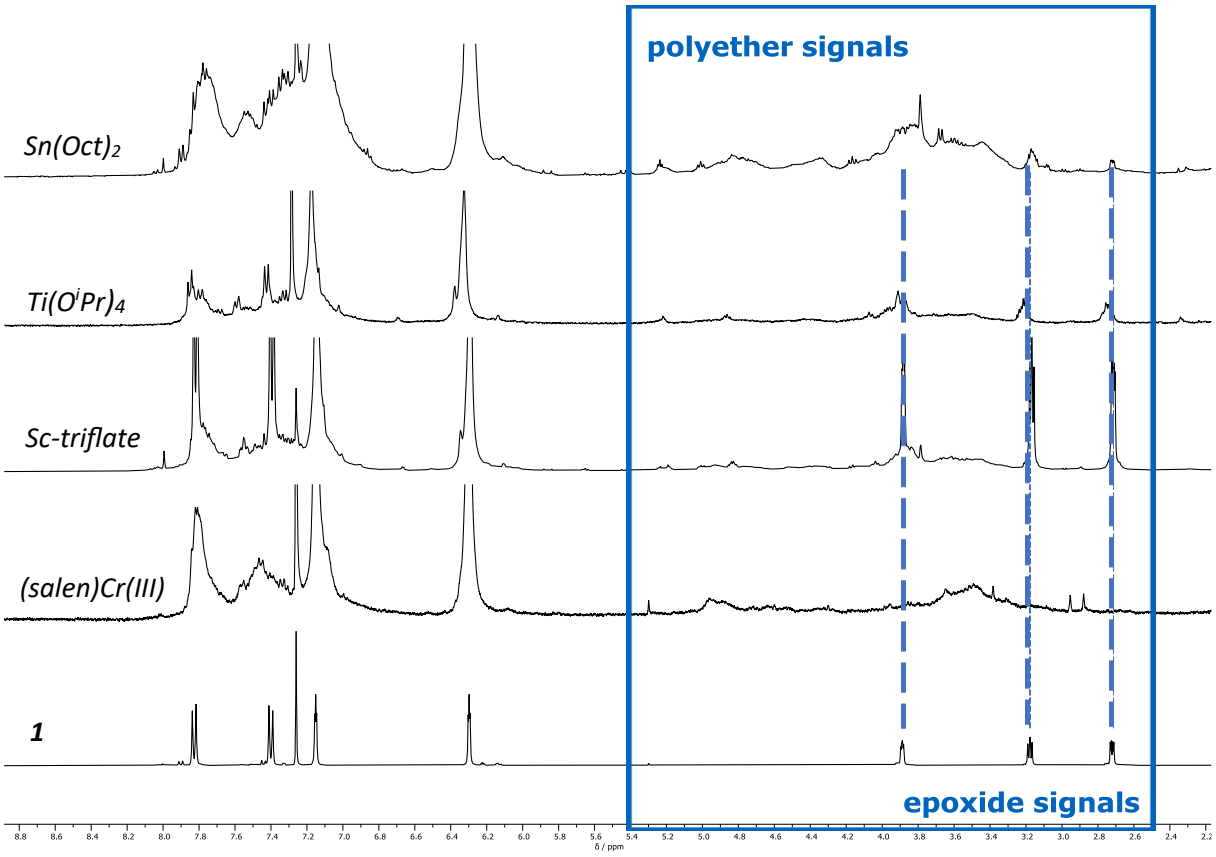

Figure 46: ^{1}H-NMR spectra of the polymerization approaches with $Sn(Oct)_2$, ($Ti(O^iPr)_4$, Sc-triflate, and (salen)Cr(III) catalyst; the ^{1}H-NMR spectrum of **1** is also set as a reference to monitor the development of epoxide to polyether signals.

The ^{1}H-NMR spectra of the $Sn(Oct)_2$ and (salen)Cr(III) catalysts clearly show the vanishing of the three epoxide multiplets between 3.21 to 2.72 ppm with proceeding polymerization. New signals are formed between 5.40 to 3.00 ppm, whose integrals represent three protons. Based on the broadening of the signals and the chemical shift, these can be assigned to the polyether backbone protons.

To summarize the usage of the herein presented transition-metal-based catalysts, $Sn(Oct)_2$ and the (salen)Cr(III) catalyst exhibit the highest conversions in ROP of **1**. The GPC data of the purified polymer, which is received via $Sn(Oct)_2$ ROP, reveals a bimodal development of the molecular weight (see appendix) in contrast to the polymer that is produced with the (salen)Cr(III) catalyst. High molecular polymer chains show a M_n of 34.0 kg mol^{-1}, whereas most of the polymer chains exhibit a M_n of 3.00 kg mol^{-1}. To keep uniformity in chain lengths and to use shorter polymerization times, the (salen)Cr(III) catalyst is finally chosen as a suitable catalyst for the ROP of **1**.

5.2.2 ROP with (salen)Cr(III) catalyst

The appliance of (salen)Cr(III) catalysts in the ROP of epoxides is already well-established by research done in the *Coates et al. group*.[289] The (salen)ligand surrounding has a great potential to be modified in many positions (see Figure 47) to find the perfect fit that harmonizes with the monomer size and its functional groups.

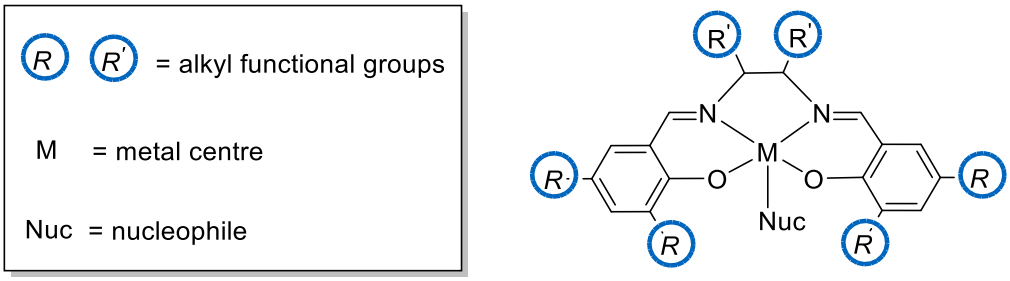

Figure 47: Schematic representation of the structural tolerance that (salen)--based catalysts offer due to a variable ligand constitution.

The Initiation of (salen) catalyst-supported ROP follows a monometallic, bimetallic, or binary initiation pathway (see scheme 12).[287] After initiation, propagation and termination follow as previously described for related ROPs.

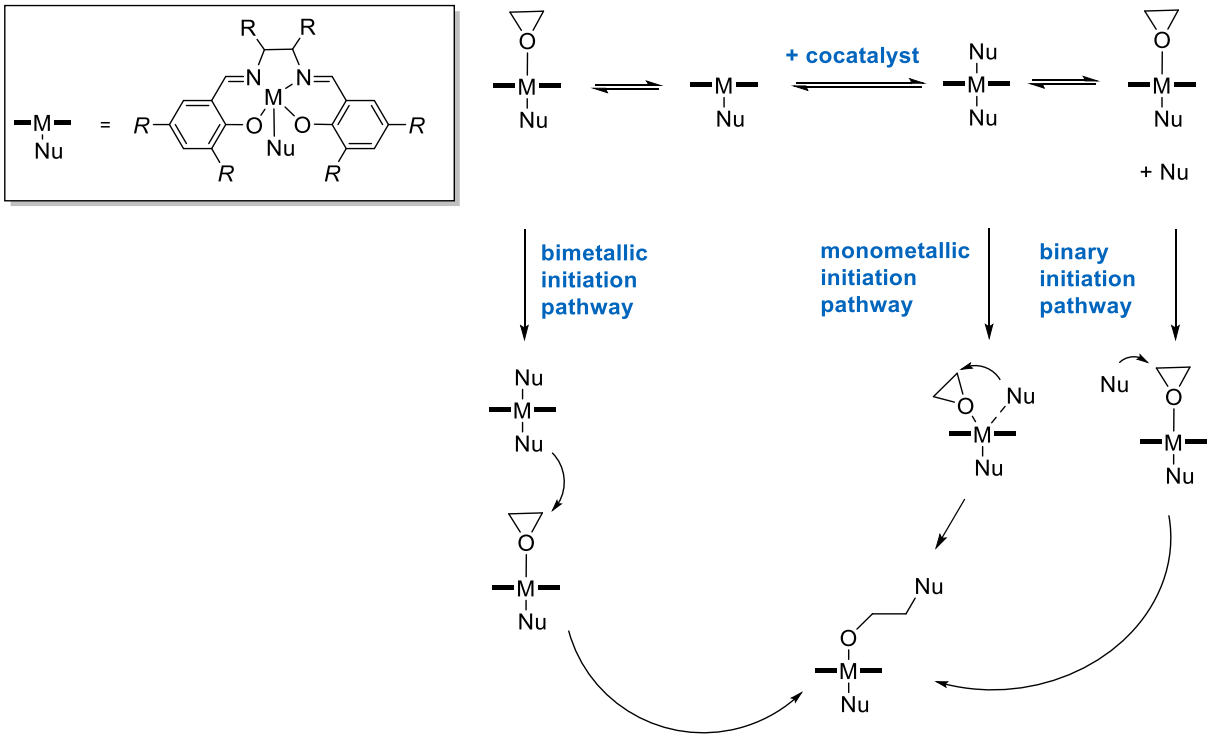

Scheme 12: Mono-, bimetallic, and binary initiation mechanism for the ROP of EO via (salen)catalyst support.

The (salen)Cr(III) catalyst, that is used in the screening experiments, is commercially available and can be used without further purification. A big advantage of this system is its rather huge tolerance against humidity. Nevertheless, **1** is sublimated three times before using it in ROP to avoid water acting as a chain transfer agent. Bulk polymerization is chosen instead of polymerizing in solution, as the chromium catalyst exhibits higher conversions and higher initiator efficiencies in bulk (yield = 95 vs. 90%, initiator efficiency = 36 vs. 22% for a 1/00 catalyst/**1** ratio).

The (salen)Cr(III) catalyst and **1** can be polymerized in different catalyst-to-monomer ratios (see Figure 48). Therefore, the catalyst and monomer are dry mixed in ratios of 1/10, 1/50, 1/100, and 1/200 and heated up to 115 °C under inert conditions. After 3 days, the solid mixture is dissolved in DCM and precipitated in pentane, to cleave off catalyst residues and unconverted monomer. Drying in a vacuum at 50 °C for 24 hours yields 93-97% of polymer in powder form. Energy dispersive X-ray analysis (EDX) measurements prove the absence of chromium catalyst residues (see appendix).

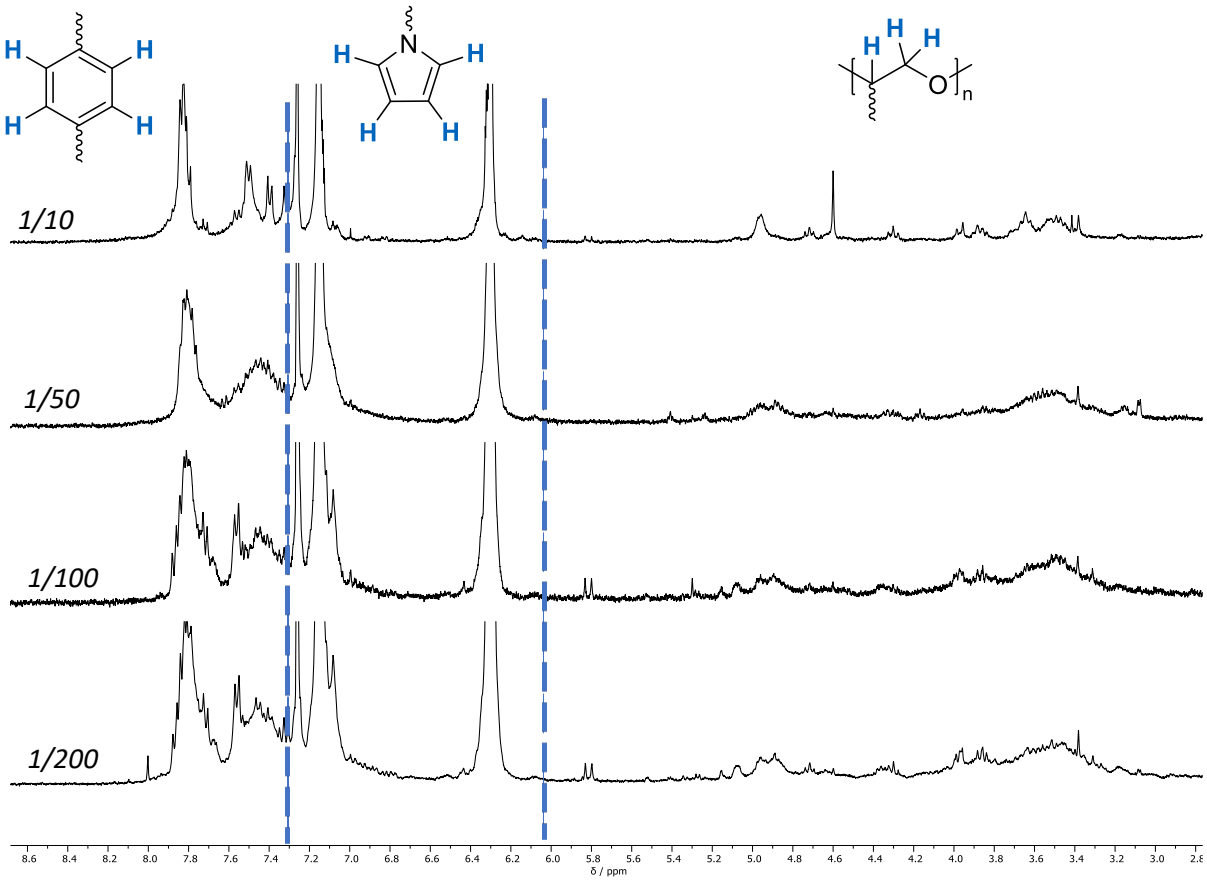

Figure 48: ^{1}H-NMR spectra of the polymers, that result from different (salen)Cr(III) catalyst to **1** ratios (1/10, 1/50, 1/100, 1/200); from 8.00 to 7.30 ppm aromatic proton signals of the benzene moiety; from 7.20 to 6.15 ppm proton signals of the sulfonamide functional group; from 5.40 to 3.00 ppm proton signals of the polyether backbone.

Table 5 exhibits an overview of the development of molecular weight distribution pursued by GPC analysis. The GPC traces show a monomodal and uniform distribution, meaning that a smooth and controlled polymerization can be assumed (see appendix). Molecular weights increase to 113 kg mol^{-1}, with dispersities ranging between 1.3 and 2.6. The significant variation in dispersity can be traced back to inhomogeneities evoked by unpropitious stirring and increased viscosity when bulk conditions are applied. To narrow these, a polymerization process with a more controlled setup up like living-type solution polymerization could be a solution.[285] Initiator efficiencies range from 18-43% and cannot be increased with additional sublimation steps of **1**. As the initiator efficiencies are rather low, a huge part of the catalyst molecules is deactivated. Therefore, the polymer chains exceed the calculated theoretical molecular weight. Due to the overlaying signals of the epoxide and the aliphatic polyether backbone signals in the ^{1}H-NMR spectra at higher conversion rates, the final polymer yield is determined gravimetrically.

Table 5: GPC-data for the ROP of **1** with varying (salen)Cr(III) catalyst to monomer ratio (1/10, 1/50, 1/100, 1/200) in bulk at 115 °C for 3 days.

catalyst/1[a]	*X*[b] *[%]*	*$M_{n,theo}$*[c] *[kg mol^{-1}]*	*$M_{n,abs}$*[d] *[kg mol^{-1}]*	*Đ*[d] *[-]*	*I_e*[e] *[%]*
1/10	96	2.50	14.2 ± 0.04	2.6 ± 0.01	18 ± 0.06
1/50	93	11.8	36.5 ± 0.03	1.9 ± 0.01	32 ± 0.04
1/100	97	24.1	67.3 ± 0.03	1.3 ± 0.01	36 ± 0.05
1/200	96	50.8	113 ± 0.05	2.4 ± 0.01	43 ± 0.05

[a] Initial catalyst to monomer ratio. [b] Conversion of monomer determined by isolated yield of polymer. [c] Theoretical molecular weight $M_{n,theo}$ = [Cat : **1**] × X_1 × 249.28 g mol^{-1}. [d] Absolute molecular weight determination and dispersity of the homopolymer in DMF (30 °C, with 25 mmol L^{-1} LiBr, triple detection, d*n/dc* = 0.152 mL g^{-1}). [e] Initiator efficiencies = $M_{n,theo}/M_{n,abs}$.

Concerning the ring-opening mechanism, **1** can be opened in two positions, both yielding a polyether backbone. As seen for catalytically supported ROP of SO, the attack of a nucleophile at the methylene or the methine position can be influenced by various parameters like temperature, electronic properties of the transition metal center, cocatalyst addition, or steric reasons.[290-291] Since **1** consists of an aromatic ring and a sulfone moiety, which decreases the electron density of the methine position, the nucleophilic attack should be favored at this more electrophilic position. To clearly understand the

underlying ROP mechanism, studies should be supported in the future using (HT)-NMR measurements and a catalyst-to-monomer ratio of 1/1.

Scheme 12 shows that the addition of a cocatalyst can influence the initiation pathway of the epoxide ROP. That's why two cocatalysts are added to the dry catalyst-monomer mixture (1/1/100 ratio of catalyst/cocatalyst/**1**) before heating up the solid mixture to 115 °C for 3 days. In this context, 4-dimethylaminopyridine (DMAP) as well as PPNCl are selected as candidates. Both cocatalysts seem to have the same effect on the (salen)Cr(III)-**1** system. The ^{1}H-NMR spectra of the resulting purified polymers show the same proton signals as the one postulated in the ROP without adding a cocatalyst. GPC traces yield no change in the molecular weights (GPC traces see appendix). Therefore, it can be assumed that adding cocatalysts does not significantly influence the ROP of **1**. Probably, DMAP and PPNCl are only badly dissolved in the molten monomer and tend not to participate during the ROP in an efficient manner.

The polymerization is run at 115 °C, 7 °C over the T_m of **1**. Decreasing the temperature is impossible, as the catalyst has to be dissolved in the molten monomer to actively participate in the ring-opening event. That's why polymerization approaches under 115 °C do not show a conversion of **1**.

To check if the stereochemistry of the (salen)Cr(III) catalyst can affect the ring-opening, the achiral version of the catalyst is synthesized (^{1}H-NMR of the achiral (salen)ligand see appendix). The bulk polymerization applies the same reaction and purification conditions as described above. Here, the polymerization proceeds similarly to the ROP with the chiral (salen)Cr(III). This suggests, that the upper part of the (salen)Cr(III) does not significantly interact with **1** and that it is not decisive for the polymerization development.

In summary, using the (salen)Cr(III) catalyst presents an easily applicable way to ring-open **1**. The applied polymerization in bulk has to deal with some disadvantages, like inhomogeneities at higher conversion and subsequently increased viscosity. Nevertheless, the catalyst produces high molecular weights and depicts a stable system with a simple reaction procedure.

5.2.3 Accessing the charge carrier functionality via post-polymerization functionalization

The polymer, which is achieved via ROP of 1, resembles the structure of PEO, which is a side group functionalized with a sulfonamide-substituted styrene unit (see scheme 13).

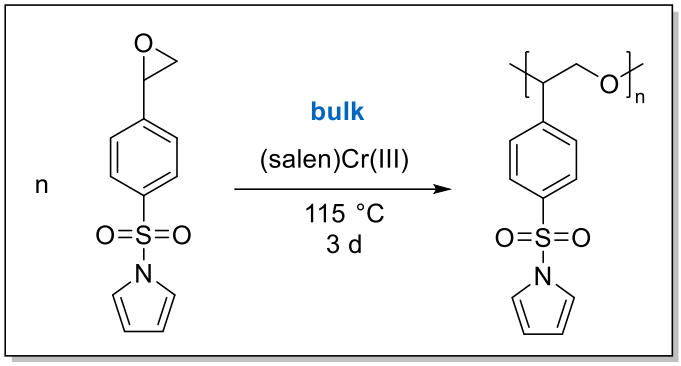

Scheme 13: Bulk ROP of **1** catalyzed by the (salen)Cr(III) catalyst at 115 °C for 3 days.

With the sulfonamide group still bound to the aromatic benzene ring, the structure is far from being a SICPE. Therefore, the polymer structure has to be modified to access the charge carrier functionality. The design of the monomer synthesis pathway makes post-polymerization functionalization inevitable. Nevertheless, the presence of the sulfonamide in its function as a protection group is necessary. A control experiment underlines the importance of the sulfonamide in relation to the polymerization process. Sodium 4-vinyl benzenesulfonate can be epoxidized with DMDO ($c \leq 0.1$ M, 1/1 ratio of substrate/DMDO) over 3 days at room temperature with a conversion of 78% (^{1}H-NMR spectrum of crude product see appendix). The resulting epoxide bears a benzene ring with a free sodium sulfonate group instead of the sulfonamide in structure **1**. When the purified sulfonate-based epoxide is dry mixed with the (salen)Cr(III) catalyst and heated up to 115 °C, no ROP is observed. Setting these results into context with the ROP of **1**, it can be assumed, that the free sulfonyl group deactivates the catalyst. Due to the density of end-standing and sterically easily accessible oxygen atoms, the oxophilic character of the transition metal could lead to the coordination of the catalyst to the free sulfonyl group. The consequence would be the prevention of the epoxide coordination and subsequent ring-opening.

Hence, strategies to deprotect the homopolymerized version of **1** need to be established. The aim is to remove the amide while forming a free lithium sulfonate moiety (see scheme 14). The success of the post-polymerization functionalization can be monitored by using ^{1}H-NMR spectroscopy. As the pyrrole group will leave the molecule, the two multiplets between 7.22 to 7.06 ppm should vanish in the polymer-NMR after deprotection and purification.

Two challenges have to be considered for this polymer-analogous reaction:

1) preservation of the polymer backbone by selecting mild reaction conditions
2) management of the polarization change from protected (rather non-polar) to deprotected (highly polar) state

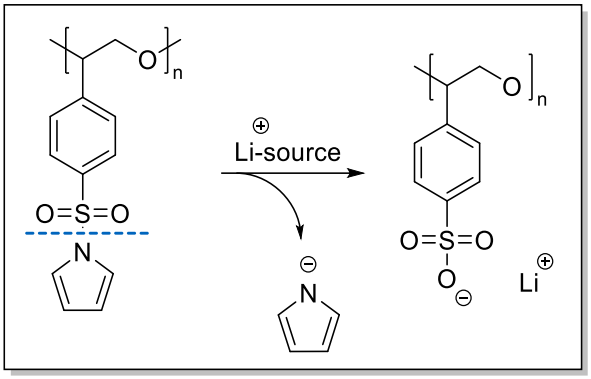

Scheme 14: Schematic execution of the sulfonamide cleavage, generating a free amide and a free sulfonyl group bound to the benzene unit.

Literature attempts to describe the cleavage of sulfonamides in most cases with aqueous, acidic reaction conditions.[292] The nitrogen gets protonated and gets cleaved off as pyrrole species. The remaining sulfonate moiety can be transferred in a second step into the respective lithium sulfonate. To test if the homopolymer of 1 is stable at low pH values, an excess of H_2SO_4 is added to a solution of the polymer in ethanol and is heated up to 70 °C for 4 days. A brown and oily solid is precipitated immediately after adding the acid to the polymer solution. After finishing the reaction, this solid is filtered off and analyzed via ^{1}H-NMR spectroscopy. The ^{1}H-NMR spectrum exhibits no cleavage of the pyrrole group, concluding that acidic and harsh reaction conditions will not support forming a free sulfonyl group. The increase of acid content is not forced, as it could protonate the polyether backbone and lead to its disassembly into smaller fragments.

Another approach to support the cleavage of the sulfonamide is the usage of an alkali base like potassium hydroxide (KOH), sodium hydroxide (NaOH), or lithium hydroxide (LiOH). Thereby, the hydroxy group attacks the positively polarized sulfur atom and cleaves off the pyrrole (see scheme 15). The negatively charged pyrrole can then be protonated in aqueous media or complexed with an alkali metal cation.[293]

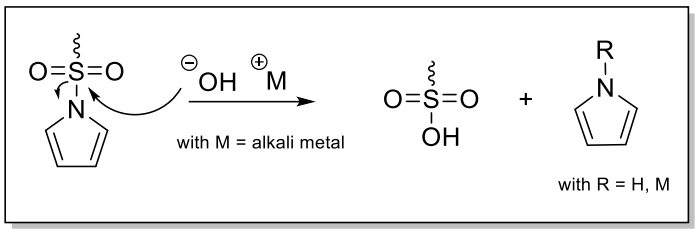

Scheme 15: Basic conditions supporting the cleavage of the sulfonamide bond between sulfur and nitrogen.

In a first attempt, KOH is dissolved in ethanol (0.1 M), then the homopolymer of **1** is added (ratio 1/400 of homopolymer/KOH), and the reaction solution is heated up to 70 °C for 16 h. During the reaction, a light brown precipitate is formed that is filtered off, washed with water, and analyzed separately via ^{1}H-NMR spectroscopy. The solvent of the reaction solution is evaporated to yield a brown solid, that is as well washed with water and analyzed. For comparison reasons, the ^{1}H-NMR spectra of the two solids are shown in Figure 49.

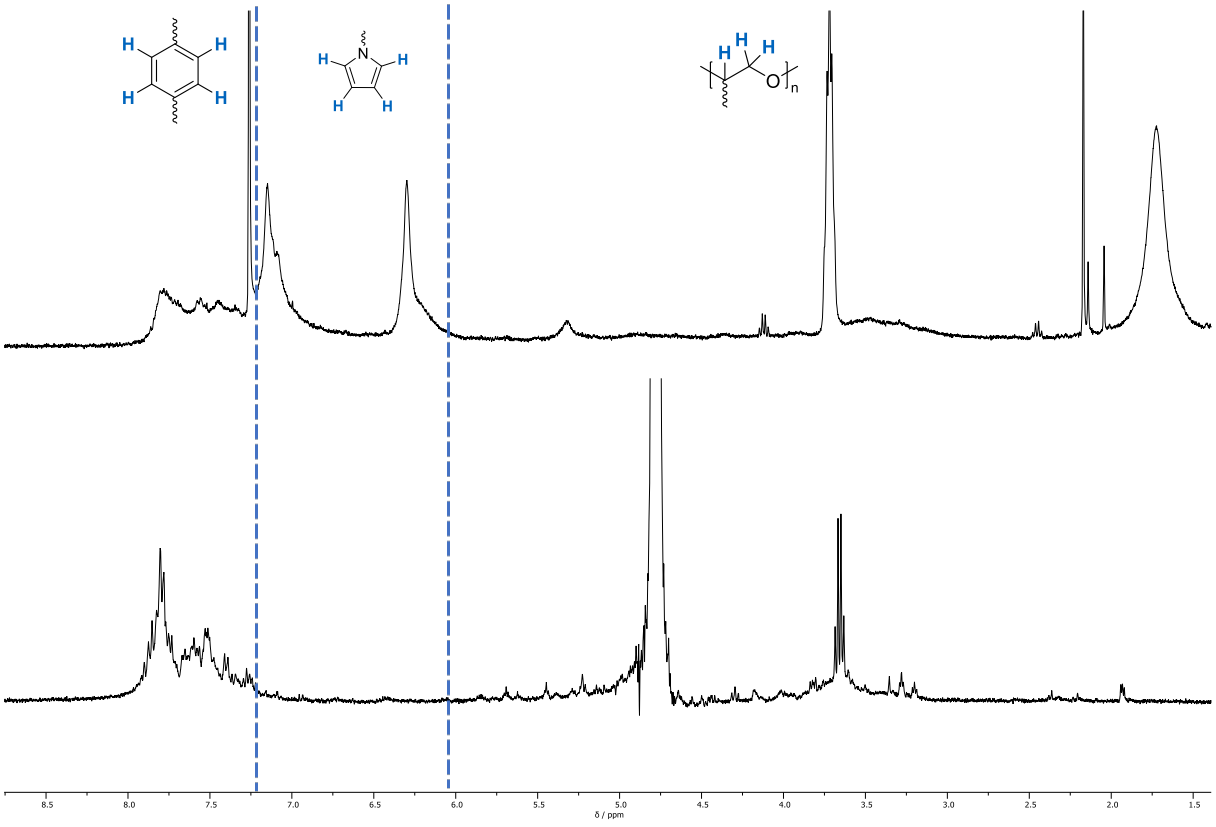

Figure 49: ^{1}H-NMR spectra of the post-polymerization modification with KOH in EtOH; top: proton signals of reaction solution; bottom: proton signals of precipitated solid during reaction.

The ^{1}H-NMR at the top presents the results of the evaporated reaction solution, while the bottom depicts the proton signals of the precipitate that is formed during the reaction. Both ^{1}H-NMR spectra show comparable signals in the region of the aromatic benzene ring (8.00 to 7.30 ppm) and the polyether backbone (5.40 to 3.00 ppm). Striking is the difference in the region between 7.20 to 6.16 ppm, where the signals of the pyrrole protons appear. In contrast to the ^{1}H-NMR of the reaction solution, the solid shows the vanishing of these signals, implying the success of the post-polymerization modification. As the isolated yield of this precipitated solid is ≤ 1%, it has to be assumed that the majority of the protected homopolymer of 1 does not participate in the reaction. Therefore, different parameters are varied to increase the isolated yield of the deprotected homopolymer (see Table 6). The experimental conditions, that are discussed above, are marked in blue as a reference.

Table 6: Parameter variation in relation to the post-polymerization functionalization of the homopolymer of **1** with KOH as cleaving reagent.

reagent	***eq. (reagent)***	***T [°C]***	***t [h]***	***solvent***	***isolated yield [%]***
KOH	400	70	16	EtOH	1
KOH	**800**	70	16	EtOH	5
KOH	800	**80**	16	EtOH	5
KOH	800	70	**72**	EtOH	5
KOH	800	70	16	**H_2O/DCM**	–
KOH	800	70	16	**MeOH**	3
NaOH	800	70	16	EtOH	3
LiOH	800	70	16	**MeOH**	3
LiOH	800	70	16	**H_2O/DCM**	–

The increase in KOH equivalents has a major influence on the isolated yield outcome compared to other parameters like temperature, reaction time, or solvent. Increasing the equivalents from 400 to 800 eq. raises the yield from 1 to 5%. Higher temperatures of 80 °C and longer reaction times of 72 h instead of 16 h do not ameliorate the yields. The bottlenecks of this polymer analogous reaction can be seen in the different solubilities of KOH and the polymer and the additionally strong solubility change during deprotection. KOH dissolves well in EtOH, which is why switching to methanol or DCM as solvents

decreases the yield to 3 or 0%, as fewer dissolved hydroxy groups participate in the post-polymerization modification. Conversely, the protected homopolymer of **1** does not dissolve well in EtOH, leading to a coiling behavior and less approachable reaction centers. In addition, the parts of the polymer chains that already bear free sulfonyl groups show a different polarity to the other polymer part, where the sulfonamide units are still anchored. Therefore, the risk of polymer chain cleavage is given, as the more polar polymer part tends to precipitate in the solution while the other part stays solvated (see Figure 50).

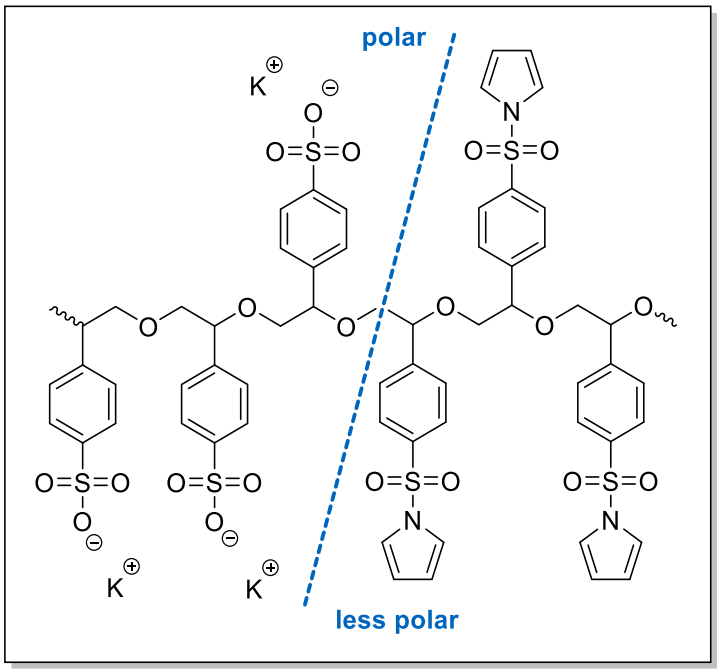

Figure 50: Schematic representation of the procedures going on during the deprotection of the sulfonamide; the parts of the polymer where the moieties with the free sulfonyl groups sit are much more polar than the polymer parts with the attached sulfonamide.

The cleavage of the sulfonamide group is also possible with NaOH or LiOH, but in their cases, lower yields of 3% are achieved compared to KOH as a deprotection reagent. The post-polymerization functionalization is transferred to a microwave setup to prevent polymer chain destruction at long reaction times. Microwave radiation can support the activation of molecules and drastically shorten reaction times and temperatures.[294] With the help of this new setup, the parameters for the KOH-supported post-polymerization functionalization can be reset. Instead of using 800 eq. KOH in EtOH at 70 °C and a reaction time of 16 h, 400 eq. of KOH at room temperature, supported by a dynamic power supply of 300 W, yield 15% of deprotected homopolymer. In conclusion, applying this microwave setup exhibits a supportive influence on the cleavage of the sulfonamide.

After receiving the potassium sulfonyl functionalized homopolymer of **1**, a salt metathesis reaction is necessary to exchange the potassium against the lithium cation. To fulfill this metathesis, a common salt like $LiClO_4$ is dissolved in a polar solvent and added to the potassium compound solution at higher temperatures.[295] Even though these salt metatheses are often performed quantitatively, they imply an additional synthesis step before reaching the final SICPE, lowering the overall yield.

Research continues with the search for a one-step post-polymerization modification, where the PEO-SICPE directly bears a lithium cation as a charge carrier without needing salt metathesis. *Li et al.* present an efficient approach, where elemental lithium is dissolved in dry methanol to form *in situ* lithium methanolate. This converts the sulfonamide groups of a porphyrin ligand into the respect lithium sulfonate functionalities.[296] The mechanism behind sulfonamide cleavage might be proposed like this: the *in situ* generated nucleophile attacks the positive polarized sulfur, so that a negatively charged pyrrole leaves the repetition unit. As intermediate, a sulfonyl substituted with a methoxy group is formed. The activated pyrrole can attack the carbon atom on the bound methoxy group to get methyliated, while the free lithium sulfonyl group is generated (see scheme 16).

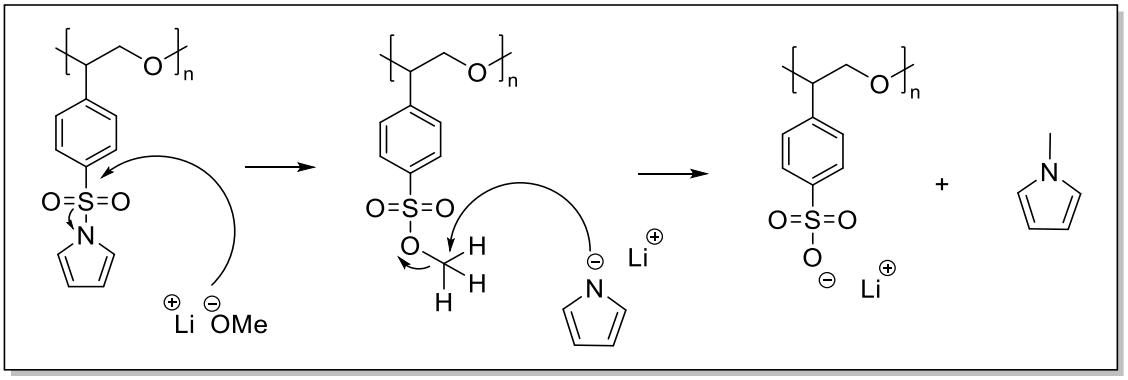

Scheme 16: Proposed mechanism for generating the free lithium sulfonate via post-polymerization functionalization with *in situ* formed lithium methanolate.

To generate *in situ* lithium methanolate, elemental lithium (10 eq. per monomer unit) is dissolved in dry MeOH at 0 °C. The homopolymer of **1** is dissolved in dry DCM and added to the solution. After letting the solution equilibrate to room temperature, it is heated up to 65 °C for six days. During the reaction, a little bit of solid precipitates that is filtered off. ^{1}H-NMR analysis reveals that the solid has the structure of the starting homopolymer. The solvent of the solution is removed, and a ^{1}H-NMR spectrum of the crude product is taken. In the following, the internal processes observed for the post-polymerization functionalization are described on the basis of the (salen)Cr(III) catalyst/**1** ratio of

1/100. All stated observations can be equally transferred to the other catalyst/monomer ratios (1/10, 1/50, 1/200).

Comparing the ^{1}H-NMR spectrum of the crude product (after treatment with elemental lithium in MeOH) with the proton signals of the protect homopolymer of **1**, a shift in both pyrrole signals can be seen (see Figure 51). The multiplets of the protected homopolymers are found at 7.20 and 6.35 ppm, while the new positions of the signals after the post-polymerization treatment are at 6.50 and 5.90 ppm. This shift indicates a successful release of the pyrrole group which can also be seen in the rising strong coloring of the solution over time. To eliminate the excessive pyrrole, the crude product is dissolved in water and extracted with DCM. Thereby, the major part of the pyrrole and still protected homopolymer fractions that did not participate in the reaction can be drawn into the DCM phase. To ensure that no minor impurities of the leaving group stay in the final homopolymer, the aqueous homopolymer solution is dialyzed against water. After dialysis and lyophilization, the proton signals of the pyrrole groups are completely removed (see Figure 51, bottom).

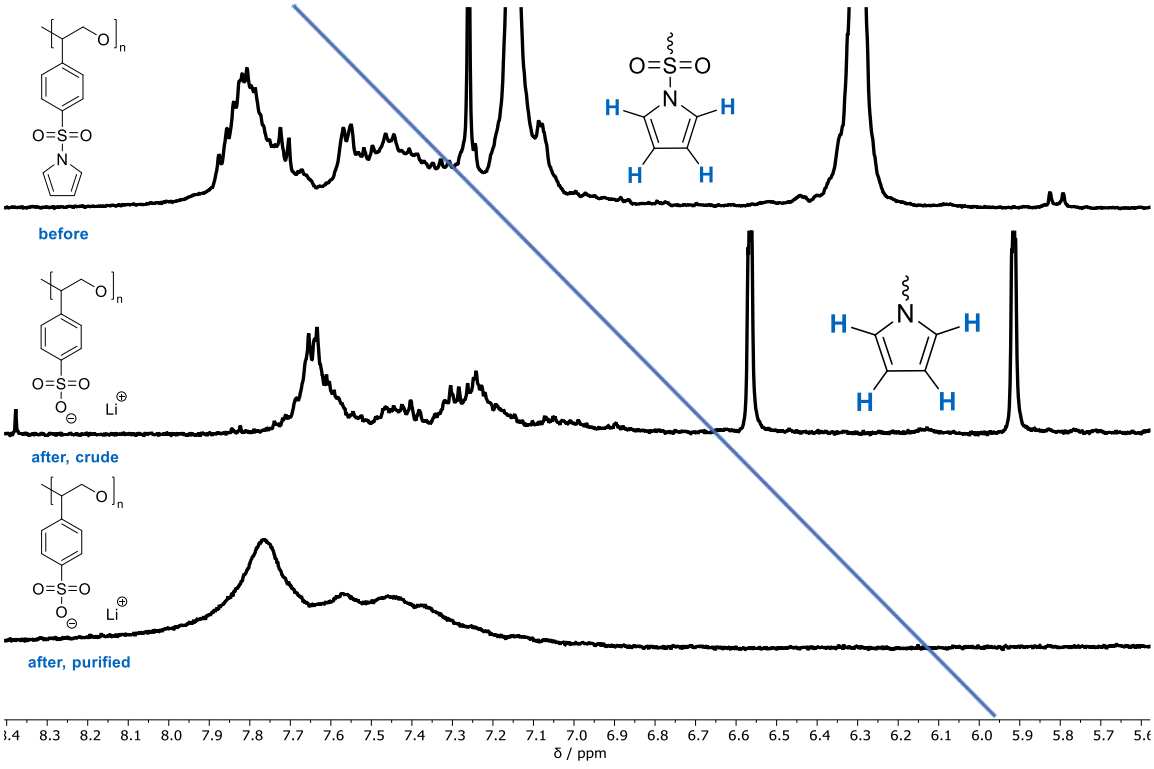

Figure 51: ^{1}H-NMR spectra related to the post-polymerization functionalization of the homopolymers of **1** by adding elemental lithium in MeOH; top: ^{1}H-NMR of the homopolymer before post-polymerization functionalization; middle: ^{1}H-NMR of crude product directly after the post-polymerization functionalization; bottom: purified deprotected homopolymer after dialysis.

To confirm the presence of the lithium cation coordinating with the generated sulfonyl group, ^{7}Li-NMR is taken of all (salen)Cr(III)/**1** ratios of deprotected homopolymers. A 0.1 M solution of LiCl is added as an internal reference (see Figure 52). For all ratios, a singlet at 0.16 ppm appears, confirming the presence of one lithium species inside of the polymers.

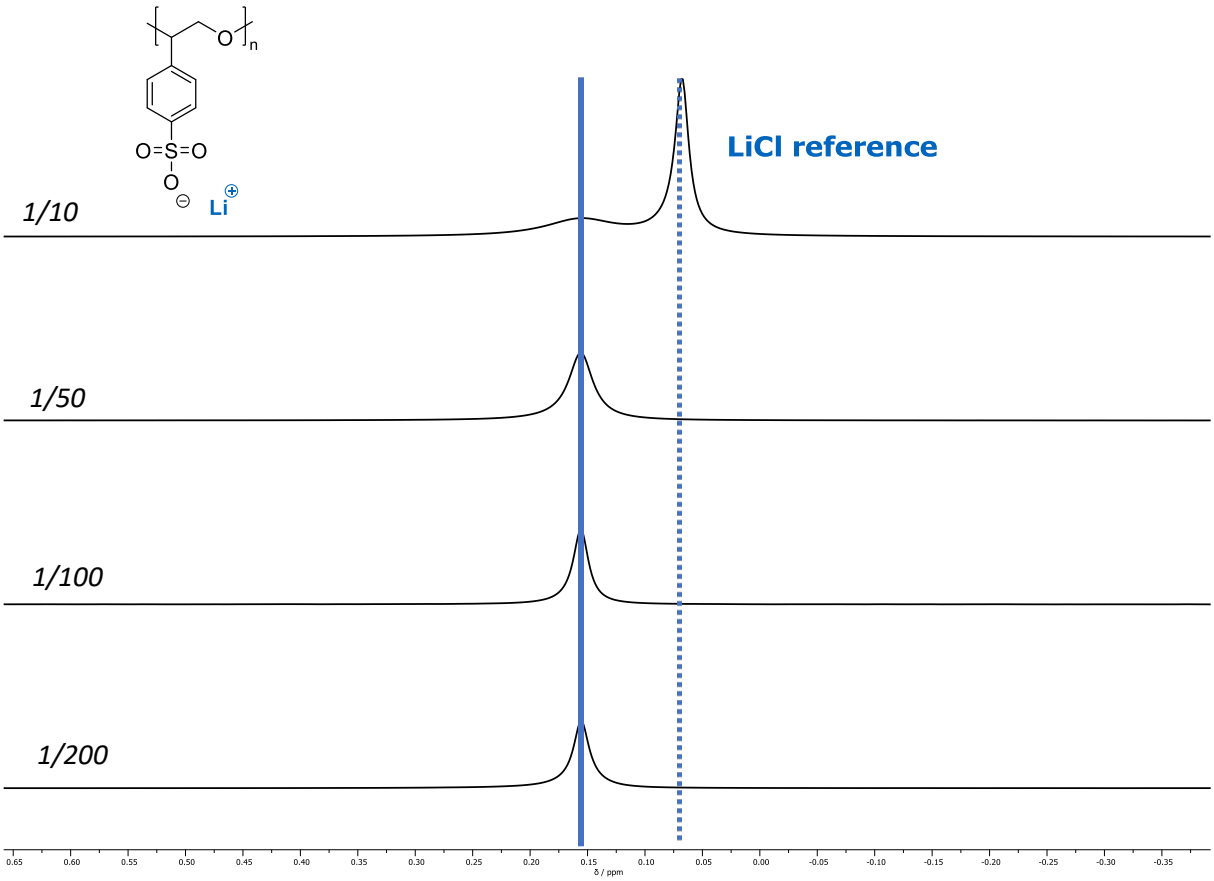

Figure 52: ^{7}Li-NMR of different (salen)Cr(III) catalyst/**1** ratios (1/10, 1/50/, 1/100, 1/200) of the homopolymers after post-polymerization functionalization; LiCl is added as an internal reference.

The yield of this post-polymerization functionalization step comprises between 38 to 40%. Aiming for shorter reaction times, the lithium equivalents per repetition unit are increased up to 20 eq. With higher activated species content inside of the solution, the reaction time can be decreased down to three days, yielding 40 to 45% of deprotected homopolymer (depending on the catalyst/monomer ratio) (full ^{1}H-NMRs of all deprotected polymers with different (salen)Cr(III) catalyst/**1** ratios see appendix).

To recheck the successful cleavage of the pyrrole group, Fourier-Transform-Infrared (FTIR) spectrometry is measured. Figure 53 depicts the spectrum of the homopolymer of **1** ((salen)Cr(III) catalyst/**1** ratio of 1/100) before post-polymerization functionalization and after (same catalyst/monomer ratio). It is clearly visible that the characteristic pyrrole bands at 1774, 1594, 1454, 1410, 1247, and 737 cm^{-1} disappear after accessing the free sulfonyl group.

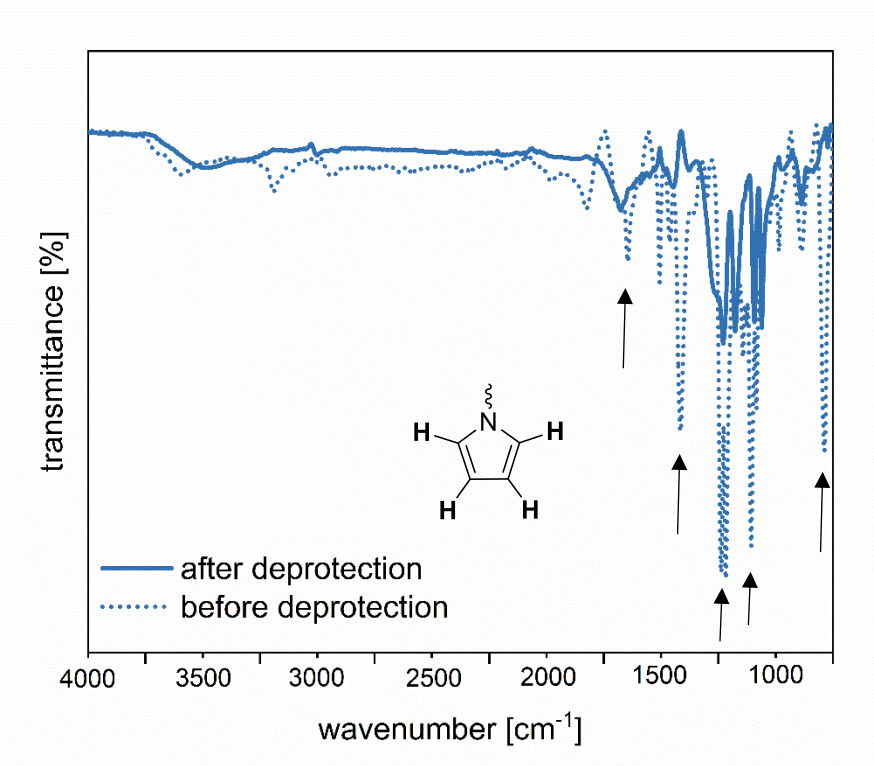

Figure 53: FTIR-spectra of the homopolymer of **1** ((salen)Cr(III) catalyst/**1** ratio of 1/100) before and after post-polymerization functionalization.

In summary, the post-polymerization functionalization with *in situ*-generated lithium methanolate can successfully cleave the pyrrole-protecting group to yield the target SICPE. The one-step synthesis step has the advantage that no salt metathesis is necessary. The increase in the yield can be discussed in future projects, as parameter variations concerning temperature, reaction time, or equivalent addition leave space for optimization. This homopolymer is the first example of a compound where a flexible PEO-backbone is functionalized with a SICPE functionality as a side group attachment. With one anionic charge carrier per repetition unit, a high density of lithium cations is generated inside of the polymer electrolyte. To monitor if the polyether backbone can intrinsically soften the material, the thermal properties of the herein-designed homopolymers are investigated in Chapter 5.2.6.

5.2.4 PSO chlorosulfonation

PSO is the polymerized version of SO, which can be easily synthesized from styrene by epoxidation with organic peracids.[297] Due to its increased steric requirement, the polymerization behavior of SO can significantly differ from EO or PO.[268] Nevertheless, organobases like *t*-BuP_4 have been established as promoting species for living type, anionic ROP of SO with high molecular weight outcome.[285] The synthesis protocol behind this organobase initiating process is easily accessible and simple in the means of executing. *t*-BuP_4 and a hydroxy group-containing initiator are added to a solution of SO in toluene. The reaction takes 20 hours before the addition of methanol terminates the active chain ends. Column chromatography can separate the polymer from the organobase and initiator residues. After evaporation of the solvent, high yields of 98% with maximal molecular weights of 21.9 kg mol^{-1} are reached.[285]

The characteristics of the PSO structure are a polyether backbone with one aromatic benzene ring per repetition unit bound to the PEO backbone. In contrast to the polyether backbone, its structural relative polystyrene (PS) exhibits aliphatic polymer chains that set a more rigid core structure. Styrene can be polymerized to yield PS via a multitude of possible radical initiation pathways.[298] Looking back at Figure 38, the aim behind the proposed post-polymerization functionalization of PSO can be cleared. Using **1** as the basis for the target SICPE, three main milestones have to be reached: monomer synthesis, anionic ROP, and post-polymerization functionalization by cleaving of the sulfonamide functionality. The access of the free sulfonyl group has to deal with polarity changes during the reaction and solubility issues, which are reflected in lower yields of around 40 to 45%. That's why, a faster and facilitated synthesis pathway would be desired, where the post-polymerization functionalization could be supported with a new and easy concept.

PSO and the target SICPE share a similar structure core, as both exhibit a polyether backbone that is bound to an aromatic ring. Therefore, the idea of functionalizing PSO by adding a functional group like chlorosulfonyl in a polymer analogous reaction comes up. The use of PSO as a starting material has several advantages:

1) SO is an available and cheap monomer
2) its ROP is well-known and -established, and the polymer can be produced in larger scales
3) there are already existing strategies concerning the chlorosulfonation of PS that could offer the potential to be transferable to PSO[299]

Scheme 17 shows what the reaction pathway towards the target SICPE could look like if PSO is used as the starting material.

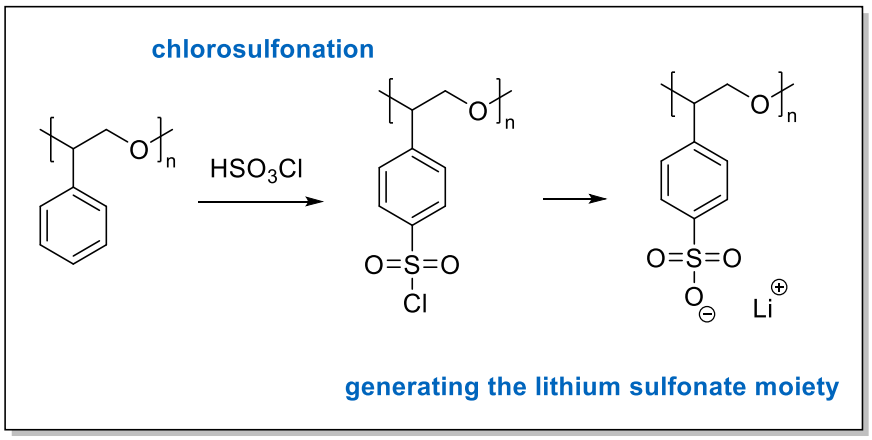

Scheme 17: Schematic representation of a potential post-polymerization functionalization of PSO involving two steps: chlorosulfonation and accessing the lithium sulfonate moiety.

This chapter aims to question the transfer efficiency of chlorosulfonation reaction protocols from PS to PSO. A starting set of reaction parameters is fixed to establish a standard for the following condition variations. A solution of HSO_3Cl (10 mL) in chloroform (30 mL) is added dropwise to a solution of PSO (100 mg) in chloroform (30 mL) at 0 °C. The reaction is heated up to 60 °C for 15 h and quenched by transferring the solution to ice. The solvent of the aqueous and the organic phase is removed, and both residues are characterized by ^{1}H-NMR spectroscopy. No proton signals are observed in the ^{1}H-NMR spectrum of the aqueous phase (spectra are taken in DMSO-d_6, MeOD-d_4, D_2O), indicating that the produced solid must possess inorganic characteristics (probably LiCl). The ^{1}H-NMR of the organic phase residue shows multiple unassignable signals (see Figure 54) that point toward the decomposition of the polymer during the reaction. A hint for the deconstruction of the polymer chains during the reaction could additionally be the color change from a white PSO starting material to a dark brown solid. An acid's presence could initialize the polyether backbone's protonation, supporting chain fragmentation and polymer decomposition. Decreasing the amount of H_2SO_4, increasing the solvent content to a more dilute solution, changing the solvent from chloroform to DCM/methanol mixtures, reducing the reaction time to shorten the contact of the polymer with the acid, or increasing the period of acid addition still depict the same results (overview of reaction conditions see table 7).

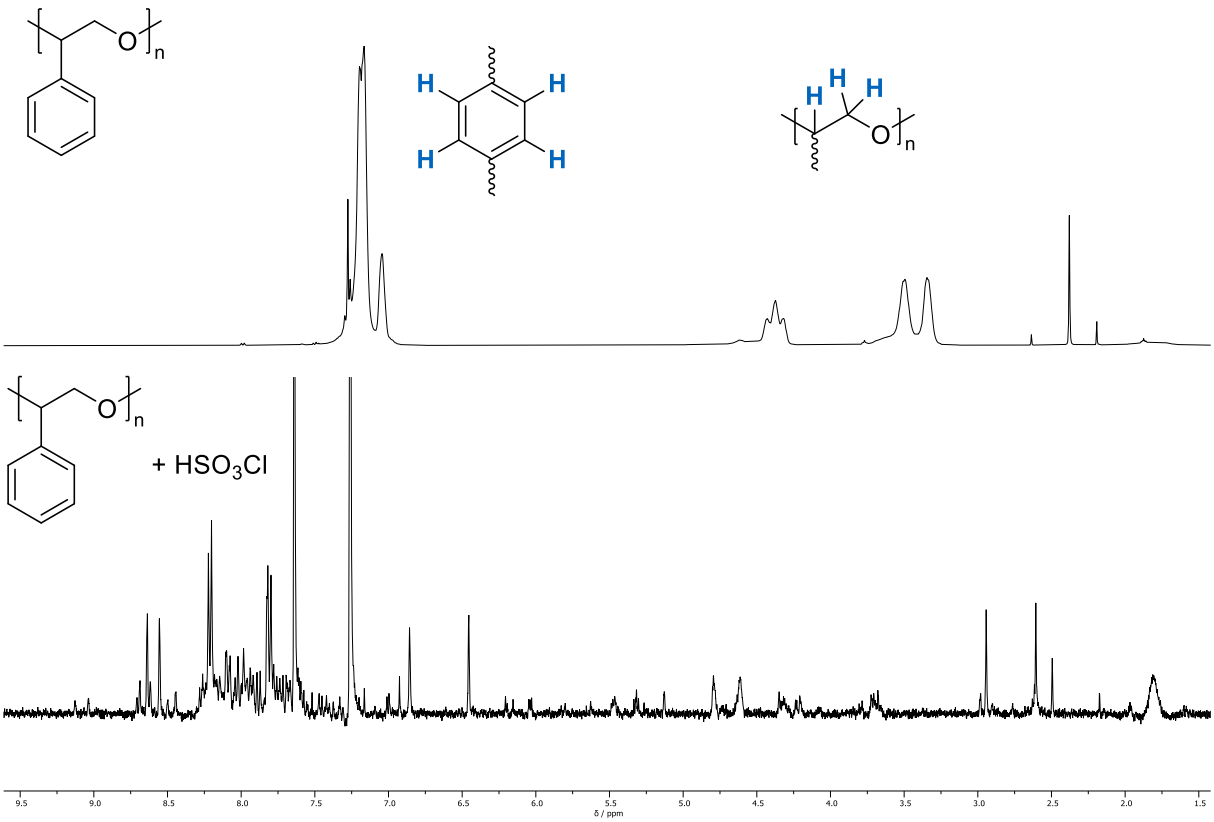

Figure 54: ^{1}H-NMR spectra of PSO before and after the treatment with chlorosulfonic acid; before post-polymerization functionalization, clean signals of PSO are observed; after the treatment with acid, the signals are split in various signals.

The stability of the polyether backbone seems to be the bottleneck of the post-polymerization functionalization of PSO. Comparing its resilience with PEO, literature can confirm the instability of the relative backbone in sulfuric acid. The acid is, for example, used in the preparation of mesoporous nanoparticles that are embedded in triblock copolymer templates consisting of PEO and polypropylene (PPO). Adding sulfuric acid to the nanocomposite, the copolymers are decomposed via ether cleavage, releasing the mesoporous framework.[300-301] Future approaches could focus on working in very diluted acidic solutions to ensure milder reaction conditions. Furthermore, introducing a stabilizing agent should be considered, which forms a weakly coordinating bond to the oxygen atom of the polyether backbone. The polyether backbone could probably be shielded to a certain extent from protonation.

Table 7: Parameter variation during the post-polymerization functionalization of PSO with sulfuric acid; the amount of added PSO and the reaction temperature of 60 °C are kept constant in all experiments; the starting conditions are marked in blue.

parameter variation	***HSO_3Cl [mL]***	***solvent***	***mL of solvent***	***t [h]***	***conversion of PSO [%]***
standard conditions	10	chloroform	60	15	–
HSO_3Cl eq.	**1-5**	chloroform	60	15	–
solvent eq	10	chloroform	**100-200**	15	–
solvent	10	**DCM, DCM/MeOH**	60	15	–
reaction time	10	chloroform	60	**1-8**	–

In summary, the idea of this simplified pathway to achieve the target SICPE is tempting. Experiments, that are carried out within the scope of this thesis, do not yield the desired substituted PSO, leaving room for improvement.

5.2.5 Structural elucidation of alternative monomer structures

Besides the polymer analogous modification of PSO, another concept is herein presented which aims to facilitate the achievement of the target SICPE. This concept involves the design of alternative monomers that facilitate post-polymerization functionalization or even prevent this process completely. Figure 55 gives an overview of the alternative monomer structures that are proposed and partially synthesized in the scope of this thesis.

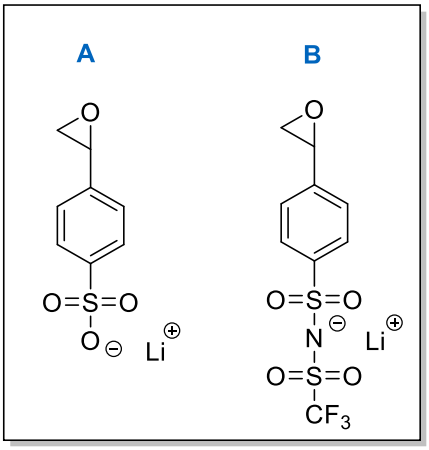

Figure 55: Proposed alternative monomer structures that present different anionic structure motifs in comparison to **1**.

The synthesis concept behind monomer A is based on the formation of sodium sulfonate substituted SO and the subsequent ion exchange of the sodium against a lithium cation (see scheme 18). The pathway to get to the sodium sulfonate substituted SO motif is already described in chapter 5.2.3. Even though the synthesis is possible, this precursor is not able to be polymerized in the presence of the (salen)Cr(III) catalyst. Therefore, the ion exchange of sodium against lithium is not promising, as the bottleneck with the free sulfonyl group and its coordination to the transition metal center will stay.

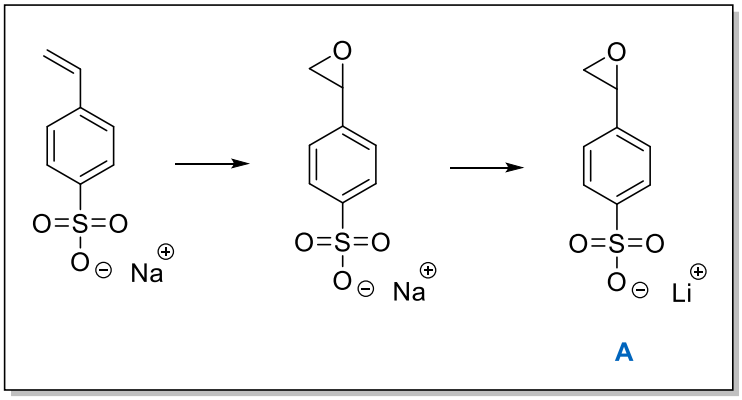

Scheme 18: Possible synthesis concept including all reaction steps towards forming monomer A.

The alternative monomer B exhibits a larger anionic structure motif compared to the free lithium sulfonyl group that is present in the target SICPE. Elongation of the anionic structure motif evokes a better delocalization of the anionic charge and enhances the lithium dissociation behavior.[302] In addition, the present CF_3-groups could probably shield the sulfonyl moieties from committing coordination with the (salen)Cr(III) catalyst. Scheme 19 proposes a possible reaction scheme towards B.

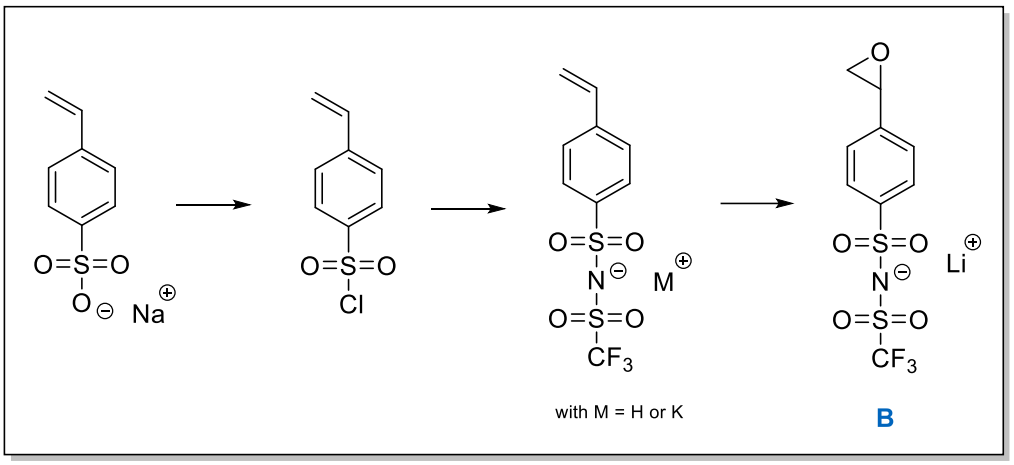

Scheme 19: Possible synthesis concept including all reaction steps towards the formation of monomer B.

The anionic motif of Monomer B resembles the structure of the TFSI anion, which is prominently applied as a lithium salt in the context of dual ion-conducting polymer electrolytes. To realize monomer B, the sodium sulfonate functionalized styrene has to be transferred into its respective chlorosulfonyl. This can be done by adding the sodium sulfonate into a solution of thionyl chloride at 0 °C. After stirring for three hours at room temperature, the reaction solution is stored in the fridge before pouring it into ice water. Extraction with toluene and subsequent purification (silica column chromatography, DCM 100%) yields the final product. As ^{1}H-NMR studies do not fully confirm the transfer into a chlorosulfonyl group (^{1}H-NMR of chlorosulfonyl substituted styrene see appendix), the molecular mass is verified via electrospray ionization mass spectrometry (ESI-MS) (m/z found 167.20 ($[M\text{-}Cl]^+$). The chlorosulfonyl reacts in a second step with DMAP, the base dipotassium hydrogen phosphate (K_2HPO_4), and trifluoromethanesulfonamide to the vinyl-terminated TFSI structure motif. The reaction is carried out in dry acetonitrile at room temperature for 72 h before the filtrate is sublimated, washed with DCM, and dried in a vacuum (^{1}H-NMR see appendix). Again, ESI-MS measurements are able to confirm the mass of the TFSI substituted styrene (m/z found 313.97 $[M\text{-}M^+]^-$). The last step of the monomer synthesis of B is the epoxidation of the vinylic double bond. Thereby, the same reaction conditions are used as in the epoxidation reaction of **1**. The oxygen transfer with *m*-CPBA in DCM is catalytically supported by adding the (salen)Mn(III) *Jacobsen* catalyst. After the quenching of the reaction solution with sodium

hydroxide, the solvent is evaporated, and a ^{1}H-NMR spectrum of the crude product is taken (see Figure 56). The characteristic epoxide multiplets between 4.30 and 3.50 ppm arise, indicating that the oxygen transfer shows promising results. Nevertheless, the aromatic proton signals of the benzene ring between 8.00 and 7.30 ppm, as well as the epoxide multiplets, tend to split up into multiple signals. Thin layer chromatography (TLC) analysis reveals the presence of more than one species that cannot be separated by common column chromatography based on rather similar polarities. Therefore, future purification approaches should focus on the general parameter optimization of the synthesis pathway, recrystallization, or, for instance, sublimation to separate the different species from each other.

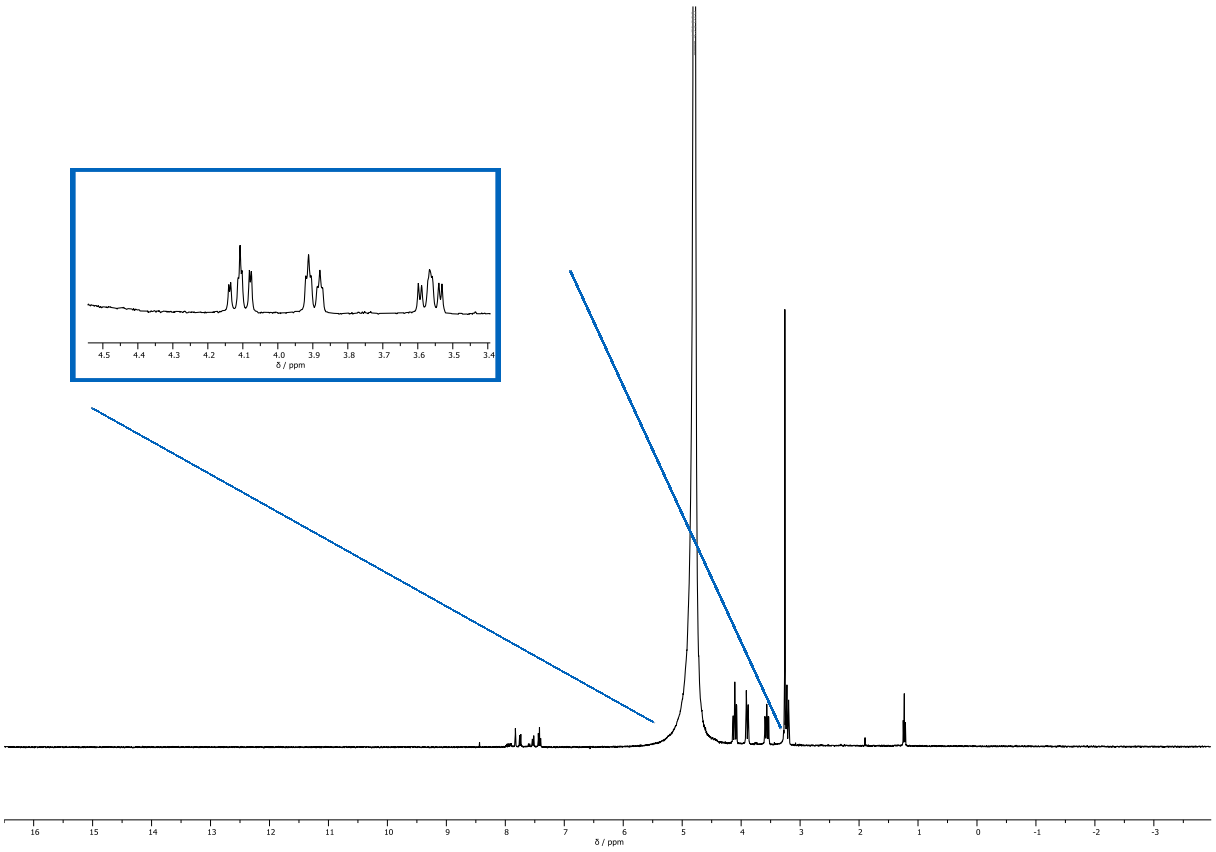

Figure 56: ^{1}H-NMR of the crude product of the epoxidation reaction of monomer B.

Even though the synthesis protocol is not yet fully optimized concerning the development of monomer B, it already shows promising pre-results. As this monomer would prevent necessary post-polymerization functionalization and exhibits additionally a refined anionic structure motif, it is worth being optimized and polymerized in prospective projects.

5.2.6 Thermal characterization

After carefully adjusting the conditions related to the polymerization of **1** and subsequent post-polymerization functionalization, the respective homopolymers are thermally characterized via thermogravimetric analysis (TGA)- and DSC- measurements. The thermal transitions within the polymer have a significant influence on the lithium migration behavior in the final SICPE. Amorphous domains within the polymer favor fast ion migration, whereas crystalline parts hinder the movement.[214] Consequently, the polymer chain mobility is always tried to be maximized at the lowest temperatures possible. Amorphous domains of polymers are mirrored via their T_g, which declares that when the polymer chains start to move slightly against each other. With rising temperatures, the mobilization of not only the amorphous polymer chains is enhanced. The crystalline domains start to melt, which can be detected via DSC measurements as T_m. The melting point clearly fixes a first-order transition with a sharp singlet signal in the optimal case, whereas the T_g shows the classical shape of a second-order transition.

The aim of the target SICPE is the combination of an improved ion movement with flexible polymer chain mobility. Thereby, the soft nature of PEO is applied in its function as a polymer backbone. The T_g of PEO depends on the molecular weight of the polymer but is arranged between −60 to −40 °C.[286] In the first step, the protected and deprotected homopolymers of **1** are tested in regard to their thermal stability. Within the TGA measurements, the samples with different (salen)Cr(III) catalyst/1 ratios are heated up to 700 or 1000 °C under synthetic air or an inert atmosphere with a heating rate of 10 K min^{-1}. For better differentiation between each catalyst-to-monomer ratio, the respective homopolymers are marked with different colors. In addition, the DTG is added to the spectra to highlight the exact onset point of decomposition. The TGA measurements of the protected homopolymers reveal that all compositions are stable up to at least 290 °C (see Figure 57). This means that their thermal resilience can be compared with commercially available PS (T_ds between 300-330 °C).[303] The first decomposition step between 290-310 °C shows 52% weight loss which can possibly be attributed to the cleavage of the sulfonamide from the aromatic ring. The second transition at elevated temperatures indicates a decomposition of the polyether backbone and aromatic ring. Compared to the herein-designed homopolymer, a PEO reference with a molecular weight of 5 kg mol^{-1} already decomposes at 98 °C. After deprotection, the respective T_ds stay located at a decomposition temperature of 300 °C (see Figure 58), indicating that the cleavage of the sulfonamide group does not influence the stability of the homopolymer. In the first decomposition step, the C-S bond is cleaved off to form a styryloxide and SO_3Li radical. Subsequently, the PSO degradation follows in the second decomposition step.

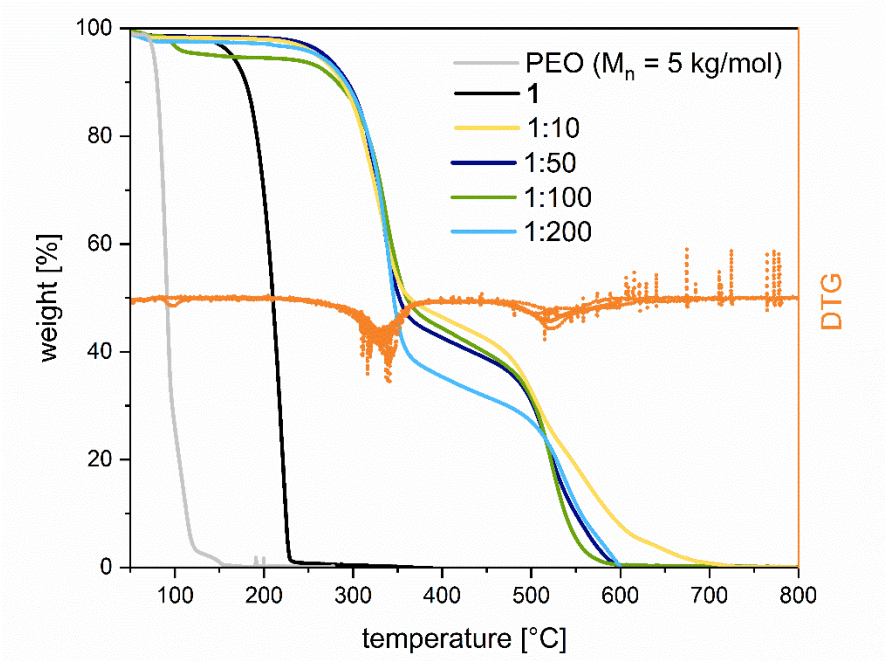

Figure 57: TGA measurements of the protected homopolymers of **1** for different (salen)Cr(III) catalyst/**1** ratios (1/10 (yellow line), 1/50 (dark blue line), 1/100 (green line), 1/200 (light blue line)) in comparison to PEO (Mn = 5 kg mol^{-1}; grey line) and **1** (black line); orange lines depict the DTG of the respective (salen)Cr(III) catalyst/**1** ratios. Every sample is heated up from 25 to 1000 °C with a heating rate of 10 K min^{-1} under synthetic air.

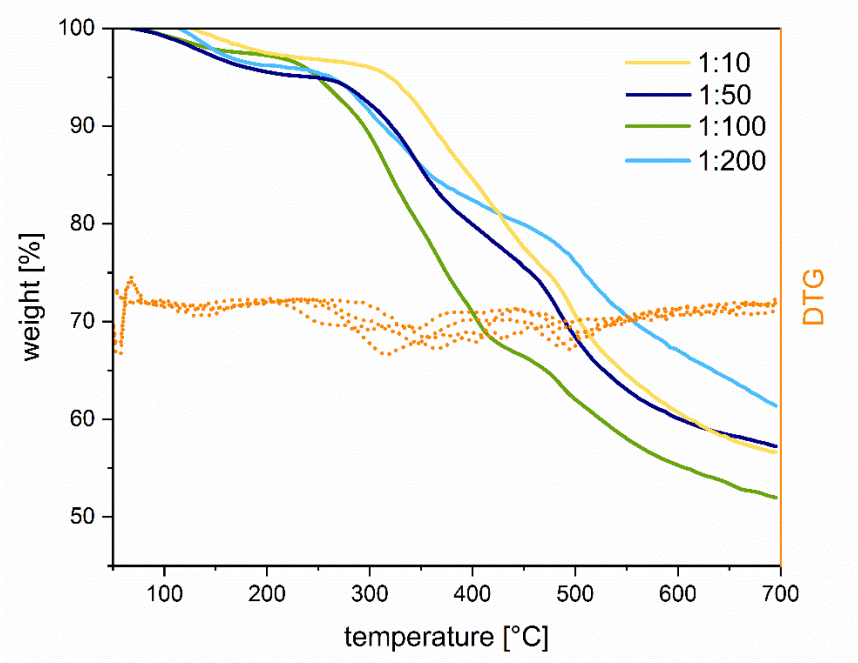

Figure 58: TGA measurements of deprotected homopolymers for different (salen)Cr(III) catalyst/**1** ratios (1/10 (yellow line), 1/50 (dark blue line), 1/100 (green line). 1/200 (light blue line)); orange lines depict the DTG of the respective (salen)Cr(III) catalyst/**1** ratios. Every sample is heated up from 50 to 700 °C with a heating rate of 10 K min^{-1} under argon.

The DSC measurements of the homopolymers of **1** (for the varied (salen)Cr(III) catalyst/**1** ratios) before and after post-polymerization functionalization are depicted in Figures 59 and 60.

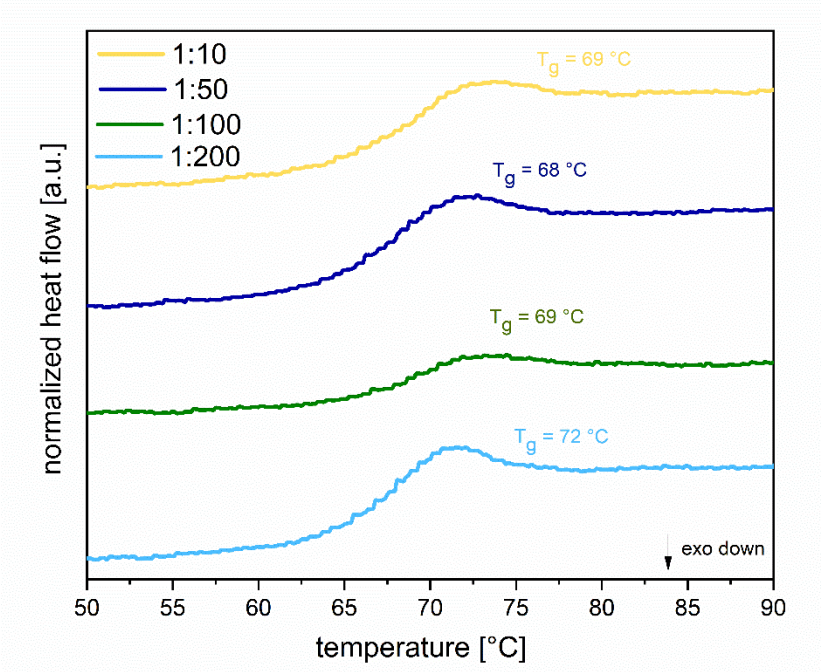

Figure 59: DSC measurements of the protected homopolymers of **1** for different different (salen)Cr(III) catalyst/**1** ratios (1/10 (yellow line), 1/50 (dark blue line), 1/100 (green line), 1/200 (light blue line)) depicting the second heating cycle in an interval of 50 to 90 °C at a heating rate of 10 K min^{-1} in a non-hermetic set up.

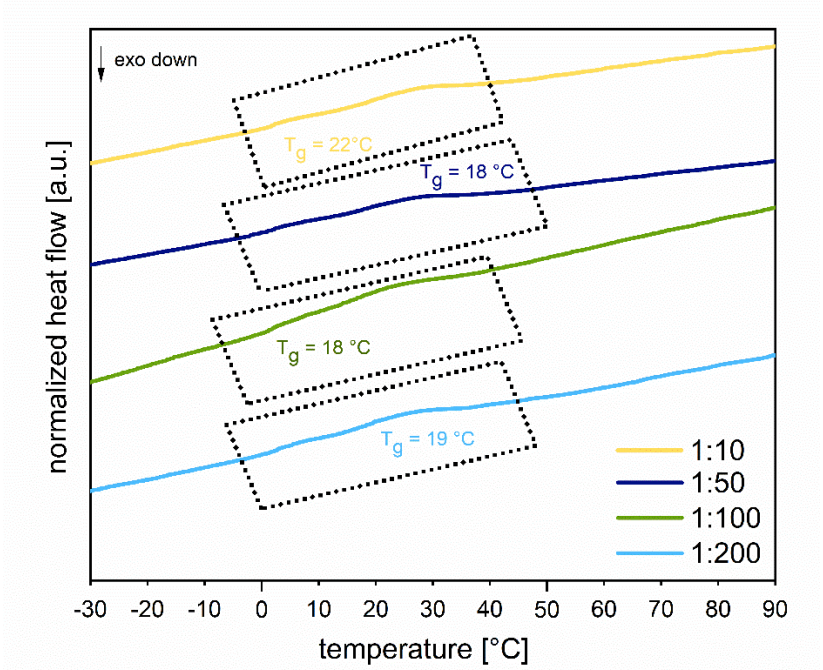

Figure 60: DSC measurements of deprotected homopolymer of **1** for different (salen)Cr(III) catalyst/**1** ratios (1/10 (yellow line), 1/50 (dark blue line), 1/100 (green line), 1/200 (light blue line)) depicting the second heating cycle in an interval of -30 to 90 °C at a heating rate of 10 K min^{-1} in a hermetic set up.

During the measurements, three cycles are measured, including a first heating, a single cooling, and a second heating cycle. The first heating cycle is neglectable due to the fact that air enclosures need to be removed and replaced by an inert gas to ensure the sole observation of the polymer properties themselves. Table 8 gives an overview of the observed thermal decomposition and transition temperatures of the protected and deprotected homopolymers of **1**.

Table 8: Overview of the T_ds and T_gs of the homopolymers of **1** before and after post-polymerization functionalization.

Catalyst/1 ratio	*Functional group*	T_d [°C]	T_g [°C]
1/10	sulfonamide	289	69
1/50	sulfonamide	302	68
1/100	sulfonamide	294	69
1/200	sulfonamide	310	72
1/10	lithium sulfonate	310	22
1/50	lithium sulfonate	287	18
1/100	lithium sulfonate	286	18
1/200	lithium sulfonate	281	19

Before post-polymerization functionalization with elemental lithium in methanol, the T_gs of the respective homopolymers are observed in the range between 68 to 72 °C, depending on the (salen)Cr(III) catalyst/**1** ratio. Due to very similar thermal transition temperatures, it can be implied that the length of the polymer chains is not decisive for the polymer chain mobility. After the cleavage of the sulfonamide group into a bound lithium sulfonate and a free pyrrole species, the T_gs shift down to 18 to 22 °C (depending on the (salen)Cr(III) catalyst/**1** ratio). The shift indicates, that the polymer chains get more flexible after the transfer towards the smaller sulfonate group. Probably, the cleavage induces a spatial rearrangement of the side groups along the backbone. The appearance of a charged functionality could lead to ionic repulsion between the sulfonate groups. As a consequence, the arrangement to a more favored side group alignment that enables an increased polymer chain flexibility could be initialized. To enable the classification of these values, PS is consulted as a reference system (focus is thereby set on the aliphatic backbone). The semi-crystalline character of PS with a T_g between 90-95 °C (depending on the molecular weight) and a T_m around 260-270 °C clearly reassures the flexible input that the PEO backbone offers in the herein-designed target SICPE.

All protected and deprotected homopolymers show the absence of a T_m over the whole temperature profile, which is scanned during the DSC measurements. This indicates that no crystalline domains are part of the homopolymeric framework. To confirm the fully amorphous character of the homopolymers, X-ray diffraction (XRD) diffractograms are investigated. Figure 61 exhibits the XRD measurements before and after post-polymerization modification. The diffractograms show only a broad background scattering signal and no sharp reflexes, as they would be expected if crystalline domains are present.

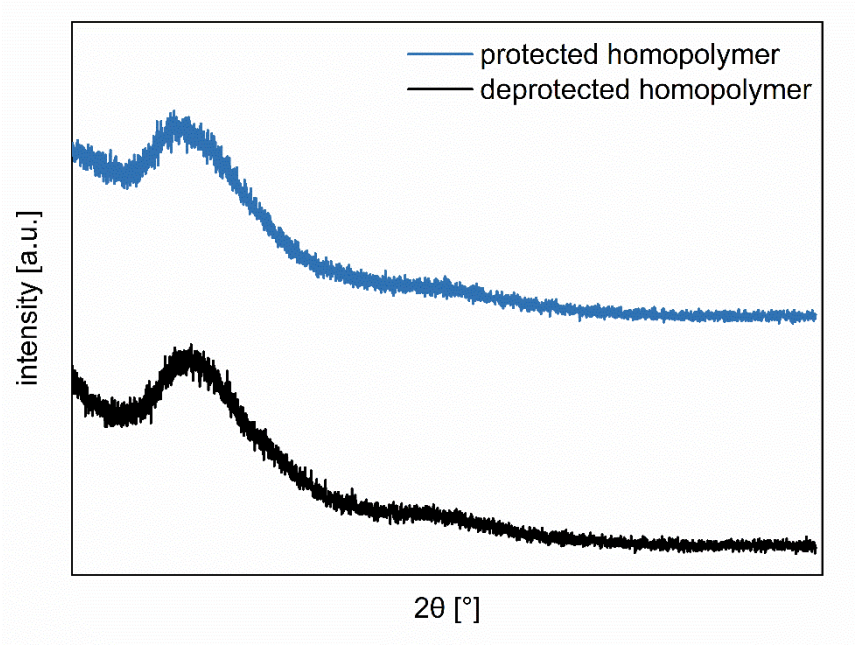

Figure 61: XRD-diffractograms of the homopolymers of **1** before and after post-polymerization functionalization; diffractograms are normalized to their maxima and referenced to the blank measurement of the background.

In summary, the high thermal stability of the target SICPE and its low T_g at room temperature promise an efficient, prospective usage in solid-state batteries. The herein-designed SICPE can resist internal temperature increases during cycling, keeps its mechanically stable core, and offers, in addition, the potential for a fast and facilitated ion movement. The performance as a solid polymer electrolyte will be discussed in the following Chapter 5.4.

5.3 Copolymerization of 1 with SO and PEG 2000

The previous chapter talked about the anionic ROP of **1**, which is catalytically supported by a (salen)Cr(III) catalyst. The resulting polymer is a homopolymer, meaning that every repetition unit bears the same anionic side groups. As a consequence, the thermal, mechanical, and, later on, electrochemical properties are holistically dictated by the initial monomer. Copolymerization is a well-known tool to smoothly finetune these properties by adding a certain amount of comonomers. The chemical composition of the comonomers can influence different intrinsic properties of the polymers. A common approach is the combination of monomers, that can establish mechanical integrity of the polymer electrolyte as well as an efficient ion transport through the solid state. The B-A-B-type P(STFSILi)-*b*-PEO-*b*-P(STFSILi) copolymer (see Figure 34), developed by *Bouchet et al.*, is a prominent example of this fusion. The "hard" P(STFSILi) block of the copolymer could be seen as the aliphatic analog to the herein-designed and synthesized SICPE. Instead of a substituted SO, the monomer unit of P(STFSILi) consists of a styrene motif that is functionalized with a large TFSI anion. The huge anionic unit facilitates the delocalization of the anionic charge and, therefore, a better lithium dissociation.[218] Looking at the thermal transition of pure P(STFSILi) in its homopolymeric form, the T_g is stated around 152 °C.[251] That means that the polymer chain mobility is restricted at ambient temperatures, forcing the battery to be used at elevated temperatures. Therefore, PEO units are added as "soft" A-block, to enable a flexible polymer chain movement already at lower temperatures. Furthermore, an additional cation transport opportunity besides the SICPE anchoring groups is unlocked by coordinating the lithium cation to the polyether backbone.[213]

In this chapter, two different A-B-type copolymer geometries are presented. Thereby, it should be monitored, how the incorporation of a second monomer can influence the thermal and prospective electrochemical properties of the respective copolymers. The screening of the comonomers is adjusted to the polymerization requirements and discussed in the context of anionic ROP. Generally, the addition of the comonomers is aiming to fulfill two major principles:

1) Charge carrier separation
2) Softening of the solid polymer electrolyte by integrating a populated amount of PEG units.

5.3.1 Comonomer screening and alignment of polymerization requirements

The terminal epoxide of **1** enables the catalytically supported anionic ROP towards a polyether backbone. To keep the polymerization procedure simple, the comonomers should also be epoxide terminated so that the (salen)Cr(III) catalyst is able to ring-open both monomers. Besides this requirement, the function of the comonomers, which they execute inside of the copolymers, must be discussed. The target SICPE exhibits a high charge density, as every repetition unit bears one anionic charge. Sometimes, this high anionic charge density can be seen as a reason for lower lithium migration behavior in SICPEs. If an increased amount of anchoring points is in close proximity, the lithium cations tend to strongly coordinate with the anions. Consequently, the migration behavior is worsened. To break up this setup while preserving the mechanical integrity SO is used as a comonomer (see Figure 62). The integrated, uncharged moieties of SO should function as charge separators between the lithium sulfonates to equalize the charge density in the polymer.

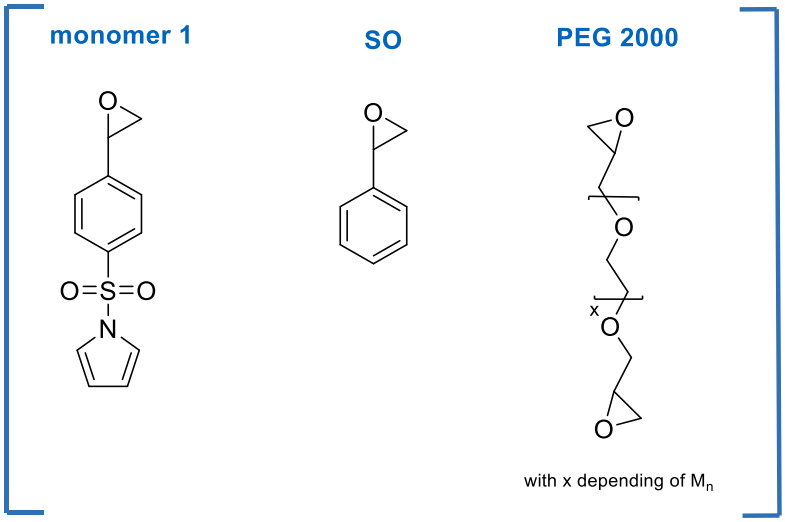

Figure 62: Comparison of structure **1** with the comonomers SO and PEG 2000, which are used as comonomers in the copolymerization formation.

The other comonomer that is used in the copolymerization synthesis is epoxy end-terminated PEG, which has a molecular weight of 2000 g mol^{-1}. The respective comonomer is abbreviated in this thesis as PEG 2000. This approach is principally aiming a softening of the solid polymer electrolyte. The PEG-formulated comonomer presents two main advantages: the terminal epoxides can be ring-opened towards a polyether backbone as is also seen when SO is used as a comonomer. The difference between the comonomers, however, lies in the setup of the functional group that is attached to the epoxide unit. SO is carrying an aromatic benzene ring that can experience π-π-ring stacking with the neighboring rings. This stacking could evoke a push of the polymer into a rigid conformation, that prevents a fast

ion transport. Using the PEG 2000 comonomer, the risk of this stacking is not given. In contrast, the PEG-modified side chain offers an additional flexibility input, as the short chains support the formation of amorphous domains. The ions have, in consequence, three possible anchoring groups that they can use for hopping: the anionic charges of the SICPE, the polyether backbones, and the PEG side groups of the comonomer.

Both comonomers fulfill the criteria for anionic ring-opening polymerization. In the following, the polymerization processes are discussed in detail. The resulting polymers are thermally analyzed and compared to the homopolymer of **1**.

5.3.2 ROP with (salen)Cr(III) catalyst

Figure 63 presents an overview of the copolymer structures that are received when **1** is copolymerized with SO and PEG 2000, respectively. The copolymer that integrates SO as a comonomer is abbreviated as copolymer **2**, while the copolymer based on the comonomer PEG 2000 is abbreviated as **3**. The polymerization process parameters do not differ from the ones applied in homopolymerization. The ROP is set up under bulk conditions, adding the (salen)Cr(III) catalyst to a dry mixture of **1** and the comonomer in a ratio of 1/100/100. After heating the solid mixture up to 115 °C for 3 days, the polymers are precipitated and dried under vacuum (^{1}H- spectra before post-polymerization modification see appendix). The post-polymerization functionalization is also based on the *in situ* generation of lithium methanolate, which cleaves of the pyrrole group (^{1}H- and ^{7}Li-NMR spectra of **2** and **3** after post-polymerization functionalization see appendix). The equivalent addition of elemental lithium is thereby oriented to the equivalent amount of **1**, which is incorporated in the final copolymer. Steric hindrance, as well as solubility issues in the molten monomer, can have a huge impact on the kinetic of ROP and the consumption of the respective monomers. To determine the final ratio of **1**/comonomer, the integrals of the ^{1}H-NMR proton signals are set into relation to each other (determination of **1**/comonomer ratio in final copolymer see appendix). As **1** and SO belong to the same structure family, their ring-opening is expected to be catalyzed with similar reaction kinetics. This theory is confirmed by means of the ^{1}H-NMR, showing also a 1:1 ratio of **1**:SO in the final copolymer **2**. Copolymer **3** compares a ratio of 1:12 (**1**:PEG 2000), which is clearly deviating from the initial one. This can be interpreted with a faster ROP of the comonomer, as it is less sterically hindered. To get a more detailed view of the polymerization process, future work should focus on the holistic elucidation of the copolymerization parameters of the applied monomers in the presence of the (salen)Cr(III) catalyst.

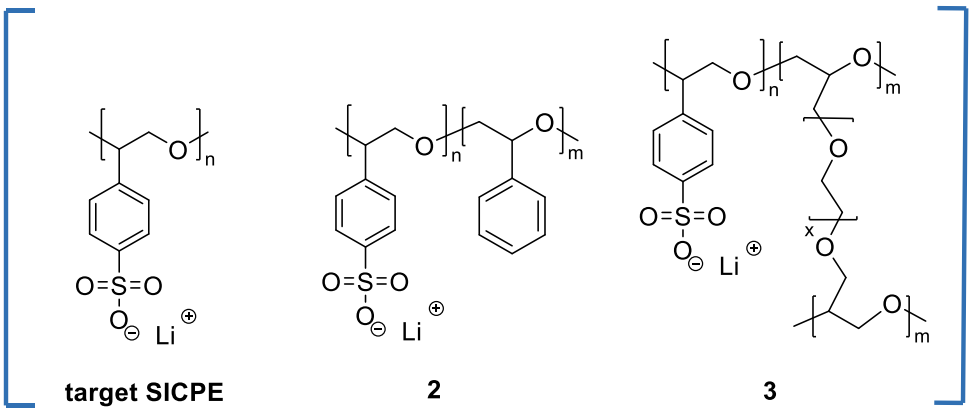

Figure 63: Structural overview of the target SICPE and the resulting copolymers that are received via copolymerization with SO and PEG 2000.

After post-polymerization functionalization, FTIR spectroscopy of the homopolymers and the respective copolymers are measured (see Figure 64). Homopolymer **1** and copolymer **2** show, based on their structural relatedness, similar vibration modes throughout the whole spectrum. At lower wavenumbers, the signals can be attributed to the aromatic fingerprint area of **1** and SO. Between 3200-3600 cm^{-1}, the broad vibration mode can be ascribed to water molecules that are absorbed based on the presence of hygroscopic sulfonate moieties. That's why this mode is only present for **1**, **2**, and **3** and not for pure PSO and polymerized PEG 2000. The additional vibrational modes of copolymer **3** differ from those of **1**, **2**, and pure PSO and, at the same time, resemble the modes of pure PEG 2000. With the excess PEG 2000 in the copolymer, this resemblance is expected.

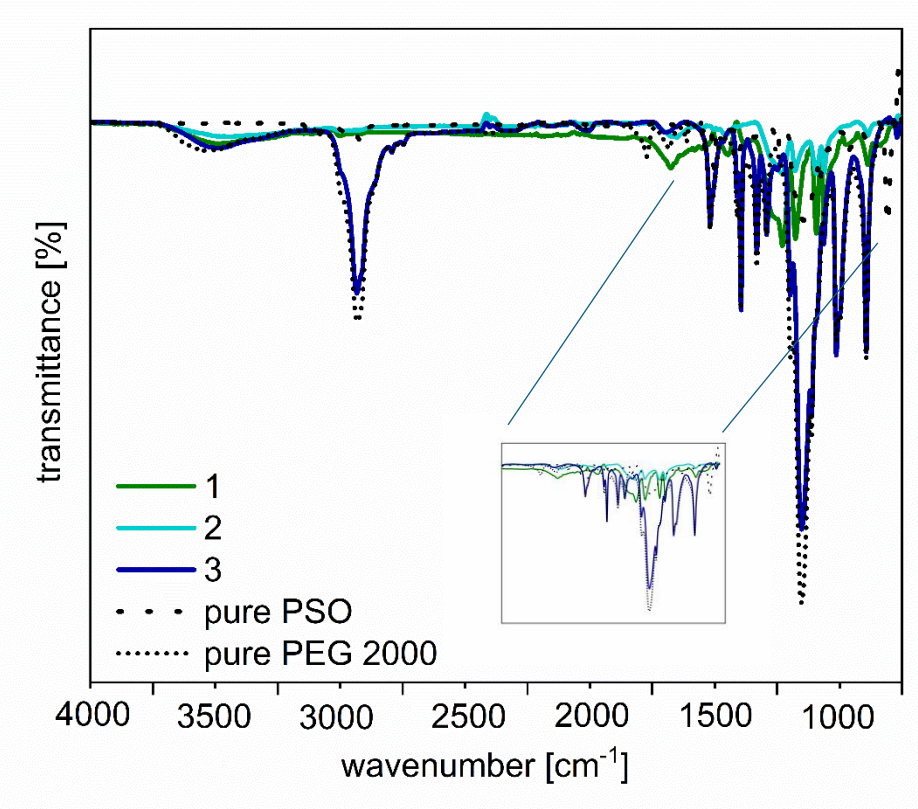

Figure 64: FTIR-spectra of target SICPE (green line) as well as the copolymers **2** (light blue line) and **3** (dark blue line) measured under ambient conditions in a range of 500-4000 cm^{-1}; as a reference, the vibrational modes of pure PSO and PEO 2000 are incorporated.

GPC analysis reveals the molecular weights of the polymers as well as the distribution of the polymer chains within the homopolymer **1** as well as the copolymers **2** and **3** (see Table 9). To create a reference, the data points of pure PSO and homopolymerized PEG 2000 are added to the analysis (all GPC traces see appendix).

Table 9: GPC-analysis of homopolymer of **1** ((salen)Cr(III)catalyst/**1** ratio of 1/100) in comparison to the copolymers **2** and **3** ((salen)Cr(III) catalyst/**1**/comonomer ratio of 1/100/100); homopolymerized PSO and PEG 2000 are added as a reference.

polymer	X^a *[%]*	$M_{n,abs}{}^b$ *[kg mol^{-1}]*	$Đ^b$ *[-]*
target SICPE	96	61.2 ± 0.04	1.2 ± 0.01
2	46	96.6 ± 0.03	1.2 ± 0.01
3	41	41.6 ± 0.03	1.6 ± 0.01
PSO	78	83.7 ± 0.05	1.2 ± 0.01
PEG 2000	64	45.2± 0.03	1.5 ± 0.01

[a] Yield of polymer. [b] Absolute molecular weight determination and dispersity of the homopolymer in DMF (30 °C, with 25 mmol L^{-1} LiBr, triple detection, d*n/dc* = 0.152 mL g^{-1} (target SICPE), 0.155 mL g^{-1} (**2**), 0.037 mL g^{-1} (**3**), 0.149 mL g^{-1} (PSO), 0.015 mL g^{-1} (PEG 2000)).

Copolymer **2** reaches the highest molecular weights of all presented polymers with a M_n of 96.6 kg mol^{-1}, while copolymer **3** represents the shortest polymer chains with a M_n of 41.6 kg mol^{-1}. By comparing these results to the homopolymerized versions of the comonomers, it is striking that their molecular weights lay in similar ranges. SO and PEG 2000 are ring-opened with the (salen)Cr(III) catalyst. The resulting PSO shows longer polymer chains than the approach when SO is polymerized with the *t*-BuP_4 organobase (83.7 kg mol^{-1} vs. 21.8 kg mol^{-1}).[285] This can be reasoned with the low initiator efficiencies of the (salen)Cr(III)catalyst itself, which produces less active chain ends where the monomer units can coordinate. PEG 2000 exhibits a M_n of 45.2 kg mol^{-1} when polymerized with the chromium catalyst. Copolymer **2** only slightly differs in molecular weight from PSO (96.6 kg mol^{-1} vs. 83.7 kg mol^{-1}), and the polymer chain lengths of copolymer **3** are observed in the same range as PEG 2000 (41.6 kg mol^{-1} vs. 45.2 kg mol^{-1}). The molecular weights of both copolymers are closer to their homopolymerized versions than to the homopolymer of **1** (M_n = 61.2 kg mol^{-1}), whereas **3** drastically differs from the molecular weights of the target SICPE and copolymer **2**. Therefore, it can be confirmed that the comonomers are preferably incorporated into the copolymer framework before the ring-opening of **1** starts. It can already be seen in the ROP of EO and its derivatives that sterically more demanding epoxides like SO show different behavior in polymerization approaches and are often more difficult to convert into the respective polyether backbone.[268] Transferring this knowledge to **1**, the sulfonamide group of **1** probably induces an additional steric demand that could lead to a delayed polymerization behavior. As **1** and SO belong to the same structural family, the polymerization behavior and the incorporation of the monomers into the copolymer stay rather comparable. Consequently, the

molecular weight of **2** rises over the molecular weight of the homopolymer of **1**. In contrast, **3** shows an excess of PEG 2000 present in the copolymer (1:12 ratio of **1**/PEG 2000), which explains the orientation of molecular weight along the results of the homopolymerized version of PEG 2000.

To confirm that 1 is chemically linked to the respective comonomers, diffusion-ordered (DOSY)-NMR spectra can be taken. The presence of one diffusion coefficient confirms the synthesis of a copolymer. If several diffusion coefficients occur, it must be assumed that more than one polymer species is present. This can often be a hint for blend formation, where two or more separated homopolymers are formed and merged together in one solid mixture. Figure 65 shows the DOSY-NMR spectra for the target SICPE and the copolymers **2** and **3**.

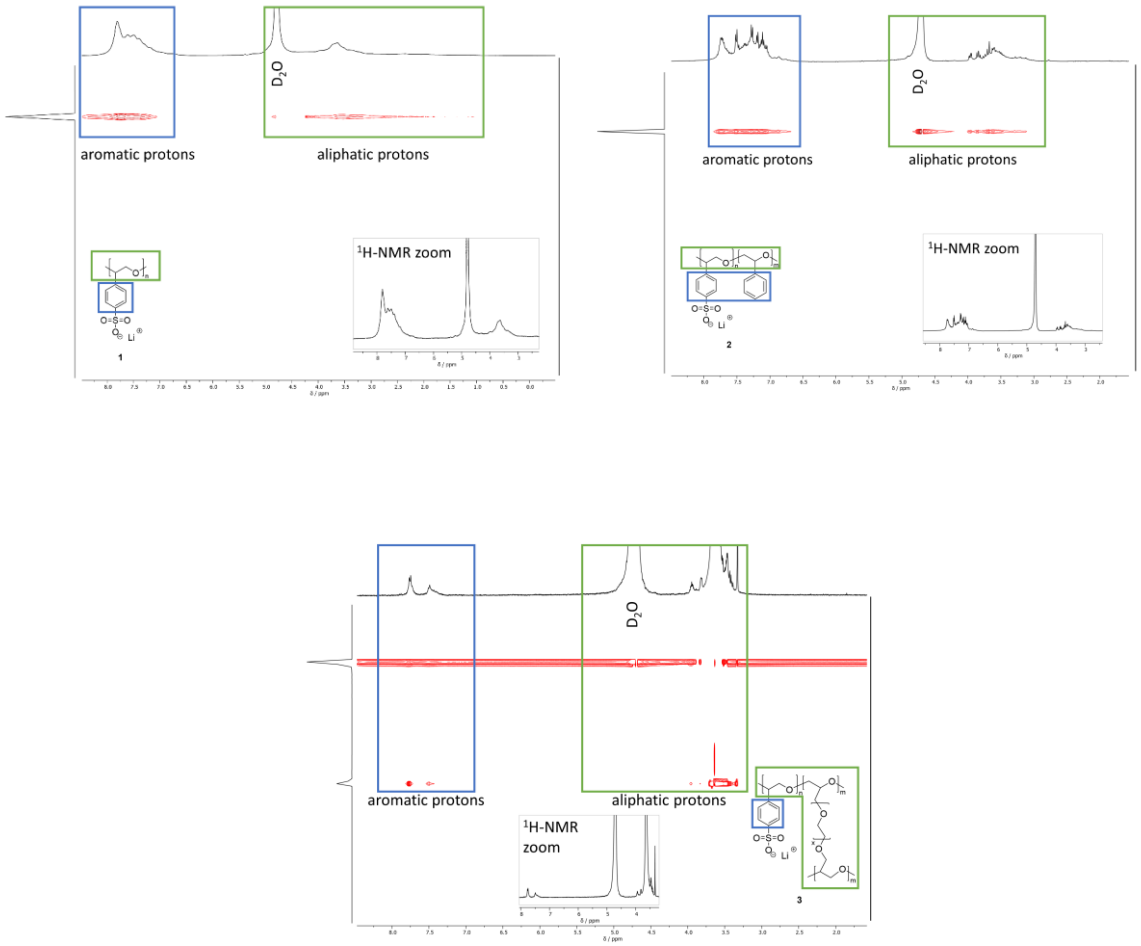

Figure 65: DOSY-NMR spectra of the target SICPE and the copolymers **2** and **3**; the aromatic protons are marked in blue, the aliphatic protons are marked in green.

Like it was expected, homopolymer **1** clearly shows only one diffusion coefficient, meaning that only one type of polymer is present in the investigated sample. This demonstrates that the chains of **1** grow

consistently without evoking any side reactions. Based on the similar main core of **1** and SO, in the ^{1}H-NMR spectrum of copolymer **2,** additional peaks in the similar range of the aromatic and aliphatic regions occur. As the DOSY-NMR also indicates only one diffusion coefficient for **2**, it can be concluded that copolymerization was successful. The absence of several diffusion coefficients reveals that monomer **1** as well as SO are attached to the same elongating polymer chains and are not polymerized separately to build up a blend type polymer. In comparison to that, copolymer **3** has two diffusion coefficients, meaning that two different types of polymers are formed. A closer look into the assignment of the diffusion coefficients to the proton signals shows that the lower diffusion coefficient correlates with the signals of **1** and PEG 2000. Therefore, the formation of copolymer **3** out of the two monomers can be assumed. The upper diffusion coefficient also correlates with **1** and the comonomer signals. That's why, probably an additional copolymer formation with a deviating composition arises, explaining the plurality of diffusion coefficients in the DOSY-NMR. Referring to the structure of PEG 2000, the bifunctionality of the comonomer leaves the opportunity to create a variety of possible copolymer designs. Different crosslinked copolymer structures are possible as both sides of the comonomer can be ring-opened towards a polyether backbone. In theory, the crosslinking process should lead to a denser and more ordered polymer network. As ordering inside of a polymer matrix often induces aggregated and less amorphous domains, the network character should be able to be confirmed in the thermal transitions of **3**.

5.3.3 Thermal characterization

The thermal properties of the target SICPE and the copolymers **2** and **3** are tested via TGA- (see Figure 66) and DSC measurements (see Figure 67). All samples show similar decomposition patterns, stable up to 290 or 330 °C. The copolymers' decomposition patterns are comparable to their homopolymerized versions' thermal stability. The target SICPE and copolymer **2** depict their first decomposition steps between 290 to 310 °C, which can potentially be attributed to the cleavage of SO_3Li radicals. As in copolymer **2,** the amount of sulfonated PSO per repetition unit is decreased due to the incorporation of unsubstituted SO as a comonomer; the weight loss of **2** within this first T_d is smaller than it is seen for **1** (52% vs. 61%). The subsequent thermal degradation at temperatures above 310 °C can be attributed to the decomposition of the remaining PSO main core. The TGA pattern of copolymer **3** shows a similar degradation pattern as pure PEG 2000 with only one T_d between 330 to 360 °C and a respective weight loss of 89%. Similar degradation in one step is also seen for related aliphatic A-B-type copolymers that also bear PEG moieties as side chains in the form of a comb-like structure.[254]

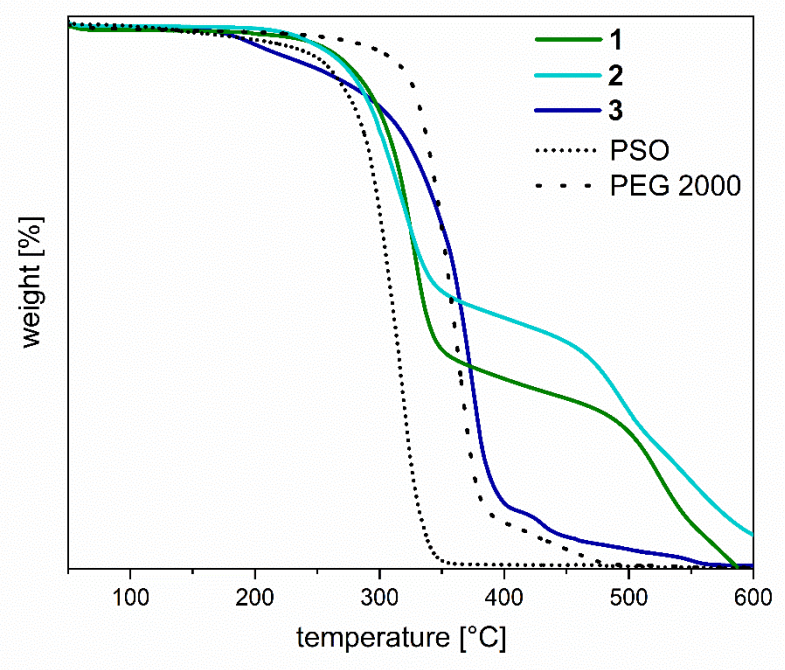

Figure 66: TGA measurements of target SICPE (green line) and copolymer **2** (light blue line) and **3** (dark blue line); for comparison reasons, the TGA curves of pure PSO (black line, small dotted) and pure PEG 2000 (black line, wide dotted) are added; every sample is heated up from 50 to 600 °C with a heating rate of 10 K min^{-1} under argon.

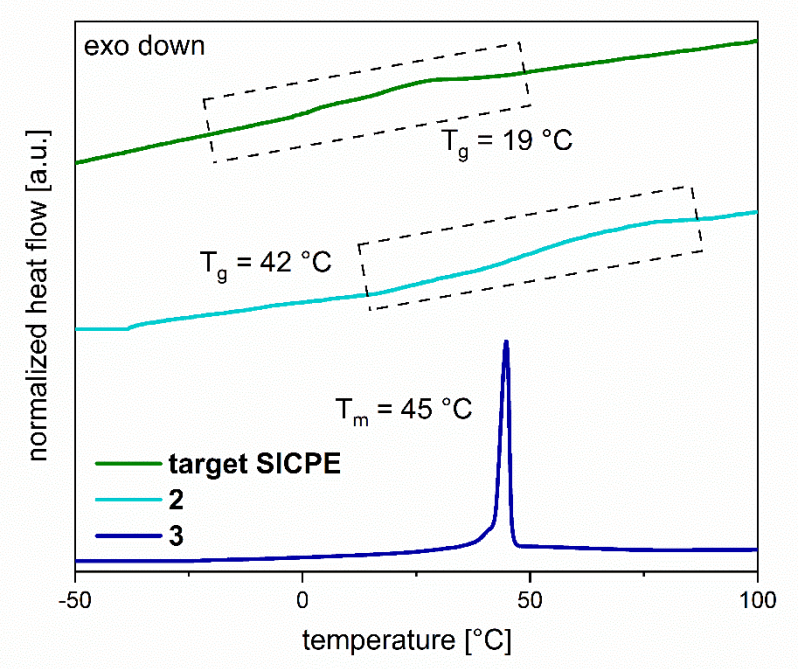

Figure 67: DSC measurements of target SICPE (green line) and copolymer **2** (light blue line) and **3** (dark blue line), depicting the second heating cycle in an interval of –50 to 100 °C at a heating rate of 10 K min^{-1} in a hermetic setup.

Within the DSC measurements, the target SICPE and **2** display the absence of a T_m in the whole temperature profile ranging from –100 to 200 °C, concluding that both polymers are fully amorphous. The T_g of the target SICPE is observed at 19 °C, and in the case of **2**, 42 °C matches the T_g of pure PSO (DSC measurement of pure PSO see appendix). The difference in thermal transition temperature can probably be explained by discussing the electronic interactions of the aromatic benzene rings present in the target SICPE and **2**. As discussed in previous chapters, conjugated aromatic ring structures develop so-called π-π-stacking when the rings are in close proximity to each other. This stacking often leads to a higher crystallinity, shifting the T_gs to increased values. Both the target SICPE and **2** show SO motifs in their polymer chains, but as the target SICPE does not exhibit SO units as charge separators, also ionic repulsion of the sulfonates must be considered. The anionic charges could influence the polymer chain growth in a way that monomers are arranged with the most spatial distance between the charges and subsequently also the benzene rings, supporting to a certain extent the suppression of π-π-interactions and directing the polymer with a lower tacticity to the larger amorphous character. Copolymer **3** depicts a sharp and intense T_m at 45 °C and no visible T_g in the whole temperature profile, meaning that the polymer shows increased crystallinity. This can probably be traced back to a possible spatial alignment of the PEG side groups that are incorporated as side chains in the comonomer. As pure PEG 2000 (DSC measurement see appendix) exhibits a T_m at 43 °C, it is assumable, that the comonomer is preferable incorporated. The formation of a more rigid polymer supports the thesis of a crosslinking mechanism which is also seen in the DOSY-NMR. If both epoxide functionalities of the PEG 2000 are ring-

opened, the formation of a crosslinked network would lead to densification and rigidification, thus showing consequently reduced chain mobility, less flexibility, and the appearance of crystalline domains with characteristic T_ms. The restricted solubility of **3** compared to the target SICPE and **2** is another hint for the buildup of a network structure.

In summary, the catalytically supported anionic ROP of **1** with SO and PEG 2000 is possible, yielding two different copolymer geometries. The target SICPE and copolymer **2** show similar thermal behavior, as their main structure cores are relatable. In contrast, copolymer **3** deviates from the target SICPE with respect to the molecular weights and the linkage between the monomer units. To check, how the polymer setup influences the lithium migration behavior within the solid electrolyte, EIS measurements are performed and discussed in the following chapters.

5.4 Elucidating the electrochemical potential behind the homo-and copolymers

After focusing on the thermal characterization of the homo- and copolymers of **1** in the previous chapters, the following part of this work highlights the so far investigated electrochemical performance of the herein-designed polymer electrolytes. As Figure 63 shows, three SICPEs are chosen to be examined in the EIS measurements: the target SICPE and the copolymers **2** and **3**. As the three polymer electrolytes present strongly deviating structural frameworks and thermal transitions, an influence of these intrinsic polymer properties on the lithium migration inside of the electrolyte is expected. To be able to measure the electrochemical properties, the polymers have to be transformed into polymer films and transferred to a coin cell setup. The following two subchapters will discuss polymer film-making techniques, the cells' assembly, and the electrochemical properties' examination. It must be noted that the work on the electrochemical properties of the target SICPE **2** and **3** is still ongoing and not yet finished. That's why this chapter presents primary results and trends that can be observed based on the first experiments carried out in collaboration with the chair of Prof. Hubert Gasteiger.

5.4.1 Polymer film making and coin cell assembly

After being synthesized and dried under vacuum conditions, the target SICPE and the two copolymers **2** and **3** are present in powder form. To transfer the powder to polymer films, the polymers need to be dissolved and subsequently processed. Due to the high polarity of the polymers, a polar solvent is the requirement for homogenous dissolving. Concerning processing, there exist different methods of shaping the films. In the scope of this work, drop casting is the method of choice for polymer film production. In the first attempts, 100 mg of the respective polymer are dissolved in 0.5 ml of water and stirred for one day at 70 °C. The polymer solution is drop cast onto the bottom compartment of a coin cell and put into the oven at 70 °C for three days. It can be observed that the polymer film already starts to be generated with a homogenous surface. Thereafter, the setup is put into vacuum at 55 °C for four days to remove trapped and residual water. The dried polymer films are transferred to a glovebox, where the coin cell is fully assembled by putting a spacer, a spring, and the top compartment of the coin cell onto the bottom compartment. The cell capping marks the end of the polymer film-making process (see Figure 68).

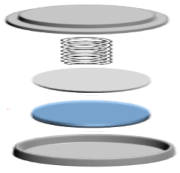

Figure 68: Basic coin cell setup for EIS-measurements when integrating a polymer film as solid electrolyte.

First EIS screening experiments with the target SICPE ((salen)Cr(III) catalyst/**1** ratio of 1/100) show a classical and expectable response for a polymer acting as solid electrolyte. In the Nyquist plot, a nicely shaped semi-circle is observed, that represents an ionic bulk conductivity of around 10^{-5} S cm^{-1} (calculations are based on the post-determined thicknesses of the polymer film). Performing the EIS measurements at varying temperatures, the activation energies for the lithium ion hopping can be extracted with an E_A of 0.69 eV (see Figure 69).

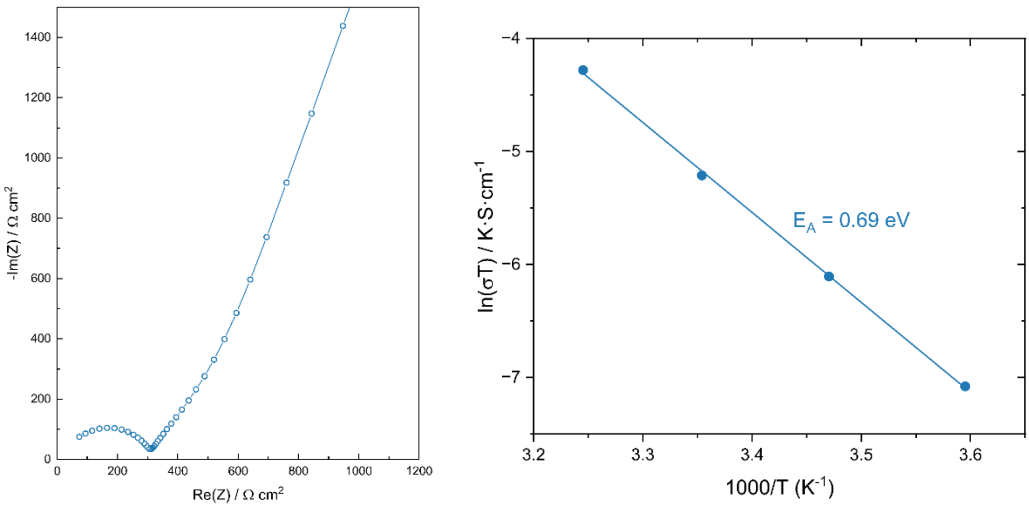

Figure 69: Nyquist plot and determination of E_A based on the EIS measurements of the target SICPE ((salen)Cr(III)catalyst/**1** ratio of 1/100); polymer films are processed in water via drop casting.

The polymer filmmaking is revised to ensure that the charge carriers are lithium cations and not protons present in the polymer electrolyte due to trapped water. Water as solvent is exchanged against dry DMSO and an additional drying step at room temperature under vacuum for two weeks is added to the polymer film processing protocol. Strikingly, these dried films do not show ionic conductivity and also do not at higher temperatures. To get a comparison, the polymer films produced in water are consequently also prepared with longer drying steps and measured again. Likewise, no bulk resistances can be observed. This lack of ion mobility leads to the conclusion that internal processes must hinder the cation movement in the dried films. Looking at the sulfonate moiety of the target SICPE, the coordination of the lithium cation to the sulfonate can be rated as rather strong, as the anionic charge delocalization is lower than in larger anions like TFSI. Therefore, the hypothesis arises that the lithium cation can only hardly dissociate from the anionic anchoring point to hop from one coordination site to the next. To proof this thesis, the target SICPE is turned into a gel polymer electrolyte, using DMSO as solvent. The dried films are transferred into the glovebox, where the coin cell assembly takes place. Before capping the cell, 10 wt% of dry DMSO is added to the dry films. The cells are capped, and EIS is measured again.

5.4.2 Examination of relation between polymer structure and electrochemical properties

The addition of 10 wt% of dry DMSO after the polymer film-making can be seen as a classical swelling experiment that is examined in gel polymer electrolytes. Figure 70 illustrates how the ion movement could potentially be influenced by the presence of DMSO. The solvent molecules could loosen the cation-sulfonate interplay by building up a solvation shell around the cation. This shell could help support the ion hopping from one coordination site to the next, transporting the lithium cations more easily through the polymer electrolyte.

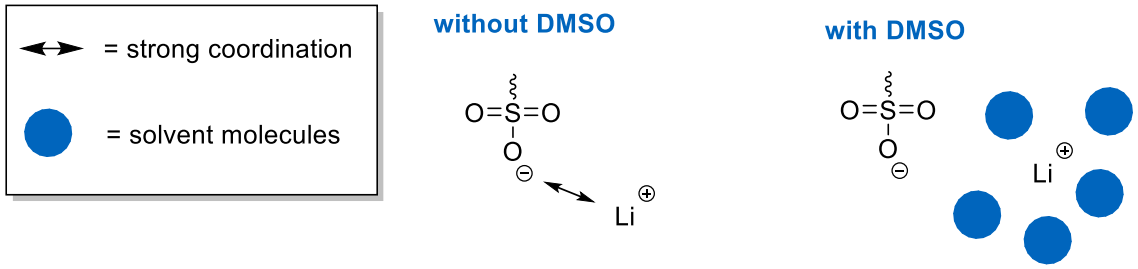

Figure 70: Illustration of the potential mode of operation that DMSO executes in its function as a polymer electrolyte swelling agent.

After measuring the EIS of the swelled target SICPE films, the characteristic semi-circle is once again observed in the Nyquist plot. This evolution supports the hypothesis that the lithium cations need some sort of swelling agent to unlock their mobility.

Based on this careful adjustment of polymer film processing, the copolymers **2** and **3** are as well transferred into their polymer film versions and swelled with 10 wt% of dry DMSO. Every measurement is performed in triplicates, and the resulting Nyquist plots can establish a trend in relation to the received bulk resistances at room temperature. The target SICPE shows the smallest bulk resistance with 30 kΩ, followed by copolymer **3** with 115 kΩ, and subsequently copolymer **2** with 225 kΩ (see Figure 71). The ionic conductivities cannot directly be read from this plot, as their film thickness is needed for their exact calculation. Nevertheless, assuming that the films show nearly the same thickness (due to similar polymer film-making processes), tendencies can be defined. The smaller the bulk resistance, the higher the ionic conductivity. That would mean that the target SICPE shows the highest ionic conductivity, followed by copolymer **3** and copolymer **2**. The performance of the target SICPE can be explained by looking at the thermal transitions of the polymers. With a T_g near room temperature, the target SICPE exhibits the most flexible polymer chains in the series. The incorporation of SO moieties into the copolymer elevates the T_g up to 42 °C, thus reducing the flexibility and, thereby, also the ionic conductivity

at room temperature. Surprisingly, copolymer **2** would depict an ionic conductivity that ranges in the middle between the target SICPE and copolymer **2**.

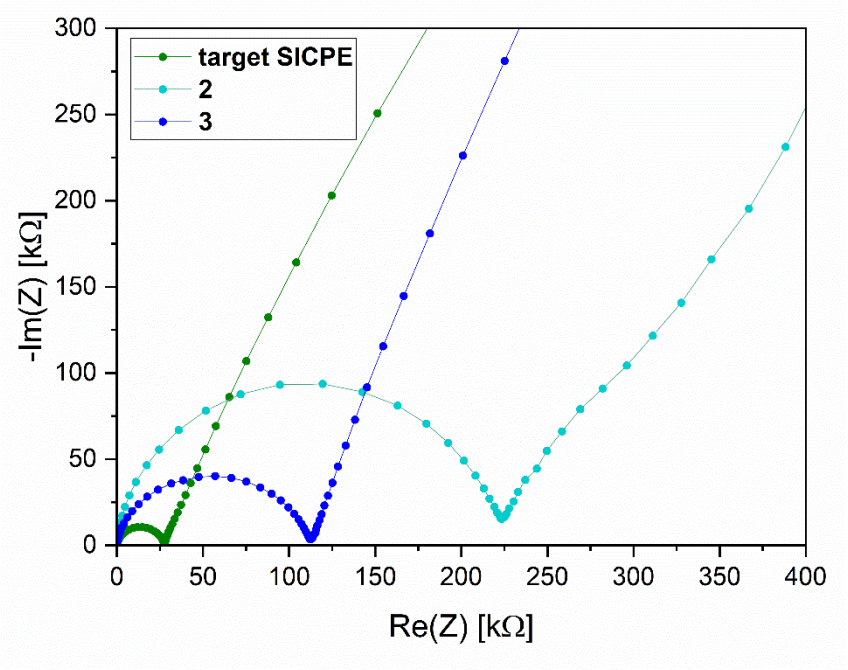

Figure 71: Nyquist plots of target SICPE and the copolymers **2** and **3** after swelling the polymer films with 10 wt% of dry DMSO.

It has to be assumed that copolymer 3 forms this distinct network structure (see DOSY-NMR results and thermal analysis) that drastically differs from the setup of the target SICPE and copolymer **2**. Probably, this networked character supports the formation of lithium ion channels or pores, that accelerate the ion migration. Microscopic analyses could prospectively clear this status.

To deeply understand the relation between polymer framework and electrochemical response, multiple electrochemical experiments have to follow. Besides the determination of the ionic conductivity, electrochemical stability has to be tested via cyclic voltammetry (CV). The electrochemical stability window defines the scope of application, in which the polymer electrolyte can be combined with the respective electrode materials. Furthermore, a symmetrical Li/polymer electrolyte/Li setup has to be established to quantify the t_{Li^+} of the respective SICPEs. For an electrolyte where only the lithium cations are mobile, t_{Li^+} should be unity. In reality, side effects often tend to lower the lithium migration efficiency. Even though the majority of the electrochemical characterizations are still under investigation, the herein-designed homo- or copolymerized versions of our target SICPE already demonstrate their applicability as charge carrier matrices. The potential of this newly developed, polyether based SICPE is now open for discussion and application.

6. Summary and outlook

This work presents the realization of the first example of a polyether backbone-based SICPE that is applicable as a solid polymer electrolyte in solid-state batteries. The resulting polymer stands out due to combining two major advantages: high polymer backbone flexibility and single ion-conduction. The respective design concept is separated into three main parts, namely, the establishment of the epoxide-terminated monomer, its anionic ROP with the corresponding protection group strategy, and the subsequent post-polymerization functionalization.

Monomer **1** is received via a three-step synthesis, including a classical chlorosulfonation as the first step. During the second step, a sulfonamide group is introduced as a protecting group, and a vinylic double bond is generated using an elimination reaction. The focus of the synthesis pathway towards **1** is centered on the epoxidation of the vinylic double bond. Its electron-deficient character tremendously impedes the oxygen transfer reaction. Hence, common epoxidation reagents like *m*-CPBA, H_2O_2, or NaOCl do not succeed in the cycloaddition. Applying a catalytically supported epoxidation strategy in the presence of a (salen)Mn(III) *Jacobsen* catalyst, the double bond is transferred into the terminal epoxide, yielding monomer **1** with an overall yield of 73%. The achievement of the epoxide is the starting point for the ring opening to generate the PEO backbone.

Thanks to the well-selected protection group strategy, restrictions related to functional group tolerance during ROP are bypassed. The oxygens of the sulfonamide group experience a shielding effect that facilitates the choice of catalyst. Aiming the anionic ROP of **1**, a selection of non-transition-metal- and transition-metal-based catalysts are presented in a broad catalyst screening. The winning candidate is the (salen)Cr(III) catalyst, which is able to polymerize **1** in different catalyst-to-monomer ratios (1/10, 1/50, 1/100, and 1/200) with molecular weights up to 113 kg mol^{-1}. The polymerization is performed in bulk at 115 °C to exceed the T_m of **1**. After the polymer workup, the sulfonamide protection group is cleaved off to give access to a lithium sulfonate moiety. After testing various reaction conditions, the usage of *in situ* formed lithium methanolate as a cleaving reagent is favored. By adding elemental lithium into dry methanol, lithium methanolate is originated, which can act as a nucleophile attacking the sulfuric center of the sulfonamide. Elevated temperatures promote the generation of the lithium sulfonate and enable to receive the target SICPE in its homopolymeric form. Challenges concerning this post-polymerization functionalization are the solubility issues of the involved reagents and strong polarization changes of the polymer that occur during the process.

Besides achieving the target SICPE along the pathway of applying the monomer synthesis of **1**, its anionic ROP, and post-polymerization functionalization, two alternative routes are presented. The first concept highlights the chlorosulfonation of PSO and the successive transfer of the chlorosulfonyl-substituted PSO into the target SICPE. PSO can easily be synthesized with the help of *t*-BuP_4 as an organobase initiator, thus exhibiting a simple way to manage polymerization with high yields. Due to the lability of the polyether backbone against acids, approaches using HSO_3Cl as a chlorosulfonation reagent only show the decomposition of PSO and no successful substitution on the aromatic ring. Future approaches should focus on a more dilute working atmosphere, milder reaction conditions, or a change in acidic reagents. In contrast to starting with a polymer and applying polymer-analogous reactions, also alternative monomer structures are discussed. The alternative monomer A depicts a free lithium sulfonate bound to a SO core, which, unfortunately, would prevent the anionic ROP with the (salen)Cr(III) catalyst. On the contrary, monomer B can potentially be a promising SICPE candidate concerning its structural properties. The SO main core still provides the polyether backbone after the anionic ROP of the epoxide functionality. In addition, the bound TFSI anion enables the delocalization of the anionic charge and supports a better dissociation behavior of the anions and lithium cations. Even though there is a need to find a suitable epoxidation strategy for the last step of monomer synthesis of B, this monomer has the potential to become a high-performing SICPE.

The polymerization properties of the (salen)Cr(III) catalyst can also be transferred to copolymerization experiments. The comonomers can simply be added to the dry mixture of the catalyst and **1** and copolymerized together, as they exhibit epoxide functionalities. The comonomer SO in copolymer **2** should function as a charge separator between the SICPE repetition units, while comonomer PEG 2000 in copolymer **3** has a plasticizing effect and should additionally support the ion hopping by supplying PEG side chains. Thermal properties show, that the target SICPE exhibits the lowest T_g between 18 to 22 °C, meaning that the polymer chains are already flexible at room temperature. Copolymer **2** shows a small rise of T_g up to 42 °C, which can potentially be explained by π-π-interactions between the aromatic rings. Surprisingly, for copolymer **3**, only a T_m at 45 °C is visible, which is why a rigidification of the polymer framework is supposed. The hereby upcoming theory of a networked polymer can be reinforced by DOSY-NMR experiments, showing two diffusion coefficients for the copolymer. To prove a polymer network's formation, microscopic images or rheological measurements should follow this thesis. In general, all homo- and copolymers that are presented in this work should be tested with regard to their mechanical properties, as the mechanical behavior has a major influence on the later applicability of the polymer electrolyte in cells operating under pressure.

This work demonstrates a first introduction to the electrochemical property testing of the target SICPE and the respective copolymers **2** and **3**. Via drop casting and the optimization of polymer film preparing techniques, coin cells are able to be set up. To exclude the influence of humidity, a long drying process is necessary before the cells are assembled. First experiments indicate that a swelling of the polymer electrolyte with 10 wt% of dry DMSO is necessary to make the lithium cations mobile inside of the electrolyte. Even though determining ionic conductivities is still ongoing, a trend in bulk resistances can be established. At this point, the expansion of EIS and CV experiments is mandatory to get a more detailed inside into the polymer structure-ion mobility relation and to make a comparison between homo- and copolymeric architectures possible. Different swelling reagents could be tested for future experiments instead of only DMSO. Linear carbonates like DEC or DMC or, for instance, ionic liquids could expand the portfolio. To establish a reference, it would also be interesting to test the protected homopolymer of **1** in its function as a dual ion-conducting polymer electrolyte. This would be achieved by adding an electrochemically stable salt like LiTFSI to the respective polymer solution.

Thinking about the future perspective of ASSBs, the focus on lithium as charge carriers inside of the solid electrolytes should be critically questioned. Lithium is not a ubiquitous, renewable resource. Thus, its stock will decrease over time, and the realization of lithium anodes will be impeded. Therefore, researchers all over the world are already discussing new solid-state technologies that provide a more sustainable future. In this context, sodium ASSBs are currently under consideration, as sodium can, for example, be found in the diversely presented salt NaCl.[304] The huge advantage of the SICPE design that is conceptualized within this work is the variable switch from lithium to a sodium conductor. Instead of using elemental lithium in the post-polymerization functionalization, also elemental sodium can be used with the same outcome (^{1}H-NMR of sodium sulfonate SICPE see appendix). This variety in design options should be seen as the opportunity to flexibly adapt to the market needs.

7. Experimental

7.1 General information

All air and moisture-sensitive compounds were prepared in heat-dried glassware using standard *Schlenk* techniques with argon (99.996 vol.-%) purchased from *Westfalen* as an inert gas.

Polymer film formation for coin cell assembly was performed inside of a LABstar pro glovebox from *MBraun* using drop casting out of the polymer/DMSO solution.

Solvents were dried with the solvent purification system MB SPS-800 from *MBraun* or over activated alumina and stored over molecular sieve (3 or 4 Å). Deuterated solvents were purchased from *Sigma-Aldrich* and dried over activated 3 Å molecular sieve.

Unless otherwise stated, all reagents and catalysts were purchased from *Sigma-Aldrich*, *ABCR GmbH* or *TCI Chemicals* and used without further purification.

7.2. Analytical methods

NMR. ^{1}H- and ^{13}C-NMR spectra were recorded on a *Bruker Ascend* 400 MHz NMR-spectrometer at 400 MHz (^{7}Li-NMR spectra measured at 300 MHz). All chemical shifts are given in parts per million (ppm) and referenced to the residual proton signal of the respective solvent. The NMR spectra were analyzed using the *MestReNova* software. Signal multiplicities are abbreviated as follows: s - singlet, d – duplet, t – triplet, m – multiplet. The coupling constant is marked as *J*,

TGA. For the sulfonamide-protected homopolymer of **1** ((salen)Cr(III) catalyst/**1** ratios of 1/10, 1/50, 1/100, 1/200), 2 mg of sample was heated from room temperature to 1000 °C with a heating rate of 10 K min^{-1} under synthetic air on a TGA Q5000 by *TA Instruments.* Analysis of mass loss was done using *TA* Analysis software. For the target SICPE ((salen)Cr(III) catalyst/**1** ratios of 1/10, 1/50, 1/100, 1/200), 2 mg of sample was heated from 50 °C to 700 °C with a heating rate of 10 K min^{-1} under argon on a *Netzsch* TG 209 F1 Libra inside a glovebox. The data was processed with the software *Netzsch* Proteus 6.

DSC. For the sulfonamide-protected homopolymer of **1** ((salen)Cr(III) catalyst/**1** ratios of 1/10, 1/50, 1/100, 1/200), about 3-4 mg were weighed in a non-hermetic aluminum pan and measured in a range of −100 °C to 220 °C (depending on the sample) with a heating and cooling rate of 10 K min^{-1} on a DSC Q2000 by *TA Instruments.* Analysis was performed using *TA* Analysis software. The same procedure was

repeated for the target SICPE ((salen)Cr(III) catalyst/**1** ratios of 1/10, 1/50, 1/100, 1/200) in a hermetic set-up. Sample preparation was performed inside a glovebox.

GPC. Average absolute molecular weights and dispersity of the sulfonamide-protected homopolymer of **1** were determined on an *Agilent* PL-GPC 50 with an integrated RI unit, two light scattering detectors (15° and 90°), and a differential pressure viscosimeter with two *Agilent* PolarGel M columns at 30 °C. 2 mg of sample were dissolved in DMF + 25 mmol L^{-1} LiBr. Absolute molecular weights and polydispersity were determined using the experimentally determined value for dn/dc.

dn/dc. For dn/dc determination, a *WGE Dr. Bures* dn/dc-2010 from PSS equipped with a 620 nm light source was used. The measurements were performed in DMF with 25 mmol L^{-1} LiBr at 30 °C with 7 different polymer concentrations.

EDX. EDX measurements were conducted on a *Hitachi* tabletop scanning electron microscope with a 10.000 magnification and an accelerating voltage of 1 kV.

FTIR. Measurements were performed on a nitrogen-cooled *Bruker Vertex* 70A spectroscope in an attenuated total reflection mode.

XRD. For sample preparation, 10 mg of the polymer was put on a scotch tape (Fa. Scotch®, Magic TapeTM8-1933R8, 3M) and measured on a Stoe STADI P-Diffraktometer equipped with a Ge (111)-monochromator for Cu K_α (λ = 1,54056 Å) and a solid detector (Dectris MYTHEN DSC 1 K). The measurement parameters consist of a measurement period of 15 minutes in a range of 2θ = 5° - 80° (1° per 10 seconds).

Microwave reaction. All microwave experiments were performed in a reactor of *CEM* with a focused microwave beam at 50 W, varying temperatures, and a dynamic power supply.

EIS. For electrochemical measurements, the homo- and copolymers were transferred into their polymer film version by dissolving the polymer powders (100 mg in 0.5 ml dry DMSO) and drop-casting them onto the bottom part of a coin cell. 10 wt% of dry DMSO was added to the polymer film, and the coin cells were assembled under inert conditions.

7.3 Synthesis procedures

The following chapter depicts the synthesis protocols for the monomers (**1** and alternative monomers) and the homo- as well as the co-polymers with the ethylene oxide derivatives (SO and PEG 2000). As the post-polymerization functionalization of PSO was unsuccessful, no synthesis protocol is fixed in this chapter.

7.3.1 Synthesis of monomer 1

The synthesis of **1** comprises a three-step synthesis route: chlorosulfonation leads to **A**, elimination, and sulfonamide protection strategy to **B**, and epoxidation to the final epoxide **1**.

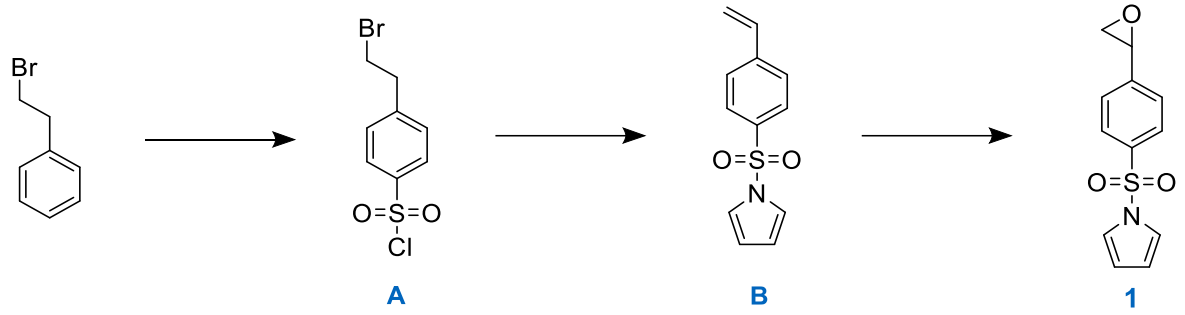

The synthesis of **A** was conducted according to literature known chlorosulfonation reactions.[305] At 0 °C (2-bromoethyl)-benzene (20.5 mL, 150 mmol, 1.0 eq) in chloroform (50 mL) was added dropwise to a solution of chlorosulfonic acid (30.0 mL, 450 mmol, 3.0 eq.) in chloroform (35 mL). The solution was stirred for 15 min at 0 °C before being warmed to room temperature. After stirring for 3 h at 25 °C, the solution was poured into ice, and the aqueous phase was extracted with DCM (3 x 100 mL). The organic phase was washed with $NaHCO_3$ solution (3 x 150 mL) and brine (3 x 150 mL) and dried over Na_2SO_4. The crude product was purified via column chromatography (pentane/diethyl ether 10/1) to obtain **A** (32.3 g, 114 mmol, 76%).

^{1}H-NMR (400 MHz, $CDCl_3$): δ (ppm) = 8.01 (d, J = 8.2 Hz, 2H), 7.48 (d, J = 8.2 Hz, 2H), 3.62 (t, J = 7.1 Hz, 2H), 3.30 (t, J = 7.1 Hz, 2H).

^{13}C-NMR (101 MHz, $CDCl_3$): δ (ppm) = 144.57, 140.24, 130.02, 129.66, 128.02, 127.36, 38.84, 31.70.

To a solution of pyrrole (10.7 mL, 155 mmol, 2.2 eq.) in dry THF (100 mL), *n*-BuLi (2.5 M in hexane, 62.0 mL, 155 mmol, 2.2 eq.) was added dropwise at −78 °C and the reaction was stirred for 10 min at this temperature. The cooling bath was removed to warm up the solution to room temperature. **A** (20.0 g, 70.5 mmol, 1.0 eq.) was dissolved in dry THF (25 mL) and added dropwise to the solution over a period of 20 min at −78 °C. After stirring overnight and removing the solvent, the residue was dissolved

in dichloromethane (100 mL) and extracted with water (2 x 150 mL) and $NaHCO_3$ solution (2 x 150 mL). The organic phases were collected and dried over Na_2SO_4. The obtained brownish solid was sublimated twice, resulting in **B** (12.8 g, 54.9 mmol, 78%).

^{1}H-NMR (400 MHz, $CDCl_3$): δ (ppm) = 7.92 (d, *J* = 8.6 Hz, 2H), 7.57 (d, *J* = 9.0 Hz, 2H), 7.30 – 7.21 (m, 2H), 6.80 (dd, *J* = 17.6, 10.9 Hz, 1H), 6.43 – 6.36 (m, 2H), 5.96 (d, *J* = 17.6 Hz, 1H), 5.52 (d, *J* = 11.0 Hz, 1H).

The synthesis of **1** was conducted according to a published epoxidation strategy by *Jacobsen et al*.[265] **B** (4.02 g, 17.3 mmol, 1.0 eq.), *N*-methylmorpholine *N*-oxide (10.1 g, 86.2 mmol, 5.0 eq.) and (*R*,*R*) (–)-[1,2-cyclohexanediamino-*N*,*N*'-bis-(3,5-di-*t*-butylsalicycliden)]-mangan(III)-chloride (438 mg, 689 µmol, 4.00 mol%) were dissolved in dry dichloromethane (400 mL) and the reaction mixture was cooled to −78 °C. After adding *m*CPBA (8.50 g, 34.5 mmol, 2.0 eq.) in small portions, the reaction is stirred at −78 °C for 45 min. The reaction solution was mixed with 1 M NaOH (380 mL), and the aqueous phase was extracted with DCM (3 x 150 mL). The combined organic layers were washed with brine (3 x 150 mL) and dried over Na_2SO_4. The crude product was purified via column chromatography (pentane/ethyl acetate 10/1) and sublimated three times to obtain **1** (2.74 g, 11.0 mmol, 64%).

^{1}H-NMR (400 MHz, CDCl3): δ (ppm) = 7.83 (d, J = 8.2 Hz, 2H), 7.40 (d, J = 8.2 Hz, 2H), 7.15 (m, 2H), 6.30 (m, 2H), 3.89 (m, 1H), 3.21 – 3.14 (m, 1H), 2.72 (m, 1H).

^{13}C-NMR (101 MHz, CDCl3): δ (ppm) = 144.4, 138.7, 127.1, 126.4, 120.8, 113.8, 77.2, 51.6, 51.5.

TGA: $T_{d,onset}$ = 195 °C.

DSC: T_m = 108 °C.

7.3.2 Synthesis of target SICPE

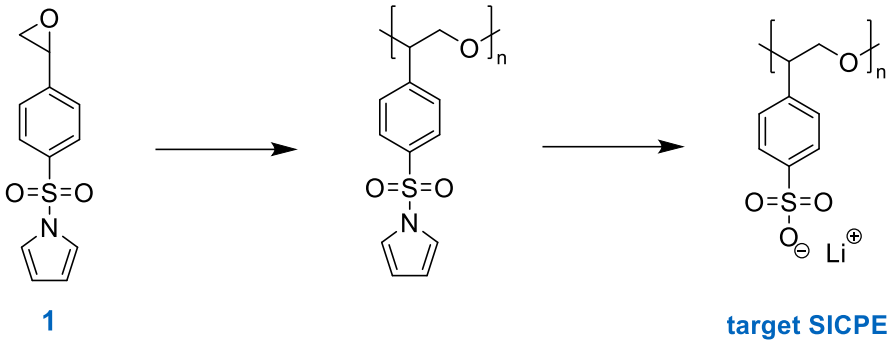

1 **target SICPE**

In an argon atmosphere, **1** was dry mixed with (*1R*,2*R*)-(+)-[1,2-cyclohexanediamino-*N*,*N*'-bis(3,5-di-*t*-butylsalicylidene)]-chromium(III)chloride ((salen)Cr(III)) catalyst in different catalyst to monomer ratios (1/10, 1/50, 1/100, 1/200) and heated up to 115 °C for 3 days. After the completion of polymerization, the solid mixture was dissolved in dichloromethane and precipitated in pentane. The solid was centrifugated and again precipitated three times to separate the polymer from the monomer and catalyst residues. To ensure that all (salen)Cr(III)-catalyst residues were washed out, EDX measurements were taken. The received polymer was dried in a vacuum at 50 °C for 24 h to obtain the protected homopolymer in powder form (96% (1/10), 93% (1/50), 97% (1/100), 96% (1/200)).

^{1}H-NMR (400 MHz, $CDCl_3$): δ (ppm) = 8.03 – 7.30 (m, 4H), 7.22 – 7.06 (m, 2H), 6.46 – 6.20 (m, 2H), 5.25 – 3.06 (m, 3H).
NMR-spectra are similar for all catalyst to monomer ratios.

$M_{n,abs}$ (DMF + LiBr) = 14.2 kg mol^{-1} (1/10), 36.5 kg mol^{-1} (1/50), 67.3 kg mol^{-1} (1/100), 113 kg mol^{-1} (1/200).

Đ (DMF + LiBr) = 2.6 (1/10), 1.9 (1/50), 1.3 (1/100), 2.4 (1/200).

dn/dc (DMF + LiBr) = 0.152 cm^3 g^{-1}.

I_e: 18% (1/10), 32% (1/50), 36% (1/100), 43% (1/200).

TGA: $T_{d,\,onset}$ = 289 °C (1/10), 302 °C (1/50), 294 °C (1/100), 310 °C (1/200).

DSC: T_g = 69.9 °C (1/10), 68.5 °C (1/50), 69.5 °C (1/100), 72.6 °C (1/200).

EDX: S (100%), Cr (0%).

FT-IR: $\tilde{\nu}$ (cm^{-1}) = 3140, 1774, 1594, 1454, 1410, 1247, 1091, 1055, 1032, 1015, 934, 833, 737.

For post-polymerization functionalization, in a glovebox, elemental lithium (20 eq. per monomer unit) was dissolved in dry MeOH. A solution of the sulfonamide-protected homopolymer of **1** in dry DCM is added and refluxed for 3 d at 65 °C. After evaporation of the solvent, the solid was dissolved in water, extracted with DCM, and dialyzed against 2 L of water. The purified polymer was dried in a vacuum at 50 °C for 24 h to yield the target SICPE (42% (1/10), 40% (1/50), 44% (1/100), 45% (1/200)).

^{1}H-NMR (400 MHz, D_2O): δ (ppm) = 8.38 – 6.89 (m, 4H), 4.90 – 2.82 (m, 3H).
NMR spectra are similar for all catalyst-to-monomer ratios.

^{7}Li-NMR (156 MHz, D_2O): δ (ppm) = 0.16 (s).
NMR spectra are similar for all catalyst-to-monomer ratios.

$M_{n,abs}$ (DMF + LiBr) = 11.3 kg mol^{-1} (1/10), 35.7 kg mol^{-1} (1/50), 61.2 kg mol^{-1} (1/100), 108 kg mol^{-1} (1/200).

Đ (DMF + LiBr) = 2.1 (1/10), 1.7 (1/50), 1.2 (1/100), 2.3 (1/200).

dn/dc (DMF + LiBr) = 0.151 cm^3 g^{-1}.

TGA: $T_{d,\,onset}$ = 310 °C (1/10), 287 °C (1/50), 286 °C (1/100), 281 °C (1/200).

DSC: T_g = 22°C (1/10), 18 °C (1/50), 18 °C (1/100), 19 °C (1/200).

FT-IR: $\tilde{\nu}$ (cm^{-1}) = 3431, 1935, 1624, 1177, 1125, 1041, 1009, 916, 835, 721.

7.3.3 Syntheses of alternative monomers

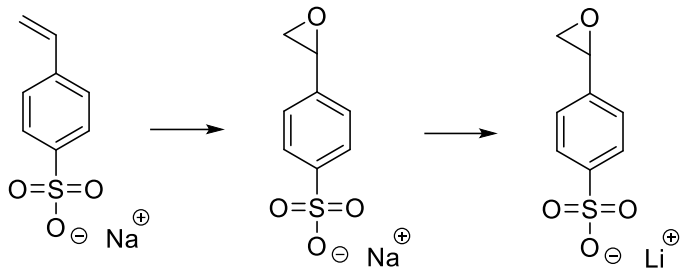

monomer alternative A

Sodium 4-vinyl benzenesulfonate (1.00 g, 4.85 mmol, 1.0 eq.) was dissolved in water (25 mL) and combined with a freshly prepared DMDO solution (c = 0.1 M, 80 mL, 1.0 eq.) in water. After stirring for three days at room temperature, the solution was extracted with DCM (4 x 150 mL). The solvent of the aqueous phase is removed, and the solid is sublimated to yield sodium 4-(oxirane-2-yl)benzenesulfonate (51%). As the polymerization with this sodium sulfonate was unsuccessful, the salt metathesis reaction of sodium against lithium was not examined.

^{1}H-NMR (400 MHz, D_2O): δ (ppm) = 7.71 (m, 2H), 7.39 (d, J = 8.14 Hz, 2H), 4.04 (m, 1H), 3.22 (m, 1H), 2.98 (m, 1H).

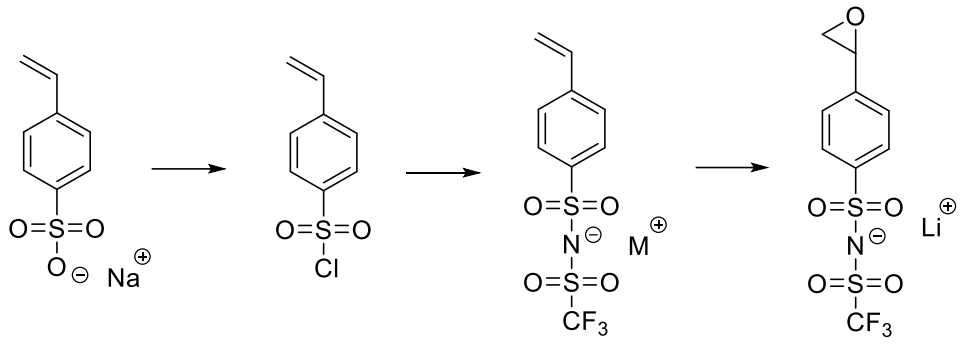

monomer alternative B

Thionyl chloride (7.99 g, 67.2 mmol,0 ° 373 eq.) and butyl catechol (29.9 mg, 180 µmol, 1.0 eq.) were dissolved in dry DMF (10 mL) at 0 °C. Sodium 4-vinyl benzenesulfonate (2.00 g, 9.70 mmol, 54 eq.) was added in small portions over a period of 15 min, and the solution was stirred for three hours at 0 °C. After letting the solution cool down in the fridge for 24 hours, the solution was poured into ice water (40 mL) and extracted with toluene (2 x 30 mL). The organic phase was washed with water (2 x 30 mL), dried with Na_2SO_4, and the solvent was evaporated. Column chromatography (silica, 100% DCM) yielded a yellow oil.

^{1}H-NMR (400 MHz, D_2O): δ (ppm) = 7.78 (d, J = 8.2 Hz, 2H), 7.63 (d, J = 8.1 Hz, 2H), 6.90 – 6.79 (m, 1H), 6.00 – 5.92 (m, 1H), 5.45 – 5.38 (m, 1H).

The yellow oil (2.27 g, 11.2 mmol, 102 eq.) was mixed with K_2HPO_4 (3.90 g, 22.4 mmol, 224 eq.), butyl catechol (18.6 mg, 110 µmol, 1.0 eq.), and DMAP (27.3 mg, 220 µmol, 2.0 eq.) in dry acetonitrile at 0 °C. Trifluoromethanesulfonamide (1.50 g, 10.1 mmol, 0.9 eq.) was slowly added, and the reaction was stirred for 72 hours at room temperature. The solution was filtered, and the filtrate was sublimated before washing it with DCM (3 x 20 mL). After drying in a vacuum, a white solid was obtained (63%).

^{1}H-NMR (400 MHz, D_2O): δ (ppm) = 7.69 (d, J = 8.1 Hz, 2H), 7.54 (d, J = 8.0 Hz, 2H), 6.81 – 6.70 (m, 1H), 5.96 – 5.87 (m, 1H), 5.39 – 5.32 (m, 1H).

For the last synthesis step, the epoxidation was carried out according to the procedure described for the cycloaddition reaction of **1**. The purification of the crude product still has to be adjusted to yield the final alternative monomer B.

7.3.4 Syntheses of copolymers and related homopolymers

Copolymer 2

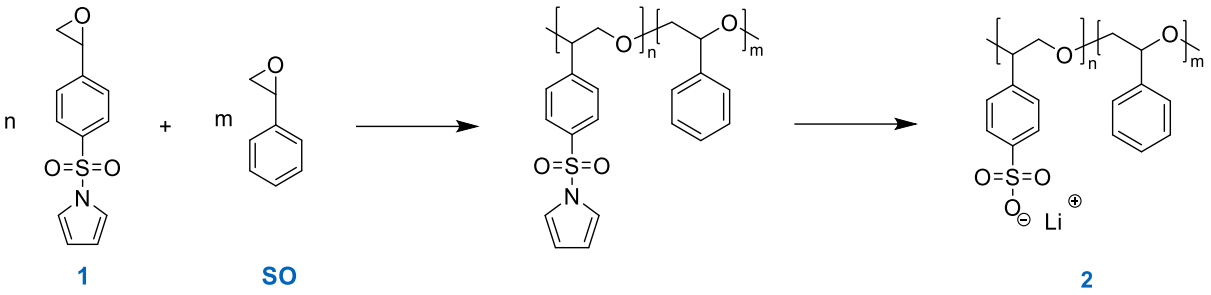

For copolymerization, **1** was dry mixed with the co-monomer SO and the (salen)Cr(III) catalyst in a ratio of 1/100/100 and heated up to 115 °C for 3 days. After polymerization, the solid mixture was dissolved in dichloromethane and precipitated in pentane. The solid was centrifugated and again precipitated three times to separate the copolymer from monomer and catalyst residues. The received polymer was dried in a vacuum at 50 °C for 24 h to obtain the polymer in powder form (92%). For post-polymerization functionalization, in a glovebox, elemental lithium (20 eq. per monomer unit) was dissolved in dry MeOH. A polymer solution in dry DCM is added and refluxed for 3 d at 65 °C. After evaporation of the solvent, the solid is dissolved in water, extracted with DCM, and dialyzed against 2 L of water. The purified polymer is dried in a vacuum to yield **2** in 46% yield.

^{1}H-NMR (400 MHz, D_2O): δ (ppm) = 7.96 – 6.73 (m, 9H), 4.67 – 2.80 (m, 6H).

^{7}Li-NMR (156 MHz, D_2O): δ (ppm) = 0.16 (s).

$M_{n,abs}$ (DMF + LiBr) = 96.6 kg mol^{-1}.

Đ (DMF + LiBr) = 1.2.

dn/dc (DMF + LiBr) = 0.155 cm^3 g^{-1}.

TGA: $T_{d,\,onset}$ = 241 °C.

DSC: T_g = 42 °C.

FT-IR: $\tilde{\nu}$ (cm^{-1}) = 2284, 1600, 1406, 1180, 1125, 1042, 1010, 835.

Copolymer 3

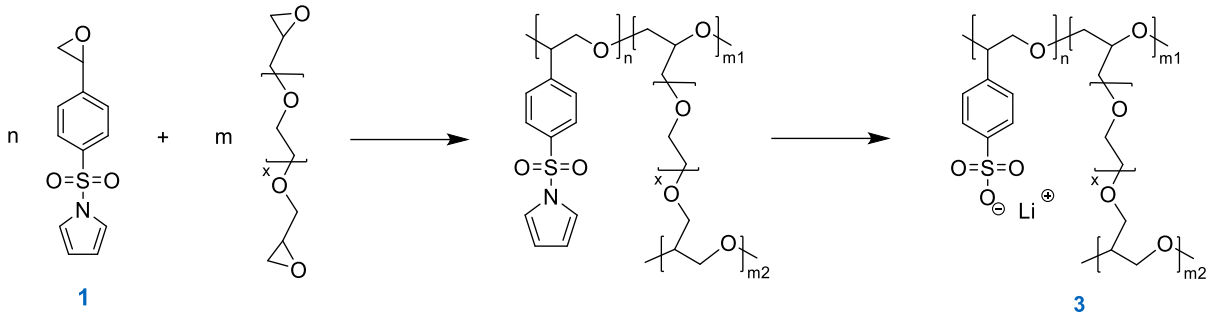

For copolymerization, **1** was dry mixed with the co-monomer poly(ethylene glycol) diglycidyl ether (2000 g mol^{-1}) and (salen)Cr(III) catalyst in a ratio of 1/100/100 and heated up to 115 °C for 3 days. After the completion of polymerization, the solid was ground and washed with an excess of pentane. The received polymer was dried in a vacuum at 50 °C for 24 h to obtain 65% of the polymer. For post-polymerization functionalization, in a glovebox, elemental lithium (20 eq. per monomer unit) is dissolved in dry MeOH. The polymer was added and refluxed for 6 d at 65 °C. After evaporation of the solvent, the solid was dissolved in water, extracted with DCM, and dialyzed against 2 L of water. The purified polymer is dried in a vacuum to yield **3** in 41% yield.

^{1}H-NMR (400 MHz, D_2O): δ (ppm) = 7.85 – 7.34 (m, 4H), 3.64 (s, 165H).

^{7}Li-NMR (156 MHz, D_2O): δ (ppm) = 0.16 (s).

$M_{n,abs}$ (DMF + LiBr) = 41.6 kg mol^{-1}.

Đ (DMF + LiBr) = 1.6.

dn/dc (DMF + LiBr) = 0.037 cm^3 g^{-1}.

TGA: $T_{d,\,onset}$ = 340 °C.

DSC: T_m = 45 °C.

FT-IR: $\tilde{\nu}$ (cm^{-1}) = 2881, 1466, 1359, 1343, 1280, 1240, 1146, 1100, 1060, 961, 841.

PSO synthesis

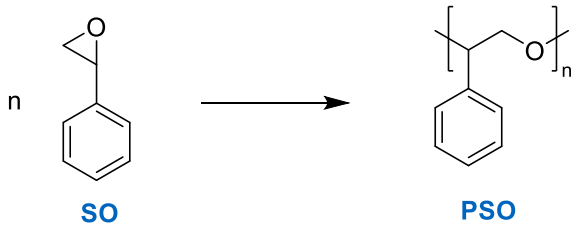

For post-polymerization functionalization purposes, the living ROP of SO was conducted according to literature procedures by using a phosphazene base initiating system.[285] 1-*t*-butyl-4,4,4-tris(dimethylamino)-2,2-bis[tris(dimethylamino)phosph-oranylidenamino]-2Λ^5,4Λ^5-catenadi(phosphazene) (*t*-Bu-P$_4$) (0.8 M in hexane, 250 µL, 200 µmol, 1.0 eq.) and SO (2.28 mL, 20.0 mmol, 100 eq.) were added to 1 mL of toluene. The reaction was kept at room temperature and terminated after 20 h by adding 10 µL of methanol. To separate the polymer from residual organobase, the solution was purified by column chromatography (aluminum oxide, 100% DCM). After drying in a vacuum at 50 °C for 24 h, PSO was obtained as a white solid (98%).

For comparison reasons in the copolymerization experiments, SO was bulk polymerized with the (salen)Cr(III) catalyst with similar parameters as mentioned above.

^{1}H-NMR (400 MHz, $CDCl_3$): δ (ppm) = 7.25 – 6.90 (m, 5H), 4.35 (t, J = 18.0 Hz, 1H), 3.40 (d, J = 62.7 Hz, 2H).

^{1}H-NMR spectrum is superposable to literature data.[285]

$M_{n,abs}$ (DMF + LiBr) = 83.7 kg mol^{-1}.

Đ (DMF + LiBr) = 1.2.

dn/dc (DMF + LiBr) = 0.149 cm^3 g^{-1}.

TGA: $T_{d,\,onset}$ = 294 °C.

DSC: T_g = 42 °C.

FT-IR: $\tilde{\nu}$ (cm^{-1}) = 2863, 1493, 1451, 1348, 1197, 1093, 1027, 913, 755.

Polymerized PEG 2000

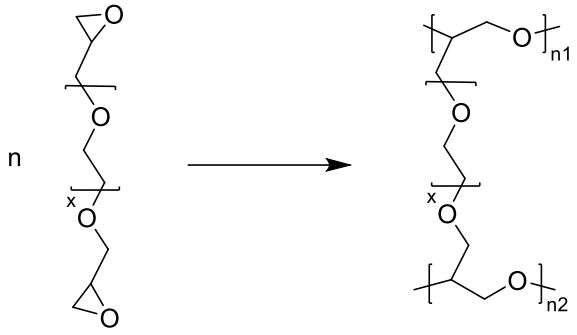

PEG 2000

In an argon atmosphere, the PEG 2000 monomer was dry mixed with the (salen)Cr(III) catalyst in a ratio of 1/100 and heated up to 115 °C for 3 days. After polymerization, the solid mixture was ground and washed with pentane. The received polymer was dried in a vacuum at 50 °C for 24 h to obtain PEG 2000 in powder form (64%).

^{1}H-NMR (400 MHz, $CDCl_3$): δ (ppm) = 3.94 – 3.37 (m, 16H).

$M_{n,abs}$ (DMF + LiBr) = 45.2 kg mol^{-1}.

Đ (DMF + LiBr) = 1.5.

dn/dc (DMF + LiBr) = 0.015 cm^3 g^{-1}.

TGA: $T_{d,\,onset}$ = 338 °C.

DSC: T_m = 43 °C.

FT-IR: $\tilde{\nu}$ (cm^{-1}) = 2880, 1721, 1466, 1343, 1280, 1242, 1101, 962, 842.

7.4 Additional analytical data

7.4.1 Data of monomer 1

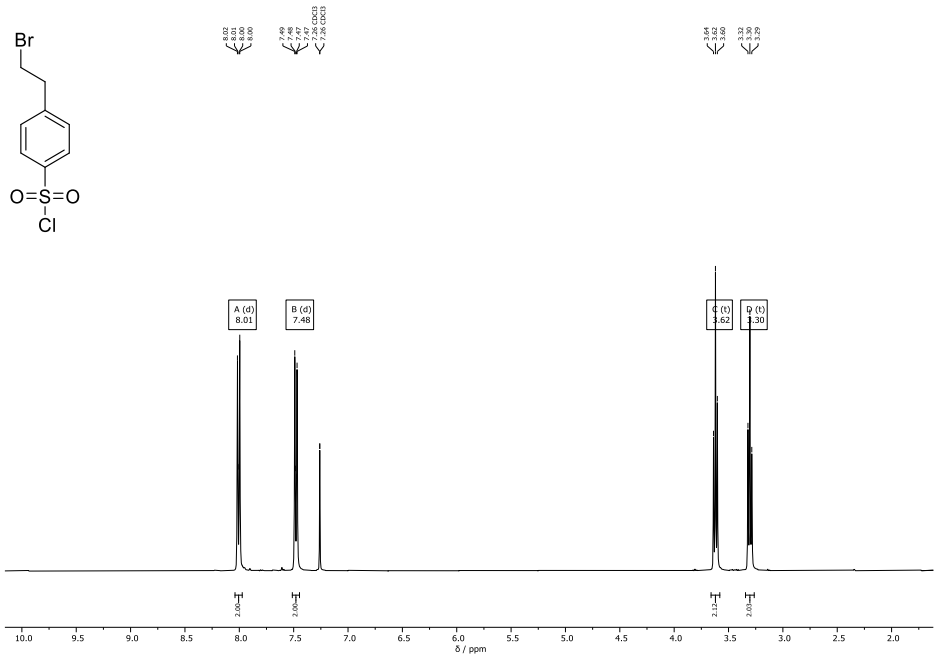

*^{1}H-NMR spectrum of **A**.*

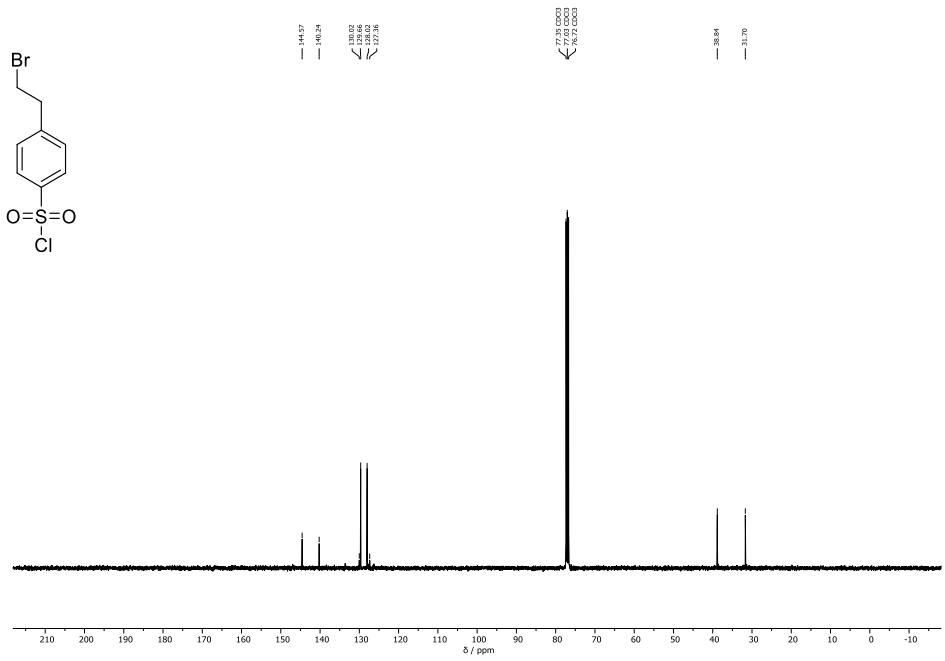

*^{13}C-NMR spectrum of **A**.*

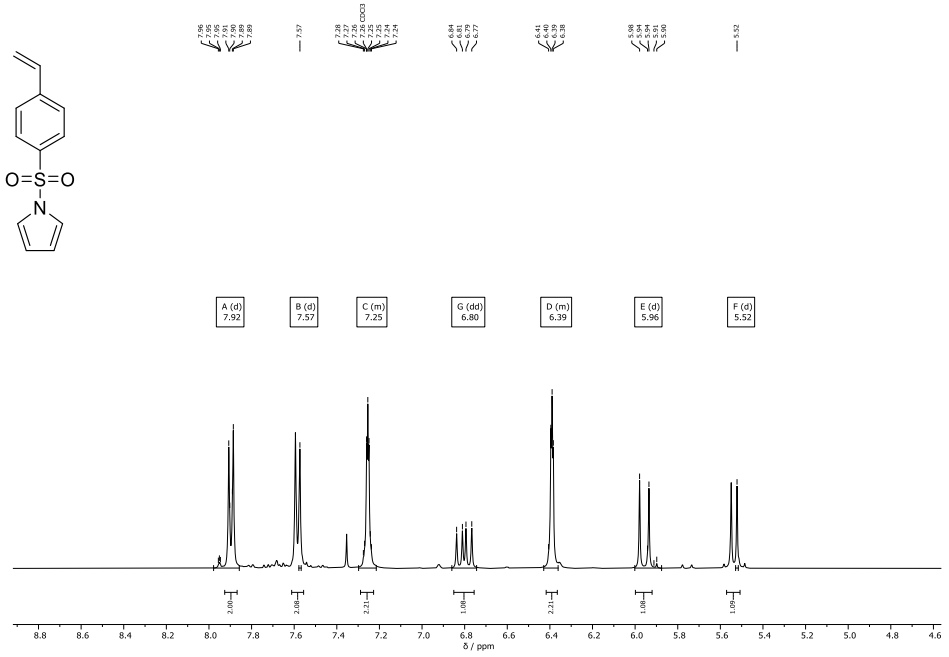

*^{1}H-NMR spectrum of **B**.*

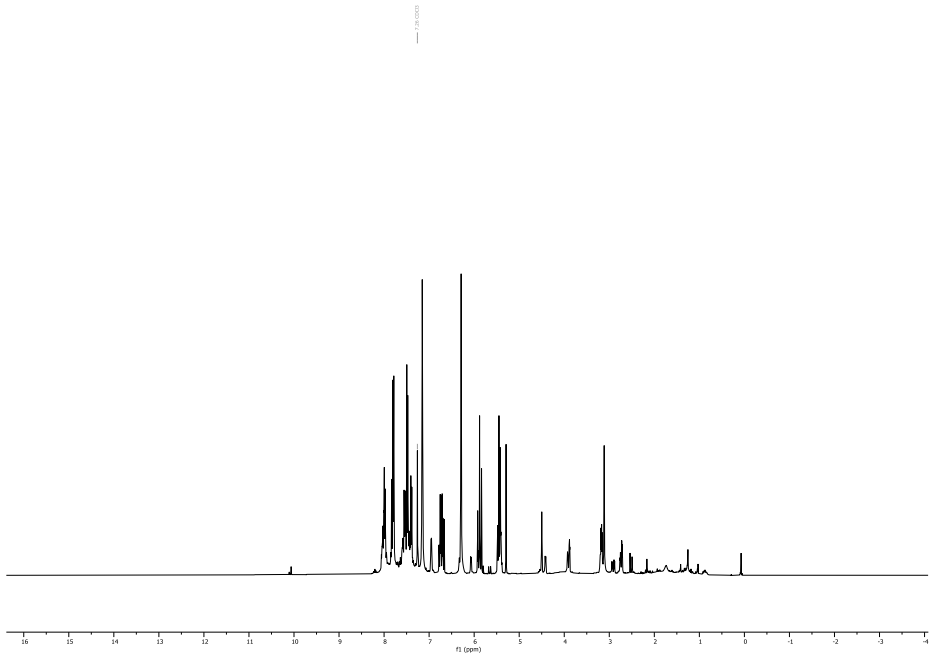

Crude ^{1}H-NMR spectrum of m-CPBA epoxidation approach of vinyl sulfonamide.

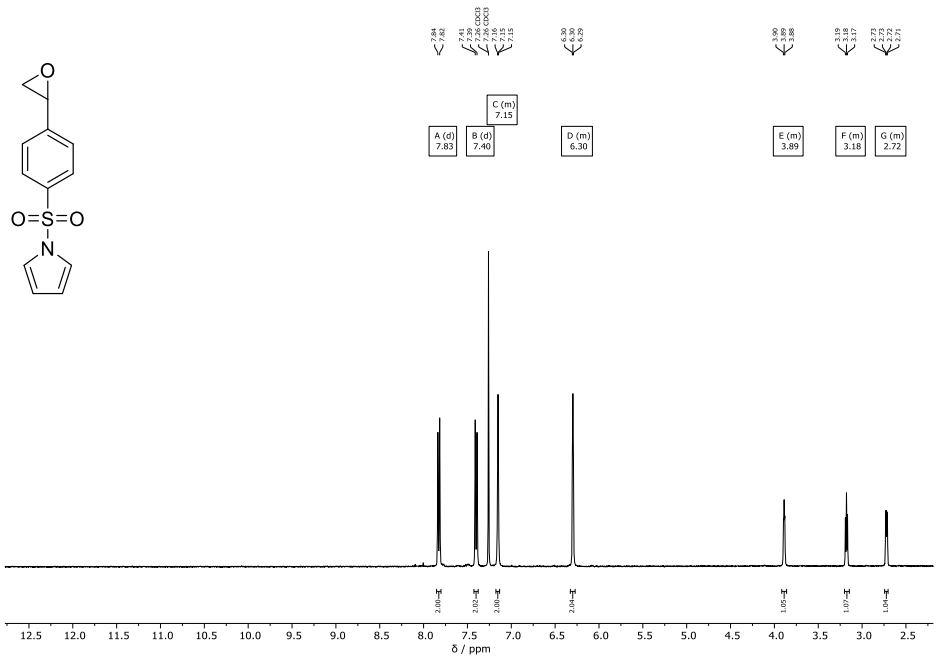

*^{1}H-NMR spectrum of **1**.*

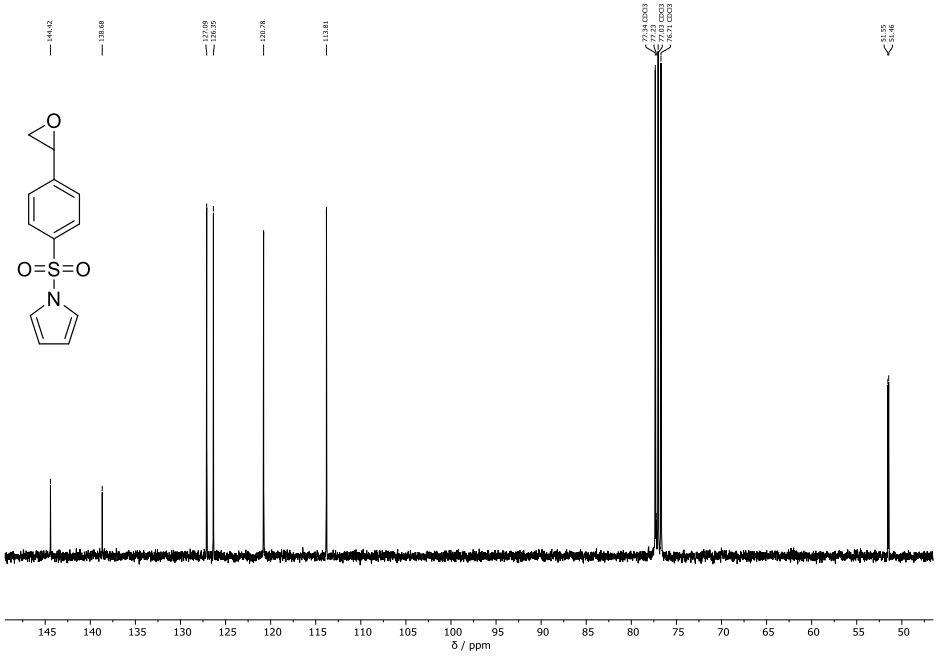

*^{13}C-NMR spectrum of **1**.*

7.4.2 Sulfonamide protected homopolymer of 1

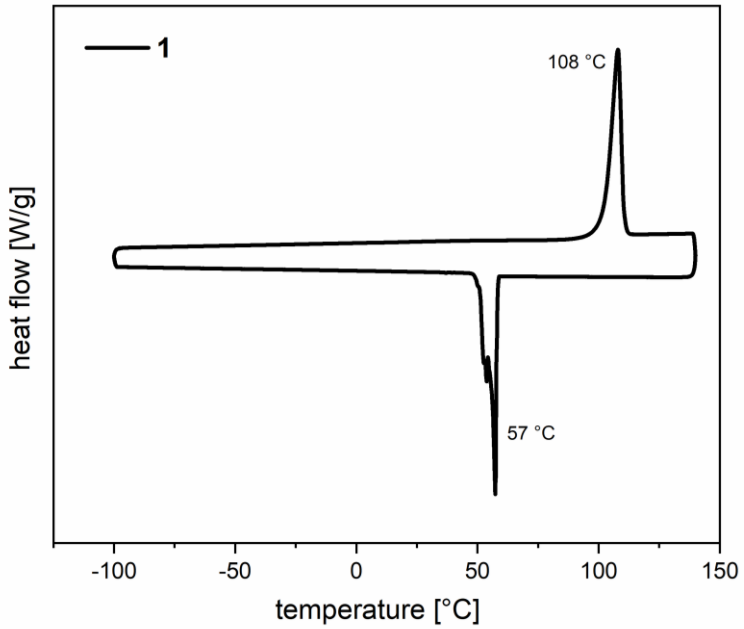

*DSC measurement of **1**.*

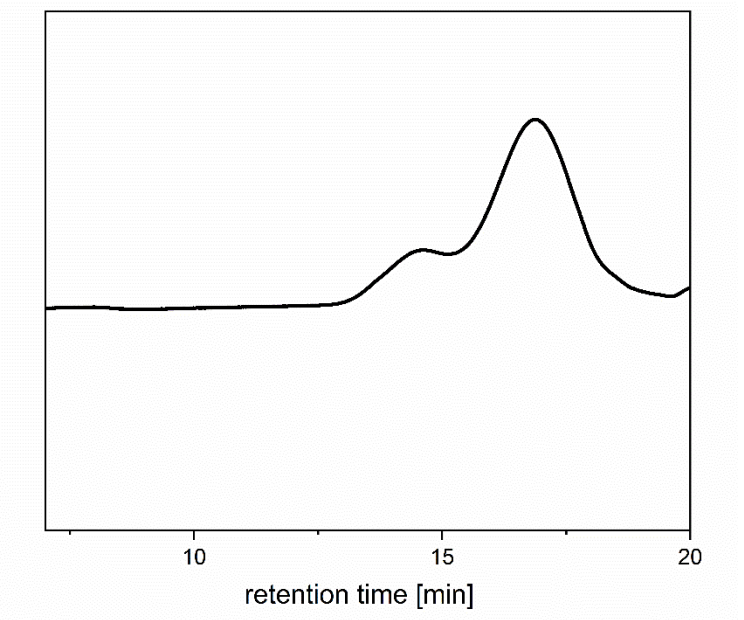

*GPC trace of ROP approach of **1** with $Sn(Oct)_2$.*

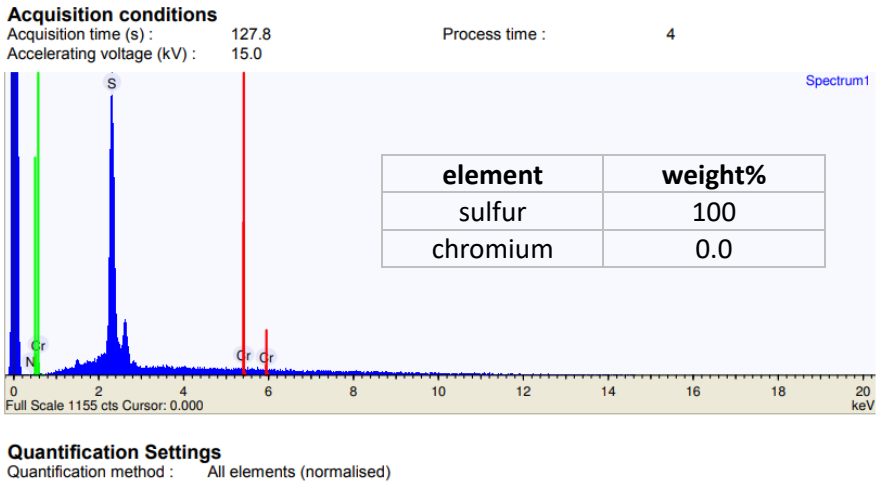

*EDX data of sulfonamide protected homopolymer of **1** ((salen)Cr(III) catalyst/**1** ratio of 1:100).*

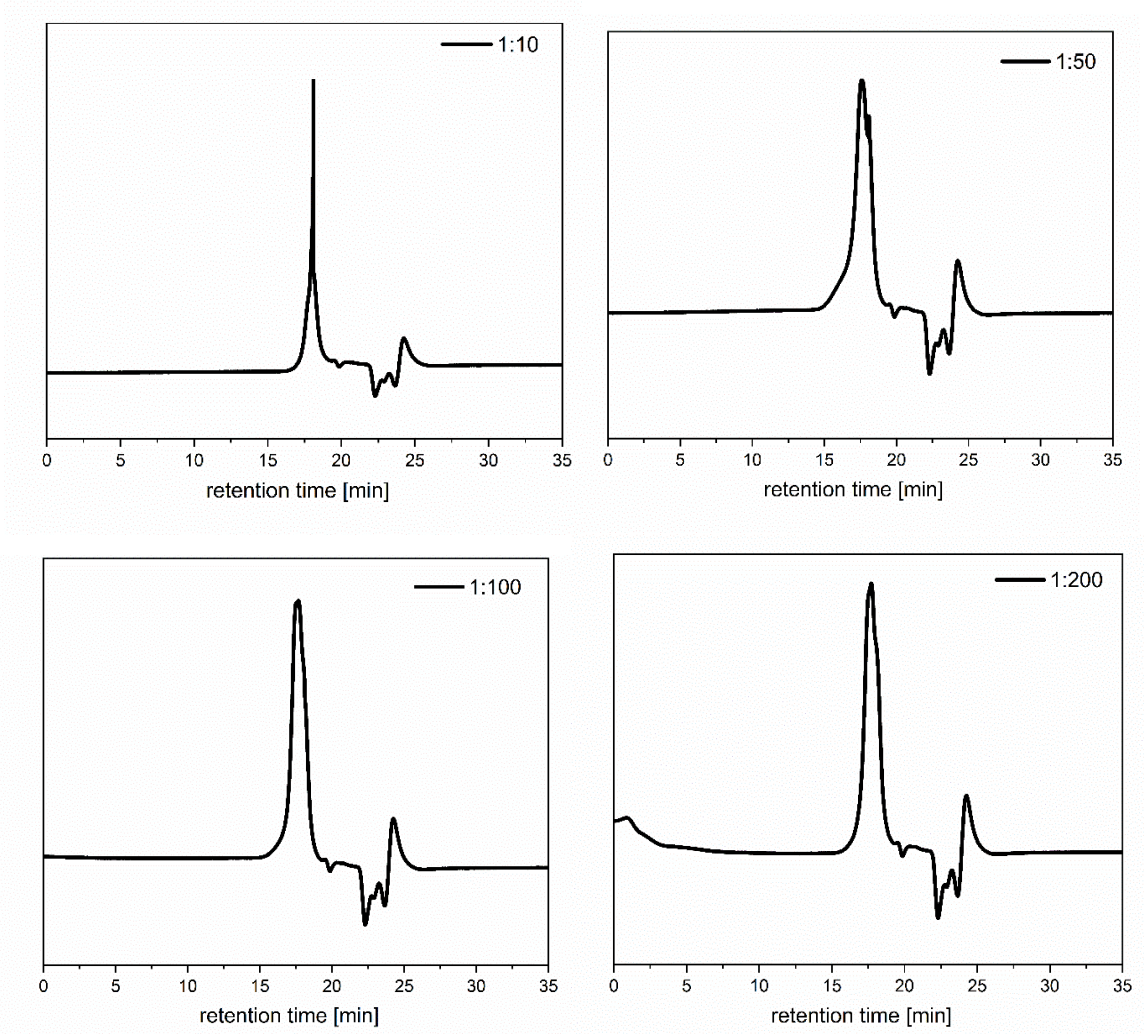

*GPC traces of sulfonamide protected homopolymers of **1** ((salen)Cr(III) catalyst/**1** ratios of 1/10, 1/50, 1/100, 1/200).*

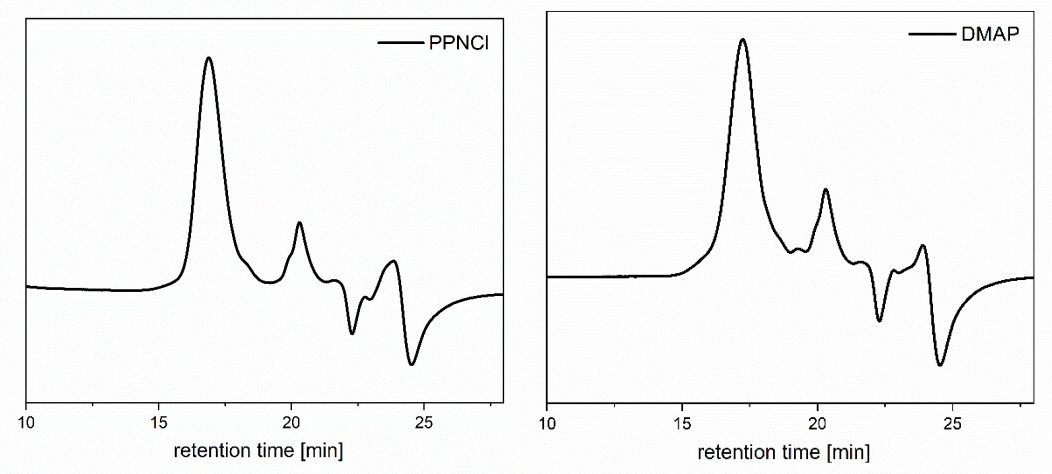

*GPC traces of ROP approaches of **1** with PPNCl and DMAP ((salen)Cr(III) catalyst/**1** ratios of 1/100).*

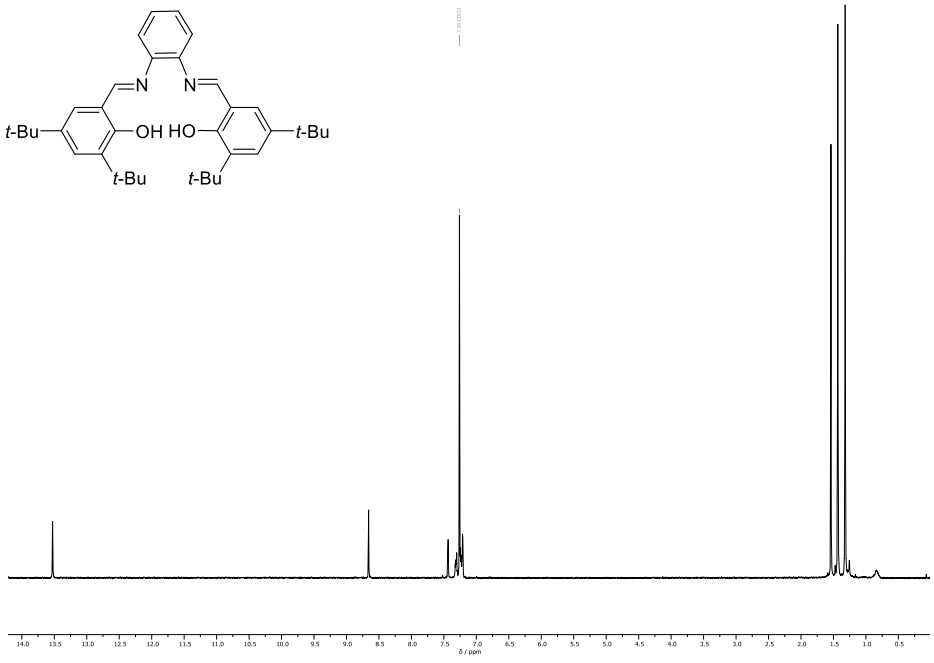

^{1}H-NMR spectrum of achiral (salen) ligand.

7.4.3 Post-polymerization functionalized homopolymers of 1

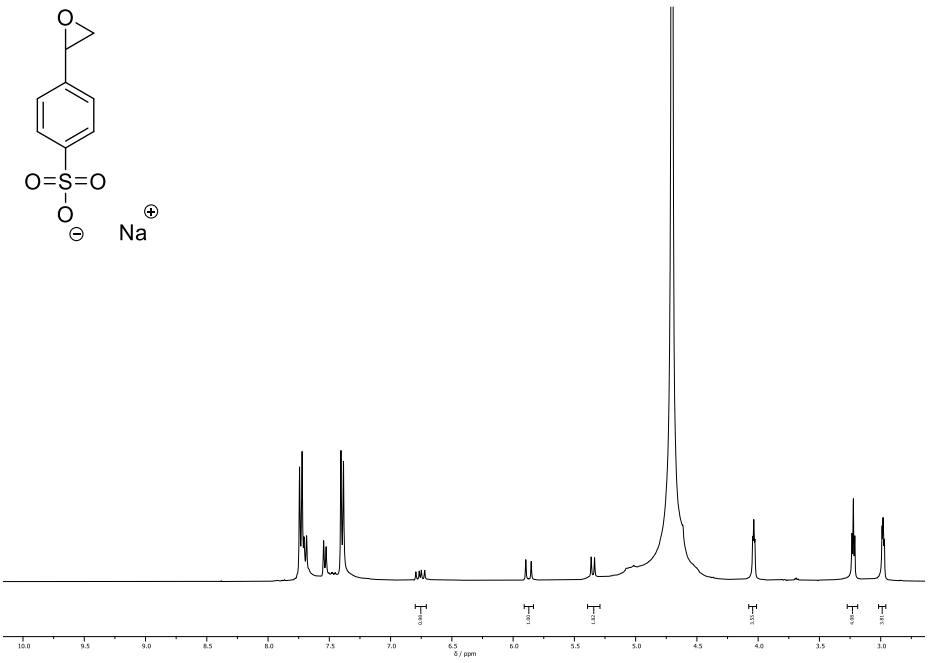

Crude ^{1}H-NMR spectrum of sodium vinylsulfonate epoxidation with DMDO.

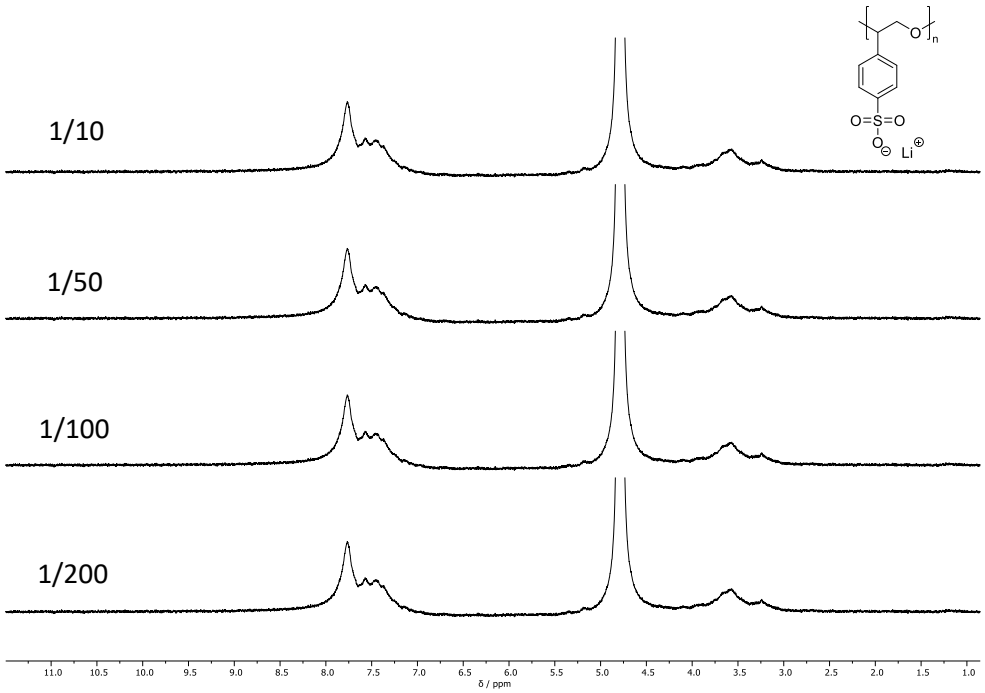

*^{1}H-NMR spectra of target SICPE ((salen)Cr(III) catalyst/**1** ratios of 1/10, 1/50, 1/100, 1/200).*

7.4.4 Alternative monomer structures

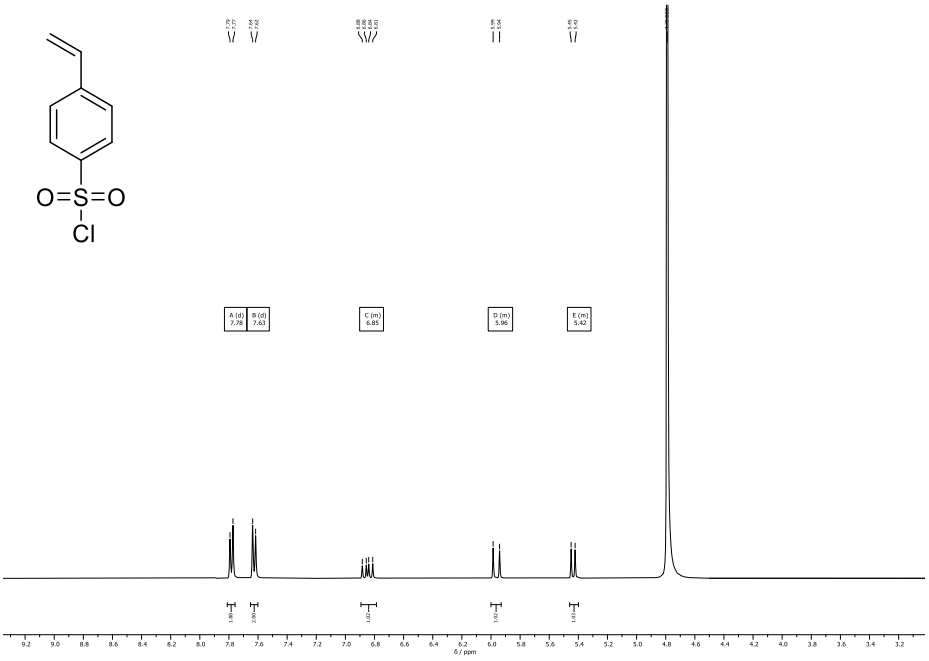

[1]H-NMR spectrum of chlorosulfonyl functionalized styrene.

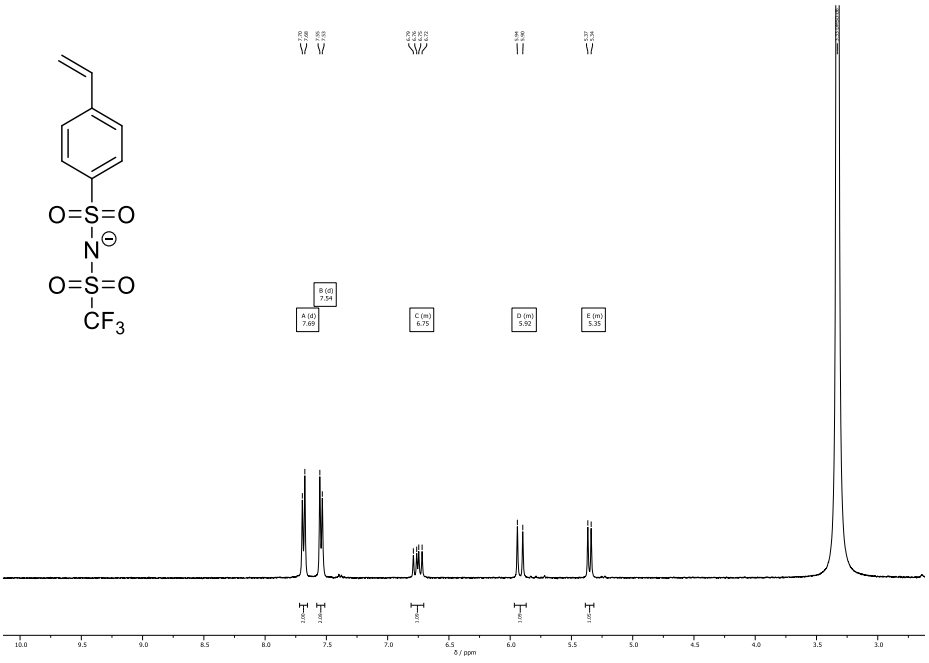

[1]H-NMR spectrum of TFSI functionalized styrene.

7.4.5 Copolymerization with SO and PEG 2000

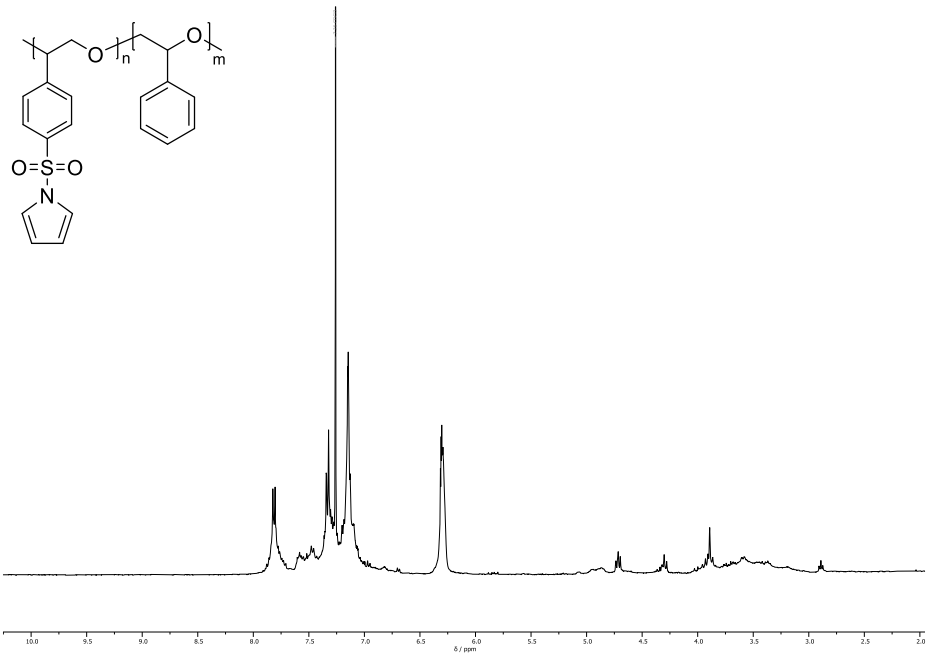

*^{1}H-NMR spectrum of copolymer **2** before post-polymerization functionalization.*

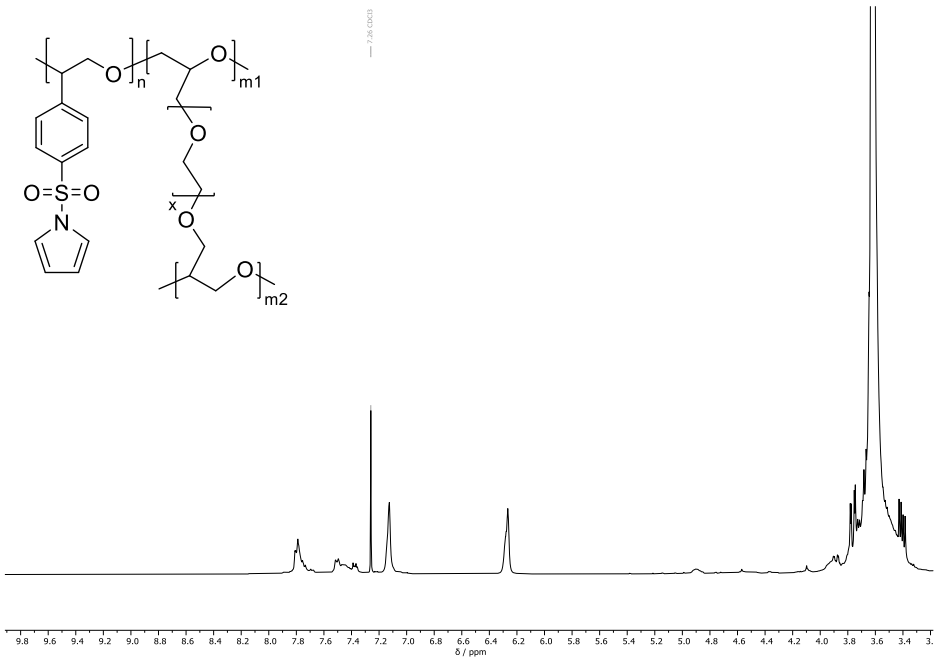

*^{1}H-NMR spectrum of copolymer **3** before post-polymerization functionalization.*

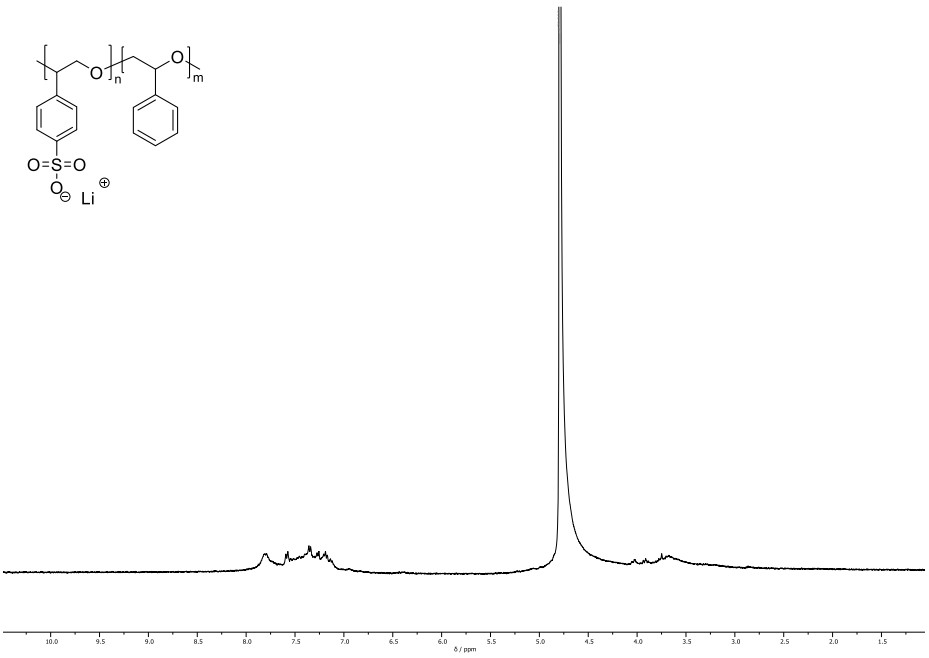

*^{1}H-NMR of copolymer **2** after post-polymerization functionalization.*

.

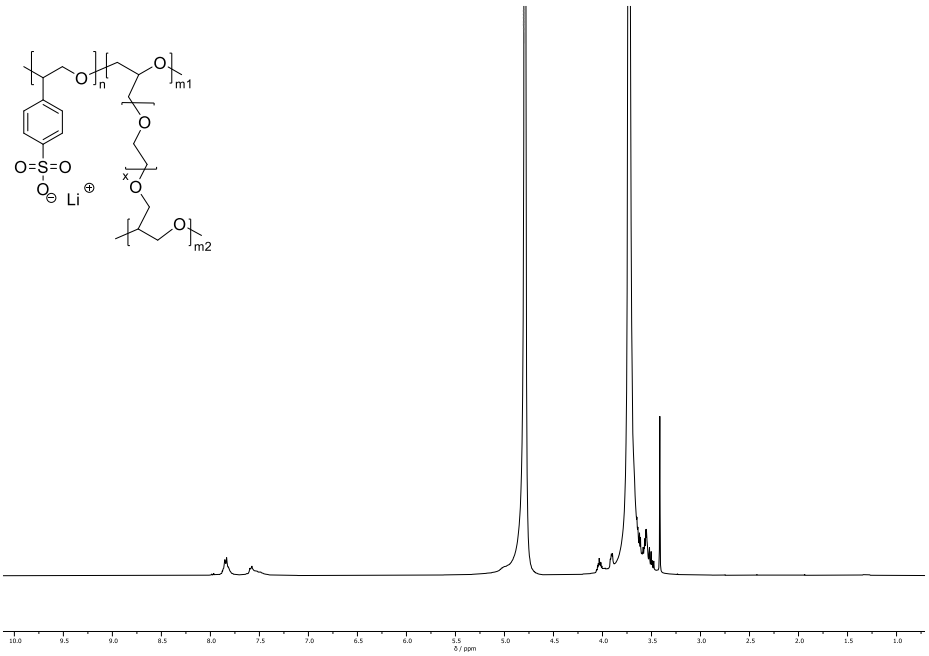

*^{1}H-NMR of copolymer **3** after post-polymerization functionalization.*

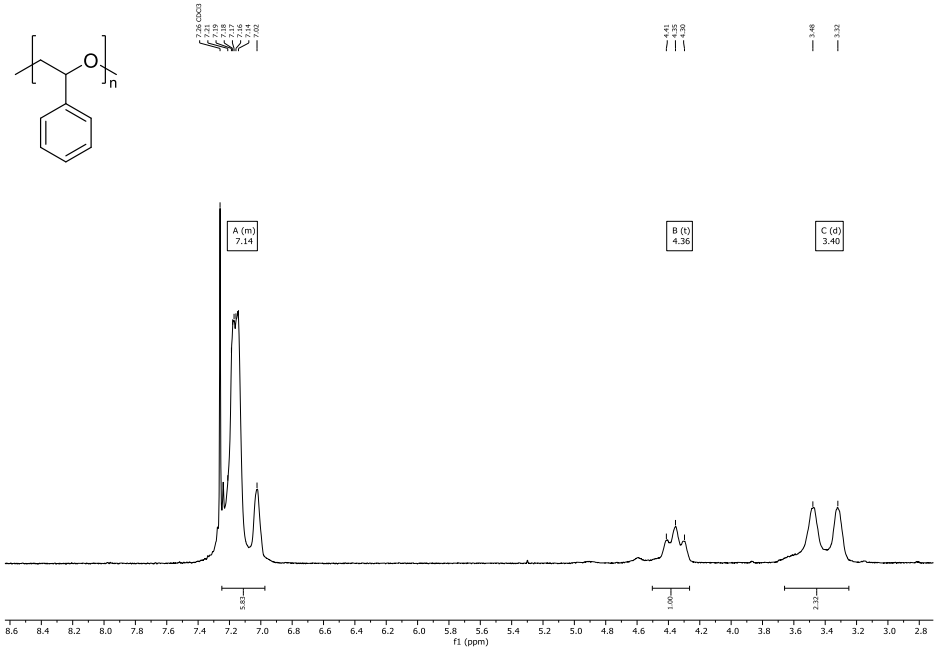

*^{1}H-NMR spectrum of **PSO**.*

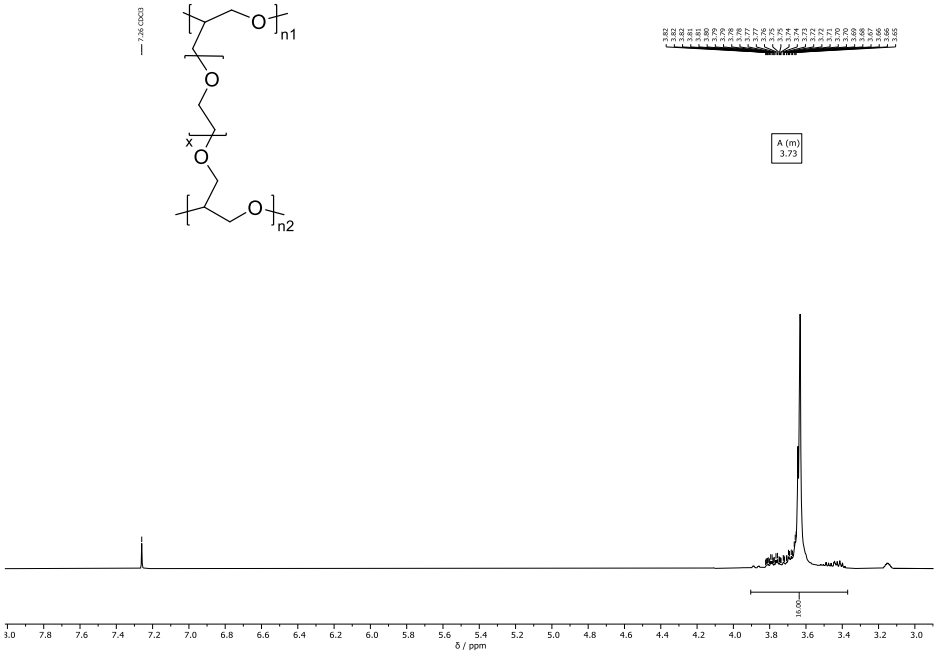

*^{1}H-NMR spectrum of **PEG 2000**.*

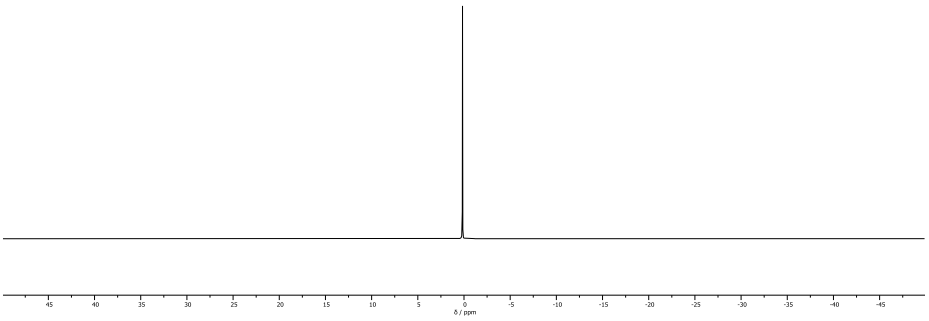

*^{7}Li-NMR spectrum of copolymer **2** after post-polymerization functionalization.*

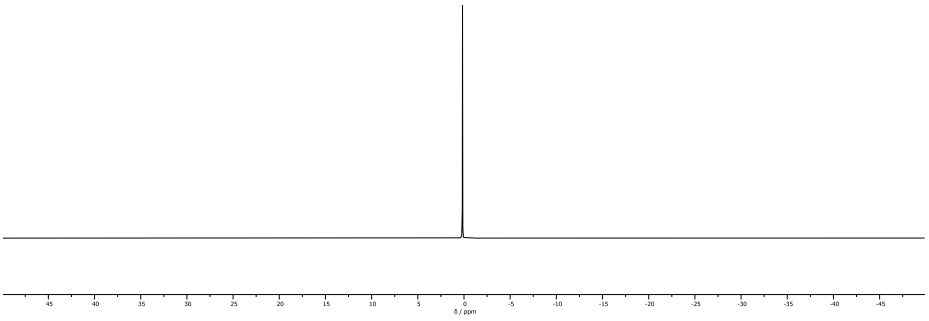

*^{7}Li-NMR spectrum of copolymer **3** after post-polymerization functionalization.*

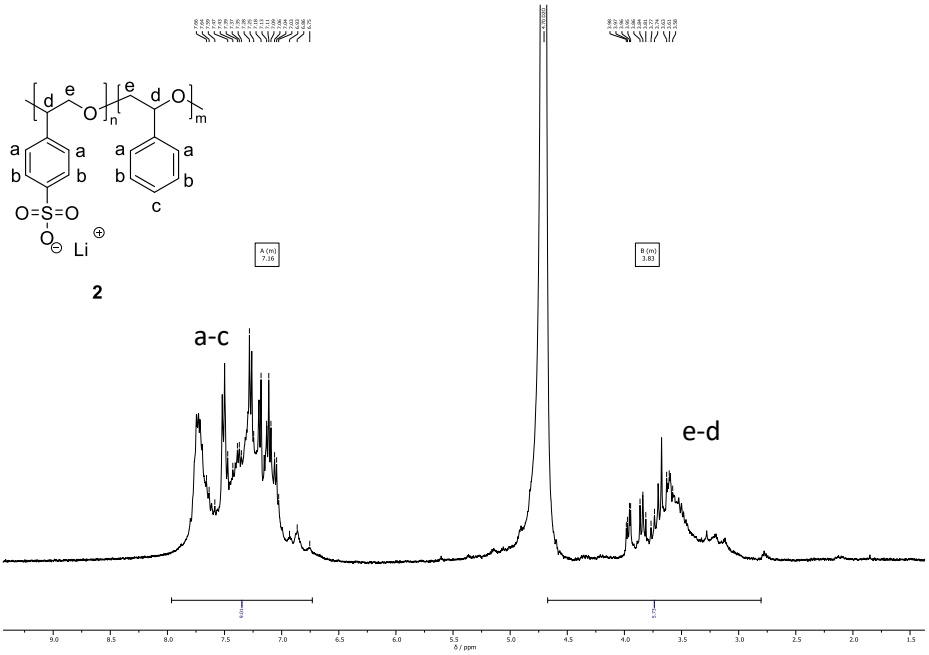

2

Monomer/comonomer ratio calculation for copolymer **2**:
9 aromatic H-atoms: 4 H-atoms from **1**, 5 H-atoms from SO
6 aliphatic H-atoms: 3 H-atoms from **1**, 3 H-atoms from SO → 1:1 ratio.

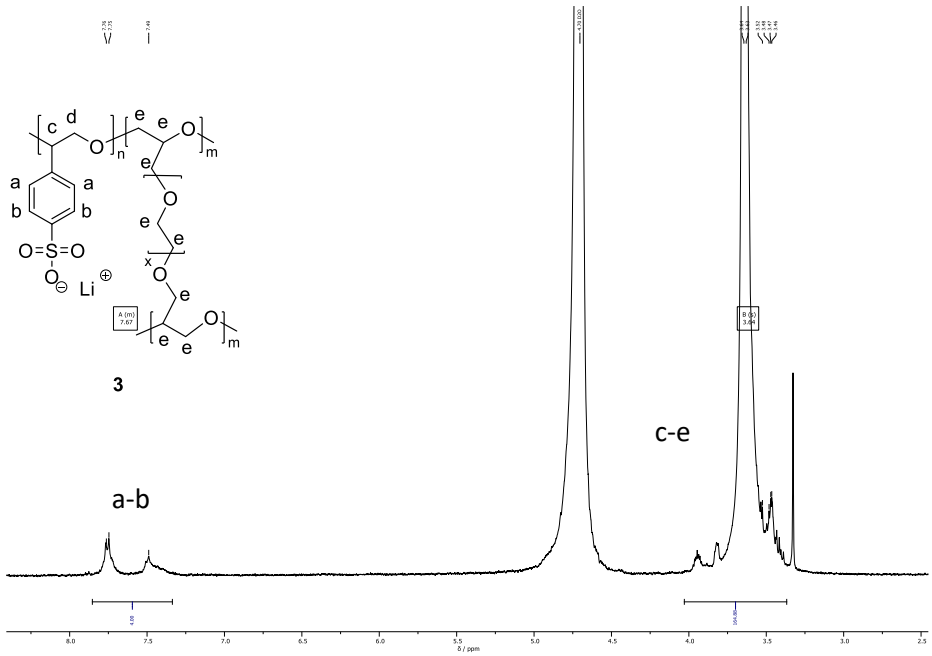

3

Monomer/comonomer ratio calculation for copolymer **2**:
4 aromatic H-atoms: 4 H-atoms from **1**
165 aliphatic H-atoms: 3 H-atoms from **1**, 162 H-atoms from PEG 2000 referring to 14 H-atoms per monomer structure → 1:12 ratio.

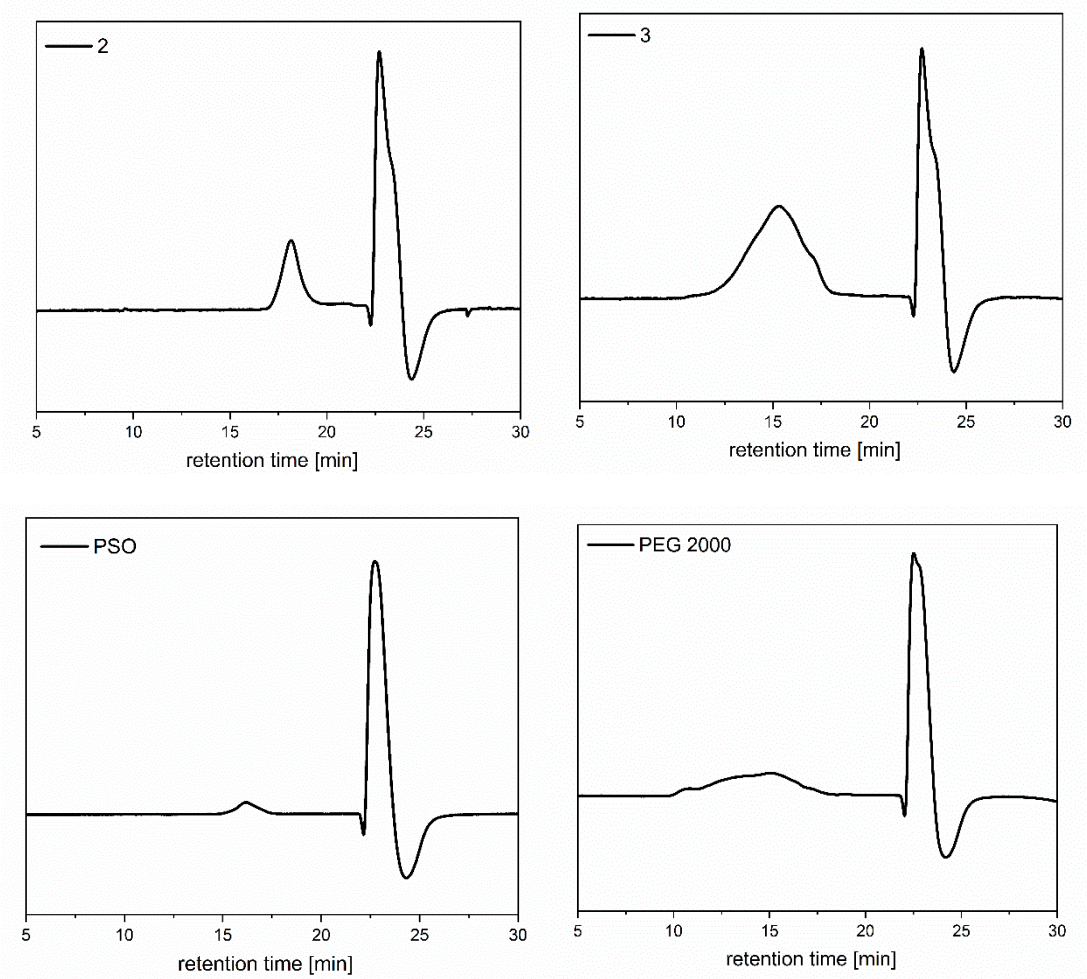

*GPC traces of target SICPE ((salen)Cr(III) catalyst/**1** ratios 1/100), the copolymers **2** and **3** ((salen)Cr(III) catalyst/**1**/comonomer ratios 1/100/100), PSO and PEG 2000.*

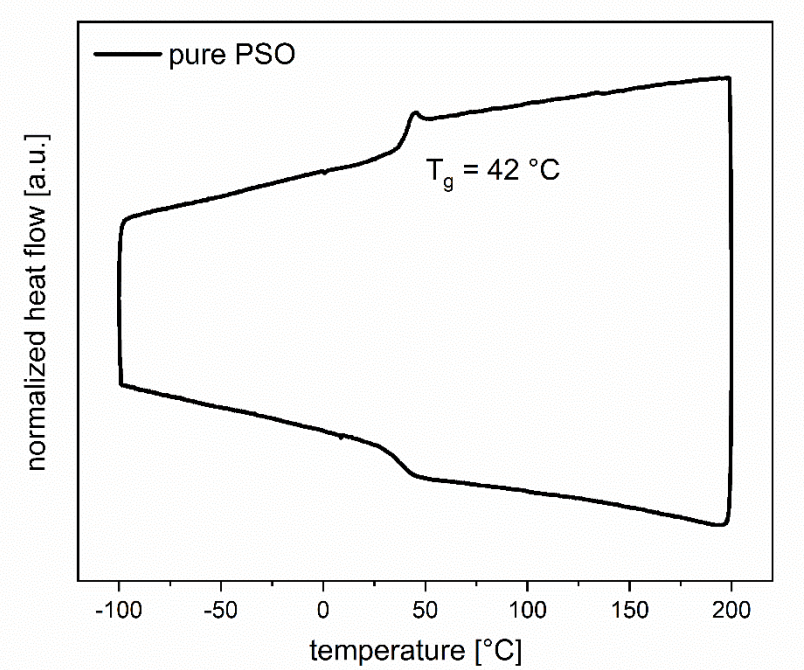

DSC measurement of pure PSO.

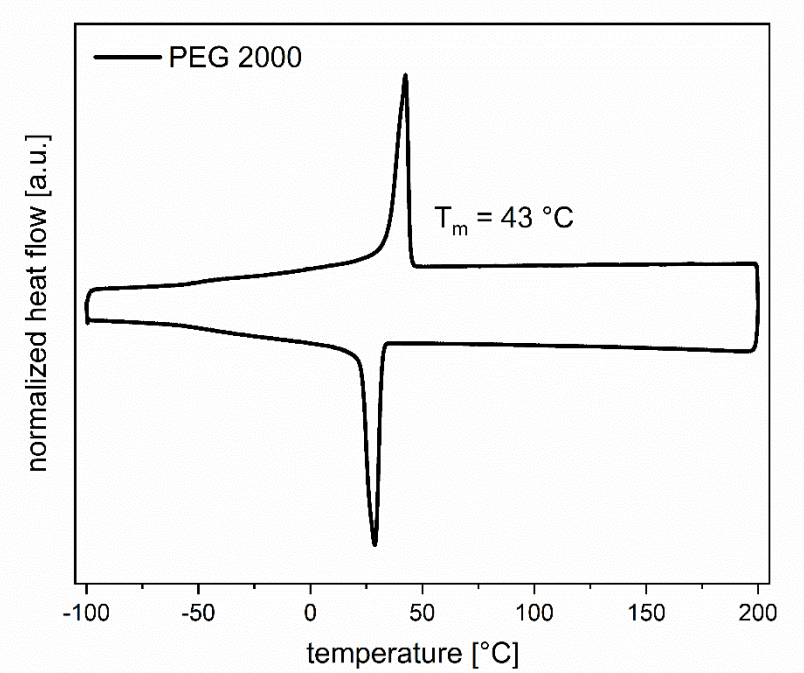

DSC measurement of pure PEG 2000.

7.4.6 Sodium solid-state battery

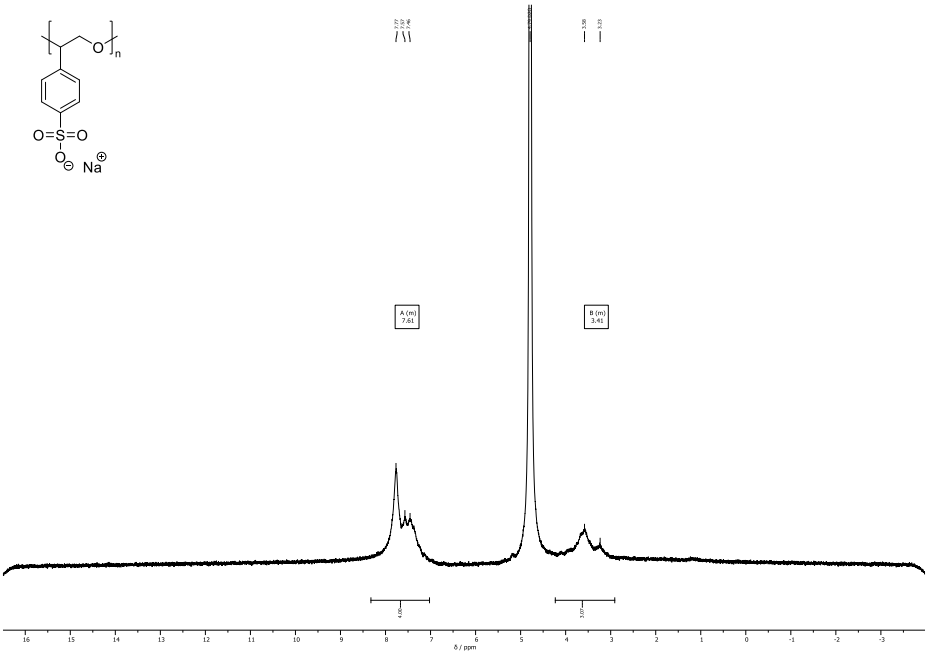

^{1}H-NMR of sodium sulfonate SICPE.

8. List of abbreviations

1-((4-(oxirane-2-yl)phenyl)sulfonyl)-1*H*-pyrrole (1)

acetonitrile (MeCN)

activated chain-end (ACE)

activated monomer (AM)

argyrodite-type Li6PS5X (LPS)

all-solid-state-batteries (ASSBs)

argyrodite-type Li6PS5X (LPS)

atom transfer radical polymerization (ATRP)

N,N'-bis(3,5-di-tert-butylsalicylidene)-1,2-cyclohexanediamino (salen)

bis(2,2,2-trifluoroethyl) carbonate (HFDEC)

bis(triphenylphosphine)iminium chloride (PPNCl)

brominated poly(phenylene oxide) (BPPO)

n-buthyllithium (n-BuLi)

copolymers of PVDF and hexafluoropropylene (PVDF-co-HFP)

coupling constant (J)

cyclic voltammetry (CV)

density functional theory (DFT)

diethylene carbonate (DEC)

differential scanning calorimetry (DSC)

diffusion ordered (DOSY)

β-diimine (BDI)

dimethylcarbonate (DMC)

4-dimethylaminopyridine (DMAP)

dimethyl sulfoxide (DMSO)

electrochemical impedance spectroscopy (EIS)

electronic vehicle (EV)

electrospray ionization mass spectrometry (ESI-MS)

enantiomeric excess (ee)

energy-dispersive X-ray (EDX)

equivalents (eq.)

ethylene carbonate (EC)

ethylene oxide (EO)

β-fluorinated sulfone (TFPMS)

fluorosulfonyl isocyanate (FI)

Fourier-transform infrared (FT-IR)

gel permeation chromatography (GPC)

glass transition temperature (Tg)

lithium bis(trifluoromethanesulfonyl)imide (LiTFSI)

lithium hydroxide (LiOH)

lithium-ion battery (LIB)

lithium oxalate polyacrylic acid borate (LiOPAAB)

lithium poly (perfluoroalkylsulfonyl)imide (LiPFSI)

lithium poly (4-styrenesulfonyl(trifluoromethylsulfonyl)imide) (LiPSTFSI)

lithium poly(4-vinylphenol)phenolate borate (LiPVPPB)

$LiFePO_4$ (LFP)

$LiNi_{0.8}Co_{0.15}Al_{0.05}O2$ (NCA)

$LiNi_{0.76}Mn_{0.14}Co_{0.10}O_2$ (NMC)

$LiMn_2O_4$ (LMO)

$Li_{10}GeP_2S_{12}$ (LGPS)

$Li_7La_3Zr_2O_{12}$ (LLZO)

$Li_{3x}La_{(2/3)-x}V'_{(1/3)-2x}TiO_3$ (LLTO)

$Li_{1+x}Al_xTi_{2-x}(PO_4)_3$ (LATP)

$LiA_2^{IV}(PO_4)_3$ (with A^{IV} = Ti, Zr, Ge, Hf) (NASICON)

$Li_{1.5}Al_{0.5}Ge_{1.5}(PO_4)_3$ (LAGP)

$Li_xPO_yN_z$ (LiPON)

meta-chloroperoxybenzoic acid (*m*-CPBA)

melting temperature (Tm)

methanol (MeOH)

methyl methacrylate (MMA)

N-methylpyrrolidine (NMP)

melting temperature (Tm)

nuclear magnetic resonance (NMR)

poly (acrylonitrile) (PAN)

poly (2-acrylamido-2-methylpropanesulfonic acid) (LiPAMPS)

polyethylene (PE)

poly (ethylene glycol) diglycidyl ether (PEG 2000)

poly ethylene glycol (PEG)

poly ethyleneimine (PEI)

poly ethylene oxide (PEO)

poly[ethylene oxide-co-2-(2-methoxyethoxy)ethyl glycidyl ether] (PEO/MEEGE)

poly(ethylene terephthalate) (PET)

potassium hydroxide (KOH)

poly (lactic acid) (PLA)

poly (lithium acrylate) (PLA)

poly (lithium vinylsulfonate) (PLVS)

poly(lithium sorbate) (poly(Li-Sorb))

poly (methyl methacrylate) (PMMA)

propylene carbonate (PC)

poly propylene (PP)

propylene oxide (PO)

poly propylene oxide (PPO)

poly 2-((propionyloxy)-methyl) lithium acrylate graft PEG950 (PPMALi-g-PEG950)

poly styrene (PS)

poly (styrene oxide) (PSO)

poly (vinyl chloride) (PVC)

poly vinylidene fluoride (PVDF)

poly (vinylpyrrolidone) (PVP)

reversible addition−fragmentation chain transfer (RAFT)

ring-opening-polymerization (ROP)

scandium(III) triflate (Sc-triflate)

single ion-conducting polymer electrolyte (SICPE)

sodium hydroxide (NaOH)

sodium hydride (NaH)

solid electrolyte interface (SEI)

solid polymer electrolyte (SPE)

styrene oxide (SO)

tetrahydrofuran (THF)

tetramethylene sulfone (TMS)

N,N,N',N'-tetramethylethylenediamine (TMEDA)

2,2,6,6-tetramethyl-1-piperidinyloxy (TEMPO)

tin(II) 2-ethylhexanoate (Sn(Oct)2)

titanium isopropoxide (Ti(OiPr)4)

thermogravimetric analysis (TGA)

thin layer chromatography (TLC)

thio-lithium ion superconductors (LiSICONs)

ultraviolet-visible (UV-Vis)

9. References

[1] K. Mohamed, Y. Nassar, H. J. El-Khozondar , E. Monaem, Z. Rajab, E. Yaghoubi, E. Yaghoubi, *Int. J. Electr. Eng. and Sustain.* **2024**, *2*, 1-20.

[2] J. B. Goodenough, *Acc. Chem. Res.* **2013**, *46*, 1053-1061.

[3] S. Chen, K. Wen, J. Fan, Y. Bando, D. Golberg, *J. Mater. Chem. A* **2018**, *6*, 11631-11663.

[4] H. Bode, *Lead-acid batteries*, John Wiley and Sons, Inc.,New York, NY, United States, **1977**.

[5] M. S. Whittingham, *Chem. Rev.* **2004**, *104*, 4271-4302.

[6] M. S. Whittingham, *Prog. Solid State Chem.* **1978**, *12*, 41-99.

[7] C. M. Julien, *Mater. Sci. Eng. R Rep.* **2003**, *40*, 47-102.

[8] M. S. Whittingham, *The Nobel Prizes 2019* **2022**, 184.

[9] T. Zheng, S. T. Boles, *Prog. Energy* **2023**, *5*, 032001.

[10] B. M. L. Rao, R. W. Francis, H. A. Christopher, *J. Electrochem. Society* **1977**, *124*, 1490.

[11] J. B. Goodenough, *J. Power Sources* **2007**, *174*, 996-1000.

[12] K. Mizushima, P. C. Jones, P. J. Wiseman, J. B. Goodenough, *Solid State Ionics* **1981**, *3-4*, 171-174.

[13] K. Mizushima, P. C. Jones, P. J. Wiseman, J. B. Goodenough, *MRS Bulletin* **1980**, *15*, 783-789.

[14] R. F. Service, *Science* **2019**, *366*, 292-292.

[15] C. Lin, J. Li, Z.-W. Yin, W. Huang, Q. Zhao, Q. Weng, Q. Liu, J. Sun, G. Chen, F. Pan, *Adv. Mater.* **2024**, *36*, 2307404.

[16] G. E. Blomgren, *J. Electrochem. Society* **2017**, *164*, A5019.

[17] H. Zhao, W.-Y. A. Lam, L. Sheng, L. Wang, P. Bai, Y. Yang, D. Ren, H. Xu, X. He, *Adv. Energy Mater.* **2022**, *12*, 2103894.

[18] H.-H. Ryu, H. H. Sun, S.-T. Myung, C. S. Yoon, Y.-K. Sun, *Energy Environ. Sci.* **2021**, *14*, 844-852.

[19] X. Zhang, H. Jia, L. Zou, Y. Xu, L. Mu, Z. Yang, M. H. Engelhard, J.-M. Kim, J. Hu, B. E. Matthews, C. Niu, C. Wang, H. Xin, F. Lin, W. Xu, *ACS Energy Lett.* **2021**, *6*, 1324-1332.

[20] Y. Wang, D. Zhao, K. Zhang, Y. Li, B. Xu, F. Liang, Y. Dai, Y. Yao, *J. Energy Storage* **2020**, *28*, 101182.

[21] W. Zhao, J. Zheng, L. Zou, H. Jia, B. Liu, H. Wang, M. H. Engelhard, C. Wang, W. Xu, Y. Yang, J.-G. Zhang, *Adv. Energy Mater.* **2018**, *8*, 1800297.

[22] J. H. Kim, *Front. batter. electrochem* **2022**, *1*.

[23] J. Asenbauer, T. Eisenmann, M. Kuenzel, A. Kazzazi, Z. Chen, D. Bresser, *Sustainable Energy Fuels* **2020**, *4*, 5387-5416.

[24] R. Yazami, *J. Power Sources* **2001**, *97-98*, 33-38.

[25] R. Yazami, P. Touzain, *J. Power Sources* **1983**, *9*, 365-371.

[26] K. Zaghib, X. Song, A. Guerfi, R. Rioux, K. Kinoshita, *J. Power Sources* **2003**, *119-121*, 8-15.

[27] C. Daniel, J. O. Besenhard, *Handbook of battery materials*, John Wiley & Sons, **2012**.

[28] L. Xing, X. Zheng, M. Schroeder, J. Alvarado, A. von Wald Cresce, K. Xu, Q. Li, W. Li, *Acc. Chem. Res.* **2018**, *51*, 282-289.

[29] V. A. Agubra, J. W. Fergus, *J. Power Sources* **2014**, *268*, 153-162.

[30] A. Yoshino, in *Lithium-Ion Batteries* (Ed.: G. Pistoia), Elsevier, Amsterdam, **2014**, pp. 1-20.

[31] P. B. Balbuena, Y. X. Wang, *Lithium-ion batteries: solid-electrolyte interphase*, World Scientific, **2004**.

[32] S. Ogawa, Profile of Akira Yoshino and overview of his invention of the LIB.

[33] M. Yoshio, H. Nakamura, N. Dimov, *Lithium Ion Rechargeable Batteries: Materials, Technology, and New Applications* **2009**, 163-178.

[34] T. Melin, R. Lundström, E. J. Berg, *Adv. Mater. Interfaces* **2022**, *9*, 2101258.

[35] H. Zhang, Y. Yang, D. Ren, L. Wang, X. He, *Energy Storage Materials* **2021**, *36*, 147-170.

[36] S. T. Mayer, J. H. Feikert, J. L. Kaschmitter, in *Conference: American Institute of Aeronautics and Astronautics conference on small satellites,Logan, UT (United States),13-16 Sep 1993; Other Information: PBD: 16 Aug 1993*, United States, **1993**, p. Medium: ED; Size: 32 p.

[37] Y. Nishi, *J. Power Sources* **2001**, *100*, 101-106.

[38] B. Scrosati, *J. Solid State Electrochem.* **2011**, *15*, 1623-1630.

[39] M. Armand, J. M. Tarascon, *Nature* **2008**, *451*, 652-657.

[40] D. Karabelli, K. P. Birke, M. Weeber, *Batteries* **2021**, *7*..

[41] M. Jia, M. Khurram Tufail, X. Guo, *ChemSusChem* **2023**, *16*, e202201801.

[42] D. Lin, Y. Liu, Y. Cui, *Nat. Nanotechnol.* **2017**, *12*, 194-206.

[43] R. Wang, W. Cui, F. Chu, F. Wu, *J. Energy Chem.* **2020**, *48*, 145-159.

[44] K. Xu, *Chem. Rev.* **2004**, *104*, 4303-4418.

[45] O. B. Chae, B. L. Lucht, *Adv. Energy Mater.* **2023**, *13*, 2203791.

[46] D. Aurbach, E. Zinigrad, Y. Cohen, H. Teller, *Solid State Ionics* **2002**, *148*, 405-416.

[47] D. Aurbach, A. Zaban, A. Schechter, Y. Ein-Eli, E. Zinigrad, B. Markovsky, *J. Electrochem. Soc.* **1995**, *142*, 2873.

[48] X.-B. Cheng, R. Zhang, C.-Z. Zhao, F. Wei, J.-G. Zhang, Q. Zhang, *Adv. Sci.* **2016**, *3*, 1500213.

[49] S. Wang, H. Xu, W. Li, A. Dolocan, A. Manthiram, *J. Am. Chem. Soc.* **2018**, *140*, 250-257.

[50] M. Jia, N. Zhao, H. Huo, X. Guo, *Electrochem. Energy Rev.* **2020**, *3*, 656-689.

[51] A. Miura, N. C. Rosero-Navarro, A. Sakuda, K. Tadanaga, N. H. H. Phuc, A. Matsuda, N. Machida, A. Hayashi, M. Tatsumisago, *Nat. Rev. Chem.* **2019**, *3*, 189-198.

[52] J. Zhang, J. Zhao, L. Yue, Q. Wang, J. Chai, Z. Liu, X. Zhou, H. Li, Y. Guo, G. Cui, L. Chen, *Adv. Energy Mater.* **2015**, *5*, 1501082.

[53] D. Park, H. Park, Y. Lee, S.-O. Kim, H.-G. Jung, K. Y. Chung, J. H. Shim, S. Yu, *ACS Appl. Mater. Interfaces* **2020**, *12*, 34806-34814.

[54] K. J. Kim, M. Balaish, M. Wadaguchi, L. Kong, J. L. M. Rupp, *Adv. Energy Mater.* **2021**, *11*, 2002689.

[55] P. Albertus, S. Babinec, S. Litzelman, A. Newman, *Nat. Energy* **2018**, *3*, 16-21.

[56] D. Lin, P. Y. Yuen, Y. Liu, W. Liu, N. Liu, R. H. Dauskardt, Y. Cui, *Adv. Mater.* **2018**, *30*, 1802661.

[57] D. Mecerreyes, L. Porcarelli, N. Casado, *Macromol. Chem. Phys.* **2020**, *221*, 1900490.

[58] D. Mecerreyes, N. Casado, I. Villaluenga, M. Forsyth, *Macromolecules* **2024**, *57*, 3013-3025.

[59] C. M. Costa, E. Lizundia, S. Lanceros-Méndez, *Prog. Energy Combust. Sci.* **2020**, *79*, 100846.

[60] K. S. Ngai, S. Ramesh, K. Ramesh, J. C. Juan, *Ionics* **2016**, *22*, 1259-1279.

[61] B. Lestriez, *C. R. Chim.* **2010**, *13*, 1341-1350.

[62] U. S. Schubert, A. Winter, G. R. Newkome, *An Introduction to Redox Polymers for Energy-Storage Applications*, John Wiley & Sons, **2023**.

[63] P. Yao, H. Yu, Z. Ding, Y. Liu, J. Lu, M. Lavorgna, J. Wu, X. Liu, *Front. Chem.* **2019**, *7*.

[64] K. Liu, Y. Wang, D.-I. Stroe, C. Fernandez, J. M. Guerrero, S. Wang, *State estimation strategies in lithium-ion battery management systems*, Elsevier, **2023**.

[65] T. Ohzuku, Y. Iwakoshi, K. Sawai, *J. Electrochem. Soc.* **1993**, *140*, 2490.

[66] J. W. Fergus, *J. Power Sources* **2010**, *195*, 939-954.

[67] L. Wang, B. Chen, J. Ma, G. Cui, L. Chen, *Chem. Soc. Rev.* **2018**, *47*, 6505-6602.

[68] M. Thackeray, A. De Kock, W. David, *Mater. Bulletin* **1993**, *28*, 1041-1049.

[69] X. Hu, F. Feng, K. Liu, L. Zhang, J. Xie, B. Liu, *Renewable Sustainable Energy Rev.* **2019**, *114*, 109334.

[70] M. Lu, W. Yang, Y. Deng, Q. Xu, *Int. J. Energy Res.* **2020**, *44*, 2604-2616.

[71] L. Ma, W. Xie, Y. Zhang, *Appl. Sci.* **2019**, *9*, 1085.

[72] Y. Chen, Y. Kang, Y. Zhao, L. Wang, J. Liu, Y. Li, Z. Liang, X. He, X. Li, N. Tavajohi, B. Li, *J. Energy Chem.* **2021**, *59*, 83-99.

[73] Y. K. Liu, C. Z. Zhao, J. Du, X. Q. Zhang, A. B. Chen, Q. Zhang, *Small* **2023**, *19*, 2205315.

[74] M. Nazri, in *Lithium Batteries: Science and Technology* (Eds.: G.-A. Nazri, G. Pistoia), Springer US, Boston, MA, **2003**, pp. 509-529.

[75] A. von Wald Cresce, K. Xu, *Carbon Energy* **2021**, *3*, 721-751.

[76] F. Decker, *Electrochemistry Encyclopedia* **2005**.

[77] M. Planté, *The London, Edinburgh, and Dublin Philosophical Magazine and Journal of Science* **1860**, *19*, 468-469.

[78] P. Ruetschi, *J. Power Sources* **1977**, *2*, 3-120.

[79] U. Köhler, C. Antonius, P. Bäuerlein, *J. Power Sources* **2004**, *127*, 45-52.

[80] M. B. Lim, T. N. Lambert, B. R. Chalamala, *Mat. Sci. Eng. R Rep.* **2021**, *143*, 100593.

[81] A. Eftekhari, *Adv. Energy Mater.* **2018**, *8*, 1801156.

[82] D. M. Seo, D. Chalasani, B. S. Parimalam, R. Kadam, M. Nie, B. L. Lucht, *ECS Electrochem. Lett.* **2014**, *3*, A91.

[83] R. Fong, U. von Sacken, J. R. Dahn, *J. Electrochem. Soc.* **1990**, *137*, 2009.

[84] D. Aurbach, M. Daroux, P. Faguy, E. Yeager, *J. Electrochem. Soc.* **1987**, *134*, 1611.

[85] Y. Ein-Eli, *Electrochem. Solid-State Lett.* **1999**, *2*, 212.

[86] G. V. Zhuang, P. N. Ross, *Electrochem. Solid-State Lett.* **2003**, *6*, A136.

[87] D. Guyomard, J. M. Tarascon, *J. Electrochem. Soc.* **1993**, *140*, 3071.

[88] S. Miyoshi, H. Nagano, T. Fukuda, T. Kurihara, M. Watanabe, S. Ida, T. Ishihara, *J. Electrochem. Soc.* **2016**, *163*, A1206.

[89] K. Shukla, V. C. Srivastava, *RSC Adv.* **2016**, *6*, 32624-32645.

[90] E. R. Logan, E. M. Tonita, K. L. Gering, L. Ma, M. K. G. Bauer, J. Li, L. Y. Beaulieu, J. R. Dahn, *J. Electrochem. Soc.* **2018**, *165*, A705.

[91] M. He, C.-C. Su, Z. Feng, L. Zeng, T. Wu, M. J. Bedzyk, P. Fenter, Y. Wang, Z. Zhang, *Adv. Energy Mater.* **2017**, *7*, 1700109.

[92] C.-C. Su, M. He, P. Redfern, L. A. Curtiss, C. Liao, L. Zhang, A. K. Burrell, Z. Zhang, *ChemElectroChem* **2016**, *3*, 790-797.

[93] H. Duncan, N. Salem, Y. Abu-Lebdeh, *J. Electrochem. Soc.* **2013**, *160*, A838.

[94] W. Li, B. Song, A. Manthiram, *Chem. Soc. Rev.* **2017**, *46*, 3006-3059.

[95] V. Aravindan, J. Gnanaraj, S. Madhavi, H. K. Liu, *Chem-Eur. J.* **2011**, *17*, 14326-14346.

[96] D. Aurbach, Y. Ein-Eli, B. Markovsky, A. Zaban, S. Luski, Y. Carmeli, H. Yamin, *J. Electrochem. Soc.* **1995**, *142*, 2882.

[97] C. Angell, C. Liu, E. Sanchez, *Nature* **1993**, *362*, 137-139.

[98] G. Newman, *J. Electrochem. Soc* **1980**, *127*, 2025.

[99] S. S. Zhang, K. Xu, T. R. Jow, *J. Electrochem. Soc.* **2002**, *149*, A586.

[100] O. Bushkova, T. Yaroslavtseva, Y. A. Dobrovolsky, *Russ. J. Electrochem.* **2017**, *53*, 677-699.

[101] M. Schmidt, U. Heider, A. Kuehner, R. Oesten, M. Jungnitz, N. Ignat'Ev, P. Sartori, *J. Power Sources* **2001**, *97*, 557-560.

[102] M. Ue, T. Fujii, Z.-B. Zhou, M. Takeda, S. Kinoshita, *Solid State Ionics* **2006**, *177*, 323-331.

[103] K. Hayashi, Y. Nemoto, S.-i. Tobishima, J.-i. Yamaki, *Electrochim. Acta* **1999**, *44*, 2337-2344.

[104] M. Ding, K. Xu, S. Zhang, K. Amine, G. Henriksen, T. Jow, *J. Electrochem. Soc.* **2001**, *148*, A1196.

[105] N. Takami, T. Ohsaki, K. Inada, *J. Electrochem. Soc.* **1992**, *139*, 1849.

[106] H. Akashi, K. i. Tanaka, K. Sekai, *J. Electrochem. Soc.* **1998**, *145*, 881.

[107] D. H. Jang, Y. J. Shin, S. M. Oh, *J. Electrochem. Soc.* **1996**, *143*, 2204.

[108] L. J. Krause, W. Lamanna, J. Summerfield, M. Engle, G. Korba, R. Loch, R. Atanasoski, *J. Power Sources* **1997**, *68*, 320-325.

[109] V. Koch, J. Goldman, C. Mattos, M. Mulvaney, *J. Electrochem. Soc.* **1982**, *129*, 1.

[110] V. Koch, *J. Electrochem. Soc.* **1979**, *126*, 181.

[111] J. Foos, J. McVeigh, *J. Electrochem. Soc.* **1983**, *130*, 628.

[112] C. W. Walker, J. D. Cox, M. Salomon, *J. Electrochem. Soc.* **1996**, *143*, L80.

[113] K. Abraham, J. Goldman, D. Natwig, *J. Electrochem. Soc.* **1982**, *129*, 2404.

[114] N. Von Aspern, G. V. Röschenthaler, M. Winter, I. Cekic-Laskovic, *Angew. Chem., Int. Ed.* **2019**, *58*, 15978-16000.

[115] J. Foropoulos Jr, D. D. DesMarteau, *Inorg. Chem.* **1984**, *23*, 3720-3723.

[116] X. Huang, *J. Solid State Electrochem.* **2011**, *15*, 649-662.

[117] H. Zhang, M.-Y. Zhou, C.-E. Lin, B.-K. Zhu, *RSC Adv.* **2015**, *5*, 89848-89860.

[118] C. M. Costa, M. M. Silva, S. Lanceros-Méndez, *RSC Adv.* **2013**, *3*, 11404-11417.

[119] M. Weighall, *J. Power Sources* **1991**, *34*, 257-268.

[120] Y. Li, H. Pu, Y. Wei, *Electrochim. Acta* **2018**, *264*, 140-149.

[121] K. Gao, X. Hu, T. Yi, C. Dai, *Electrochim. Acta* **2006**, *52*, 443-449.

[122] S.-J. Gwon, J.-H. Choi, J.-Y. Sohn, Y.-E. Ihm, Y.-C. Nho, *Nuclear Instruments and Methods in Physics Research Section B: Beam Interactions with Materials and Atoms* **2009**, *267*, 3309-3313.

[123] J. Ko, B. Min, D.-W. Kim, K. Ryu, K. Kim, Y. Lee, S. Chang, *Electrochim. Acta* **2004**, *50*, 367-370.

[124] Q. Wang, B. Zhang, J. Zhang, Y. Yu, P. Hu, C. Zhang, G. Ding, Z. Liu, C. Zong, G. Cui, *Electrochim. Acta* **2015**, *157*, 191-198.

[125] S.-J. Chun, E.-S. Choi, E.-H. Lee, J. H. Kim, S.-Y. Lee, S.-Y. Lee, *J. Mater. Chem.* **2012**, *22*, 16618-16626.

[126] Y. Chen, S. Zhuo, Z. Li, C. Wang, *EnergyChem* **2020**, *2*, 100030.

[127] H. Shirakawa, E. J. Louis, A. G. MacDiarmid, C. K. Chiang, A. J. Heeger, *J. Chem. Soc., Chem. Commun.* **1977**, 578-580.

[128] O. A. Kozarenko, V. S. Dyadyun, M. S. Papakin, O. Y. Posudievsky, V. G. Koshechko, V. D. Pokhodenko, *Electrochim. Acta* **2015**, *184*, 111-116.

[129] A. G. Macdiarmid, S.-L. Mu, N. L. Somasiri, W. Wu, *Mol. Crysta. Liq. Cryst.* **1985**, *121*, 187-190.

[130] U. D. Chavan, P. Prajith, B. Kandasubramanian, *Chem. Eng. J. Adv.* **2022**, *12*, 100416.

[131] F. Wu, S. Wu, R. Chen, J. Chen, S. Chen, *Electrochem. Solid-State Lett.* **2010**, *13*, A29.

[132] L. Zhan, Z. Song, J. Zhang, J. Tang, H. Zhan, Y. Zhou, C. Zhan, *Electrochim. Acta* **2008**, *53*, 8319-8323.

[133] P. Jiménez, E. Levillain, O. Alévêque, D. Guyomard, B. Lestriez, J. Gaubicher, *Angew. Chem., Int. Ed.* **2017**, *56*, 1553-1556.

[134] V. Barsykov, V. Khomenko, *Mater. Sci. Appl. Chem.* **2010**.

[135] H. Chen, M. Ling, L. Hencz, H. Y. Ling, G. Li, Z. Lin, G. Liu, S. Zhang, *Chem. Rev.* **2018**, *118*, 8936-8982.

[136] V. A. Nguyen, C. Kuss, *J. Electrochem. Soc.* **2020**, *167*, 065501.

[137] N. H. Kwon, *Solid State Sciences* **2013**, *21*, 59-65.

[138] T.-H. Le, Y. Kim, H. Yoon, *Polymers* **2017**, *9*, 150.

[139] T. M. Higgins, S.-H. Park, P. J. King, C. Zhang, N. McEvoy, N. C. Berner, D. Daly, A. Shmeliov, U. Khan, G. Duesberg, *ACS Nano* **2016**, *10*, 3702-3713.

[140] J. Ouyang, *Displays* **2013**, *34*, 423-436.

[141] H. Zhong, A. He, J. Lu, M. Sun, J. He, L. Zhang, *J. Power Sources* **2016**, *336*, 107-114.

[142] A. Magasinski, B. Zdyrko, I. Kovalenko, B. Hertzberg, R. Burtovyy, C. F. Huebner, T. F. Fuller, I. Luzinov, G. Yushin, *ACS Appl. Mater. Interfaces* **2010**, *2*, 3004-3010.

[143] M. Ling, J. Qiu, S. Li, C. Yan, M. J. Kiefel, G. Liu, S. Zhang, *Nano Lett.* **2015**, *15*, 4440-4447.

[144] G. Zheng, Y. Yang, J. J. Cha, S. S. Hong, Y. Cui, *Nano Lett.* **2011**, *11*, 4462-4467.

[145] R. Deng, M. Wang, H. Yu, S. Luo, J. Li, F. Chu, B. Liu, F. Wu, *Energy Environ. Mater.* **2022**, *5*, 777-799.

[146] W. Kang, N. Deng, J. Ju, Q. Li, D. Wu, X. Ma, L. Li, M. Naebe, B. Cheng, *Nanoscale* **2016**, *8*, 16541-16588.

[147] D.-W. Wang, Q. Zeng, G. Zhou, L. Yin, F. Li, H.-M. Cheng, I. R. Gentle, G. Q. M. Lu, *J. Mater. Chem. A* **2013**, *1*, 9382-9394.

[148] D. Bresser, S. Passerini, B. Scrosati, *Chem. Commun.* **2013**, *49*, 10545-10562.

[149] T. Li, X. Bai, U. Gulzar, Y. J. Bai, C. Capiglia, W. Deng, X. Zhou, Z. Liu, Z. Feng, R. Proietti Zaccaria, *Adv. Funct. Mater.* **2019**, *29*, 1901730.

[150] S. J. Visco, L. C. DeJonghe, *J. Electrochem. Soc.* **1988**, *135*, 2905.

[151] P. G. Bruce, S. A. Freunberger, L. J. Hardwick, J.-M. Tarascon, *Nat. Mater.* **2012**, *11*, 19-29.

[152] K. Abraham, Z. Jiang, *J. Electrochem. Soc.* **1996**, *143*, 1.

[153] C. V. Amanchukwu, J. R. Harding, Y. Shao-Horn, P. T. Hammond, *Chem. Mater.* **2015**, *27*, 550-561.

[154] V. S. Bryantsev, V. Giordani, W. Walker, M. Blanco, S. Zecevic, K. Sasaki, J. Uddin, D. Addison, G. V. Chase, *J. Phys. Chem. A.* **2011**, *115*, 12399-12409.

[155] R. Black, S. H. Oh, J.-H. Lee, T. Yim, B. Adams, L. F. Nazar, *J. Am. Chem. Soc.* **2012**, *134*, 2902-2905.

[156] G. Girishkumar, B. McCloskey, A. C. Luntz, S. Swanson, W. Wilcke, *J. Phys. Chem. Lett.* **2010**, *1*, 2193-2203.

[157] T. Janoschka, M. D. Hager, U. S. Schubert, *Adv. Mater.* **2012**, *24*, 6397-6409.

[158] L. Shacklette, M. Maxfield, S. Gould, J. Wolf, T. Jow, R. Baughman, *Synth. Met.* **1987**, *18*, 611-618.

[159] K. Nakahara, S. Iwasa, M. Satoh, Y. Morioka, J. Iriyama, M. Suguro, E. Hasegawa, *Chem. Phys. Lett.* **2002**, *359*, 351-354.

[160] T. Suga, H. Ohshiro, S. Ugita, K. Oyaizu, H. Nishide, *Adv. Mater.* **2009**, *21*, 1627-1630.

[161] K. Nakahara, S. Iwasa, J. Iriyama, Y. Morioka, M. Suguro, M. Satoh, E. J. Cairns, *Electrochim. Acta* **2006**, *52*, 921-927.

[162] J.-K. Kim, J.-H. Ahn, G. Cheruvally, G. S. Chauhan, J.-W. Choi, D.-S. Kim, H.-J. Ahn, S. H. Lee, C. E. Song, *Met. Mater. Int.* **2009**, *15*, 77-82.

[163] Y. Wang, C. Liu, R. Pan, Z. Chen, *Energy* **2017**, *121*, 739-750.

[164] L. Kong, L. Wang, J. Zhu, J. Bian, W. Xia, R. Zhao, H. Lin, Y. Zhao, *Chem. Commun.* **2021**, *57*, 12587-12594.

[165] C. Fang, J. Li, M. Zhang, Y. Zhang, F. Yang, J. Z. Lee, M.-H. Lee, J. Alvarado, M. A. Schroeder, Y. Yang, B. Lu, N. Williams, M. Ceja, L. Yang, M. Cai, J. Gu, K. Xu, X. Wang, Y. S. Meng, *Nature* **2019**, *572*, 511-515.

[166] C. Monroe, J. Newman, *J. Electrochem. Soc.* **2005**, *152*, A396.

[167] K. L. Jungjohann, R. N. Gannon, S. Goriparti, S. J. Randolph, L. C. Merrill, D. C. Johnson, K. R. Zavadil, S. J. Harris, K. L. Harrison, *ACS Energy Lett.* **2021**, *6*, 2138-2144.

[168] B. Li, Y. Chao, M. Li, Y. Xiao, R. Li, K. Yang, X. Cui, G. Xu, L. Li, C. Yang, *Electrochem. Energy Rev.* **2023**, *6*, 7.

[169] K. Funke, *Sci. Technol. Adv. Mater.* **2013**, *14*, 043502.

[170] M. Faraday, *Philos. Trans. R. Soc. London* **1839**, 1-12.

[171] C. Tubandt, F. Lorenz, *Z. Phys. Chem.* **1914**, *87*, 543-561.

[172] B. Owens, M. Munshi, in *Proceedings of the Symposium on History of Battery Technology, Vol. 87*, Electrochemical Society, **1987**, p. 199.

[173] M. D. Ingram, *J. Non-Cryst. Solids* **1991**, *131*, 955-960.

[174] P. V. Wright, *J. Macromol. Sci.-Chem.* **1989**, *26*, 519-550.

[175] P. V. Wright, *Br. Polym. J.* **1975**, *7*, 319-327.

[176] M. B. Armand, *Annu. Rev. Mater. Sci.* **1986**, *16*, 245-261.

[177] J. Janek, W. G. Zeier, *Nat. Energy* **2016**, *1*, 1-4.

[178] D. Karabelli, K. P. Birke, M. Weeber, *Batteries* **2021**, *7*, 18.

[179] J. Lau, R. H. DeBlock, D. M. Butts, D. S. Ashby, C. S. Choi, B. S. Dunn, *Adv. Energy Mater.* **2018**, *8*, 1800933.

[180] N. Minafra, S. P. Culver, C. Li, A. Senyshyn, W. G. Zeier, *Chemistry of Materials* **2019**, *31*, 3794-3802.

[181] C. Cao, Z.-B. Li, X.-L. Wang, X.-B. Zhao, W.-Q. Han, *Front. Energy Res.* **2014**, *2*, 25.

[182] R. Kanno, T. Hata, Y. Kawamoto, M. Irie, *Solid State Ionics* **2000**, *130*, 97-104.

[183] N. Kamaya, K. Homma, Y. Yamakawa, M. Hirayama, R. Kanno, M. Yonemura, T. Kamiyama, Y. Kato, S. Hama, K. Kawamoto, *Nat. Mater.* **2011**, *10*, 682-686.

[184] P. Bron, S. Johansson, K. Zick, J. r. Schmedt auf der Günne, S. Dehnen, B. Roling, *J. Am. Chem. Soc.* **2013**, *135*, 15694-15697.

[185] S. Wenzel, S. Randau, T. Leichtweiß, D. A. Weber, J. Sann, W. G. Zeier, J. r. Janek, *Chemistry of Materials* **2016**, *28*, 2400-2407.

[186] Z. Zhang, S. Chen, J. Yang, J. Wang, L. Yao, X. Yao, P. Cui, X. Xu, *ACS Appl. Mater. Interfaces* **2018**, *10*, 2556-2565.

[187] R. P. Rao, S. Adams, *Phys. Status. Solidi. A.* **2011**, *208*, 1804-1807.

[188] Y.-G. Lee, S. Fujiki, C. Jung, N. Suzuki, N. Yashiro, R. Omoda, D.-S. Ko, T. Shiratsuchi, T. Sugimoto, S. Ryu, *Nat. Energy* **2020**, *5*, 299-308.

[189] D. Ravaine, *J. Non-Cryst. Solids* **1980**, *38*, 353-358.

[190] M. Tatsumisago, *Solid State Ionics* **2004**, *175*, 13-18.

[191] N. Machida, T. Shigematsu, *Chem. Lett.* **2004**, *33*, 376-377.

[192] M. Tatsumisago, M. Nagao, A. Hayashi, *J. Asian Ceram.* **2013**, *1*, 17-25.

[193] J. Schnell, T. Günther, T. Knoche, C. Vieider, L. Köhler, A. Just, M. Keller, S. Passerini, G. Reinhart, *J. Power Sources* **2018**, *382*, 160-175.

[194] P. Knauth, *Solid State Ionics* **2009**, *180*, 911-916.

[195] R. Murugan, V. Thangadurai, W. Weppner, *Ang. Chem. Int. Ed.* **2007**, *46*, 7778.

[196] A. Dumon, M. Huang, Y. Shen, C.-W. Nan, *Solid State Ionics* **2013**, *243*, 36-41.

[197] I. Kokal, M. Somer, P. Notten, H. Hintzen, *Solid State Ionics* **2011**, *185*, 42-46.

[198] A. Duvel, A. Kuhn, L. Robben, M. Wilkening, P. Heitjans, *J. Phys. Chem. C.* **2012**, *116*, 15192-15202.

[199] Y. Jin, P. J. McGinn, *Electrochim. Acta* **2013**, *89*, 407-412.

[200] O. Bohnke, *Solid State Ionics* **2008**, *179*, 9-15.

[201] J. A. Alonso, J. Sanz, J. Santamaría, C. León, A. Várez, M. T. Fernández-Díaz, *Angew. Chem.* **2000**, *112*, 633-635.

[202] C. W. Ban, G. M. Choi, *Solid State Ionics* **2001**, *140*, 285-292.

[203] C. Chen, K. Amine, *Solid State Ionics* **2001**, *144*, 51-57.

[204] Z. Jian, Y. S. Hu, X. Ji, W. Chen, *Adv. Mater.* **2017**, *29*, 1601925.

[205] J. Fu, *Solid State Ionics* **1997**, *96*, 195-200.

[206] S.-G. Ling, J.-Y. Peng, Q. Yang, J.-L. Qiu, J.-Z. Lu, H. Li, *Chin. Phys. B* **2018**, *27*, 038201.

[207] B. Key, D. J. Schroeder, B. J. Ingram, J. T. Vaughey, *Chemistry of materials* **2012**, *24*, 287-293.

[208] Z. Wu, Z. Xie, A. Yoshida, Z. Wang, X. Hao, A. Abudula, G. Guan, *Renewable Sustainable Energy Rev.* **2019**, *109*, 367-385.

[209] C. Yada, Y. Iriyama, T. Abe, K. Kikuchi, Z. Ogumi, *Electrochem. Commun.* **2009**, *11*, 413-416.

[210] J. Wolfenstine, J. L. Allen, J. Sakamoto, D. J. Siegel, H. Choe, *Ionics* **2018**, *24*, 1271-1276.

[211] L. Yue, J. Ma, J. Zhang, J. Zhao, S. Dong, Z. Liu, G. Cui, L. Chen, *Energy Storage Materials* **2016**, *5*, 139-164.

[212] C. Berthier, W. Gorecki, M. Minier, M. Armand, J. Chabagno, P. Rigaud, *Solid State Ionics* **1983**, *11*, 91-95.

[213] W. H. Meyer, *Adv. Mater.* **1998**, *10*, 439-448.

[214] W. Gorecki, M. Jeannin, E. Belorizky, C. Roux, M. Armand, *J. Phys.: Condens. Matter* **1995**, *7*, 6823.

[215] M. Marzantowicz, F. Krok, J. R. Dygas, Z. Florjańczyk, E. Zygadło-Monikowska, *Solid State Ionics* **2008**, *179*, 1670-1678.

[216] S. Kripotou, C. Psylla, K. Kyriakos, K. N. Raftopoulos, J. Zhao, G. Zhang, S. Pispas, C. M. Papadakis, A. Kyritsis, *Macromolecules* **2016**, *49*, 5963-5977.

[217] W. Gorecki, M. Jeannin, E. Belorizky, C. Roux, M. Armand, *J. Phys.: Condens. Matter* **1995**, *7*, 6823.

[218] R. Bouchet, S. Maria, R. Meziane, A. Aboulaich, L. Lienafa, J.-P. Bonnet, T. N. Phan, D. Bertin, D. Gigmes, D. Devaux, *Nat. Mater.* **2013**, *12*, 452-457.

[219] L. Edman, A. Ferry, M. M. Doeff, *J. Mater. Res.* **2000**, *15*, 1950-1954.

[220] C. Yi, W. Liu, L. Li, H. Dong, J. Liu, *Funct. Mater. Lett.* **2019**, *12*, 1930006.

[221] R. Tanaka, M. Sakurai, H. Sekiguchi, H. Mori, T. Murayama, T. Ooyama, *Electrochim. Acta* **2001**, *46*, 1709-1715.

[222] P. P. Soo, B. Huang, Y. I. I. Jang, Y. M. Chiang, D. R. Sadoway, A. M. Mayes, *J. Electrochem. Soc.* **1999**, *146*, 32-37.

[223] F. Yuan, H.-Z. Chen, H.-Y. Yang, H.-Y. Li, M. Wang, *Mater. Chem. Phys.* **2005**, *89*, 390-394.

[224] D. R. Sadoway, *J. Power Sources* **2004**, *129*, 1-3.

[225] M. Watanabe, T. Endo, A. Nishimoto, K. Miura, M. Yanagida, *J. Power Sources* **1999**, *81-82*, 786-789.

[226] S. Li, K. Jiang, J. Wang, C. Zuo, Y. H. Jo, D. He, X. Xie, Z. Xue, *Macromolecules* **2019**, *52*, 7234-7243.

[227] Y. Yu, Y. Cheng, J. Ren, E. Cao, X. Fu, W. Guo, *J. Appl. Polym. Sci.* **2015**, *132*.

[228] Y. Ito, K. Kanehori, K. Miyauchi, T. Kudo, *J. Mater. Sci.* **1987**, *22*, 1845-1849.

[229] C. W. Walker, M. Salomon, *J. Electrochem. Soc.* **1993**, *140*, 3409.

[230] M. S. Michael, M. M. E. Jacob, S. R. S. Prabaharan, S. Radhakrishna, *Solid State Ionics* **1997**, *98*, 167-174.

[231] A. Manuel Stephan, *Eur. Polym. J.* **2006**, *42*, 21-42.

[232] L. Long, S. Wang, M. Xiao, Y. Meng, *J. Mater. Chem. A.* **2016**, *4*, 10038-10069.

[233] S. B. Aziz, T. J. Woo, M. F. Z. Kadir, H. M. Ahmed, *J. Sci.: Adv. Mater. Devices* **2018**, *3*, 1-17.

[234] J.-W. Choi, G. Cheruvally, Y.-H. Kim, J.-K. Kim, J. Manuel, P. Raghavan, J.-H. Ahn, K.-W. Kim, H.-J. Ahn, D. S. Choi, *Solid State Ionics* **2007**, *178*, 1235-1241.

[235] G. Appetecchi, S. Scaccia, S. Passerini, *J. Electrochem. Soc.* **2000**, *147*, 4448.

[236] W. Wang, E. Yi, A. J. Fici, R. M. Laine, J. Kieffer, *J. Phys. Chem. C.* **2017**, *121*, 2563-2573.

[237] A. Manuel Stephan, K. S. Nahm, *Polymer* **2006**, *47*, 5952-5964.

[238] B. Scrosati, F. Croce, L. Persi, *J. Electrochem. Soc.* **2000**, *147*, 1718.

[239] W. Wang, E. Yi, A. J. Fici, R. M. Laine, J. Kieffer, *J. Phys. Chem. C.* **2017**, *121*, 2563-2573.

[240] H. Yang, N. Wu, *Energy Sci. Eng.* **2022**, *10*, 1643-1671.

[241] M. Dirican, C. Yan, P. Zhu, X. Zhang, *Mater. Sci. Eng. R Rep.* **2019**, *136*, 27-46.

[242] D. Zhou, D. Shanmukaraj, A. Tkacheva, M. Armand, G. Wang, *Chem* **2019**, *5*, 2326-2352.

[243] S. Guhathakurta, K. Min, *Polymer* **2010**, *51*, 211-221.

[244] Y. Luo, L. Gao, W. Kang, *J. Energy Chem.* **2024**, *89*, 543-556.

[245] D. J. Bannister, G. R. Davies, I. M. Ward, J. E. McIntyre, *Polymer* **1984**, *25*, 1291-1296.

[246] C. Cao, Y. Li, Y. Feng, P. Long, H. An, C. Qin, J. Han, S. Li, W. Feng, *J. Mater. Chem. A.* **2017**, *5*, 22519-22526.

[247] K. Deng, Q. Zeng, D. Wang, Z. Liu, Z. Qiu, Y. Zhang, M. Xiao, Y. Meng, *J. Mater. Chem. A.* **2020**, *8*, 1557-1577.

[248] M. Heishi, H. Niwa, T. Uno, M. Kubo, T. Itoh, *Electrochim. Acta* **2013**, *114*, 54-59.

[249] T. Itoh, Y. Mitsuda, T. Ebina, T. Uno, M. Kubo, *J. Power Sources* **2009**, *189*, 531-535.

[250] W. W. Cui, D. Y. Tang, *J. App. Polym. Sci.* **2012**, *126*, 510-518.

[251] R. Meziane, J.-P. Bonnet, M. Courty, K. Djellab, M. Armand, *Electrochim. Acta* **2011**, *57*, 14-19.

[252] Q. Shi, L. Xue, D. Qin, B. Du, J. Wang, L. Chen, *J. Mater. Chem. A.* **2014**, *2*, 15952-15957.

[253] Y. Zhu, X. Gao, X. Wang, Y. Hou, L. Liu, Y. Wu, *Electrochem. Commun.* **2012**, *22*, 29-32.

[254] S. Feng, D. Shi, F. Liu, L. Zheng, J. Nie, W. Feng, X. Huang, M. Armand, Z. Zhou, *Electrochim. Acta* **2013**, *93*, 254-263.

[255] A. M. Stephan, T. Prem Kumar, N. Angulakshmi, P. Salini, R. Sabarinathan, A. Srinivasan, S. Thomas, *J. Appl. Polym. Sci.* **2011**, *120*, 2215-2221.

[256] S. Lou, F. Zhang, C. Fu, M. Chen, Y. Ma, G. Yin, J. Wang, *Adv. Mater.* **2021**, *33*, 2000721.

[257] M. Wittig, P. Pfändner, B. Rieger, *Polymer Chemistry* **2024**, *15*, 3071-3076.

[258] D. Obermayer, D. Znidar, G. Glotz, A. Stadler, D. Dallinger, C. O. Kappe, *J. Org. Chem.* **2016**, *81*, 11788-11801.

[259] T. Janosik, H. Shirani, N. Wahlström, I. Malky, B. Stensland, J. Bergman, *Tetrahedron* **2006**, *62*, 1699-1707.

[260] H. Mikula, D. Svatunek, D. Lumpi, F. Glöcklhofer, C. Hametner, J. Fröhlich, *Org. Process Res. Dev.* **2013**, *17*, 313-316.

[261] A. Baumstark, P. Vasquez, *J. Org. Chem.* **1988**, *53*, 3437-3439.

[262] S. Laha, R. Kumar, *J. Catal.* **2001**, *204*, 64-70.

[263] E. T. ba Saka, I. Acar, H. Kantekin, İ. Kani, *Synth. Met.* **2013**, *169*, 12-17.

[264] T.-S. Lai, S. K. Lee, L.-L. Yeung, H.-Y. Liu, I. D. Williams, C. K. Chang, *Chem. Commun.* **2003**, 620-621.

[265] M. Palucki, P. J. Pospisil, W. Zhang, E. N. Jacobsen, *J. Am. Chem. Soc.* **1994**, *116*, 9333-9334.

[266] H. R. Allcock, D. T. Welna, A. E. Maher, *Solid State Ionics* **2006**, *177*, 741-747.

[267] A. Wurtz, *Ann. Chim. Phys* **1863**, *69*, 317-354.

[268] J. Herzberger, K. Niederer, H. Pohlit, J. Seiwert, M. Worm, F. R. Wurm, H. Frey, *Chem. Rev.* **2016**, *116*, 2170-2243.

[269] O. Nuyken, S. D. Pask, *Polymers* **2013**, *5*, 361-403.

[270] M. Moeller, K. Matyjaszewski, *Polymer science: a comprehensive reference*, Newnes, **2012**.

[271] A.-L. Brocas, C. Mantzaridis, D. Tunc, S. Carlotti, *Prog. Polym. Sci.* **2013**, *38*, 845-873.

[272] C. Mangold, F. Wurm, B. Obermeier, H. Frey, *Macromol. Rapid Commun.* **2010**, *31*, 258-264.

[273] S. Hiki, K. Kataoka, *Bioconjugate Chem.* **2010**, *21*, 248-254.

[274] H. Otsuka, Y. Nagasaki, K. Kataoka, *Langmuir* **2004**, *20*, 11285-11287.

[275] Y. Xie, S. Duan, M. L. Forrest, *Drug Discoveries Ther.* **2010**, *4*, 240.

[276] Y. Sarazin, J.-F. Carpentier, *Chem. Rev.* **2015**, *115*, 3564-3614.

[277] N. Spassky, *Makromolekulare Chemie. Macromolecular Symposia* **1991**, *42-43*, 15-49.

[278] I. Dimitrov, C. Tsvetanov, *Polymer Science: a comprehensive reference* **2012**, 551-569.

[279] N. Hadjichristidis, H. Iatrou, S. Pispas, M. Pitsikalis, *J. Polym. Sci. A. Polym. Chem.* **2000**, *38*, 3211-3234.

[280] H. L. Hsieh, *Journal of Polymer Science Part A: General Papers* **1965**, *3*, 153-161.

[281] I. Natori, S. Inoue, *Macromolecules* **1998**, *31*, 4687-4694.

[282] C. Billouard, S. Carlotti, P. Desbois, A. Deffieux, *Macromolecules* **2004**, *37*, 4038-4043.

[283] D. Chakraborty, A. Rodriguez, E. Y.-X. Chen, *Macromolecules* **2003**, *36*, 5470-5481.

[284] H. Schlaad, H. Kukula, J. Rudloff, I. Below, *Macromolecules* **2001**, *34*, 4302-4304.

[285] H. Misaka, R. Sakai, T. Satoh, T. Kakuchi, *Macromolecules* **2011**, *44*, 9099-9107.

[286] M. I. Childers, J. M. Longo, N. J. Van Zee, A. M. LaPointe, G. W. Coates, *Chem. Rev.* **2014**, *114*, 8129-8152.

[287] S. Klaus, M. W. Lehenmeier, C. E. Anderson, B. Rieger, *Coord. Chem. Rev.* **2011**, *255*, 1460-1479.

[288] G. Schwach, J. Coudane, R. Engel, M. Vert, *J. Polym. Sci. A. Polym. Chem.* **1997**, *35*, 3431-3440.

[289] C. A. L. Lidston, S. M. Severson, B. A. Abel, G. W. Coates, *ACS Catal.* **2022**, *12*, 11037-11070.

[290] N. D. Harrold, Y. Li, M. H. Chisholm, *Macromolecules* **2013**, *46*, 692-698.

[291] S. Abbina, V. K. Chidara, G. Du, *ChemCatChem* **2017**, *9*, 1343-1348.

[292] D. Weisblat, B. Magerlein, D. Myers, *J. Am. Chem. Soc.* **1953**, *75*, 3630-3632.

[293] T. Ozaki, H. Yorimitsu, G. J. Perry, *Chemistry–A European Journal* **2021**, *27*, 15387-15391.

[294] G. Sabitha, S. Abraham, B. S. Reddy, J. Yadav, *Synlett* **1999**, *1999*, 1745-1746.

[295] Q. Ma, Y. Xia, W. Feng, J. Nie, Y.-S. Hu, H. Li, X. Huang, L. Chen, M. Armand, Z. Zhou, *RSC Adv.* **2016**, *6*, 32454-32461.

[296] Z. Li, J. v. Lier, C. C. Leznoff, *Can. J. Chem.* **1999**, *77*, 138-145.

[297] M. S. Batra, R. Dwivedi, R. Prasad, *ChemistrySelect* **2019**, *4*, 11636-11673.

[298] V. Percec, B. Barboiu, *Macromolecules* **1995**, *28*, 7970-7972.

[299] C. R. Martins, G. Ruggeri, M.-A. De Paoli, *J. Braz. Chem. Soc.* **2003**, *14*, 797-802.

[300] C.-M. Yang, B. Zibrowius, W. Schmidt, F. Schüth, *Chemistry of Materials* **2004**, *16*, 2918-2925.

[301] X. Zhuang, X. Qian, J. Lv, Y. Wan, *Appl. Surf. Sci.* **2010**, *256*, 5343-5348.

[302] S. Feng, D. Shi, F. Liu, L. Zheng, J. Nie, W. Feng, X. Huang, M. Armand, Z. Zhou, *Electrochim. Acta* **2013**, *93*, 254-263.

[303] S. L. Malhotra, J. Hesse, L.-P. Blanchard, *Polymer* **1975**, *16*, 81-93.

[304] C. Zhao, L. Liu, X. Qi, Y. Lu, F. Wu, J. Zhao, Y. Yu, Y. S. Hu, L. Chen, *Adv. Energy Mater.* **2018**, *8*, 1703012.

[305] M. A. Alisi, N. Cazzolla, R. Costi, R. Di Santo, G. Furlotti, A. Guglielmotti, L. Polenzani, Google Patents, **2014**.

List of figures

List of schemes

List of tables

Publications

The following published publication is included in parts of this thesis:

M. Wittig, P. Pfändner, B. Rieger, *Polymer Chemistry* **2024**; title: Synthesis of a sulfonamide functionalized poly(styrene oxide) and illustration of a potential post-polymerization strategy

The following published publication is beyond the scope of this thesis:

C. Thomas[+], M. Wittig[+], B. Rieger, *ChemCatChem* **2022**, *14*, e202200841; title: The puzzling question about the origin of the second electron in the molecular photocatalytic reduction of CO_2

[+]these authors contributed equally to this work

Conference contributions

Macromolecular Colloquium Freiburg 2023, 16-17 February 2023; poster title: Synthesis of a conceptual new single ion-conducting polymer electrolyte (SICPE) for all-solid-state batteries

244th ECS meeting Gothenburg, Sweden, 8-12 October 2023; poster title: Synthesis of a conceptual new single ion-conducting polymer electrolyte for all-solid-state batteries

ACS Spring 2024 New Orleans, America, 17-21 March; poster title: Design concept of a PEO-based single-ion conducting polymer electrolyte for all-solid-state batteries